Applications of superparamagnetic nanoparticles for the separation and recovery of PGM metals from acidic wastewater solutions

By Joyce Tsepiso Khutlane

Dissertation presented for the Degree of Doctor of Philosophy at Stellenbosch University

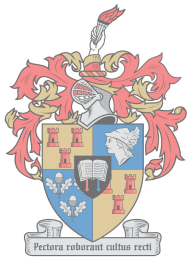

UNIVERSITEIT
iYUNIVESITHI
STELLENBOSCH
UNIVERSITY

Promotor: Dr. Rehana Malgas-Enus

Co-promotor: Prof Klaus R. Koch

Faculty of Science

December 2018

Stellenbosch University https://scholar.sun.ac.za

DECLARATION

By submitting this thesis/dissertation electronically, I declare that the entirety of the work contained therein is my own, original work, that I am the sole author thereof (save to the extent explicitly otherwise stated), that reproduction and publication thereof by Stellenbosch University will not infringe any third-party rights and that I have not previously in its entirety or in part submitted it for obtaining any qualification.

Joyce Tsepiso Khutlane

Copyright © 2018 Stellenbosch University

All rights reserved

Stellenbosch University https://scholar.sun.ac.za

ABSTRACT

South Africa is one of the leading countries in the production of precious metals (Au and PGMs). The refinery final stages for recovering precious metals makes use of two hydrometallurgical processes: solvent extraction and extraction with ion exchangers. Even though both methods improved the recovery of these metals from the ore, they still suffer from setbacks ranging from large amounts of secondary waste solutions, expensive solvents and resins, and filtration in terms of the use of ion exchange resins for extraction. Therefore, a need for the development of simple and environmentally friendly refining processes is required to minimize the recurrence of the abovementioned setbacks.

Naked magnetic iron oxide nanoparticles (MIONs) are promising materials for adsorption studies of metal ions/complexes from wastewater due to their versatile magnetic properties, which allow a facile remote control, separation and analyte recovery from solution. This work makes use of magnetite nanoparticles (MIONs) which are superparamagnetic and less expensive compared to adsorbents used by the South African refineries for extraction of Au(III)-Cl, Pd(II)-Cl and Pt(IV)-Cl complexes from acidic aqueous solutions.

Synthesis of naked MIONs was carried out by using the chemical co-precipitation method. Naked MIONs successfully sorbed Au(III), Pd(II) and Pt(IV) complexes from acidic aqueous solutions, showing a higher adsorption affinity for Au(III)-Cl species compared to Pd(II) and Pt(IV) species. The adsorption kinetics of the three metal complexes using naked MIONs followed a *pseudo*-second-order kinetic mode, indicating that the chemical adsorption was the rate-limiting step. The equilibrium adsorption of Au(III)-Cl species onto naked MIONs at pH 1.0, pH 3.0 and pH 5.0, was fitted with Langmuir adsorption isotherms. It was found that the experimental data was in reasonably good agreement with the Langmuir model, suggesting that Au forms a monolayer coverage on the surface of naked MIONs. The adsorption capacities were as follows: 10.44 $mg.g^{-1}$, 18.98 $mg.g^{-1}$, and 27.25 $mg.g^{-1}$ respectively. The proposed mechanism responsible for adsorption of Au(III), Pd(II) and Pt(IV) complexes onto naked MIONs was governed by the electrostatic attractions and metal reduction. These naked MIONs were found to be unstable at pH1, which is usually the conditions used for extraction in the mining industry.

Stellenbosch University https://scholar.sun.ac.za

To circumvent this problem, the surface of MIONs was functionalised with aliphatic carboxylic acids, dendrimer micelles and then with both carboxylic acids and dendrimer micelles. Characterisation of naked MIONs and functionalised MIONs was carried out by IR, PXRD, FESEM, HRTEM and ICP-OES. Competitive adsorption of Au(III), Pd(II), and Pt(IV) complexes onto naked MIONs and functionalised MIONs was explored by varying solution pH and the contact time. The dendrimer micelles played a vital role in adsorption of Pd(II) and Pt(IV) complexes. Adsorption kinetics followed a *pseudo*-second-order kinetics model. The adsorption isotherms all obeyed the Langmuir model in the case of Au(III), Pd(II), and Pt(IV) complexes by naked MIONs and, adsorption isotherm for Au(III) and Pd(II) complexes using modified MIONs obeyed Langmuir, while adsorption of Pt(IV) species followed the Freundlich model. The desorption studies showed that the best desorption reagents were 1.0 M HNO_3 and 1.0 M HNO_3/0.5 M thiourea. The modified MIONs were stable at low pH, even at pH1, and the extraction potential of the modified MIONs were comparable to that of the naked MIONs.

Stellenbosch University https://scholar.sun.ac.za

OPSOMMING

Suid-Afrika is een van die voorste lande in die vervaardiging van edelmetale (Au en PGM's). Die finale stappe van die raffinadery vir die herstel van edelmetale, maak gebruik van twee hidrometallurgiese prosesse: oplosmiddel ekstraksie en ekstraksie met ioonuitruilers. Alhoewel beide metodes die herstel van hierdie metale van die erts verbeter het, ly hulle steeds aan terugslae wat wissel van groot hoeveelhede sekondêre afvaloplossings, duur oplosmiddels en harse, en filtrasie in terme van die gebruik van ioonruilharse vir ekstraksie. Daarom is 'n behoefte aan die ontwikkeling van eenvoudige en omgewingsvriendelike verfyningsprosesse nodig om die herhaling van bogenoemde terugslae te verminder.

Naakte magnetiese ysteroksiednanodeeltjies (MION's) is ‘n belowende materiaal vir adsorpsiestudies van metaalione/komplekse uit afvalwater as gevolg van hul veelsydige magnetiese eienskappe, wat 'n maklike afstandbeheer, skeiding en analietherstel van oplossing moontlik maak. Hierdie werk maak dus gebruik van magnetietnanodeeltjies (MION's) wat superparamagneties en goedkoper is in vergelyking met adsorbente wat deur die Suid-Afrikaanse raffinaderye gebruik word as ekstraktante vir Au (III)-Cl, Pd(II)-Cl en Pt(IV)]-Cl-komplekse uit suurwaterige oplossings.

Sintese van naakte MION's is uitgevoer met behulp van die chemiese ko-presipitasie metode. Naakte MIONs het die Au(III), Pd(II) en Pt(IV) komplekse suksesvol ekstrak van suurwaterige oplossings, die Au(III)Cl spesies toon ‘n hoër absorpsie affiniteit as vir Pd(II) en Pt(IV) spesies. Die adsorpsiekinetika van die drie metaalkomplekse wat naakte MION's gebruik het, volg ‘n *pseudo*-tweede-orde kinetiese modus, wat aandui dat die chemiese adsorpsie die tempobeperkende stap was. Die ewewigsabsorpsie van die Au(III)-Cl spesies op naakte MION's by pH 1.0, pH 3.0 en pH 5.0, was aangepas met Langmuir-adsorpsie-isoterme. Daar is bevind dat die eksperimentele data in 'n redelike goeie ooreenkoms met die Langmuir-model was, wat monolaag dekking van Au op die oppervlak van naakte MIONs voorgestel het. Die adsorpsiekapasiteite was soos volg: 10.44 $mg.g^{-1}$, 18.98 $mg.g^{-1}$ en 27.25 $mg.g^{-1}$ onderskeidelik. Die voorgestelde meganisme wat verantwoordelik is vir die adsorpsie van Au(III), Pd(II) en Pt(IV) komplekse op naakte MION's, is beheer deur die elektrostatiese aantreklikhede en metaalreduksie. Hierdie naakte MIONs was onstabiel by pH1, wat gewoonlik die kondisie is wat gebruik word in die mynbedryf.

Stellenbosch University https://scholar.sun.ac.za

Om hierdie probleem te omseil, is die oppervlak van MION's gefunksionaliseer met alifatiese karboksielsure, dendrimeermiselle en dan met beide karboksielsure en dendrimeermiselle. Karakterisering van naakte MION's en gefunksionaliseerde MION's is uitgevoer deur IR, PXRD, FESEM, HRTEM en ICP-OES. Kompeterende adsorpsie van Au(III), Pd(II) en Pt(IV) komplekse op naakte MION's en gefunksionaliseerde MION's is ondersoek deur verskillende oplossing pH en die kontaktyd. Die dendrimeermiselle het 'n belangrike rol gespeel in die adsorpsie van Pd(II) en Pt(IV) komplekse. Adsorbsiekinetika volg die pseudo-tweede-orde kinetika model. Die adsorpsie-isoterme was gehoorsaam aan die Langmuir-model in die geval van Au(III), Pd(II) en Pt(IV) komplekse deur naakte MION's en adsorptie isoterm vir Au(III) en Pd(II) komplekse deur gefunksionaliseerde MIONs volg Langmuir, terwyl adsorpsie van Pt(IV) spesies die Freundlich-model gevolg het. Die desorptiestudies het getoon dat die beste desorpsie-reagense 1,0 M HNO_3 en 1.0 M HNO_3 / 0.5 M tiokoors was. Die gefunksionaliseerde MIONs was stabiel teen lae pH en selfs teen pH1, terwyl die ekstraksie potensiaal vergelykbaar was met dit van die naakte MIONs.

Stellenbosch University https://scholar.sun.ac.za

ACKNOWLEDGEMENTS

With the deepest gratitude I wish to thank the following people and organisations:

My supervisor Dr Rehana Malgas-Enus for her supervision, guidance, encouragement, and an unwavering support throughout my postgraduate studies. I don't have enough words to express my gratitude to her. A big thank you to my co-supervisor Prof Klaus R. Koch for his support and contribution to this work. My colleagues at RME-Nano group (especially Dr Angelique Blanckenberg) and PGMs group.

I would also thank the following people and their organisations

- Stellenbosch University for hosting me
- Stellenbosch University technical staff at Central Analytical Facility (CAF)
- Two Stellenbosch University researchers and their research groups
    - Prof Selwyn Mapolie and Dr Robert Luckay
- Electron Microscope Unit at the University of the Western Cape for assistance with transmission electron microscopy (TEM) imaging.
- Powder X ray diffraction at iThemba Labs: Dr Remy
- Powder X ray diffraction at the University of Johannesburg: Dr Nomvano Mketo

A big thank you to my family: Palesa Khutlane, Malihobo Khutlane, my brother Tefo V. Khutlane and extended family. The following two people supported me when I was at the point of giving up: Mr Lerato Lerato and Dr Nomvano Mketo. From the bottom of my heart, thank you!

Another big thank you to the following people for their love and support: Motena Mapesela, **Likeleko Damane**, Oluwatimilehin Okeowo, Hezron Ogutu, Manana Moletsane, Verusca Naicker, Dr Olufemi Olaoye, Claire Naize, Dr Lebusetsa Taleli, Maponts'o Mosili, Dr Mosotho George and Jack Phatsoane.

None of this work would have been possible without generous funding from the Department of Chemistry and Polymer science, Stellenbosch University and NRF.

Above all, I give my thanks to my Lord Jesus Christ, for it is through His kindness that everything became possible. He deserves all the glory.

Stellenbosch University https://scholar.sun.ac.za

TABLE OF CONTENTS

Stellenbosch University https://scholar.sun.ac.za

Stellenbosch University https://scholar.sun.ac.za

Stellenbosch University https://scholar.sun.ac.za

Stellenbosch University https://scholar.sun.ac.za

Stellenbosch University https://scholar.sun.ac.za

Stellenbosch University https://scholar.sun.ac.za

Stellenbosch University https://scholar.sun.ac.za

LIST OF ABBREVIATIONS

^{13}C NMR	carbon nuclear magnetic resonance
^{1}H NMR	proton nuclear magnetic resonance
ATR	attenuated total reflectance
C5-acid	hexanoic acid
C11-acid	lauric acid
C15-acid	palmitic acid
C_{aq}	metal ions concentration in aqueous solution after adsorption
C_e	metal ions equilibrium concentration
C_i	metal ion initial concentration
Cn-G3 DAB PPI	generation 3 diaminobutane poly(propylene imine) dendrimer micelles
Cn-acid	aliphatic carboxylic acids (fatty acids)
DAB-PPI	diaminobutane poly(propylene imine)
DENs	dendrimer encapsulated nanoparticles
DD	deionised distilled
DTA	differential thermal analysis
FESEM	field emission scanning electron microscopy
FTIR	Fourier transform infrared spectroscopy
FWHM	full width at half maximum height
G3 DAB-PPI	generation 3 diaminobutane poly(propylene imine)
h	initial adsorption rate for *pseudo*-second order model
HRTEM	high resolution transmission electron microscopy
ICP	inductively coupled plasma spectroscopy
ICP-OES	inductively coupled plasma optical emission spectroscopy
IR	infrared
k_1	*pseudo*-first-order rate constant
k_2	*pseudo*-second-order rate constant
k_F	Freundlich constant
k_{id}	intraparticle diffusion rate constant
k_L	Langmuir constant

Stellenbosch University https://scholar.sun.ac.za

LMCT	ligand-to-metal charge transfer
m	mass
MSPE	magnetic solid phase extraction
MIONs	magnetic iron oxide nanoparticles
M	molar mass
PAMAM	poly(amido amine) dendrimer
PPI	poly(propylene imine) dendrimer
PXRD	powder X-ray diffraction
PZC	point of zero charge
nm	nanometer
q	adsorption capacity
q_e	adsorption capacity at equilibrium
q_t	adsorption capacity at time, t.
q_{cal}	calculated adsorption capacity
q_{exp}	experimental adsorption capacity
G3 DAB PPI	generation 3 dibutane poly(propylene) imine dendrimers
DENs	dendrimer encapsulated nanoparticles
DSNs	dendrimer stabilised nanoparticles
R^2	linear regression correlation coefficient
R_L	dimensionless equilibrium parameter
SAED	selected area electron diffraction
t	time (min)
TEM	transmission electron microscopy
TGA	thermogravimetric analysis
THF	tetrahydrofuran
UV-Vis	ultraviolet-visible light spectroscopy
VSM	vibrating sample magnetometer
XRD	X-ray diffraction
XPS	surface-sensitive quantitative spectroscopy

Stellenbosch University https://scholar.sun.ac.za

LIST OF FIGURES

Stellenbosch University https://scholar.sun.ac.za

Stellenbosch University https://scholar.sun.ac.za

Stellenbosch University https://scholar.sun.ac.za

Stellenbosch University https://scholar.sun.ac.za

Stellenbosch University https://scholar.sun.ac.za

Stellenbosch University https://scholar.sun.ac.za

Stellenbosch University https://scholar.sun.ac.za

Stellenbosch University https://scholar.sun.ac.za

Stellenbosch University https://scholar.sun.ac.za

Stellenbosch University https://scholar.sun.ac.za

Stellenbosch University https://scholar.sun.ac.za

Stellenbosch University https://scholar.sun.ac.za

LIST OF TABLES

Stellenbosch University https://scholar.sun.ac.za

Stellenbosch University https://scholar.sun.ac.za

LIST OF EQUATIONS

Stellenbosch University https://scholar.sun.ac.za

Stellenbosch University https://scholar.sun.ac.za

CHAPTER 1 : LITERATURE AND BACKGROUND

1.1 INTRODUCTION

Platinum group metals (PGMs) comprise of a group of six elements, namely platinum (Pt), palladium (Pd), rhodium (Rh), iridium (Ir), ruthenium (Ru) and osmium (Os).[1–4] PGMs are very rare elements and most PGM-bearing ores are extremely low-grade, with mined ore grades ranging from 2 to 6 grams per tonne.[5] Their deposits have been found in the norite belt of the Bushveld Igneous Complex covering the Transvaal Basin in South Africa, the Stillwater Igneous Complex in Montana, United States, the Thunder Bay District of Ontario, Canada, and the Norilsk Complex in Russia.[3]

PGMs and gold (Au) are known as precious metals due to rare occurrence and economic value compared to other metals.[2,4,6] The demand for PGMs and Au is increasing world-wide due to their multiple applications in various fields. PGMs and Au are used as catalysts in chemical processes, jewellery manufacture, and in biomedicine applications.[3,4,7] The largest use of PGMs today is as catalytic converters which are pollution control devices fitted to cars, trucks, motorcycles, and non-road mobile machinery. In catalytic converters, PGMs are coated onto a substrate housed in the exhaust system where they act as catalysts to reduce harmful emissions to legislated levels. The high recyclability of PGMs and Au means that they can be re-used many times, thus ensuring that their impact on the environment is kept as low as possible.

Since the introduction of automobile catalytic converters, scientists predict that the concentration of PGMs in various environments have increased. The increased deposition of these metals is raising concern about the environmental impact and toxicity of these elements to living organisms.[8,9] Therefore, some researchers are now investigating toxicity of PGMs. One such study by Lindell in the toxicity of Pt confirmed that it causes Platinosis in humans.[10] Therefore, the recovery of precious metals from wastewater solutions does not only present a high economic benefit but could also contribute to the reduction of their pollution in the environment.[11]

Considering the above discussion, the recovery of PGMs and Au from secondary sources and wastewater solution is of utmost importance. Methods used for the recovery of precious metals from solutions include precipitation, ion exchange, and solvent extraction processes. Each method has its own advantages and disadvantages.[7,12,13] Nevertheless, these recovery methods

Stellenbosch University https://scholar.sun.ac.za

sometimes suffer from drawbacks such as by-product toxic sludge production, excessive time-consumption, and high costs. Comparatively, adsorption is a highly effective and economical way to recover precious metal ions. Hence, in recent years, due to the increased environmental and economic restrictions, considerable attention has been focused on research of different types of low-cost and effective adsorbents, such as charcoal ash, zeolite, and biosorbents for the recovery of precious metal ions.

Several researchers have examined the potential use of magnetic iron oxide nanoparticles (MIONs) in the removal and recovery of precious metals from wastewater.[14–16] MIONs possess remarkable magnetic properties such as superparamagnetism, high saturation field, extra anisotropic contributions or shifted loops after field cooling.[11,17,18] Consequently, these particles only exhibit magnetic properties in the presence of a magnetic field and lose their magnetism when the field is removed. Therefore, the adsorbent is easily directed and recovered from the solution using magnetic decantation, rather than the conventional filtration which is associated with many problems.

1.2 OVERVIEW OF SEPARATION AND RECOVERY TECHNIQUES

PGMs and Au are recovered from the ore and secondary spent materials. The sources of secondary spent materials include jewellery, spent automotive catalytic converters, electronic scrap, and spent dental and orthopaedic materials. Therefore, the processing of such materials can be complicated as the material needs to be well prepared and homogenised. The basic flow chart that summarises the steps followed for recovery of precious metals from spent materials is shown in **Figure 1.1**. [19,20] The main techniques used for the recovery of PGMs are pyrometallurgical and hydrometallurgical processes.

1.2.1 Pyrometallurgical processes

Pyrometallurgical processes are carried out to produce concentrate. PGMs are enriched in the metal phase or converted to easily-treated compounds by relevant pyrometallurgical treatment, then followed by refining technology to recover PGMs. These processes include crushing, batching, granulation, incineration and smelting in a furnace, or blast furnace at high temperature and separation.[4,19] Pyrometallurgical processes have become the traditional method for the recovery of PGMs from spent catalysts. For instance, electric arc furnace smelting and plasma smelting technology, has been used for PGMs recovery from auto-

Stellenbosch University https://scholar.sun.ac.za

catalysts in industry. In South Africa, the concentration of PGMs is still less than 10 gt^{-1} ore, hence the physical and pyrometallurgical processes are required to concentrate it.[4,19,20] The principal flow sheet of recovering PGMs by a pyrometallurgical process is shown in **Figure 1.2**.

1.2.2 Hydrometallurgical processes

Hydrometallurgical processes play a significant role in the extraction and recovery of PGMs and Au from various sources. The key steps in the hydrometallurgical process comprise of the dissolution of the material bearing precious metals in *aqua regia* or in acids such as hydrochloric acid, nitric and sulphuric acid, and in the presence of oxygen, iodine, bromine, chlorine, and hydrogen peroxide.[3,20]

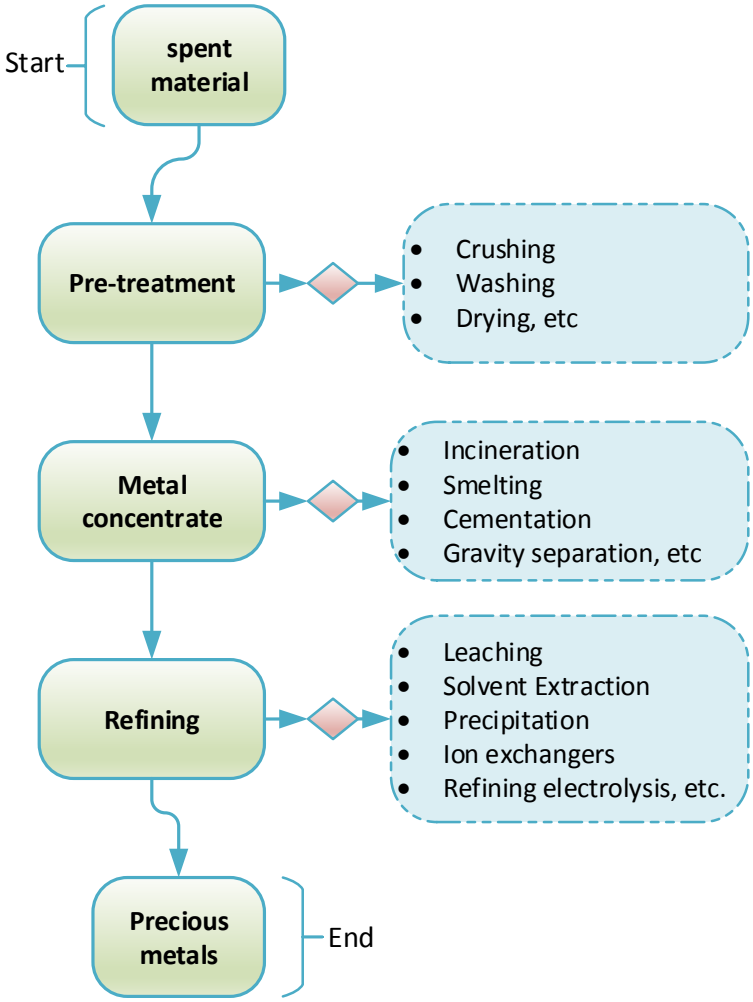

Figure 1.1: Basic flow-chart for processing the ore and spent secondary materials for the recovery of PGMs and Au.[20]

Stellenbosch University https://scholar.sun.ac.za

The solutions are then subjected to separation and purification procedures, including precipitation, cementation, solvent extraction, adsorption, and ion exchange, that are adapted to isolate and concentrate the metals of interest.[3,20–22] A summary of an advanced refinery used by Matthey Rustenburg Refiners in South Africa is shown schematically in **Figure 1.3**. For simplicity, only the major separations are presented.

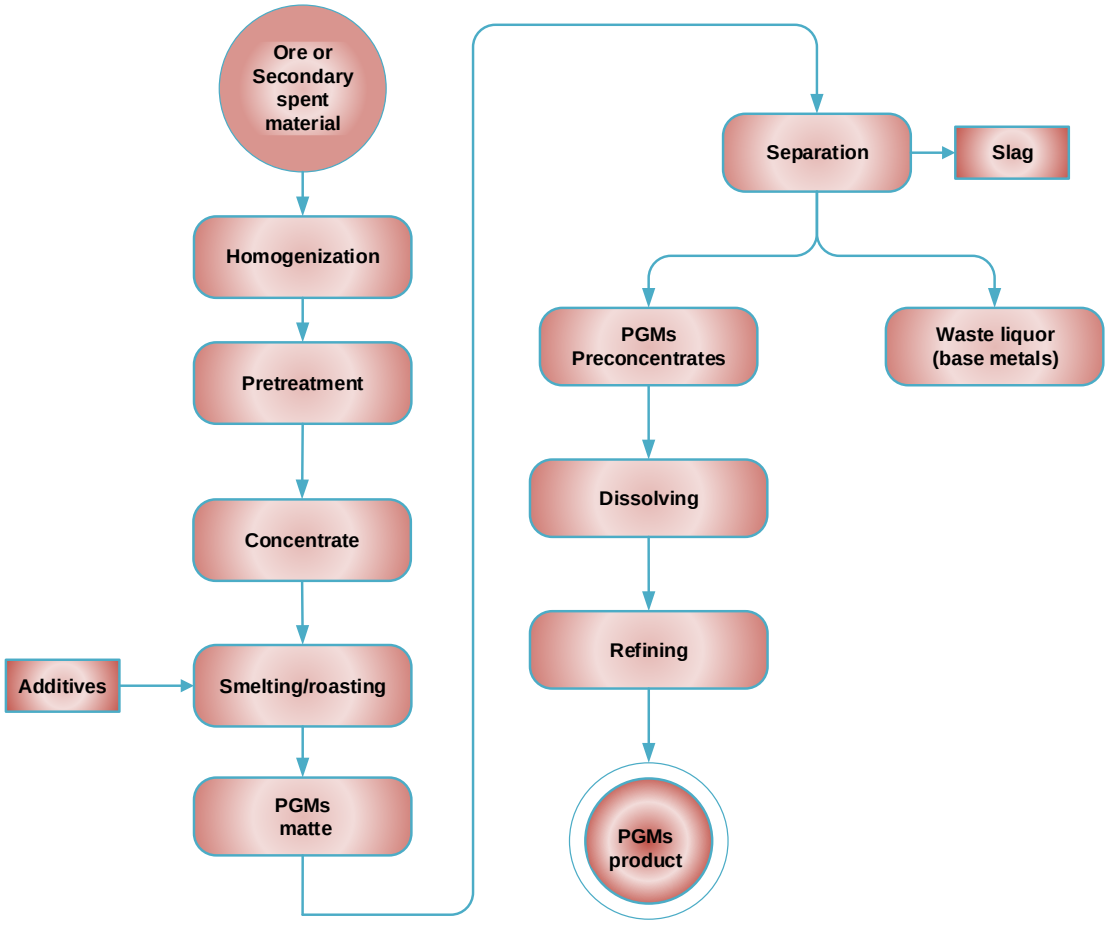

Figure 1.2: The principal flow sheet pertaining to the removal of precious metals by pyrometallurgical processes.[3]

1.2.2.1 Gravimetric precipitation

Precipitation is one of the earliest analytical techniques used for separation and recovery of precious metals from solutions.[4,7,20] The recovery of precious metals by this method is achieved through hydroxide and sulphide precipitation from solutions. Sulphide precipitation of metal ions is a feasible alternative due to the high stability of metal sulphides and low solubility. Kasaini and Siame examined sulphide precipitation of Pt and selected base metals (Fe, Co, and Cr). The effects of concentration, residence time and acidic condition on the precipitation

Stellenbosch University https://scholar.sun.ac.za

kinetics were investigated. The rate of Pt precipitation was understood to be faster than the precipitation of the base metals at lower $Na_2S_2O_3$ concentration levels (0.05M).[12]

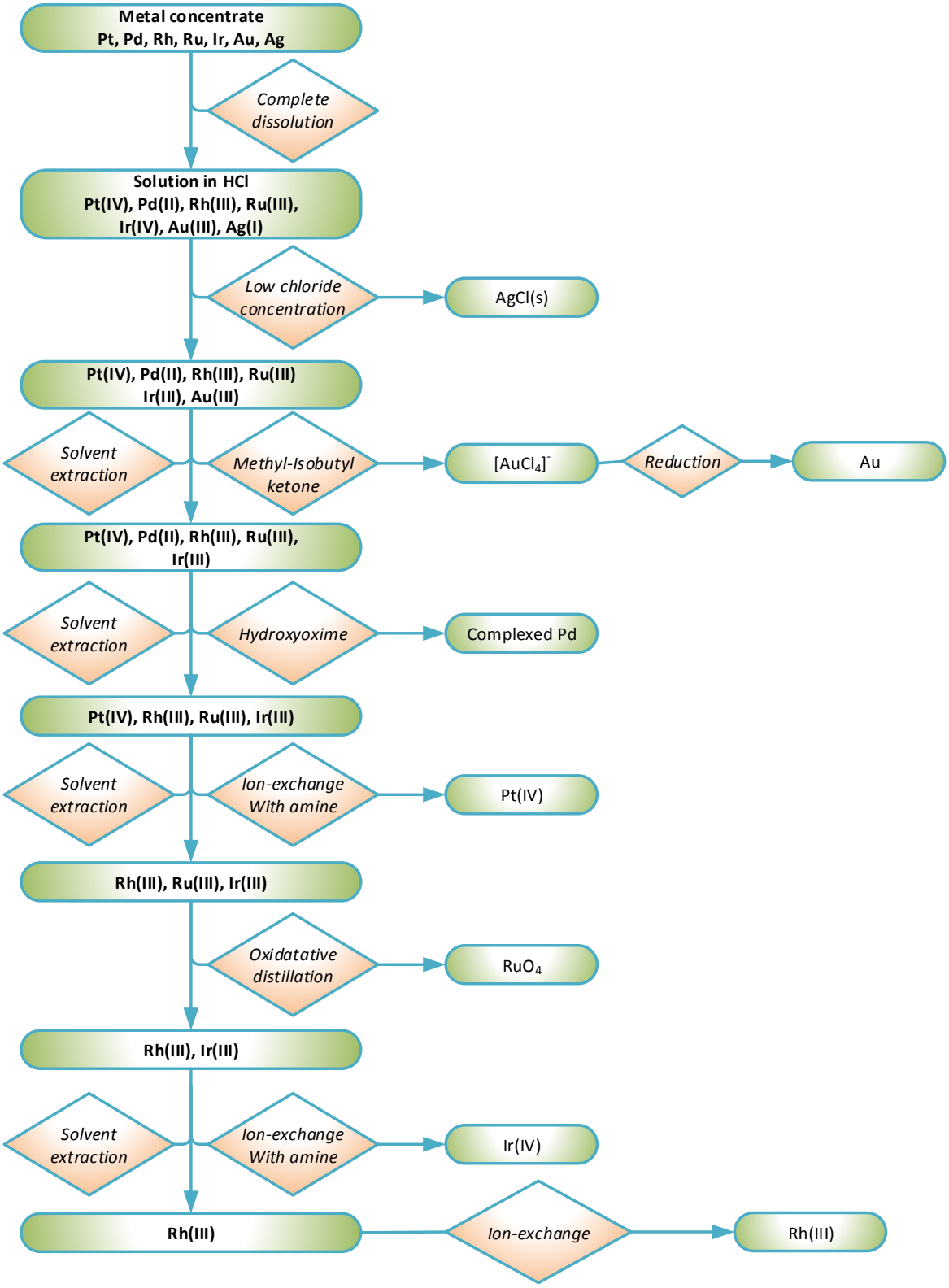

Figure 1.3: Modern refining method incorporating solvent extraction/ion exchange processes.[4]

Stellenbosch University https://scholar.sun.ac.za

Nevertheless, the precipitation method is inadequate in terms of separation efficiency. Problems may include co-precipitation and formation of "cake" that could block filters during the filtration step. Consequently, processing after precipitation is considered tedious because washing and filtration steps may have to be repeated several times. This leads to the use of numerous unit operations and recycle streams in commercial PGM refineries, which results in lengthy, labour-intensive refining operations and inevitable losses in recovery.[1,7]

1.2.2.2 Solvent extraction

The aforementioned challenges associated with recovery of PGMs by precipitation resulted in the implementation of other methods like solvent extraction which greatly simplified refining schemes.[4] It has been used commercially for the recovery of PGMs since 1970 by Matthey Rustenburg Refinery. This method is well suited to the recovery of PGMs and Au due to the great tendency of these precious metals to form complexes with organic complexing agents.[19] For instance, solvating reagents such as methyl *iso*butyl ketone (MIBK) or dibutylcarbitol (Butex) have been successfully used for the recovery of Au.

The solvent extraction process comprises of three basic steps:

1. An extraction step, which involves a selective extraction of a given metal,
2. A scrubbing step which involves removal of co-extracted metals, and
3. A stripping step, which involves removal of the extracted metal from the organic phase.

This method offers many advantages, such as high selectivity and metal purity. Furthermore, complete removal of metals is possible using multi-stage extraction. On the other hand, some operations have reported practical drawbacks associated with this technique. For example, slow extraction rate, high production costs and use of large volumes of organic solvents.[17,13]

1.2.2.3 Solid-phase extraction

Solid-phase extraction methods have also been incorporated into PGM refineries, either to compliment or replace solvent extraction methods.[4] A number of anion-exchange resins, such as Amberlite IRA 400 and the Superlig series are available in the market and have been used successfully in ion exchange processes.[4,12] However, resins constitute a huge proportion of the operational budget in metallurgical plants.[12,5]

Stellenbosch University https://scholar.sun.ac.za

Some of the South African refineries employ both solvent extraction and ion exchange technology for the recovery of PGMs and Au as shown in **Figure 1.3**. These processes delivered increased PGM recoveries. Nevertheless, these operations still have some shortcomings, which include filtration of the sorbent material, expensive resins and organic solvents, and steps that require several procedures. Therefore, there has been a great improvement in the development of methods used for the recovery of PGMs and Au from solutions, but there is room for improvement in terms of the operation costs and making the processes greener. In this work, the use of magnetic nanoparticles for extraction of PGMs and Au from aqueous solutions is explored.[15,23]

1.3 MAGNETIC SOLID-PHASE EXTRACTION

The term magnetic solid-phase extraction (MSPE) was first introduced by Šafaříková and Šafařík in 1999, despite being in use for more than two decades earlier.[24] In 1973, a primary application of MSPE was introduced in biotechnological applications by Robinson *et al*.[25] Twenty three years later, Towler *et al*.[26] used manganese dioxide coated magnetite as a sorbent material for radium, lead, and polonium recovery from seawater samples.

Compared with other solid phase extraction techniques, magnetic solid phase extraction is easy and convenient. MSPE employs magnetic nanoparticles as sorbent materials. Magnetic sorbents represent one of the most exciting prospects in analytical nanotechnology since they are easily directed, manipulated and isolated from the matrix by using an external magnetic field.[27–30] The majority of analytical chemists prefer to use novel magnetic solid phase extraction (MSPE), with the aim of avoiding the disadvantages in SPE, as it requires less time and labour.[31] The steps carried out during MSPE have been summarised in **Figure 1.4**.[32]

Briefly summarising the steps followed in MSPE shown in **Figure 1.4**, the magnetic adsorbent is added to the sample solution containing an analyte of interest. The analyte is adsorbed onto the surface of the magnetic materials. Then, the adsorbent material loaded with the analyte is separated from the aqueous medium with a magnet. The analyte can be eluted from the surface of the nanoparticles *via* a suitable solvent. Furthermore, sample pre-treatment is greatly simplified using MSPE. Since packing of a column with the sorbent, in the case of batch-mode operation, is not required as the phase separation is achieved by applying an external magnetic field.[13,33]

Stellenbosch University https://scholar.sun.ac.za

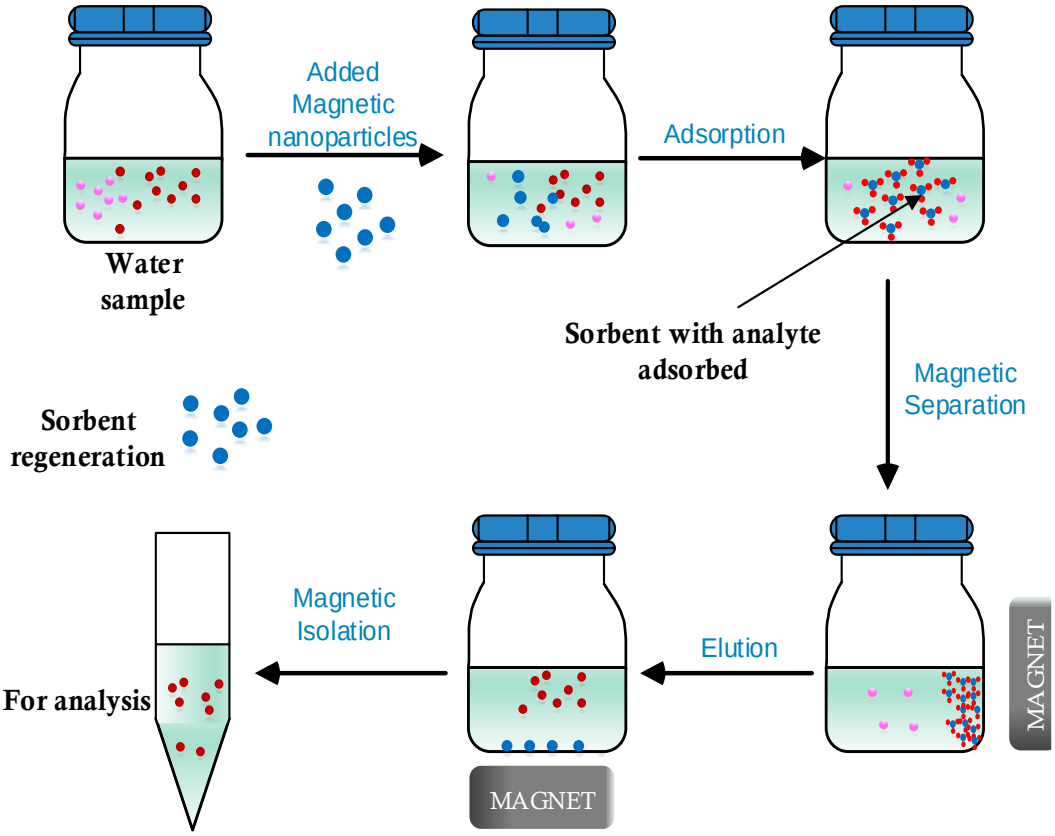

Figure 1.4: Steps followed in magnetic solid phase extraction.[13]

1.4 PROPERTIES OF MAGNETIC MATERIALS

Magnetic properties of nanomaterials can be attributed to magnetic moments and the net magnetization in the presence and absence of an applied magnetic field. Magnetic moments are associated with an individual electron of an atom. In the presence of magnetic field, the orbital motion of electrons generates an atomic current loop which opposes an external field. Furthermore, each electron is assumed to spin around an axis; parallel or antiparallel to its respective neighbours in the same crystal lattice. Therefore, depending on the magnetic response, magnetic materials can be classified as diamagnets, paramagnets, ferromagnets, ferrimagnets or antiferromagnets. **Figure 1.5** shows the net magnetic dipole arrangement for each of these types of magnetic materials.[34–36]

1.4.1 Diamagnetism

In the presence of a magnetic field, the orbital motion of electrons generates an atomic current loop which opposes the applied field. All materials displaying this type of weak repulsion to a

Stellenbosch University https://scholar.sun.ac.za

magnetic field are known to be diamagnetic. In the absence of an applied field, diamagnetic materials do not have magnetic dipoles. However, upon application of a field, the material produces a magnetic dipole that is oriented opposite to the applied field repelling the magnetic field. This phenomenon is illustrated in **Figure 1.5**.[37] The action against the applied field means that diamagnetic materials have a negative magnetic susceptibility. Therefore, diamagnetic materials have a negative susceptibility (χ) and weakly repel an applied magnetic field (**Figure 1.6**).[35,38]

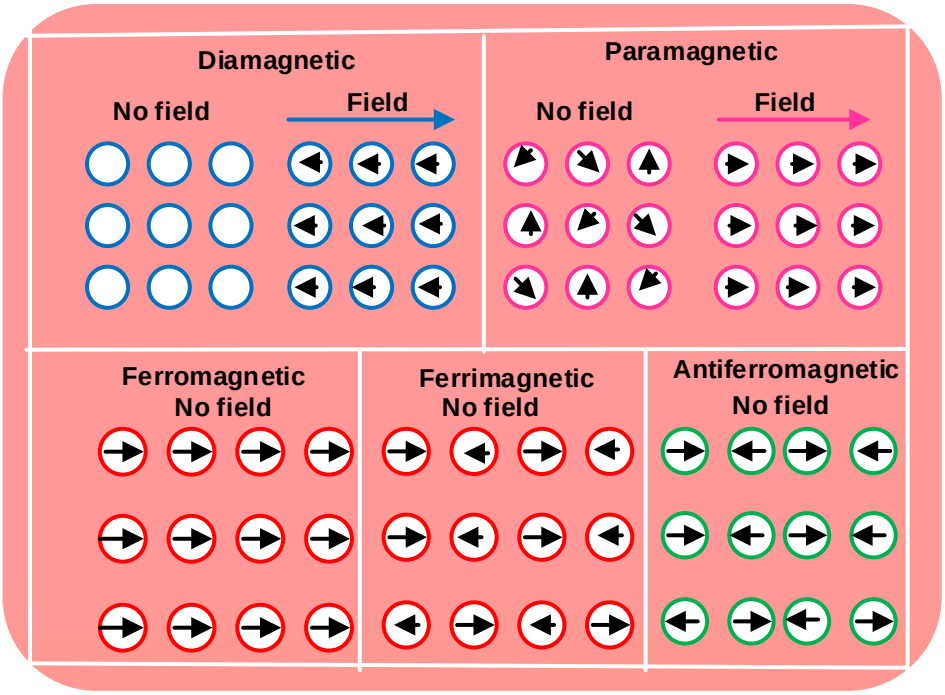

Figure 1.5: Magnetic dipole moments of the materials in the absence and presence of an external magnetic field.[35]

1.4.2 Paramagnetism

Paramagnetic materials are distinguished by their unpaired electronic configuration. Unlike, diamagnetic materials, they have magnetic moments both in the absence and presence of an applied field (**Figure 1.5**).[37,39] Hence, paramagnetism is due to the spin or orbital angular momenta of these unpaired electrons.[38] However, the magnetic moment of individual paramagnetic atoms in a material is only weakly coupled to each other, and at room temperature, thermal energy is sufficient to overcome these interactions to eliminate any net magnetic moment.[39]

Stellenbosch University https://scholar.sun.ac.za

1.4.3 Ferri- and Ferromagnetism

Ferromagnetic materials retain their magnetic properties, even when a magnetic field is removed. When subjected to an applied field, individual magnetic moments of their atoms are aligning with this field, and when the field is removed, part of this alignment is retained, and the material is magnetised. This is illustrated in **Figure 1.5**. On the other hand, ferromagnetic materials atoms or ions tend to assume an order of arrangement, but the nonparallel arrangement in a zero-applied field below Néel temperature (the temperature of spontaneous parallel or antiparallel orientation of spins between magnetic nanoparticles and the corresponding microscopic phases).[40] Normally, within a magnetic domain, substantial net magnetization results from the antiparallel, alignment of neighbouring non-equivalent sublattices.[34] Ferrimagnetism occurs mainly in magnetic oxides known as ferrites. Nonetheless, spontaneous alignments that produce ferrimagnetism are entirely disrupted above a temperature called the Curie point.[35]

When ferromagnetic materials are exposed to an alternating magnetic field, its magnetization will trace out a loop called a hysteresis and it is related to the existence of magnetic domains in the material. A hysteresis loop shows the relationship between the induced magnetic flux density and the magnetizing force (M-H). The loop is generated by measuring the magnetic flux of a material while the magnetizing force is changed. The major parameters used to describe the strength and magnetization of materials obtained from the hysteresis loop include the following: coercive field, H_c, the external magnetic field directed to magnetic dipoles in material, which is necessary to reduce magnetization to zero; saturation magnetization, M_s, the point at which all the spins are aligned with the magnetic field and the third parameter is the residual magnetization M_R, which shows remaining magnetization at zero applied field. However, when MIONs are superparamagnetic, the M-H curve does not show hysteresis, and the forward and backward magnetization curves overlap completely and are almost negligible.[18] **Figure 1.6** shows the magnetic behaviour under the influence of an applied field.

1.4.4 Antiferromagnetism

Materials exhibiting atomic magnetic moments of equal magnitude, which are arranged in an antiparallel pattern are antiferromagnetic. The exchange interaction couples the moments in a way that they are antiparallel, therefore, leaving a zero-net magnetization. (**Figure 1.5)**.[27]

Stellenbosch University https://scholar.sun.ac.za

Antiferromagnetism exists at lower temperature, but still above the Néel temperature, where thermal energy is sufficient to cause the equal and oppositely aligned atomic moments to fluctuate randomly leading to a disappearance of their long-range order. In this state, the materials exhibit paramagnetic behaviour.[27,34,37]

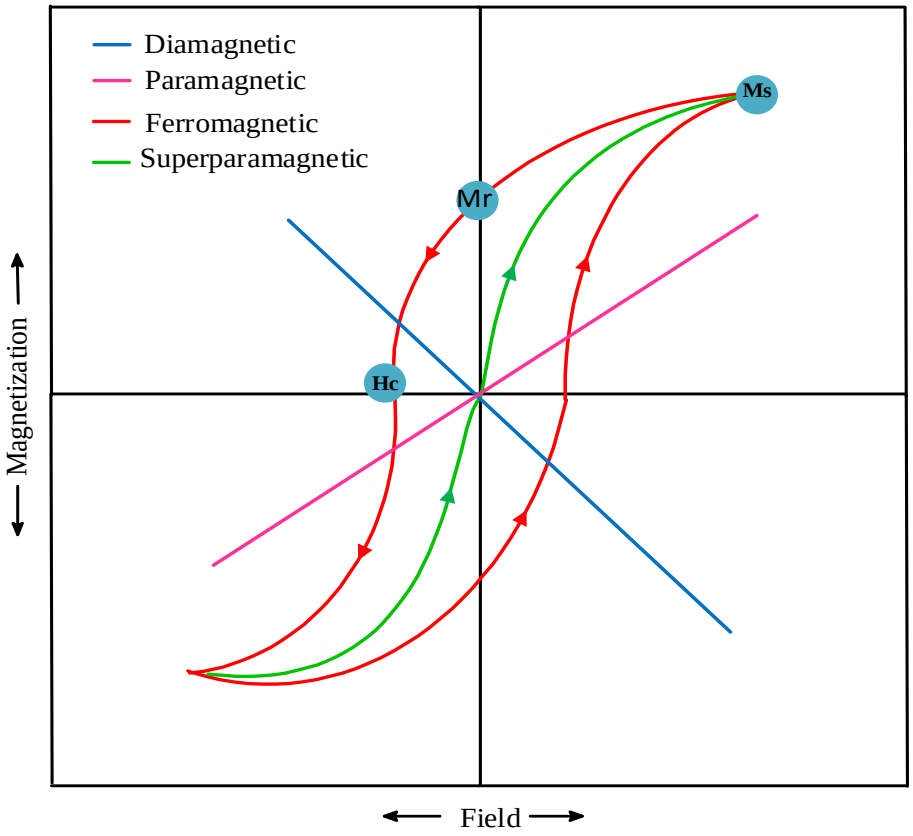

Figure 1.6: Magnetic behaviour under the influence of an applied field.[35]

1.4.5 Superparamagnetism

When reduced to very small sizes, ferri- and ferromagnetic nanoparticles become superparamagnetic. In this regime, particles exist as single domains and act as a "single super spin" that exhibits high magnetic susceptibility. The particles exhibit a response reminiscent to those of paramagnetic materials.[35] In the absence of an external field, they have zero average magnetic moments. However, magnetic moments observed in the presence of an applied field, increase rapidly in the direction of applied field.[27] Hence, superparamagnetic materials become magnetised only when exposed to an external magnetic field, but exhibit no remnant magnetization when the field is removed. This behaviour of superparamagnetic nanoparticles is depicted in **Figure 1.6**.

Stellenbosch University https://scholar.sun.ac.za

Figure 1.7 shows the transition from a superparamagnetic to a ferromagnetic system. Under an external magnetic field, domains of both ferromagnetic and superparamagnetic nanoparticles are aligned towards the direction of the applied field. Superparamagnetic nanoparticles do not have domain walls. In the absence of an external field, ferromagnetic nanoparticles maintain a net magnetization, whereas superparamagnetic nanoparticles exhibit no net magnetization due to rapid reversal of the magnetic domain structures. Ds and Dc shown in the figure represents superparamagnetic and critical size thresholds respectively.

1.5 SYNTHESIS OF MAGNETIC SORBENTS

In the recent years, considerable effort has been dedicated to the design and fabrication of nanostructured materials with specific functional properties.[41–43] Magnetic sorbents are normally synthesised using three steps: synthesis of magnetic nanoparticles (the core), the coating of the magnetic core with the organic or inorganic material (shell) and modification of the resultant core-shell structure (**Figure 1.8**).[44] In some instances, magnetic nanoparticles which makes the core are used as adsorbents without modifying them with the organic or inorganic materials.[45]

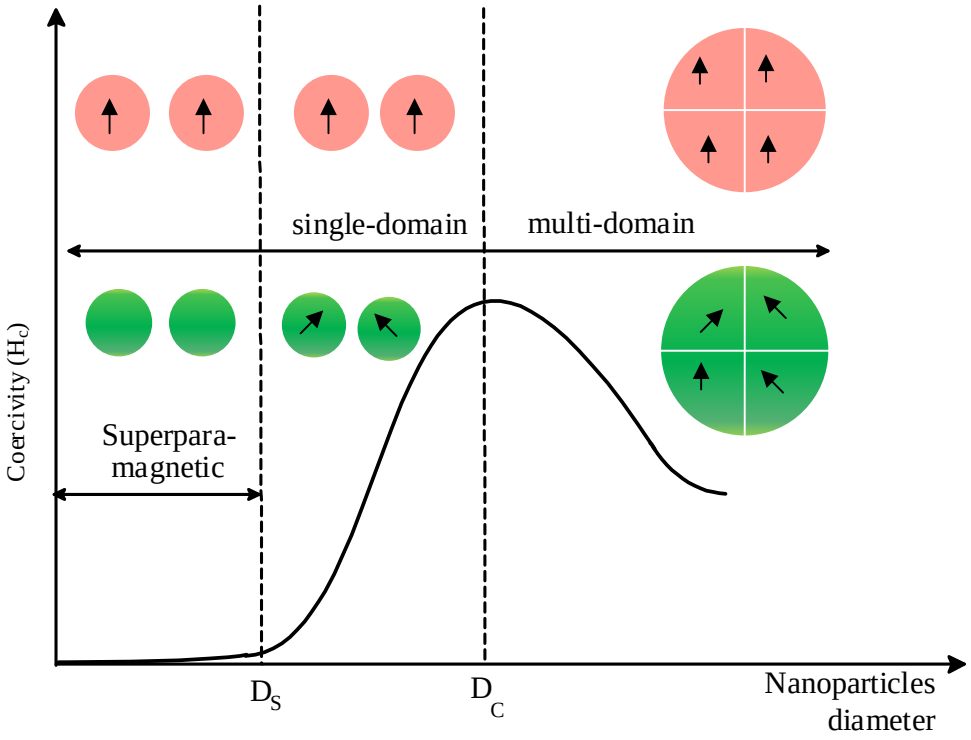

Figure 1.7: Transition from superparamagnetic to ferri- and /or ferromagnetic nanoparticles.[37]

Stellenbosch University https://scholar.sun.ac.za

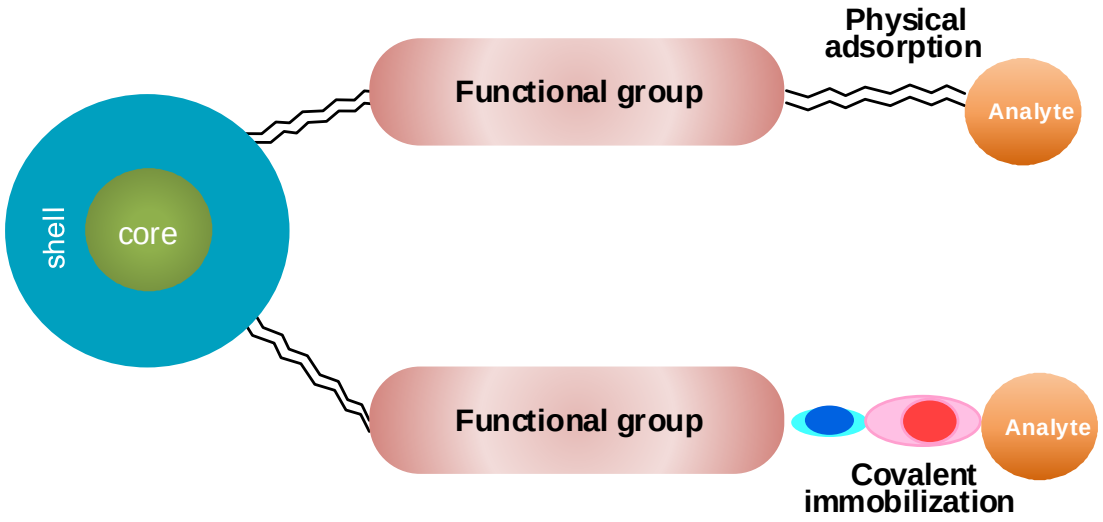

Figure 1.8: Functionalisation of a core-shell type structure of magnetic nanoparticles [46]

1.5.1 Synthesis of magnetic nanoparticles (the core)

Many synthetic approaches used to prepare magnetic nanoparticles have been discussed in the literature.[36,47–49] The properties of the nanoparticles are governed by their method of preparation. It is therefore paramount to understand the various synthetic methods used for the preparation of nanoparticles, as well as the applicable characterisation techniques. Numerous reviews discussing various approaches used for the preparation of magnetic nanoparticles are found in literature. These appraoches are divided into chemical, physical and biological methods.[36,48,50–52,53] Among these three methods, chemical methods are usually favoured, since chemical methods allow for the control of 'size' and 'shape' of the nanoparticles. Chemical methods used for the synthesis of magnetic nanoparticles include the following: co-precipitation, microemulsion, thermal decomposition and hydrothermal, and are briefly discussed in the subsequent subsections.

1.5.1.1 Chemical Co-precipitation

Chemical co-precipitation is the most commonly used method for the preparation of MIONs. This remarkable method was developed by Massart.[54] Preparation of the nanoparticles by this method involves simple co-precipitation of ferrous and ferric salts under an inert atmosphere. Adding a base, such as ammonium hydroxide or sodium hydroxide, to the mixture results in the formation of a black precipitate which consists of magnetite nanoparticles.[32,54,55] Some of the benefits of using co-precipitation include but are not limited to the following: it does not

Stellenbosch University https://scholar.sun.ac.za

require the use of toxic solvents and metal precursor complexes, and the reaction proceeds at temperatures under 100 °C.[52]

However, there is generally a lack of control over particle size, morphology, and composition of the magnetic nanoparticles prepared by co-precipitation methods.[18] Size, shape, and composition of the MIONs depend on the experimental parameters such as the anion of the salt (e.g., chloride, sulphates, and nitrates), pH, ionic strength, and temperature. Thus, it is understood that particles prepared by co-precipitation are polydisperse.[17,40,47] This might be due to the complicated set of pathways that lead to the formation of magnetite.[52] In recent years, there have been some improvements to this method, thus allowing for the production of monodisperse nanoparticles.[17,56]

1.5.1.2 Thermal decomposition

Another method that is used for the preparation of magnetic nanoparticles is thermal decomposition. This method was pioneered by Hyeon and co-workers.[57] The preparation methods adopted from thermal decomposition are considered as 'a hot-injection approach', wherein the metal complex such as $Fe(acac)_3$ is injected into a hot reaction mixture containing a high boiling temperature solvent and then heated in a closed or open reaction vessel.[18,57,58] The reaction is carried out in the presence of a surfactant such as oleic acid or oleylamine. Narrow size distribution and highly crystalline magnetic nanoparticles are obtained.[18,59] Although, this method has the advantage of producing highly monodispersed particles, its great disadvantage is that, it results in nanoparticles that generally dissolve in nonpolar solvents restricting their use for medicinal and water treatment purposes.[17]

1.5.1.3 Hydrothermal synthesis

Magnetic nanoparticles prepared by hydrothermal synthesis are highly crystalline and monodisperse. Synthesis of nanoparticles by this method involves oxidation of iron(II) salts in air, followed by addition of a base such as NaOH. The mixture formed is aged in an autoclave at the temperature of up to 250 °C.[17,18] This method is regarded as one of the successful ways of growing crystals of magnetite and maghemite nanoparticles. Crystals are generated by using the wet chemistry techniques of crystallising the substance in a sealed container at high temperature (usually at the temperature of 130 °C to 250 °C) in aqueous or non-aqueous solutions and under pressure (from 0.3 Mpa to 4 Mpa).[60] In this approach, the reaction time,

Stellenbosch University https://scholar.sun.ac.za

temperature and oxidising agents play an important role in the final products and determine the particle size, crystallinity and magnetic properties.[61] Although hydrothermal method is one of the techniques that are currently crucial for the preparation of magnetic nanoparticles, one of its main drawbacks is the slow reaction kinetics at any given temperature. To improve the kinetics of crystallisation during the hydrothermal synthesis, the utilisation of the microwave assisted heating techniques are required.[16]

1.5.1.4 Microemulsion

Another method that is widely employed for the preparation of magnetite nanoparticles is the microemulsion method. This method comprises three components: water, oil, and an amphiphilic molecule (called a surfactant). The nanodroplets of the aqueous phase are trapped within assemblies of surfactant, dispersed in a continuous oil phase.[17,32] These nanocavities (typically 1-50 nm in diameter) contain an iron salt solution as a precursor for nanoparticle formation; and similarly provide a confinement that limits particle nucleation, growth, and agglomeration. The molar ratio of water to surfactant determines the size of the reverse micelle (nanocavity). The method entails the mixing of water-in-oil microemulsions which contain the desired reactants; in the process, micro droplets continuously collide, coalesce, and break again allowing nanoparticles to form. Finally, filtration and centrifugation processes collect the precipitate. However, these methods require several washing steps and further stabilisation treatments, as particles might aggregate during washing.[16] Large amounts of solvent are required for scale-up, and this is not desirable according to the green chemistry legislation.[16,17]

Each of these methods has advantages and disadvantages. **Table 1.1** summarises the advantages and disadvantages of the above-mentioned synthetic methods for the preparation of magnetic nanoparticles.

1.5.2 Stabilization/protection of magnetic nanoparticles (the shell)

A common problem associated with naked nanoparticles is their instability over longer periods of time.[62] This manifests in two main ways: firstly, loss of dispersibility, where small nanoparticles aggregate and form large particles with the reduced surface area. Secondly, loss of magnetism where they easily oxidise in the air due to their high chemical activity. Therefore, it is important to develop proper protection strategies to chemically stabilise naked nanoparticles against damage during their various applications.

Stellenbosch University https://scholar.sun.ac.za

Table 1.1: Summary and comparison of the synthetic methods used for preparation of magnetic nanoparticles

Synthetic methods	Reagents	Advantages	Disadvantages	References
Co-precipitation	$FeCl_2$, $FeCl_3$, NaOH or NH_4OH	Very simple ambient conditions Easy surface functionalisation	Broad size distribution Poor crystallinity Basic pH is required	[49,54,63]
Thermal decomposition	Iron(II) salts, surfactants	Narrow size distribution High crystallinity Size and morphology control	High temperature (~300 °C) Requires organic solvents Hydrophobic particles	[17,57]
Hydrothermal	Iron salts, surfactants	Aqueous media Size control	High temperature High pressure Special reactors or autoclaves are required	[61,64]
Microemulsion	Oil/water/surfactant	Narrow size range High crystallinity Size and morphology control	Low yield Requires large amounts of organic solvents	[65–67]

Stellenbosch University https://scholar.sun.ac.za

Naked magnetic iron oxide nanoparticles (naked MIONs) exhibit a hydrophilic character due to the presence of hydroxyl groups on the surface. This creates hydrophilic interaction between the particles causing their agglomeration. For stability amongst particles, there should be a balance between the attractive and repulsive forces acting between the particles. The hydroxyl groups provide a versatile synthetic tool to attach different functionalities on the surface of magnetic nanoparticles (**Figure 1.9**).[68] Therefore, through the hydroxylic groups, the surface of magnetic nanoparticles could be modified with either organic and/or inorganic materials.[36,62,69]

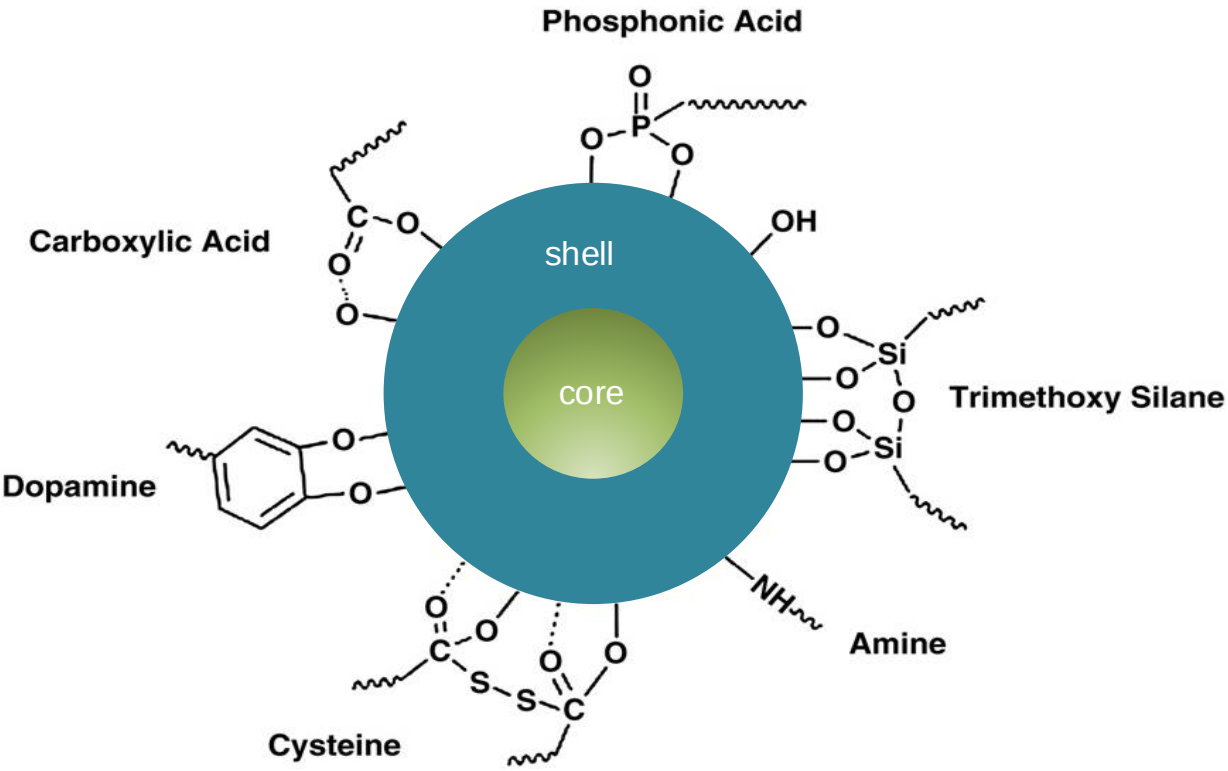

Figure 1.9: Organic moieties which can be used to functionalise magnetic nanoparticles.[29]

1.5.2.1 Organic coating

Several approaches have been developed to functionalise MIONs, including *in situ* and post-synthesis methods. Some of the organic molecules used to stabilise MIONs in the literature include, carboxylic acid, citric acid, oleic acid, silane, natural polymers (dextran, starch, chitosan, etc.), and synthetic polymers (poly(vinyl acetate (PVA), peroxyacetic acid (PAA), alginate, dendrimers etc.).[29,68]

Stellenbosch University https://scholar.sun.ac.za

1.5.2.1.1 Surfactants and small organic molecules

Surfactants, also referred to as small organic molecules, chemically attach to the surface of magnetic nanoparticles *via* functional groups such as alkoxysilane, phosphoric acids, carboxylic acids, and amines (**Figure 1.9**). Surfactants that form a covalent bond with the surface of magnetic nanoparticles, are good stabilisers. On the other hand, physical adsorption of the surfactant on the magnetic nanoparticle by either electrostatic interactions or hydrogen bonding, shows limited stabilisation of the nanoparticles.[17,40,70]

Oleic acid and oleylamine are the most commonly used organic molecules for the stabilisation of MIONs.[36,40,71,72] Many literature articles prove that these carboxylic acids form a covalent bond with MIONs.[73,74] Oleic acid is widely used to stabilise MIONs because it forms a dense protective monolayer, producing highly uniform MIONs.

Some other commonly used stabilisers include phosphoric acid and dopamine. Phosphoric acids forms a strong affinity for magnetic nanoparticle surfaces through the formation of Fe-O-P bonds.[75–77] Dopamine coordinates to the magnetic nanoparticle surface as a result of the improved orbital overlap of the five-membered ring.[78,79]

1.5.2.1.2 Polymers

Various reports discuss the many approaches applied in coating magnetic nanoparticles with polymers[17,23,80–82] Polymer stabilised magnetic nanoparticles are prepared by *in situ* and post-synthesis coatings.[36] Polymer coating of magnetic nanoparticles has more advantages over small molecule coating as it provides an increased repulsive force to balance the magnetic and the *van der Waals* attractive forces acting on the nanoparticles. Example of polymers used for synthesis of polymer stabilised magnetic nanoparticles include poly(ethylene glycol), poly(acrylamide) poly(*N*-isopropyl acrylamide), dextran, chitosan and dendrimers.[68,83–85] Due to their multiple functional groups and chelating properties, dendrimer functionalised magnetic nanoparticles are considered to be more interesting and used for many technological applications.[86–89]

Stellenbosch University https://scholar.sun.ac.za

1.5.2.1.2.1 Dendrimers

Dendrimers represent a unique class of polymers with three covalently bonded components: a core, interior branch cells, and terminal branch cells.[90–92] The *pseudo*-spherical shape of the dendrimer arises from its structure which emanates from a core, and just like a tree it grows outwards with each subsequent branching molecule. A schematic representation of a dendrimer molecule is shown in **Figure 1.10**.

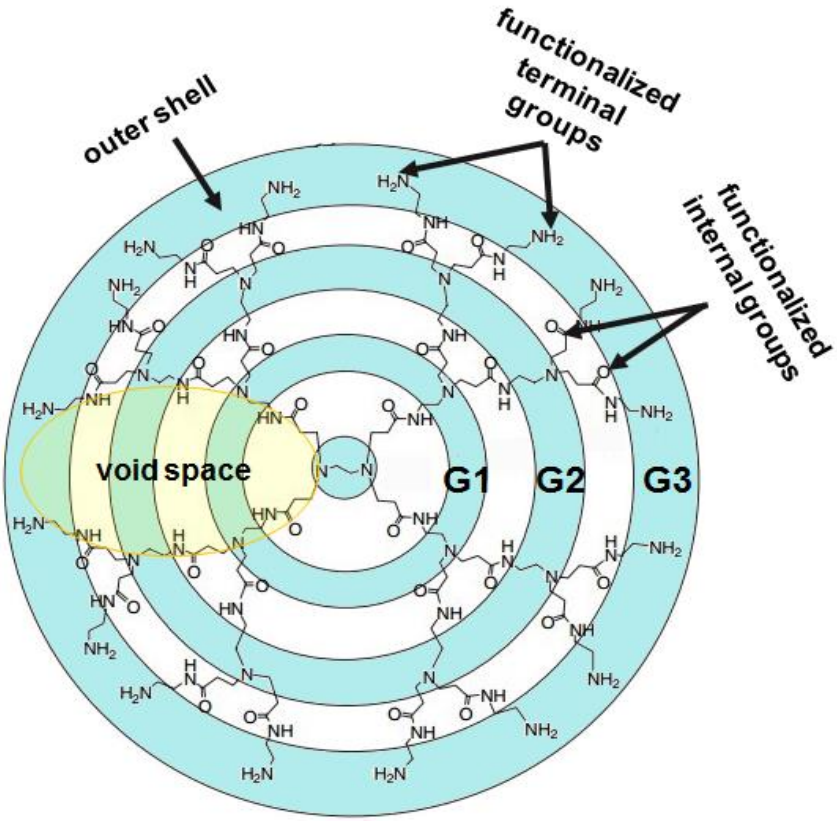

Figure 1.10: Dendrimer's structural components and properties illustrated using a generation 3 (G3) poly(amidoamine) (PAMAM) dendrimer.[93]

One of the fascinating properties of the dendritic architecture is the high number of functional end groups which is in contrast to linear polymers.[94] Furthermore, dendrimers can be synthesised to have different functional groups on their periphery (outer shell). Hence, the dendrimers can be tailored to have different properties such as solubility and thermal stability. Among these investigations, the host−guest interaction (or inclusion chemistry) of dendrimers toward a list of guests such as drugs, dyes, surfactants, catalysts, bio-macromolecules, metal

Stellenbosch University https://scholar.sun.ac.za

ions and metal nanoparticles have held great scientific interest due to their key roles in the broad applications of dendrimers.[95]

1.5.2.1.2.2 General methods of dendrimer synthesis

Many new classes of dendrimers have been synthesised since the first synthesis of poly(propylene imine) (PPI) dendrimers by Vogtle *et al* in 1978.[90,96] The two methods used for the synthesis of dendrimers are the divergent and convergent methods. The divergent method is considered as the "top-down" approach. The synthesis of dendrimers with divergent approach involves the stepwise growth of the dendrimer with a multifunctional core, which is extended outward by a series of reactions, usually Michael addition reactions. Subsequently, convergent method is considered as the "bottom-up" approach. The dendrimer is built by first making small molecules called wedges that are also coordinated to each and eventually attached to a core.

1.5.2.2 Inorganic coating

There has been great progress in the synthesis of organic coated magnetic nanoparticles, as several inorganic materials have been used to preserve the stability of magnetic nanoparticles including silica, carbon, or precious metals such as gold and platinum.[46] Inorganic materials can also be modified with organic functional groups, with the aim of improving the efficiency of magnetic nanoparticles for various applications such as biological and metal ion sorption.[18]

1.5.2.2.1 Silica

Among the aforementioned inorganic materials, silica is the most common compound for preparing the functionalised MIONs.[17,18,32,72] Unlike other inorganic coating materials, silica is an inert molecule that forms a coating on the surface of magnetic nanoparticles and prevents their dipolar attraction. Variations of silica shell on the surface of nanoparticles can be easily controlled by varying the concentration of ammonia and the ratio of silane to water.[17,18] Furthermore, silica-coating helps in coordinating various biological or other ligands to the nanoparticle surface.

There are three methods used to produce silica coated magnetic nanoparticles and these include the Stöber method, microemulsion and aerosol pyrolysis approach.[17,18] Stöber's method

Stellenbosch University https://scholar.sun.ac.za

involves *in situ* hydrolysis and condensation of a sol-gel precursor on the surface of the nanoparticles.[18] Briefly, magnetic sorbents are prepared by first dispersing pre-synthesised iron oxide nanoparticles in alcohol, this is followed by addition of a silane molecule to the mixture, and finally, the drop-wise addition of aqueous ammonium solution into the mixture results in the formation of a silica-coated iron oxide material. On the other hand, the microemulsion method makes use of the reverse micelles to confine and control silica shell thickness on nanoparticles.[18,61] However, this method requires much effort to separate the core-shell nanoparticles from a large amount of surfactants associated with the microemulsion system. The third method is the aerosol pyrolysis, where iron oxide magnetic nanoparticles are prepared by aerosol pyrolysis of a precursor mixture composed of silicon alkoxides and metals compound in a flame environment.[18,72]

1.5.2.2.2 Carbon

Carbon-coated iron oxide magnetic nanoparticles have been attracting more attention in recent years.[16,18,28] Carbon coating on MIONs creates an effective oxidation barrier and prevents their corrosion.[28] Different approaches used for preparation of carbon coated magnetic nanoparticles include electric arc discharge, hydrothermal methods, and catalytic pyrolysis of organic compounds.[28,97]

Several researchers used electric arc discharge methods to prepare carbon-encapsulated iron oxide magnetic nanoparticles. The average size of the particles produced by this method depends on the phase of the precursor. Initially, the precursor is injected into thermal plasma, providing the necessary conditions to induce a reaction. Under the condition of thermal plasma, the precursor decomposes into radicals, atoms, and ions forming a high temperature ionized gas. The high concentration of species and high temperature in the plasma arc induce a difficult process, associated with a fast quenching of gas species. During this process, the gas species react and condense to form particles.[98] Chaitoglou *et al*.[99] prepared iron encapsulated in carbon nanoparticles using a modified arc discharge method. The iron core was completely shielded by carbon in the resultant nanoparticles.

1.6 APPLICATIONS OF MAGNETIC NANOPARTICLES

Magnetic nanomaterials have attracted considerable attention in various research field such as catalytic materials, pigments, coatings, gas sensors, magnetic recording devices, magnetic data

Stellenbosch University https://scholar.sun.ac.za

storage media, magnetic resonance imaging (MRI), drug delivery, magnetic hyperthermia, bio-separation, and biotechnological processing.[11,15,100] More recently, the use of magnetic nanomaterials in solving environmental issues is receiving great attention.

1.6.1 Magnetic nanomaterials in medicine and biological sciences

Magnetic nanoparticles have been used as contrast agents in MRI imaging for location and diagnosis of brain and liver lesions or tumours.[101] MRI is one of the most powerful non-invasive imaging methods utilised in clinical medicine; it is based on the relaxation of protons in tissues.[18,102] Upon accumulation in tissues, magnetic nanomaterials enhance proton relaxation of specific tissues compared with that in the surrounding tissues, hence serving as MRI contrast agents.

Magnetic particles are used as drugs delivery or antibodies agents to the organs or tissues altered by diseases.[32] The process of drug localization using magnetic delivery systems is based on the competition between forces exerted on the particles by blood compartment, and magnetic forces generated from the magnet, i.e. applied field. When the magnetic forces exceed the linear blood flow rates in arteries (10 $cm.s^{-1}$) or capillaries (0.05 $cm.s^{-1}$), the magnetic particles are retained at the target site and maybe internalised by the endothelial cells of the target tissue. For this application the use of nanoparticles favours the transport through the capillary systems of organs and tissues avoiding vessel embolism.[32]

Other more interesting applications of magnetic nanomaterials in biological sciences include support for enzymes, cell labelling, and cell separation.[51,85,103] For cell separation, magnetic particles with appropriately tailored surface characteristics can be used to facilitate the separation of biomolecules, to sort specific cell types from a cell population, or to deliver drugs to a target organ in the body. One way to prepare a magnetic carrier is to coat magnetic nanomaterial with appropriate antibodies, specific to the cell type to be separated. Then this nanomaterial is attached to the specific type of cells in a mixing chamber and exposed to a magnetic field gradient. The magnetic nanomaterial with the selected cells are captured and thus separated from the rest of the stream.

Stellenbosch University https://scholar.sun.ac.za

1.6.2 Magnetic nanomaterials in environmental applications

Water pollution by heavy metals and dyes from industries has become a serious problem because of their adverse effects on ecological systems and human health.[104,105] Heavy metals and dyes are discharged into the environment and the water streams by the mining, metal finishing, painting and printing processes, pesticides and fertilisers manufacturer. The major concern about heavy metals is that most of them are highly toxic, carcinogenic and mutagenic at relatively low concentrations. Moreover, heavy metals are non-biodegradable and thus they tend to accumulate in living organisms.

There are more than 100 000 types of dyes which are used in different industries including paper, plastic, leather, pharmaceutical, food, cosmetic and textile.[106] However, dyes can be toxic to the aquatic life, and can be mutagenic and carcinogenic.[107] The adsorption of synthetic dyes onto adsorbents is considered to be a simple and economical method for their removal from water and wastewater.[107] In particular, adsorption onto activated carbon appears to have the best prospect for eliminating dyes. Nonetheless, activated carbon is produced from wood or coal therefore considered to be expensive. Hence, in recent years, many researchers have focused on the use of various cheaper adsorbents instead of activated carbon.[106,108] Konicki *et al*.[108] recently explored kinetics studies of two basic dyes, basic yellow 28 (BY28) and basic red 46 (BR46) onto Fe@graphite core-shell nanocomposite particles. This nanocomposite material was dispersible into and easily separated from water by the external magnetic field. The equilibrium adsorption data were analysed by Langmuir, Freundlich and Temkin isotherm models and were fitted with the Langmuir model. Maximum adsorption capacity was found to be 52.4 $mg.g^{-1}$ and 46.7 $mg.g^{-1}$ for BY28 and BR46, respectively.

1.7 SUMMARY AND SCOPE OF THESIS

As stated above, there has been a great improvement in establishing of methods for the recovery of PGMs from the ore and various solutions. On the laboratory scale, solid phase extraction is the most common method used and is considered as the most reliable way of removing metal ions from aqueous solutions. However, solid phase extraction still suffers from some drawbacks that essentially cannot be ignored such as removal of the adsorbent after extraction by filtration.[13]

Stellenbosch University https://scholar.sun.ac.za

1.8 AIMS AND OBJECTIVES

Bearing the above literature discussions in mind, the aims and objectives of this study were as follows:

- To synthesise new magnetic materials for adsorption of Au(III), Pd(II), and Pt(IV) complexes from aqueous acidic solutions.
- Synthesis and characterisation of naked magnetite iron oxide nanoparticles (naked MIONs).
- Synthesis of generation 3 diaminobutane (propylene imine) dendrimer micelles with different alkyl lengths (**DM_n**, where n = 5, 11 and 15).
- Stabilisation of MIONs with **DM_n** and/or with aliphatic carboxylic acids of different chain lengths (**C_n-acids**, whereby n = 5, 11 and 15).
- MIONs functionalised with **C_n-acids** were further modified with **DM_n**, forming a double surfactant layer on the surface of MIONs.
- A detailed study on adsorption of individual metals complexes of Au(III), Pd(II), and Pt(IV) by naked MIONs from acidic aqueous solution using ICP-OES and UV-Vis spectroscopy.
- Studying competitive adsorption of Au(III), Pd(II), and Pt(IV) complexes from acidic solutions using naked MIONs and modified MIONs.

This work is divided into six chapters, where **Chapter 1** covers the literature background on the methods that are used for recovery of PGMs from solutions. Moreover, the focus for this chapter was on the use of superparamagnetic iron oxide nanoparticles: their synthesis, modification with both organic and inorganic compounds, and their use in various technological applications. The chapter incorporated brief discussions on dendrimers, their structural orientation and synthetic methods.

Magnetite nanoparticles produced using some chemical co-precipitation protocols reported in the literature are normally have traces of other iron oxide species. To produce purely magnetite nanoparticles, **Chapter 2** discusses the optimisation of this method by varying the total Fe concentration and temperature. Characterisation of naked MIONs was carried out using infrared spectroscopy (IR), powder X-ray diffraction (PXRD), field emission scanning electron microscopy (FESEM), and high resolution transmission electron microscopy (HRTEM).

Stellenbosch University https://scholar.sun.ac.za

In **Chapter 3**, naked MIONs synthesised using optimised reaction conditions established in **Chapter 2** were used as adsorbents for individual metal complexes of Au(III), Pd(II), and Pt(IV) from aqueous acidic solutions. Preliminary results of using naked MIONs as adsorbent materials for these precious metal complexes as carried out by Dr Eugene Lakay.[109] The concentration of these metals complexes as measured using inductively coupled plasma optical emission spectroscopy (ICP-OES) and the speciation studies were preformed using ultraviolet-visible light (UV-Vis) spectroscopy. A possible mechanism that explains the interaction between each metal complex with the surface of naked MIONs was proposed.

In **Chapter 4**, functionalisation of naked MIONs with various organic ligands: G3 DAB PPI dendrimer micelles (**DM_n**, (whereby n = 5, 11, and 15)) and aliphatic carboxylic acid (**C_n-acids**, whereby n = 5, 11 and 15) was carried out. The synthesis of **DM_n** was carried out by modifying commercially purchased G3 DAB PPI dendrimers with the following alkyl acid chlorides hexanoyl chloride, lauryl chloride, and palmitoyl chloride. The modified MIONs were characterised with the following analytical techniques: IR, thermogravimetric analysis (TGA), derivative thermal analysis (DTA), PXRD, HRTEM, SAED and ICP-OES.

Some of the modified MIONs and naked MIONs were tested for competitive adsorption of Au(III), Pd(II), and Pt(IV) complexes from acidic aqueous solution (**Chapter 5**). The competitive batch adsorption experiments were carried out by varying two parameters: solution pH and the contact time. Desorption of the three metals was carried out using the following stripping solutions: HNO_3, thiourea and a mixture of HNO_3 and thiourea.

Chapter 6 gives the summary of the research findings, conclusions and future work.

Stellenbosch University https://scholar.sun.ac.za

CHAPTER 2 : SYNTHESIS AND CHARACTERISATION OF NAKED MIONS

2.1 INTRODUCTION

This chapter covers the synthesis and characterisation of the naked magnetite nanoparticles, referred to as naked magnetic iron oxide nanoparticles (naked MIONs). The synthesis of naked MIONs was carried out using a chemical co-precipitation method. The reaction conditions were optimised by varying temperature (30 °C, 60 °C and 90 °C) and the total iron concentration (Fe^{2+} and Fe^{3+}, at 0.125 M, 0.250 M and 0.375 M). Resultant nanoparticles were characterised using infrared spectroscopy (IR), powder X-ray diffraction (PXRD), field emission scanning electron microscopy (FESEM), high resolution transmission electron microscopy (HRTEM), and vibrating sample magnetometer (VSM).

Many different scientific disciplines have an interest in magnetite and maghemite nanoparticles due to their superparamagnetic properties.[29,110,111] Magnetite (Fe_3O_4), is a black ferromagnetic mineral consisting of an inverse spinel crystal structure containing 32 O^{2-} anions, 16 Fe^{3+} cations, and 8 Fe^{2+} cations. It differs from most other iron oxides in that it contains both divalent and trivalent iron ions. Maghemite (γ-Fe_2O_3), on the other hand, has a structure like that of magnetite. However, it is composed of only Fe^{3+} ions in the trivalent state. Maghemite has a cubic crystal structure, with a unit cell containing 32 O_2^- ions, 21⅓ Fe^{3+} ions and 2⅓ vacancies.

Magnetite nanoparticles are prepared mainly using the following methods: co-precipitation, hydrothermal synthesis, thermal decomposition, colloidal, and high-energy ball mill.[18,36,112] These methods have been summarised in **Chapter 1**. Choosing a suitable method should be done with due diligence. The co-precipitation is considered as the best method for the synthesis of magnetite nanoparticles used for adsorption of metal ions from solutions. Though, the co-precipitation method produces polydispersed nanoparticles (widely distributed nanoparticles) with average particle size usually less than 20 nm. Therefore, they show extraordinary properties such as large surface to volume ratios and superparamagnetism.

2.1.1 Characterisation techniques

The application of nanoparticles depends on their unique properties. Hence, characterisation of the nanoparticles is very important. Some of the techniques used to characterise magnetic nanoparticles have been briefly discussed below:

Stellenbosch University https://scholar.sun.ac.za

2.1.1.1 Particle size

TEM analysis detects a difference in electron density which allows observation of the particle size (crystalline and amorphous parts), shape, and size distribution of nanomaterials.[36,46,113] Analysis of TEM images give an average particle size based on number-weight mean value. Therefore, analysis of the images must be performed on a statistically significant number of particles. X-ray diffraction (XRD) is another universal tool used to determine the particle size of nanomaterials. The crystal size can be calculated from the line broadening from the XRD pattern using the Scherrer equation. [1, 2] X-ray line profile analysis is, in general, an averaging method. XRD is noted for its simplicity in sample preparation, and it can provide structural information regarding mean grain size, and the microstrain in the entire sample. Another powerful technique used to characterise nanoparticle size is small-angle neutron scattering (SANS). It also gives information about polydispersidy, the shape and even the structure of the nanoparticles. Furthermore, extended X-ray absorption fine structure (EXAFS) gives information on the particle size, especially for small sizes. Photon correlation spectroscopy (PCS), also called dynamic light scattering (DLS) or quasi-elastic light scattering (QELS), is a common technique to obtain nanoparticle size. The determination of the diffusion coefficient of the nanoparticles in solution gives access to the hydrodynamic radius of a corresponding sphere and the polydispersity of the colloidal solution. This radius is an intensity-weighted mean value.[113]

2.1.1.2 Morphology and shape

SEM gives information about the morphology of the magnetic nanoparticles. Another technique that determines the crystallinity of magnetic nanoparticles is selected area electron diffraction (SAED). The surface area of magnetic nanoparticles, their porosity, and mean diameter are determined by nitrogen adsorption-desorption according to the Brunauer-Emmett-Teller (BET) method.[114]

2.1.1.3 Composition and surface properties

Common methods for detecting the surface functional groups for magnetic nano-sorbents are FTIR and XPS. Other physicochemical techniques, such as atomic and chemical force microscopy (AFM and CFM), thermogravimetric analysis (TGA), differential scanning calorimetry (DSC), X-ray photoelectron spectroscopy (XPS), thermally programmed

Stellenbosch University https://scholar.sun.ac.za

desorption, Fourier transform infrared spectroscopy (FTIR), conductimetry, potentiometry, and solid-state NMR, have been used to investigate the surface properties of coated iron oxide nanoparticles. It is worth noting that these techniques are used to describe the nature and strength of the bonding between the iron oxide surface and the coating, and to understand the influence of the coating on the magnetic properties of the nanoparticles.

2.1.1.4 Magnetism

Magnetic properties of magnetic nanoparticles are conventionally studied using two techniques: SQUID magnetometry and vibrating sample magnetometry (VSM).[115] Like most conventional magnetization probes, both techniques are not element specific but rather measures the overall magnetization.

2.1.2 Co-precipitation method

The co-precipitation method is probably the simplest way to produce magnetite particles. A base is added to an aqueous mixture of Fe^{2+} and Fe^{3+} at a 1:2 molar ratio. The stoichiometric reaction for the synthesis of magnetite nanoparticles using co-precipitation is as shown in **Equation 2.1**.[34,56]

Equation 2.1: $$Fe^{2+} + 2Fe^{3+} + 8OH^{-} \rightarrow Fe_3O_4 + 4H_2O$$

The thermodynamics of this reaction show that complete precipitation should be expected at pH levels between 9 and 14.[72] To control the reaction kinetics, which strongly related with the oxidation speed of iron species, the reaction should be performed in a non-oxidising environment.[34,36,72] Otherwise, magnetite nanoparticles might be oxidised as shown in **Equation 2.2**.

Equation 2.2: $$Fe_3O_4 + 0.25O_2 + 4.5H_2O \rightarrow 3Fe(OH)_3$$

Kim and co-workers recently elucidated on the mechanistic path for the formation of magnetite nanoparticles by co-precipitation. Their study confirmed that magnetite nanoparticles formation results from phase transformation rather than the direct reaction of Fe^{2+} and Fe^{3+} in the aqueous phase.[52] **Equation 2.3** to **Equation 2.6** shows the set of phase transformations involved in producing magnetite nanoparticles.[52]

Stellenbosch University https://scholar.sun.ac.za

Equation 2.3 $$Fe^{3+} + 3OH^- \rightarrow Fe(OH)_3$$

Equation 2.4 $$Fe(OH)_3 \rightarrow FeOOH + H_2O$$

Equation 2.5 $$Fe^{2+} + 2OH^- \rightarrow Fe(OH)_2$$

Equation 2.6 $$FeOOH + Fe(OH)_2 \rightarrow Fe_3O_4 \downarrow + 2H_2$$

2.2 RESULTS AND DISCUSSION

2.2.1 Synthesis of naked MIONs

The synthetic method was optimised by varying two parameters: temperature and the total iron concentration. The molar ratio of Fe^{2+}: Fe^{3+} chloride salts was kept at 1:2 for all the experiments. The reactions were performed using batch mode and the synthesis was carried out using Schlenk techniques, under nitrogen gas to avoid the hydrolysis of the metal ion precursors. The reaction conditions are shown in **Table 2.1**.

Table 2.1: Conditions used for synthesis of naked MIONs by co-precipitation method.

Reaction	Temperature (°C)	Total (Fe^{2+} and Fe^{3+}) conc. (M)	$FeCl_3{\cdot}6H_2O$ mass (g)	$FeSO_4{\cdot}7H_2O$ mass (g)	NH_4OH volume (ml)
S1	30	0.125	2.26	1.16	5.19
S2	30	0.250	4.51	2.32	7.79
S3	30	0.375	6.76	3.48	10.39
S4	60	0.125	2.26	1.16	5.19
S5	60	0.250	4.51	2.32	7.79
S6	60	0.375	6.76	3.48	10.39
S7	90	0.125	2.26	1.16	5.19
S8	90	0.250	4.51	2.32	7.79
S9	90	0.375	6.76	3.48	10.39

The resultant nanoparticles were referred to as **S1** to **S9**. Synthesis was carried out in a 250 ml Schleck tube under nitrogen gas as shown in **Figure 2.1**. Schlenk tubes were immersed in an oil bath which was heated with a hot plate fitted with a temperature control probe or thermocouple. Briefly summarising the synthetic procedure, $FeSO_4{\cdot}7H_2O$ and $FeCl_3{\cdot}6H_2O$ salts in a molar ratio of 1:2 molar ratio was dissolved in distilled deionized (DD) water under nitrogen. Ammonium hydroxide (33 %) was subsequently added drop wise (with a syringe) to

Stellenbosch University https://scholar.sun.ac.za

the reaction mixture. Upon addition of NH_4OH, a brown precipitation was immediately formed. The color of the precipitate changed to green and finally black. The black colour indicates that the nanoparticles were magnetite.[52,116,117] **Figure 2.1** summarises the steps taken during the synthesis of naked MIONs using chemical co-precipitation method.

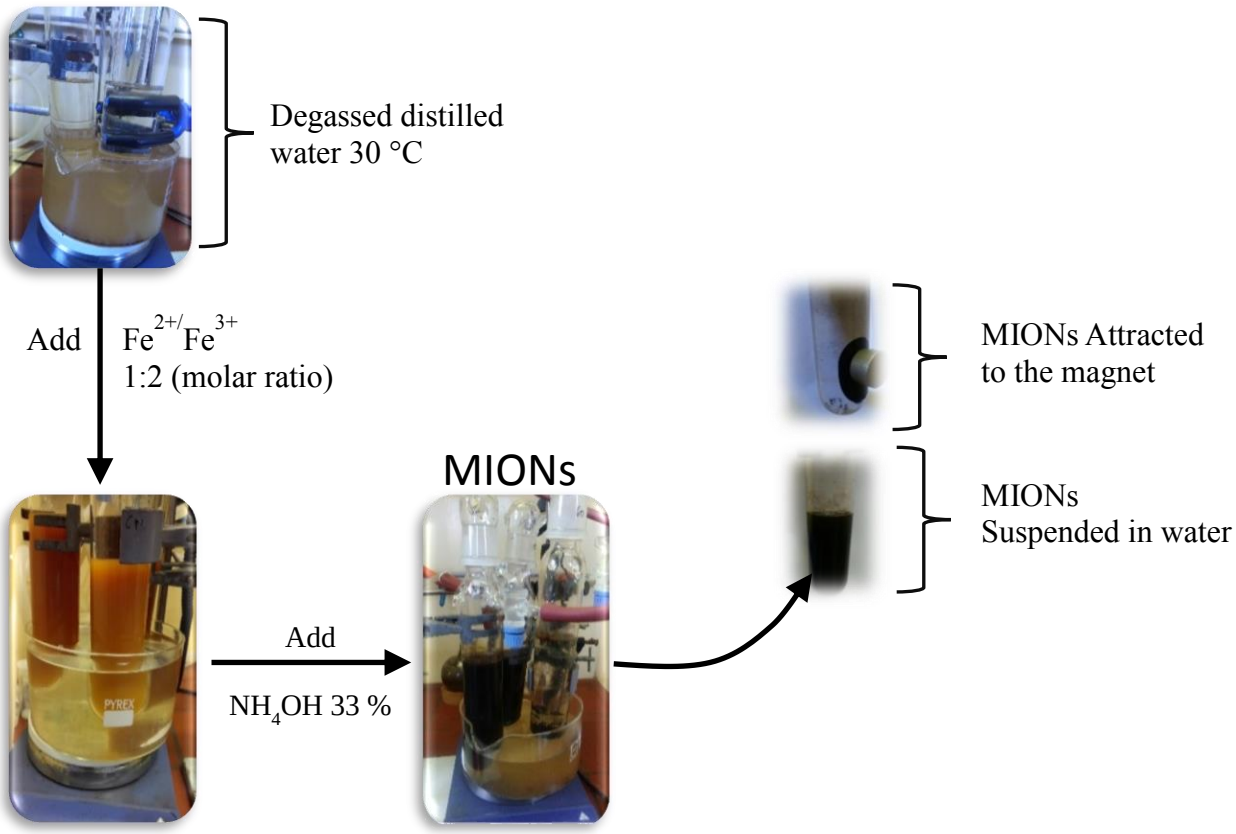

Figure 2.1: Schematic presentation of the co-precipitation synthesis of magnetic iron oxide nanoparticles.

2.2.2 Characterisation of naked MIONs

Naked MIONs, **S1** to **S9**, were studied for their structural and morphological characteristics using the following analytical techniques: infrared spectroscopy (IR), powder X-ray diffraction (PXRD), field emission scanning electron microscopy (FESEM), and high resolution transmission electron microscopy (HRTEM).

2.2.2.1 Infrared spectroscopy

Naked MIONs prepared at the temperature of 30 °C using different total iron concentration: 0.125 M, 0.250 M, and 0.375 M, respectively were characterised using IR spectroscopy. As

Stellenbosch University https://scholar.sun.ac.za

shown in **Figure 2.2**, overlaid IR spectra of the resulted naked MIONs (**S1**, **S2** and **S3**) were portrayed. The samples were diluted with KBr, ground into a fine powder and pressed into a pellet. Magnetite is a mixed cubic oxide and contains 2/3 Fe^{3+} and 1/3 Fe^{2+} cations. Hence, the absorption bands at $\lambda = 583$ cm^{-1} and 440 cm^{-1} (**S3**) may be assigned to Fe-O stretching modes of the tetrahedral and octahedral sites respectively. Furthermore, the bands at $\lambda = 3430$ cm^{-1} and 1631 cm^{-1} can be assigned to the bending and stretching vibration of water absorbed on the surface and the crystal lattice of the naked MIONs.[115] The spectra also show additional bands at round $\lambda = 1127$ cm^{-1} and 1052 cm^{-1}. These bands can be ascribed to the unreacted FeOOH or $Fe(OH)_2$ species, which is an intermediate in the synthesis of magnetite nanoparticles. The figure shows that the spectra of **S2** and **S3** exhibited similar absorption bands to that of **S1**.

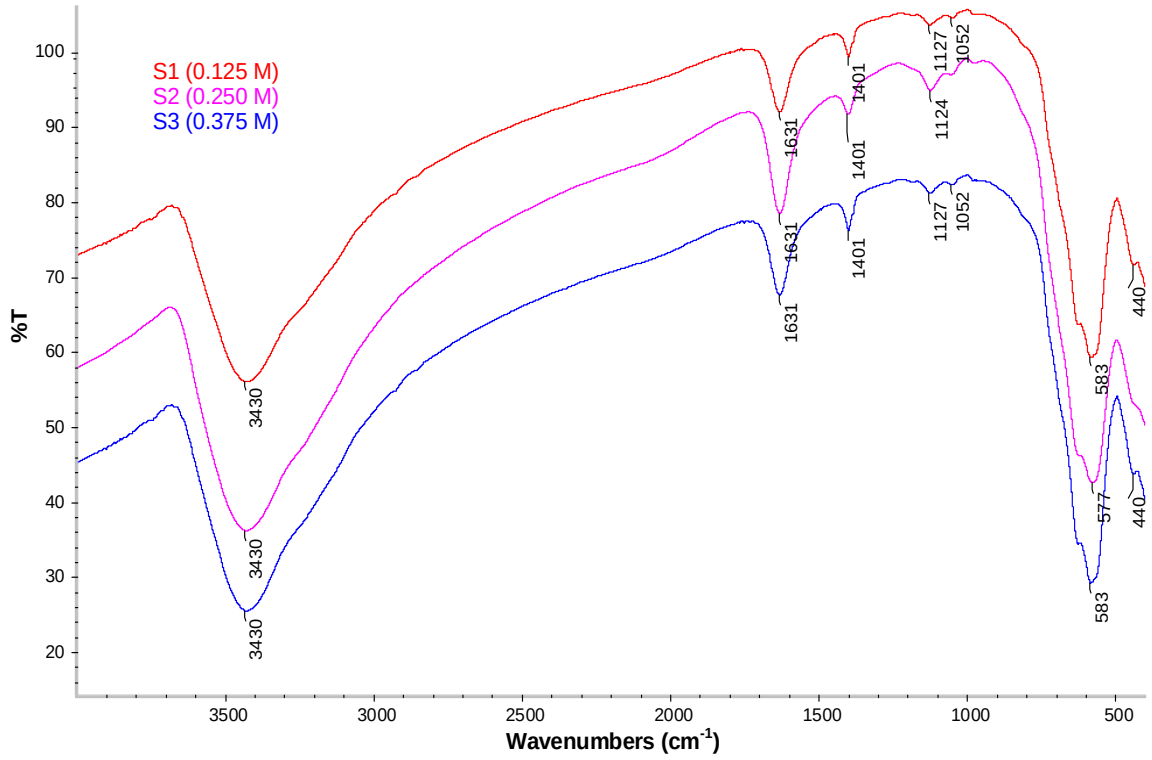

Figure 2.2: Infra-red spectra of magnetic iron oxide nanoparticles synthesised at 30 °C.

The overlaid spectra of naked MIONs (**S4, S5** and **S6)** prepared at 60 °C are presented in **Figure 2.3**. All spectra show similar absorption bands. For instance, the IR spectrum of **S5** shows absorption bands at around $\lambda = 3434$ cm^{-1} and 1631 cm^{-1} ascribed to water molecules on the surface of the nanoparticles and also forming part of the nanoparticle crystal structure. An absorption band at around $\lambda = 583$ cm^{-1} corresponds to the Fe-O vibrating bonds. The absence of additional bands shows that pure magnetite nanoparticles were produced at 60 °C.

Stellenbosch University https://scholar.sun.ac.za

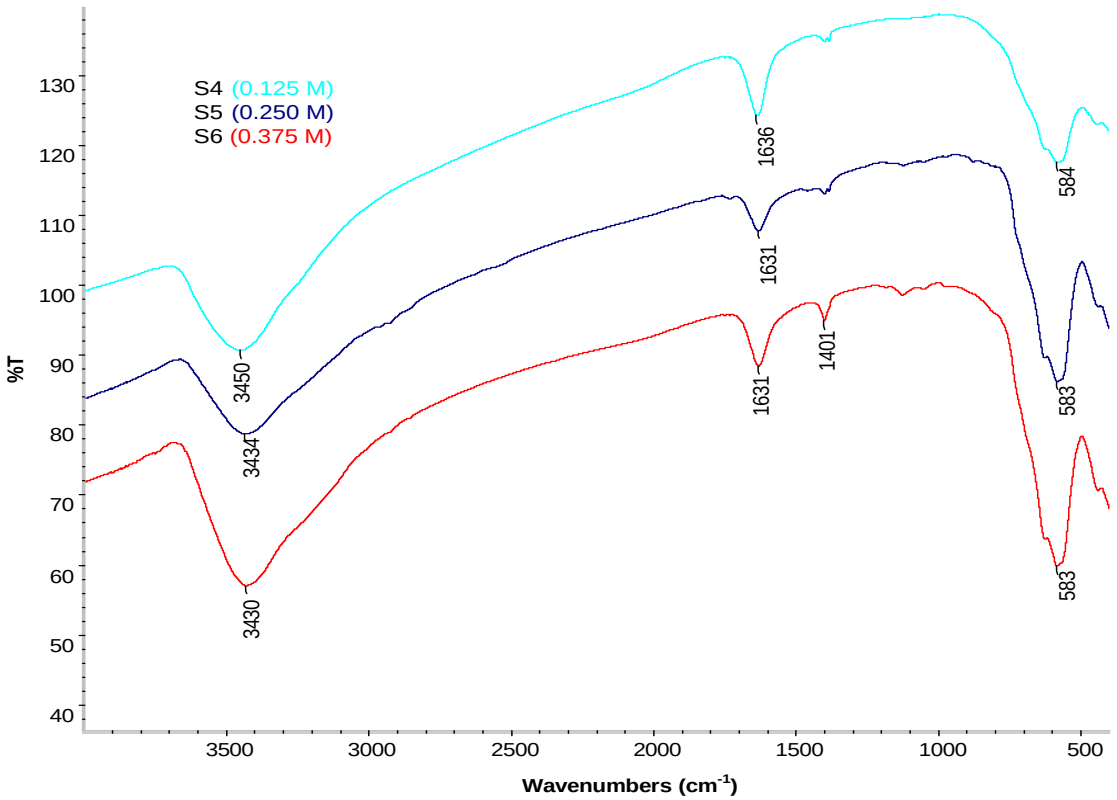

Figure 2.3: Infra-red spectra of magnetic iron oxide nanoparticles synthesised at 60 °C.

The IR spectra of naked MIONs (**S7**, **S8** and **S9**), prepared at a higher temperature, 90 °C, are shown in **Figure 2.4**. The spectrum of **S7** shows two absorption bands at around λ= 3329 cm^{-1} and λ = 584 cm^{-1}. This type of spectrum is characteristic for pure magnetite nanoparticles.[115] On the contrary, IR spectra of **S8** and **S9** display additional absorption bands at around λ = 1129 cm^{-1}, 1053 cm^{-1} and 979 cm^{-1}. This indicates that **S8** and **S9** were not only magnetite nanoparticles but contained a mixture of other iron oxide species.

Considering the above IR results, pure magnetite nanoparticles were prepared at the temperature at 60 °C and the total iron concentration of 0.125 M and 0.250 M.

Stellenbosch University https://scholar.sun.ac.za

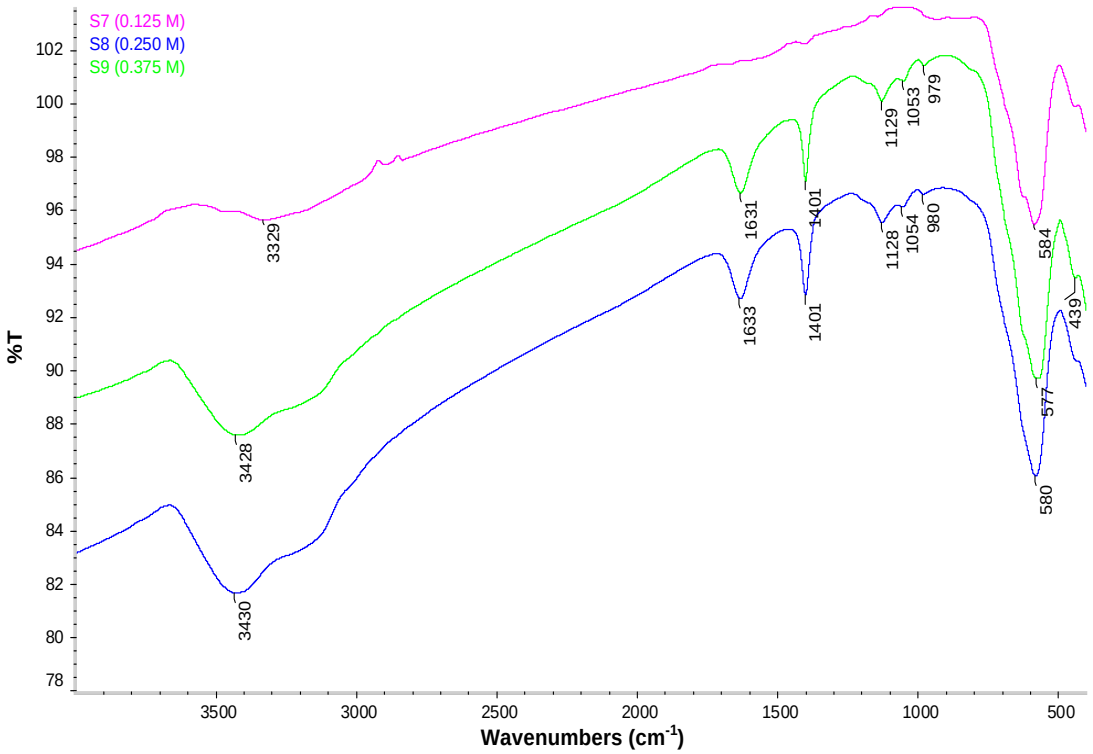

Figure 2.4: Infra-red spectra of magnetic iron oxide nanoparticles synthesized at 90 °C.

2.2.2.2 Powder X-ray diffraction

The crystallinity and phase purity of the naked MIONs were examined by powder X-ray diffraction (PXRD). **Figure 2.5 (a)** shows overlaid diffractograms of naked MIONs (**S1**, **S2**, and **S3**) prepared at 30 °C. Diffractogram of **S1** shows diffraction peaks with the miller indices (*hkl*) values: (220), (311), (400), (422), (511) and (440). These diffraction patterns matched well with those of standard magnetite samples, as per JCPDS cards No. 00-011-0614 with a cubic spine structure. The diffractogram of **S2** and **S3** showed additional peaks not corresponding to diffraction patterns of magnetite. These peaks can be ascribed to the other phases of iron oxide nanoparticles or intermediates shown in **Equation 2.4** to **Equation 2.6**. The observation confirms the infrared spectroscopy results. Hence, naked MIONs prepared at 30 °C contained other, unwanted iron oxide species. **Figure 2.5 (b)** shows diffractograms of naked MIONs (**S4**, **S5** and **S6)** prepared at 60 °C. These diffractograms show diffractions peaks corresponding to those of standard magnetite. The diffraction peaks for other phases of iron oxide other than magnetite are not observed, thus confirming the purity of the nanoparticles prepared at 60°C.

Stellenbosch University https://scholar.sun.ac.za

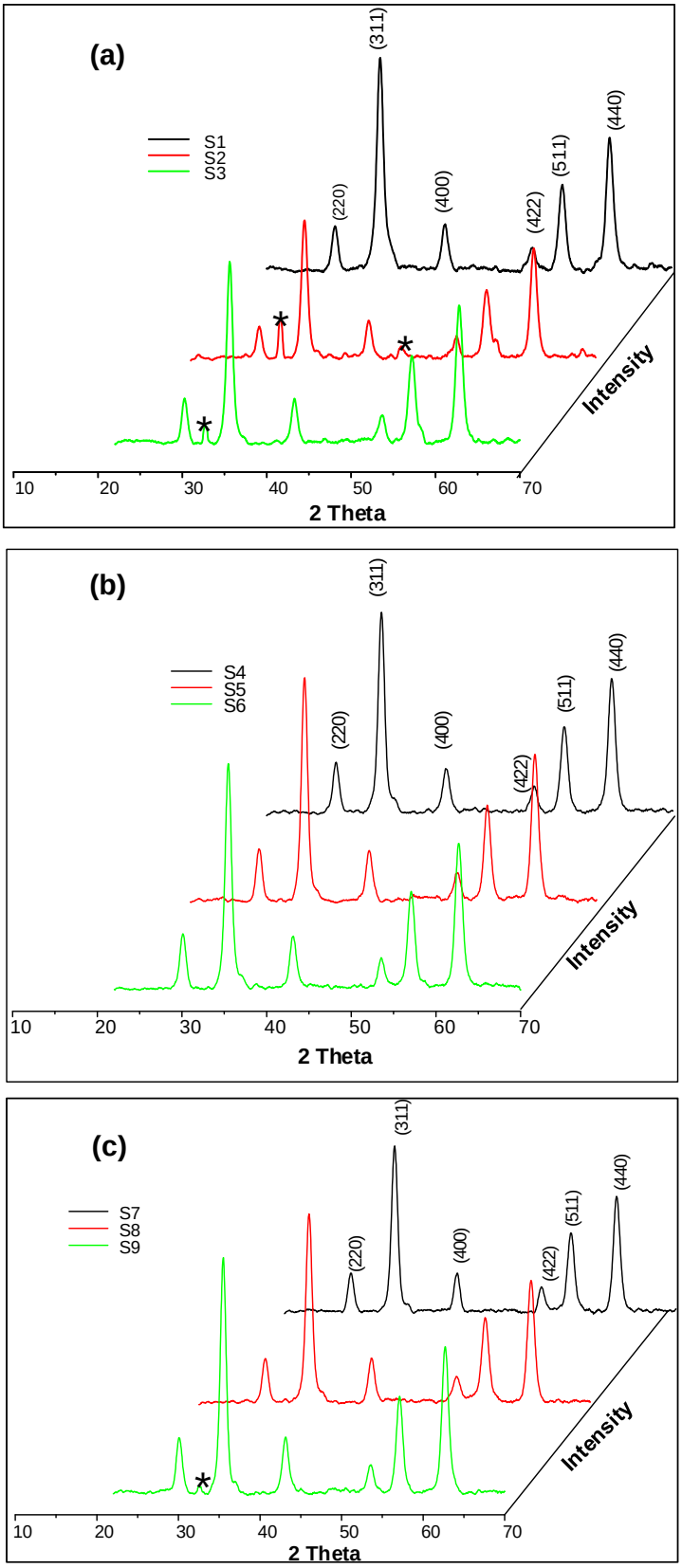

Figure 2.5(a-b): Powder X-ray diffraction analysis of the naked MIONs prepared at 30 °C, 60 °C and 90 °C using various total iron concentrations**.**

Stellenbosch University https://scholar.sun.ac.za

Naked MIONs prepared at 90 °C (**S7**, **S8** and **S9**) were also characterised using PXRD. Overlaid diffractograms of **S7**, **S8** and **S9** are shown in **Figure 2.5 (c)**. All these diffractograms show diffraction peaks which were indexed at *hkl* values: (220), (311), (400), (422), (511) and (440) corresponding to standard magnetite as per JCPDS card No. 00-011-0614. However, the diffractogram for **S9** shows small diffraction peaks which is also exhibited in the diffractograms of naked MIONs prepared at 30 °C, indicating that **S9** contained a small fraction of other iron oxide impurities.

Therefore, as per PXRD analysis, the optimised reaction conditions to produce pure magnetite nanoparticles are: total iron concentration ranges of 0.125 M at the temperature of 30 °C and 90 °C, as well as total iron concentration of 0.125 M, 0.250 M and 0.375 M at 60 °C.

The average crystallite size (<D>, nm) was calculated using the Debye-Scherrer equation (**Equation 2.7**).[1, 2] The full width at half maximum height (FWHM) of the three intense diffraction peaks indexed at (311), (511) and (440) was used to determine the particle size. However, the peak indexed at (311) is more defined than other peaks and is therefore believed to give reliable particle size values.

Equation 2.7:
$$D_{hkl} = \frac{k\lambda}{\beta\cos\theta}$$

Where D_{hkl} is the crystallite size (nm), λ is the radiation wavelength, β is the full width at half maximum height (FWHM), θ is the Bragg angle (degrees).

The average particle sizes of **S1** to **S9** are summarised in the bar chart shown in **Figure 2.6**. As seen in the figure, there is no significant difference in particle size determined with the diffraction peak indexed at (311) and the size determined using the average of the three diffraction peaks.

The particle size of naked MIONs (**S1** to **S9**) was in the range 11 nm to 12 nm. Thus, varying total metal iron concentration (0.125 M, 0.250 M and 0.375 M) and temperature (30 °C, 60 °C and 90 °C) did not have a significant effect on particle size. However, it should be noted that the average particle size corresponds to the size of magnetite nanoparticles reported in the literature.[36]

Stellenbosch University https://scholar.sun.ac.za

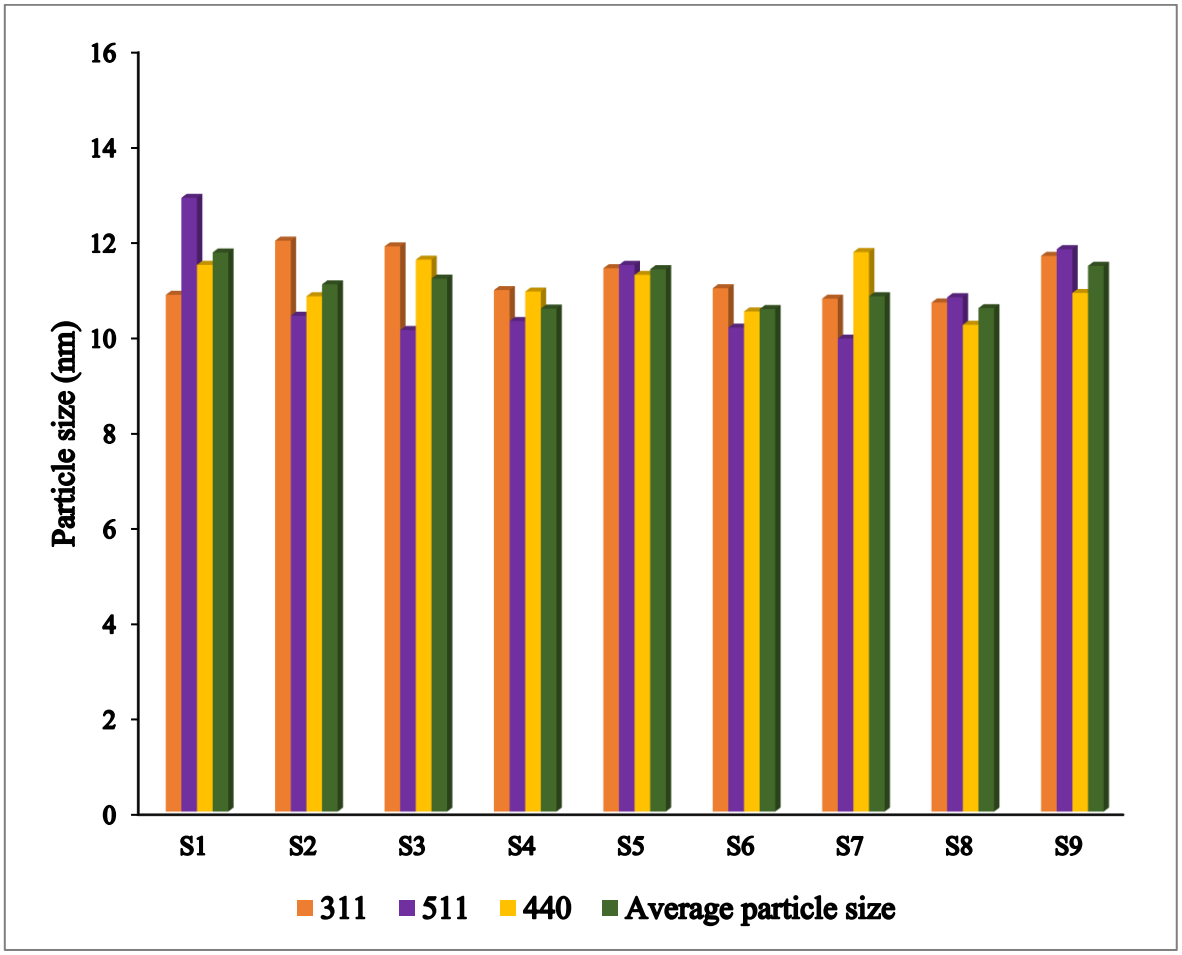

Figure 2.6: Particle size of naked MIONs (**S1** to **S9**) determined using PXRD analysis.

2.2.2.3 Field emission scanning electron microscopy

The field emission scanning electron microscopy (FESEM) analysis was conducted to study the morphology of naked MIONs. **Figure 2.7** shows the FESEM images of naked MIONs prepared using reaction **S1** to **S9** (**Table 2.1**). All FESEM images of naked MIONs prepared at 30 °C exhibited spherical shapes irrespective of the total iron concentration. The FESEM images of naked MIONs prepared at 60 °C also exhibited spherical nanoparticles. Increasing the total iron concentration did not influence the morphology of the nanoparticles. On the contrary, nanoparticles produced at 90 °C increased in size with an increase in total iron concentration. At high temperature, particle mobility is increased hence, high concentration would result in collision of the particles promoting particle growth. According to FESEM analysis, temperature did not have a significant effect on particle morphology.

Stellenbosch University https://scholar.sun.ac.za

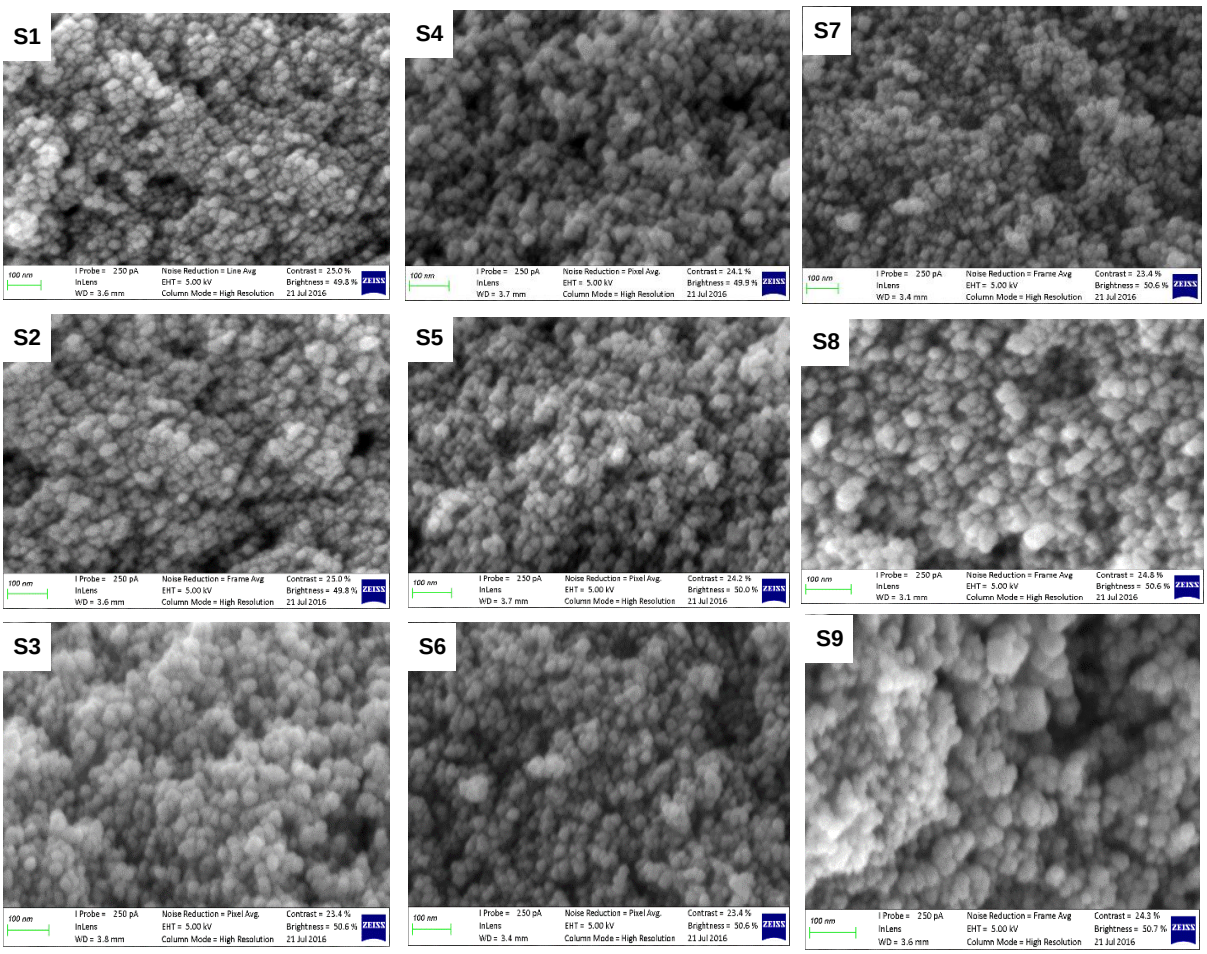

Figure 2.7: FESEM images of **S1** to **S9** prepared at 30 °C, 60 °C and 90 °C using different total metal concentration of 0.125 M, 0.250 M and 0.375 M.

2.2.2.4 High resolution transmission electron microscopy

The HRTEM analysis was conducted to determine the average particle size, size distribution, and morphology of naked MIONs. The HRTEM images of **S1**, **S2** and **S3** are shown in **Figure 2.8**. All the three images show spherical agglomerated (collision of nanoparticles resulting into the formation of bigger particles) and polydispersed nanoparticles. The average particle size of **S1**, **S2** and **S3** as shown in **Figure 2.8** are as follows 9.2±2.3 nm, 10.4±2.5 nm and 10.8±1.8 nm, respectively. Therefore, the average particle sizes of naked MIONs slightly increased with a increase in total iron concentration. However, total iron concentration did not have a significant effect in particle dispersity (various sizes of the nanoparticles). The figure also shows the selected area electron diffraction (SAED) of **S1**, **S2** and **S3**. As shown in the figure, **S1**, **S2**, and **S3** exhibited the d-spacing corresponding to the respective miller indices *(hkl)*: (220), (311), (400), (440) and (511).

Stellenbosch University https://scholar.sun.ac.za

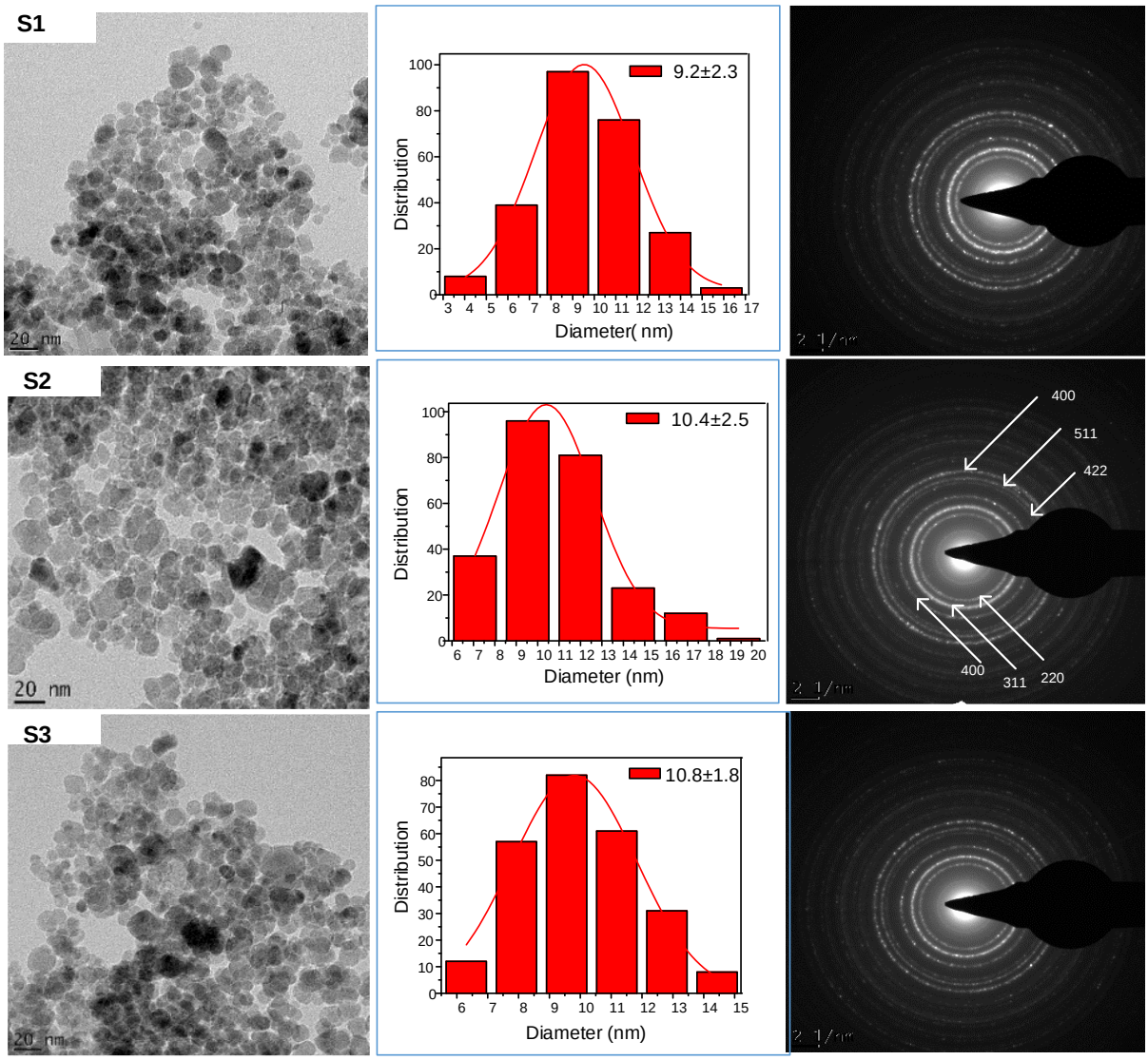

Figure 2.8: HRTEM images, particle size histograms and SAED of the naked MIONs (**S1**, **S2** and **S3**) prepared at 30 °C using different total iron concentration.

HRTEM images of naked MIONs prepared at 60 °C (**S4**, **S5**, and **S6)** with a total iron concentration of 0.125 M, 0.250 M, and 0.357 M respectively are shown in **Figure 2.9.** The particles of **S4**, **S5**, and **S6** are generally spherical, agglomerated and polydispersed. The average particle sizes of **S4**, **S5** and **S6** are 10.6±1.7 nm, 11.6±1.9 nm and 10.2±1.4 nm respectively. Therefore, the effect of iron concentration did not affect the average particle size of naked MIONs. The SAED diffraction of **S4**, **S5**, and **S6** shows miller indices corresponding to that of magnetite indicating that naked MIONs were magnetite nanoparticles. HRTEM images and corresponding histograms of naked MIONs prepared at 90 °C (**S7**, **S8** and **S9)** are shown in **Figure 2.10**. All images showed spherical and agglomerated nanoparticles. The

Stellenbosch University https://scholar.sun.ac.za

average particles for **S7**, **S8** and **S9** are as follows: 11.1±1.7 nm, 12.3±2.3 nm and 12.5±2.1 nm, respectively.

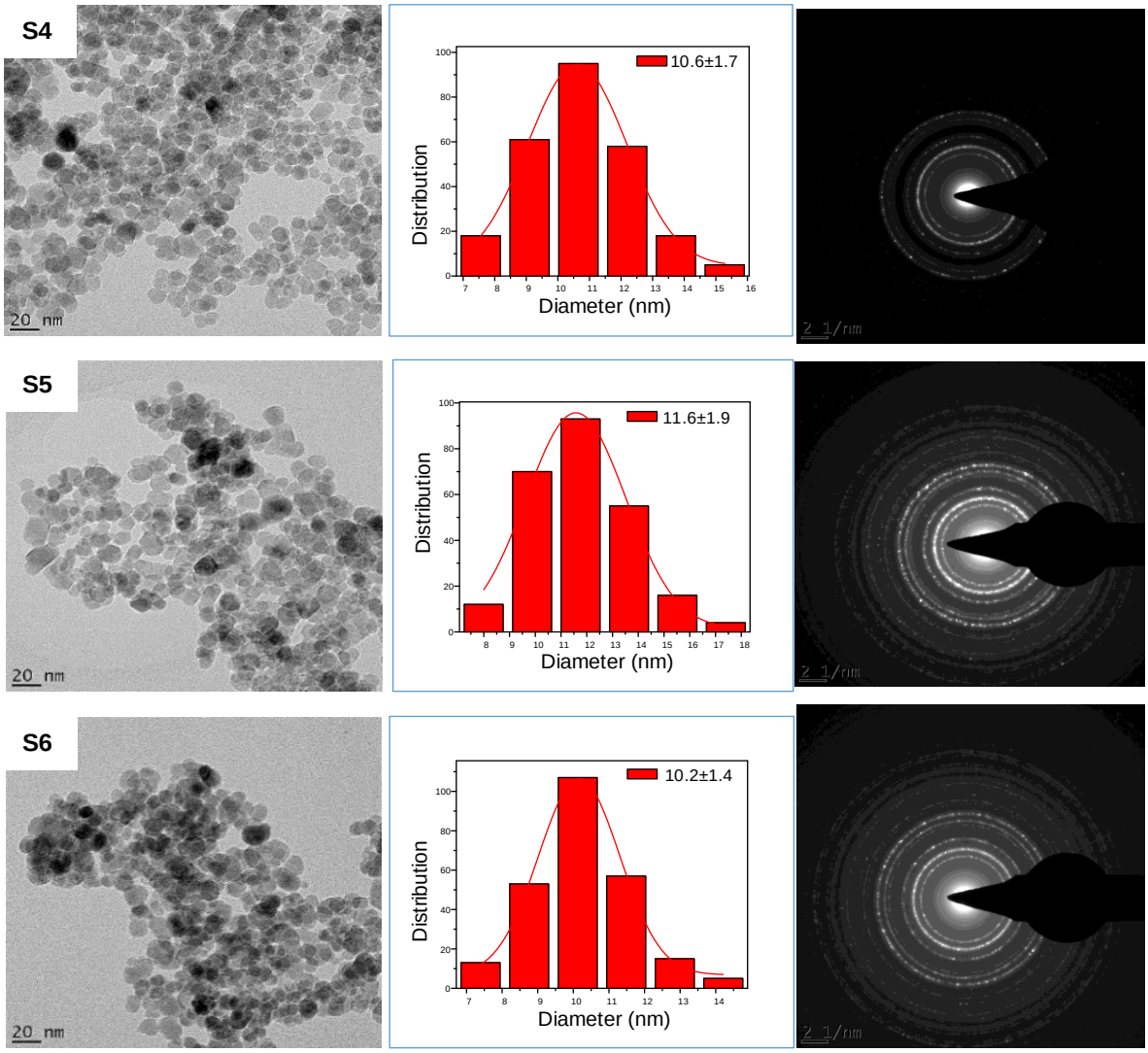

Figure 2.9: HRTEM images, particle size histograms and SAED of the naked MIONs (**S4**, **S5** and **S6**) prepared at 60 °C using different total iron concentration.

As depicted by HRTEM results, the average particle sizes of naked MIONs prepared at 30 °C (**S1, S2** and **S3**) were generally smaller than the average particle sizes of naked MIONs prepared at 60 °C (**S4**, **S5** and **S6**) and 90 °C (**S7, S8** and **S9)**. The increase in particle size can be attributed to an increase in particle mobility which in turn promoted their collision thereby increasing the particle size. On another front, increasing metal precursor ions concentration did not have a significant effect at higher temperatures (60 °C and 90 °C). However, naked MIONs prepared using total Fe ions concentration of 0.125 M were generally small compared to

Stellenbosch University https://scholar.sun.ac.za

particles prepared with a higher metal precursor concentration of 0.250 M and 0.375 M. The EDX shows Fe, O and Cu (which is from the grid used for the sample preparation). No other elements are present confirming the purity of the sample.

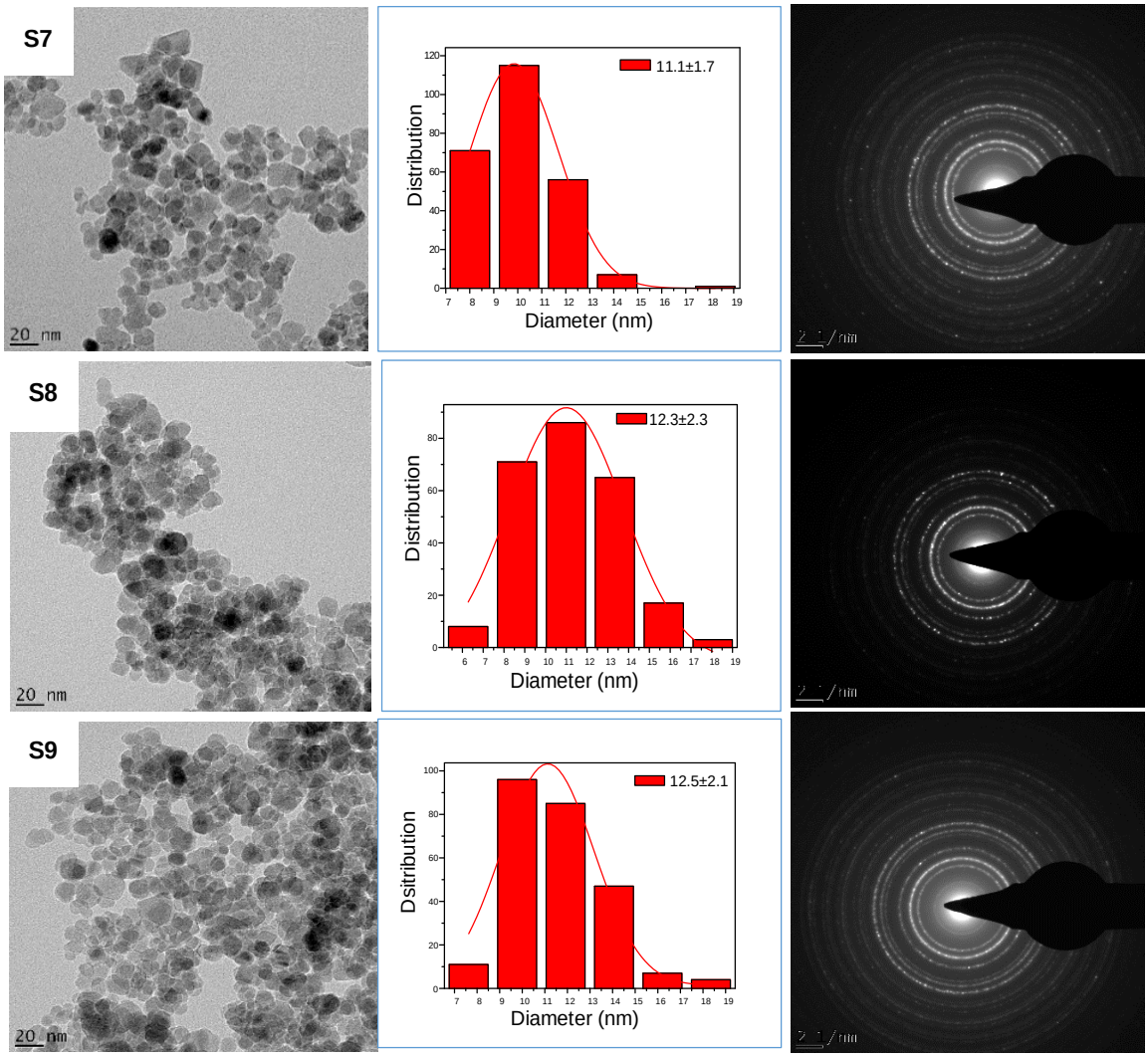

Figure 2.10: HRTEM images, particle size histograms and SAED of the naked MIONs (**S7**, **S8** and **S9**) prepared at 90 °C using different total iron concentration.

Studies of nanomaterials require the accurate determination of particle size. Hence, several analytical techniques are used to determine their particle sizes. In very small particle size regime, (nanometre scale), there is a good correlation between HRTEM counting and XRD results.[36] The reason for this is that the size provided by XRD corresponds to the average of the smallest undistorted regions separated by more-or-less sharp contours in the TEM micrograph. Hence, the average particle sizes of naked MIONs determined from HRTEM analysis were compared to particle sizes determined using Debye-Scherrer equation. A

Stellenbosch University https://scholar.sun.ac.za

summary of particle sizes of naked MIONs determined using both techniques is shown in **Table 2.2**. As seen in the figure, the average particle size of naked MIONs correlated well the size determined using Scherrer equation.

Table 2.2: Average particle size of Naked MIONs as determined by HRTEM and PXRD analysis

Sample	Temperature (°C)	Total Fe conc. (Fe^{2+} and Fe^{3+}) M	Particle size (nm)	
			HRTEM	PXRD
S1	30	0.125	9.20±2.3	10.84
S2	30	0.250	10.4±2.5	11.98
S3	30	0.375	10.8±1.8	11.86
S4	60	0.125	10.6±1.7	10.94
S5	60	0.250	11.6±1.9	11.4
S6	60	0.375	10.2±1.4	10.98
S7	90	0.125	11.1±1.7	10.76
S8	90	0.250	12.3±2.3	10.68
S9	90	0.375	12.5±2.1	11.66

2.3 CONCLUSION

Magnetite nanoparticles (naked MIONs) were synthesised using controlled co-precipitation of Fe(II) and Fe(III) with the molar ratio of 2:1. The reaction was performed under anaerobic conditions using NH_4OH as a base. The synthetic method was optimised by varying temperature (30 °C, 60 °C and 90 °C) and the total iron concentration (0.125 M, 0.250 M and 0.375 M). Infrared spectroscopy and powder X-ray diffraction (PXRD) analysis were used to determine the purity of naked MIONs. Average particle size and crystallinity of naked MIONs was characterised using HRTEM, PXRD, and selected area electron diffraction (SAED). Based on PXRD and SAED results, naked MIONs produced using all the reaction conditions were mainly magnetite. However, naked MIONs prepared at 60 °C with the total iron (Fe^{2+} and Fe^{3+}) concentration of 0.125 M to 0.250 M (**S4** and **S5**) produced the purest magnetite. The average particle sizes of **S4** and **S5** the nanoparticle according to HRTEM and PXRD was in the range of 10.00 nm to 11.00 nm which correspond to the average particle size of magnetite nanoparticles reported in the literature.

Stellenbosch University https://scholar.sun.ac.za

2.4 EXPERIMENTAL

All the chemicals were purchased from Merck and Sigma-Aldrich and were used without further purification. Distilled deionized water (Milli-Q, 18 MΩ cm) was deoxygenated by bubbling with pure N_2 gas for 30 min prior to use.

2.4.1 Synthesis of naked magnetic iron oxide nanoparticles by co-precipitation

Naked MIONs were prepared using chemical co-precipitation. The synthetic method was optimized by varying the total concentration of the precursor metals (Fe^{2+} and Fe^{3+}) but keeping their molar ratio 1:2. The optimum reaction conditions were: temperature of 60 °C and precursor concentration of 0.125 M. The metal ion precursors were dissolved in degassed distilled deionized water and stirred for 10 min. Upon dropwise addition of an excess amount of NH_4OH (33 %) to the resultant mixture, a green precipitate was formed. The colour of the precipitation changed to green, brown and then black, signifying the formation of naked MIONs in the form of magnetite. The reaction was stirred for a further 30 min to ensure complete precipitation of the precursor ions. The black solid was separated by magnetic decantation, washed several times with double distilled water until the pH of the water was 7. The final product (**S4** and **S5**) was then washed with ethanol (50 mL × 2) and dried at 40 °C in the oven. The MIONs are air sensitive, hence they were kept under nitrogen, in a desiccator. Precaution was taken during washing and characterization of naked MIONs. Exposure to air over a prolonged period resulted in oxidation, which was observed visually (colour change from black to brown) and it could be confirmed with PXRD.

2.4.2 Characterisation techniques

2.4.2.1 Attenuated total reflection infrared spectroscopy

Infrared spectra were recorded using PerkinElmer spectrum Two IR spectrometer. A very small amount of dried MIONs were mixed with dried KBr salt finely ground and pressed into a pellet. A sample of finely crushed pure KBr was used as the background. The spectra were collected between 4000 and 400 cm^{-1} using 32 scans at a nominal resolution of 4.0 cm^{-1} and were presented without background correction.

Stellenbosch University https://scholar.sun.ac.za

2.4.2.2 Powder X-ray diffraction

Structural properties of the MIONs obtained were investigated by Powder X-ray diffraction (XRD) with a Siemens D8 Advance diffractometer using Cu Kα radiation (λ = 1.540 Å) operated at 40 kV and 30 mA. XRD patterns were recorded in the range 10 – 90º (2θ) with a scan step of 0.02°. The average crystallite size (<D>, nm) was calculated from line broadening analysis using the Debye-Scherrer formula.[1, 2]

2.4.2.3 Field emission scanning electron microscopy

Particle morphology was characterised using CMi SEM MERLIN (FE-SEM) composed of GEMINI II column, a process chamber with a 5-axes motorized stage, and a semi-automatic airlock. Images were captured using In-lens detector at a high resolution. Samples preparation only involved drying the MIONs overnight, spreading them on a carbon tape and coating them with either gold or carbon sputter.

2.4.2.4 High resolution electron microscopy

Particle size and distribution were determined using JEOL-1200EXII electron microscope, high resolution transmission electron microscopy (HRTEM). An accelerating voltage of 250 KV was used throughout. A drop of sample was placed on a carbon-coated 200 mesh copper grid. The sample was dried under UV lamp and attached to the sample holder. The mean diameter and size distribution of naked MIONs were determined by measuring more than 250 individual naked MIONs from the HRTEM image using ImageJ, a public domain image processing program.[4]

Stellenbosch University https://scholar.sun.ac.za

CHAPTER 3 : SORPTION OF Au(III), Pd(II) and Pt(IV) COMPLEXES BY NAKED MIONs

3.1 INTRODUCTION

In this chapter, sorption of Au(III)-Cl, Pd(II)-Cl, and Pt(IV)-Cl species/complexes by naked MIONs(**S4**) from acidic aqueous solution is investigated using batch experiments. The following parameters which might affect sorption are investigated: shaking speed, amount of adsorbent, initial metal complex concentration, and solution pH. The kinetic sorption experiments are analysed using three kinetic models: *pseudo*-first-order, *pseudo*-second-order, and intraparticle diffusion. Sorption isotherm studies for Au(III)-Cl species are analysed using Langmuir and Freundlich sorption isotherms. UV-Vis experiments are carried out to get information about the speciation of these three metal species before and after sorption. Stability of the naked MIONs is studied by analysis of the concentration of iron leached into the solution during sorption. The crystal structure of naked MIONs after sorption of Au(III)-Cl, Pd(II)-Cl and Pt(IV)-Cl species is done using powder X-ray diffraction. A possible mechanism responsible for the removal of these precious metal species by naked MIONs is also discussed.

3.2 THE CHEMISTRY OF Au(III), Pd(II) AND Pt(IV) CHLORIDE COMPLEXES IN AQUEOUS SOLUTION

3.2.1 General chemistry

Gold is an extraordinary ductile and malleable metal, which is in demand in jewellery manufacturing, high-technological industries and medical applications, because of its unique physical and chemical properties. Gold reacts with all the halogens, most vigorously with bromine, which undergoes an exothermic reaction with gold powder at room temperature to produce Au_2Br_6.[118] Therefore, gold forms a range of complexes with halogens. However, gold chloro species have been studied more extensively.[14,119,120]

Palladium (Pd) and platinum (Pt) belong to a group of precious metals called the platinum group metals (PGMs). They are regarded as primary PGMs while the other four metals; iridium (Ir), ruthenium (Ru), rhodium (Rh) and osmium (Os) are regarded as the insoluble PGMs.[2] Like other PGMs, Pd and Pt form a range of complexes with a variety of different

Stellenbosch University https://scholar.sun.ac.za

ligands. Their chloro species are the most commonly studied compared to other PGMs.[121–124] Chloride solution is the only cost effective medium in which all the PGMs can be brought into solution and concentrated.[4]

3.2.2 Chlorido species of Au(III), Pd(II) and Pt(IV) complexes in aqueous solutions

The chlorido species of Au(III), Pd(II) and Pt(IV) in aqueous solutions are known and have been studied for many years.[125–128] The anionic complexes undergo acid and alkali hydrolysis (replacement of chlorides by H_2O and OH^- ligands, respectively). The extent of hydrolysis depends on the total metal concentration, pH of the solution and chloride ion concentration due to changes in the ionic strength.

3.2.2.1 Au(III)

It is well documented that gold complexes are labile in solution, with the overall speciation being affected by the solution pH and ionic composition of the aqueous environment.[119,129] At the pH < 2.0, Au(III)-Cl forms a square planar complex, $AuCl_4^-$.[14] This complex is stable and soluble, and therefore has been used in many geochemical and biogeochemical studies, including ligand exchange kinetics and mechanism sorption and biogeochemistry.[119,130,131] In aqueous solutions, $AuCl_4^-$ undergoes acid and alkali hydrolysis and produces a range of chlorido, aqua and hydroxy complexes. Peck *et al.*[127] carried out an extensive study on the speciation of $AuCl_4^-$ in 1 M NaCl aqueous solutions using UV-Vis sorption and Raman spectroscopy to elucidate the mechanisms of Au transport and deposition related to the formation of Au deposits in Geology. Their study confirmed that at ambient temperature and pressure in a 1 M NaCl solution, Au(III)-Cl species occurs as square planar complexes. Again, at low pH, the dominant complex is $AuCl_4^-$. Furthermore, increasing solution pH to pH > 10 results in the replacements of the chloride ligands by hydroxide ligands, where the dominant species is $AuCl(OH)_3^-$.

In another study, Ogata and Nakano studied the recovery of gold using tannin gel adsorbent synthesized from natural condensed tannin. The sorption results suggested that tannin gel is very useful as an adsorbent for gold.[129] The study included an insight in the speciation of $AuCl_4^-$ in aqueous solution as it affects the sorption behaviour of Au(III)-Cl species in aqueous solution. They calculated the molar fractions of the various gold species as a function

Stellenbosch University https://scholar.sun.ac.za

of pH with the equilibrium constants at 0.01 M of chloride ion concentration. The equilibrium constants for the hydrolysis reactions are shown in **Equation 3.1**(a-b). The adsorption of gold was found to take place through the reduction of trivalent gold complexes to metallic gold on the surface of the tannin polymer composing the gel particles.

Equation 3.1(a-d):

$$a)\ Au(OH)_4^- + H^+ + Cl^- \leftrightarrow AuCl(OH)_3^- + H_2O \qquad K_1 = 10^{8.51}$$

$$b)\ Au(OH)_3^- + H^+ + Cl^- \leftrightarrow AuCl_2(OH)_2^- + H_2O \qquad K_2 = 10^{8.06}$$

$$c)\ AuCl_2(OH)_2^- + H^+ + Cl^- \leftrightarrow AuCl_3(OH)^- + H_2O \qquad K_3 = 10^{7.00}$$

$$d)\ AuCl_3(OH)^- + H^+ + Cl^- \leftrightarrow AuCl_4^- + H_2O \qquad K_4 = 10^{6.07}$$

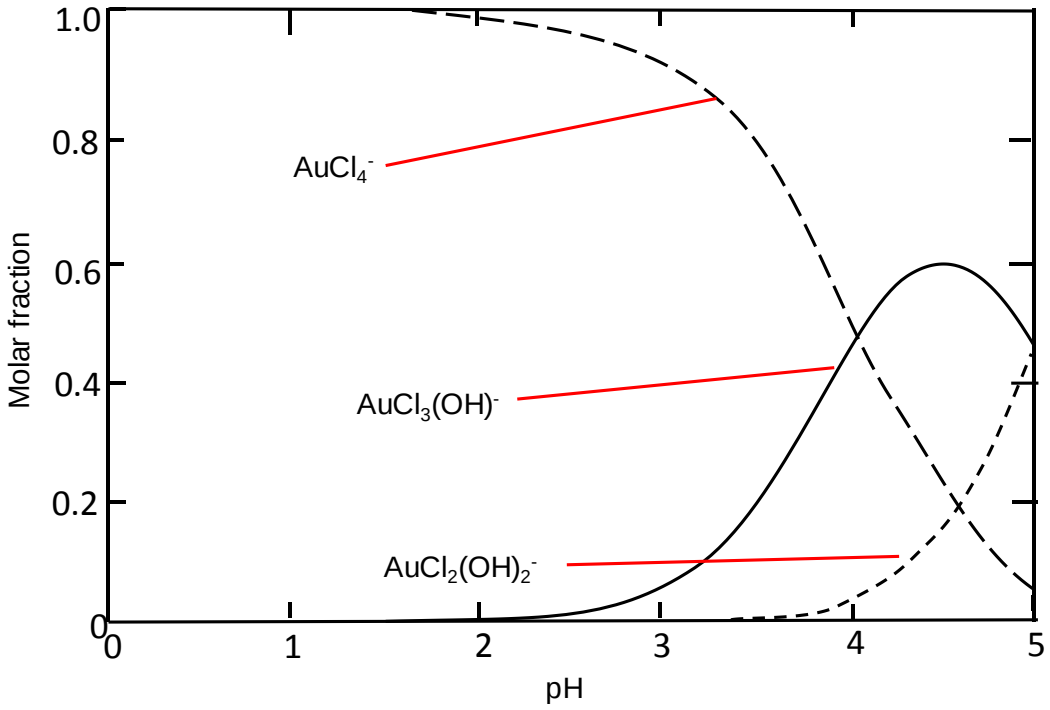

Figure 3.1: Distribution diagram of the hydrolysis reaction of $[AuCl_4]^-$ in aqueous solutions.[129]

3.2.2.2 Pd(II) and Pt(IV) complexes

Speciation of Pd(II)-Cl and Pt(II/IV)-Cl complexes in aqueous solutions have been studied extensity in the literature.[125,132] In highly acidic chloride-rich aqueous process solutions, the

Stellenbosch University https://scholar.sun.ac.za

PGMs predominantly exist as stable anionic complexes of the type $[MCl_x]^{n-x}$, where M is the metal, n is the oxidation state of the metal, and x is typically 4 or 6.[133] Dependent on the solution conditions, the $[MCl_x]^{n-x}$ complexes may undergo varying degrees of aquation and/or hydrolysis (or deprotonation) reactions, leading to several $[MCl_{x-y}(H_2O)_y]^{n-x+y}$ and $[MCl_{x-z}(OH)_z]^{n-x}$ species in solution (with n = 2-4, x = 4 or 6, and y, z = 0-6).[133]

3.2.2.2.1 Pd(II)

It is well known that Pd(II)-Cl forms quite stable complexes with chloride.[123] These complexes are assumed to form square planar complexes and can be represented by the general formula $[PdCl_n(H_2O)_{4-n}]^{2-n}$ (n = 0-4).[134] Tait *et al.*[125] carried out a detailed study on the effect of $[Cl^-]$, pH and temperature on speciation of Pd(II)-Cl in aqueous solutions at ambient to elevated temperatures using UV-Vis and Raman spectroscopy. At the pH of 2.0 and increasing the concentration of chloride from 0.00 M to 0.37 M, the following species were identified: $PdCl_4^{2-}$, $PdCl_3(H_2O)^-$, and $PdCl_2(H_2O)_2$. The spectrum obtained after the addition of 0.37 M NaCl matched to $PdCl_4^{2-}$. Therefore, at the pH < 2.0 and high chloride concentration, the Pd(II)-Cl complex exist as $PdCl_4^{2-}$ complex. Furthermore, the spectrum of Pd(II)-Cl with no added chloride corresponded to that of $PdCl_2(H_2O)_2$.

In another study, Kriek and Roux carried out a detailed study on spectrophotometric investigation of the complexation of Pd(II)-Cl with chloride and bromide at 25 °C.[135] The change in chloride concentration resulted into the formation of different Pd(II)-Cl complexes and hence a difference UV-Vis spectra as shown in **Figure 3.2**. Similar to Elding, Cruywagen and Kriek, the $PdCl_4^{2-}$ complexes has the highest sorption band with a maximum absorbance at 224 nm and a lower sorption band at 282 nm.[134,135] These charge transfer bands, caused by the transition of electrons from the chloride ligands to molecular orbitals localized primarily on Pd, are shifted towards shorter wavelengths with higher energies when chloride is substituted by water in the complexes. The stepwise formation constants for the chloride system correlated with the previous work of Elding, and Cruywagen and Kriek.[134,135]

3.2.2.2.2 Pt(IV)

The Pt(IV)-Cl species exhibit an octahedral coordination with the general formula $[PtCl_n(H_2O)_{6-n}]^{4-n}$ (n = 0-6). At low temperature, very acidic pH, and moderate to high Cl^- concentration, the dominant Pt(IV) species is $PtCl_6^{2-}$. Similar to the Pd system, the decrease

Stellenbosch University https://scholar.sun.ac.za

in [Cl^-] and/or increase in temperature, both species dissociate to complexes of lower ligand number.[136] As mentioned earlier, PGM chlorido complexes were studied as early as 1960 using UV-Vis and Raman sorption spectroscopy. However, the Pt(IV) chloride complexes were not examined to the same extent as the Pd(II)-Cl and Pt(II)-Cl analogy.

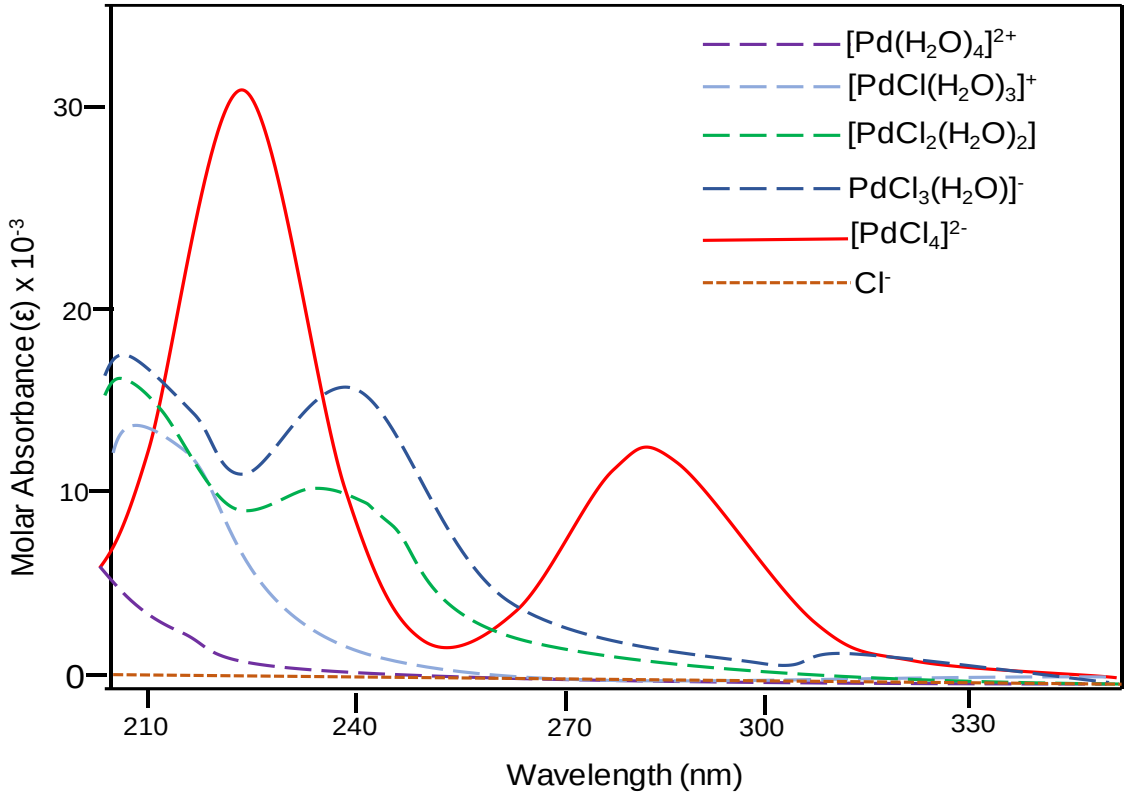

Figure 3.2: Calculated molar Sorption spectra of $[PdCl_n(H_2O)_{4-n}]^{2-n}$ (n = 0-4).

3.3 SORPTION OF PRECIOUS METALS BY METAL OXIDE ADSORBENTS

Since the last few years, the search for potential sorbents to recover precious metals from solution has acquired attention.[1,7,11] Various authors have examined the potential use of metal oxides, such as iron oxides, manganese oxides, and aluminium oxides as sorbents to recover precious metals from wastewater and leach solutions.[15,137] Iron oxides which are ubiquitous in subsurface environments, were studied intensively amongst these metal oxides.[14,138]

Alorro *et al.*[139] studied the recovery of Au(III)-Cl species from chloride solution using synthetic and naturally-occurring magnetite powders and studied various parameters that might affect the adsorption process such as pH, contact time, chloride concentration etc. The results of the study indicated that synthetic magnetite demonstrated selectivity towards Au,

Stellenbosch University https://scholar.sun.ac.za

Pt and Pd, and to a minor extent, Cu and Ni. The natural magnetite was found to be selective towards Au only. Maximum Au adsorption was achieved at pH 6–7 for both types of magnetite. At this pH, maximum Au uptake values of 4.4 mmol/g and 5.0 mmol/g were obtained for synthetic and natural magnetite, respectively. Increased chloride concentration decreased the Au uptake capacity for both synthetic and natural magnetite. Furthermore, Machesky *et al*.[14] examined sorption of Au(III)-Cl species by goethite (FeOOH) reported that the species were adsorbed in an inner-sphere, bidentate mechanism at low surface coverage, while the loading capacity of Au(III)-Cl was determined to be 0.2 mmol g^{-1} at pH 4.

In another study, Uheida *et al*.[15] studied the adsorption of Pd(II), Rh(III) and Pt(IV) complexes using magnetite nanoparticles from dilute hydrochloric acid solutions. Several parameters influencing the adsorption, such as contact time and metal concentrations, were studied. The fast equilibrium time of less than 20 min achieved for all metals was attributed to the large surface area and high surface reactivity of the magnetite nanoparticles. The maximum loading capacities for adsorption of Pd(II), Rh(III), and Pt(IV) complexes by magnetite nanoparticles were determined to be 0.103, 0.149, and 0.068 mmol/g respectively.

The surface of iron oxide adsorbents has hydroxyl groups on their surface and are represented using the notation, ≡FeOH. These surface hydroxyl groups are essential to the surface reactions of various processes that occur at the interface between the oxide surface and an electrolyte solution. The active surface group at the iron oxide surface are amphoteric, which can bind or release protons as shown by **Equation 3.2** and **Equation 3.3**. Both protonation and deprotonation change the total proton concentration and surface charge density, resulting in the sorption of cations and ligands at the metal oxide surface.

Equation 3.2 $\equiv \mathrm{FeOH} + \mathrm{H^+} \rightarrow \equiv \mathrm{FeOH_2^+}$

Equation 3.3 $\equiv \mathrm{FeOH} \rightarrow \mathrm{FeO^-} + \mathrm{H^+}$

The number of charged surface sites increases with increasing ionic strength and a decrease in pH. These characteristics are observed for magnetite. The pH_{pzc} refers to the pH value where the total net particle charge is zero. The pH_{pzc} for magnetite is in the range of 6.0 to 8.2.[7, 20]

Stellenbosch University https://scholar.sun.ac.za

The adsorption of metal complex on iron oxide surfaces can be explained using two mechanisms: inner-sphere and outer-sphere complexation. In the case of inner-sphere coordination, there is a direct bond between the adsorbed ion or molecule and the surface functional group while with the outer-sphere complexation, at least one water molecule is interposed between the surface site and the adsorbed species.[14,138] Electrostatic attraction is dominating outer-sphere complexation, whereas inner-sphere complexation involves to some extent covalent bonding. These mechanisms have been illustrated in **Figure 3.3**. Indications of which mechanism that is the dominating can be given by the sorption behaviour.

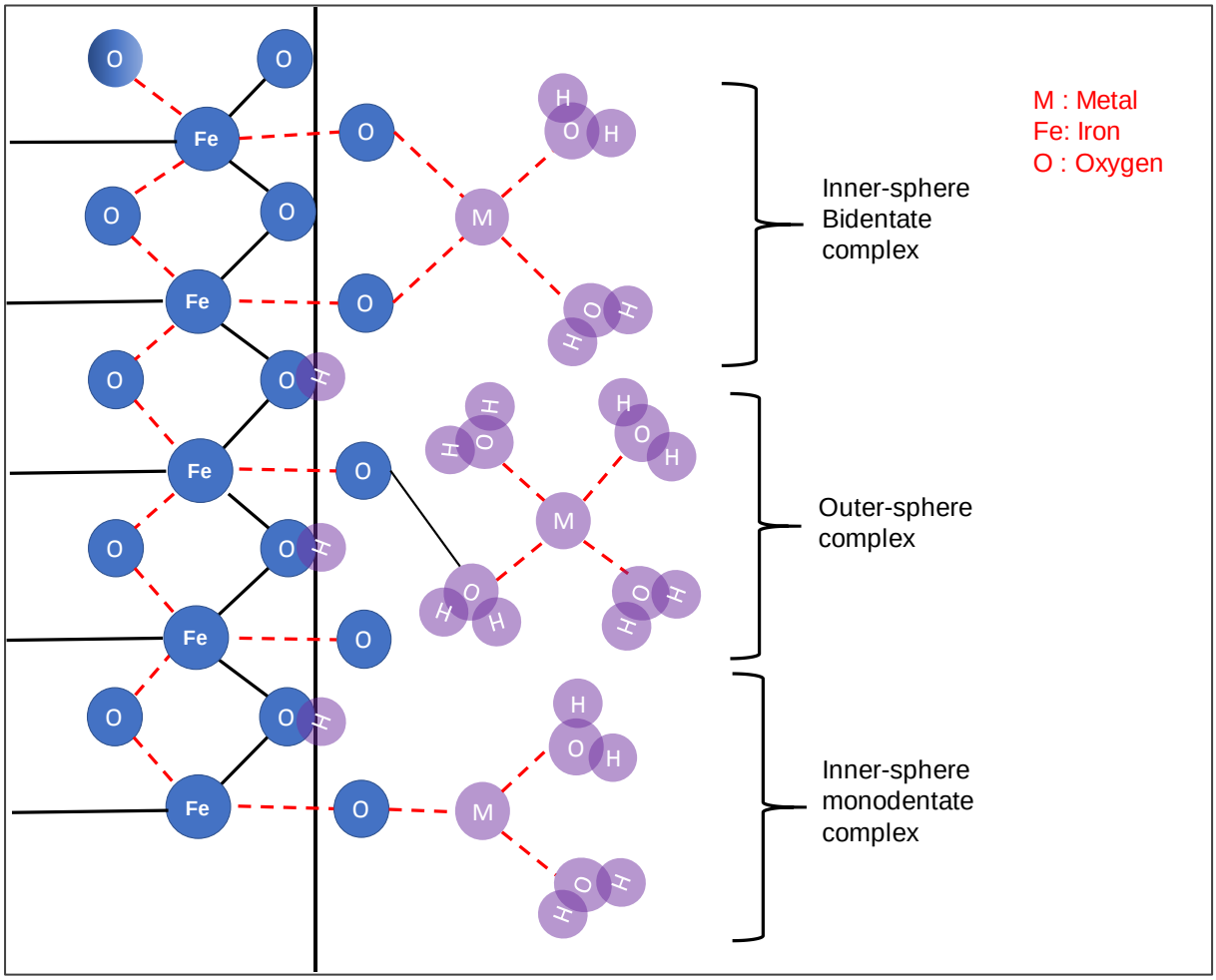

Figure 3.3: Schematic indicating the formation of inner-sphere and outer-sphere complexes at the solid-solution interface.[140]

Stellenbosch University https://scholar.sun.ac.za

3.4 RESULTS AND DISCUSSIONS

3.4.1 Batch sorption studies of Au(III), Pd(II) and Pt(IV) complexes by naked MIONs

Sorption of Au(III)-Cl, Pt(IV)-Cl and Pd(II)-Cl complexes by naked MIONs (**S4**) was carried out using setting up individual batch sorption experiments for each metal complex separately. Sorption of species from solutions using magnetic nanoparticles is called magnetic solid phase extraction (MSPE).[32] A brief discussion on MSPE was covered in **Chapter 1**. All experiments were carried out using the protocol summarised schematically in **Figure 1.4** of **Chapter 1**.[13,33] The samples were shaken with a Labcon mechanical shaker for a prescribed period. At the end of each run, naked MIONs (**S4**) were separated from the solution as shown in **Figure 3.4** and the remaining solution was transferred into 10 mL or 15 mL conical centrifuge tubes. The concentration of the metal ions was determined before and after sorption by ICP-OES.

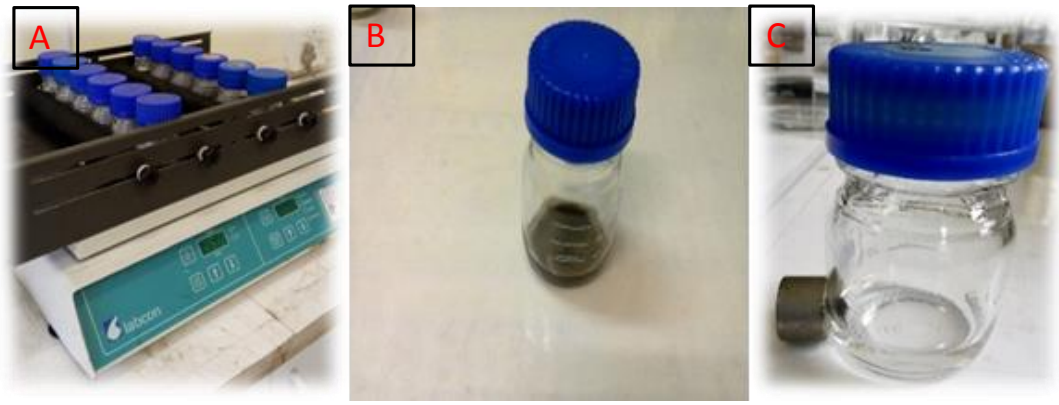

Figure 3.4: (**A**) shows the shaker used for all sorption experiments, loaded with Schott bottles used as sorption vessels, (**B** and **C**) shows the Schott bottles with the naked MIONs suspended in an aqueous solution containing an analyte of interest, and naked MIONs attracted to the magnet.

The concentration of Au(III)-Cl, Pt(II)-Cl and Pd(IV)-Cl complexes were determined before and after sorption by ICP-OES. Their speciation was studied by UV-Vis spectroscopy. The sorption capacity was calculated using **Equation 3.4** while the removal efficiencies were determined using **Equation 3.5.**

Equation 3.4

$$q = (C_i - C_{aq})\frac{V}{m}$$

Equation 3.5

$$\%Re = \frac{(C_i - C_{aq})}{C_i} \times 100\ \%$$

Stellenbosch University https://scholar.sun.ac.za

Where *q* represents sorption capacity and %Re represents the percentage of the metal removed from solution. In both equations, C_i represents initial metal chloro complex concentration (mg/L), C_{aq} represents metal chloro anionic concentration in aqueous solution (mg/L) after Sorption, V represents volume of the aqueous phase (mL) and m dosage of the adsorbent (g).

3.4.1.1 Effect of the shaking speed on sorption of Au(III) complexes

Shaking or mixing of the samples is an important parameter to be investigated when carrying out solid phase extraction experiments to ensure optimal interaction between the solid and the liquid phase. Batch experiments were conducted at 120 rpm, 150 rpm, and 200 rpm. Shaking speed optimisation was only carried out for single batch sorption of Au(III)-Cl species. The experiments were carried out at room temperature (25±2 °C) and the initial Au(III)-Cl concentration used for all the three batch experiments was 51 mg/L, while the mass of naked MIONs was 30.3 mg. The volume of the solution and pH were10 mL and 2.5 respectively. The results are depicted in **Figure 3.5**.

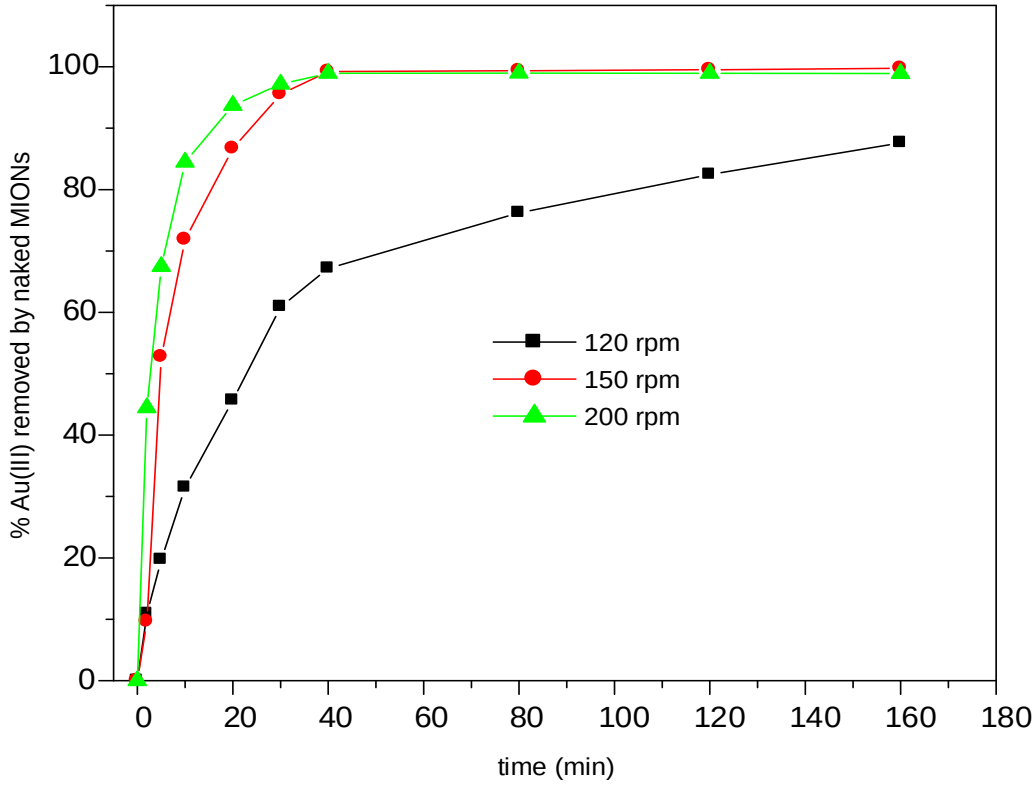

Figure 3.5: Effect of the mechanical shaker speed on Sorption of Au(III)-Cl from acidic solution by naked MIONs. Experimental conditions: [Au(III)]: 51 mg/L, mass of naked MIONs: 30.3 mg, total aqueous phase: 10 mL, pH: 2.5 and temperature: 25±2 °C.

Stellenbosch University https://scholar.sun.ac.za

A rapid increase in sorption of Au(III)-Cl for the first 10 min of sorption can be attributed to availability of the vacant sites.[42] This applies to all the three batch sorption experiments. However, the effect of shaking speed played a vital role in sorption of Au(III)-Cl by the naked MIONs, as increasing the shaking speed resulted in an increase in the percentage removal of Au(III)-Cl. For instance, shaking the samples at 120 rpm achieved a removal percentage of about 80 % after 160 min. But, increasing the shaking speed to 150 rpm increased the percentage removal to 100 % after only 40 min. However, increasing the shaking speed from 150 rpm to 200 rpm did not have a significant effect on percentage removal of Au(III)-Cl from solution. As expected, an increase in the stirring speed from 150 rpm to 200 rpm, led to an increase in the rate of adsorption of Au(III)-Cl species from solution. The sorption equilibrium also slightly decreased when shaking at 150 rpm to 200 rpm. Since there was only a slight difference in percentage removal of Au(III)-Cl when the shaking speed was increased from 150 rpm to 200 rpm, all subsequent batch sorption experiments were conducted at 150 rpm.

3.4.1.2 Effect of the amount of naked MIONs on sorption of Au(III), Pd(II), and Pt(IV) complexes

The effect of adsorbent doses on sorption of Au(III)-Cl species was investigated by varying the amount of naked MIONs and keeping other conditions the same. The three batch experiments were carried out using 10.3 mg, 20.2 mg and 30.3 mg of naked MIONs respectively. The sorption was carried out at room temperature (25±2 °C), the concentration of Au(III)-Cl was 10 mg/L, the aqueous solution pH was at 2.5, the volume of the aqueous phase was 10 mL and the shaking speed was 150 rpm. The results obtained are presented in **Figure 3.6**.

The figure shows that Au(III)-Cl removal percentages from solution increased with time for all the three batch experiments. About 95 % removal of Au(III)-Cl was achieved for all the three batch experiments. However, the figure shows a significant difference in sorption equilibrium reached by each batch experiment. For instance, using 20.3 mg of naked MIONs shifted sorption equilibrium to 40 min, while 30.4 mg of naked MIONs decreased sorption equilibrium to 10 min. The difference in sorption rate with an increase in amount of naked MIONs can be attributed to the increase in sorption site and hence decreasing the time to reach an equilibrium.

Stellenbosch University https://scholar.sun.ac.za

Another important observation is that, a rapid sorption was observed in the early stages and very slowly decreased towards the end of the sorption. Again, a large fraction on the total amount of Au(III)-Cl was removed within a short time. A similar trend has been reported in the literature on sorption of metal ions/species by nano-adsorbents, where the sorption was fast in the early stages and gradually decreases until equilibrium is reached.[42,141,142] The initial stage implies an external surface diffusion, the second stage is usually gradual, while final stage if characterized by the equilibrium state. The fast sorption in the initial stages might be due to many surface sites available for sorption. After a lapse of time, the remaining surface sites are difficult to access. The sorption kinetics for sorption of Au(III)-Cl by naked MIONs are explained in the later **Section 3.4.3**.

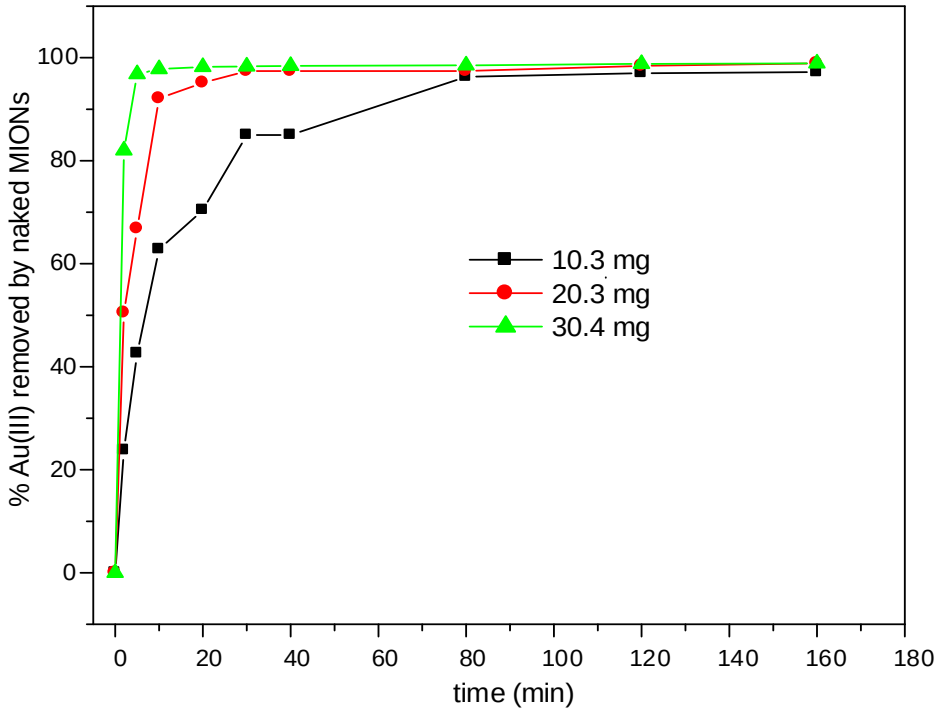

Figure 3.6: Effect of the amount of naked MIONs on Sorption of Au(III)-Cl from acidic solution by naked MIONs. Experimental conditions: [Au(III)]: 10 mg/L, total aqueous phase: 10 mL, pH: 2.5, temperature: 25±2 °C and shaker speed: 150 rpm.

Single component-batch sorption studies for the effect of the adsorbent doses in sorption of Pd(II)-Cl by naked MIONs were investigated by varying the amount of naked MIONs as follows; 10.5 mg, 20.4 mg and 30.6 mg. Other conditions were as follows: initial Pd(II)-Cl concentration; 10 mg/L, total aqueous phase; 10 mL, pH; 2.5, temperature: 25±2 °C and shaker speed: 150 rpm.

Stellenbosch University https://scholar.sun.ac.za

The results for the effect of the amount of naked MIONs on sorption of Pd(II)-Cl complexes is shown in **Figure 3.7**. The figure shows that the amount of naked MIONs plays a vital role in sorption of Pd(II)-Cl complexes by naked MIONs, since the removal percentages increased with an increase in the naked MIONs doses. As portrayed in the figure, sorption equilibrium was reached within 2 min to 5 min. However, the maximum percentage removal of Pd(II)-Cl complexes by naked MIONs using similar conditions used for sorption of Au(III)-Cl complex were very low. To improve sorption of Pd(II)-Cl complexes, the amounts of naked MIONs were increased. The two new sorption batch experiments were carried out using 60.4 mg and 90.3 mg of naked MIONs. The graph depicts that while 30.6 mg of naked MIONs removed only 30 % of Pd(II)-Cl complex after 120 min, increasing the amount of naked MIONs to 60.4 mg and 90.3 mg led to an increased Pd(II)-Cl complex removal percentage to around 50 % and 61 % respectively.

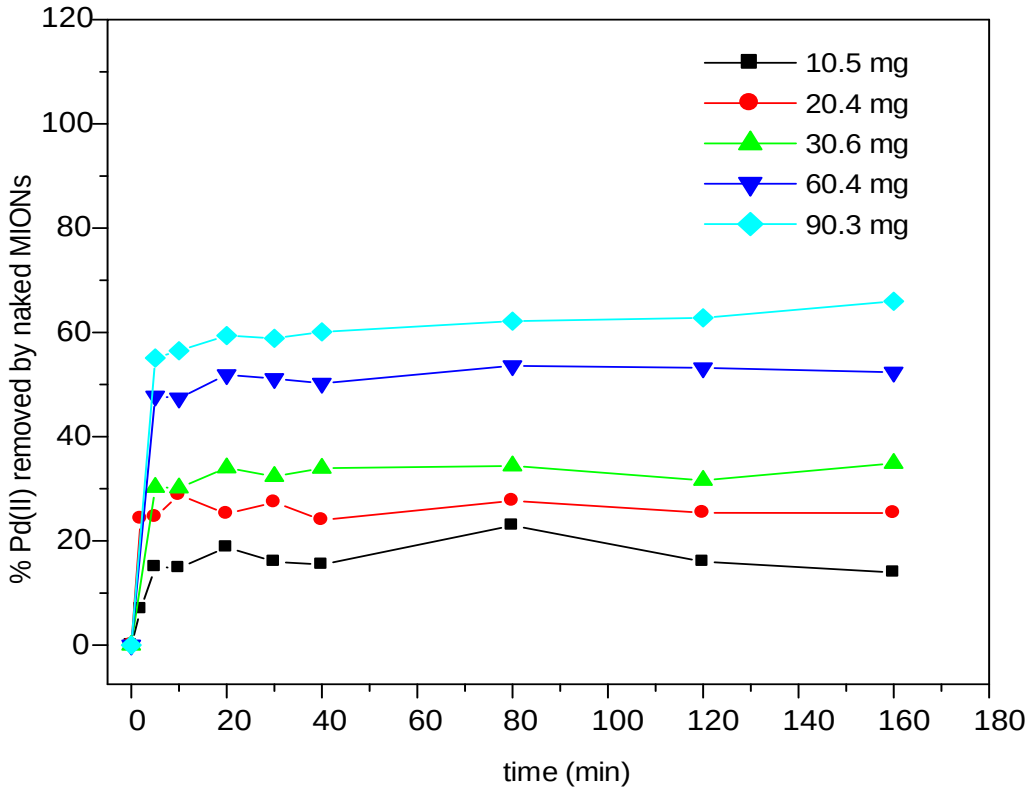

Figure 3.7: Effect of the amount of naked MIONs on Sorption of Pd(II)-Cl from acidic solution by naked MIONs. Experimental conditions: [Pd(II)]: 10 mg/L, total aqueous phase: 10 mL, pH: 2.5, temperature: 25±2 °C and shaker speed: 150 rpm.

The effect of the amount of naked MIONs in sorption of Pt(IV)-Cl complexes from acidic aqueous solution was performed by varying the amount of naked MION as follows: 30.1 mg,

Stellenbosch University https://scholar.sun.ac.za

60.1 mg and 90.1 mg. Other experimental conditions were as follows: [Pt(IV)]; 10 mg/L, total aqueous phase; 10 mL, pH; 2.5, temperature: 25±2 °C and shaker speed: 150 rpm. The results are shown in **Figure 3.8**. As shown in the figure, removal percentage of Pt(IV)-Cl complex for the three sorption batch experiments increased with time. The amount of naked MIONs played an important role in sorption Pt(IV)-Cl by naked MIONs. As seen in **Figure 3.8**, 30.1 mg of naked MIONs removed 75 % of Pt(IV)-Cl and 90.13±0.11 mg removed about 90 % of Pt(IV) from solution. Once again, this can be attributed to an increase in sorption sites. It is also important to point out that removal of Pt(IV) from solution was rapid in the first 10 minutes of sorption and the sorption equilibrium was reached after 40 min.

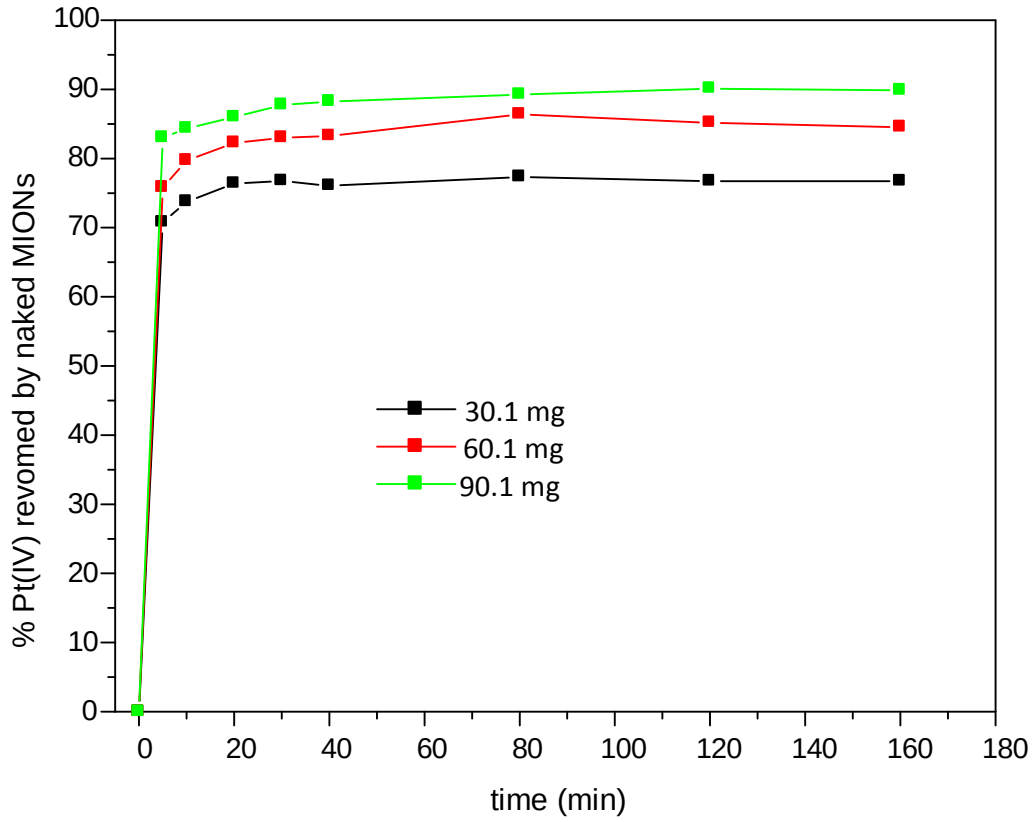

Figure 3.8: Effect of the amount of naked MIONs on sorption of Pt(IV)-Cl complex from acidic solution by naked MIONs. Experimental conditions: [Pt(IV)]: 10 mg/L, total aqueous phase: 10 mL, pH: 2.5, temperature: 25±2 °C and shaker speed: 150 rpm.

Adsorption results for the effect of the amount of naked MIONs in sorption of these three metal complexes shows very interesting results. Sorption was carried out at the pH of 2.5 and as discussed earlier, at low pH and high Cl^- concentration, Au(III)-Cl, Pd(II)-Cl and Pt(IV)-Cl exists as anionic complexes: $AuCl_4^-$, $PdCl_4^{2-}$ and $PtCl_6^{2-}$ respectively. As depicted by the

Stellenbosch University https://scholar.sun.ac.za

results above, sorption affinity of Au(III)-Cl, Pd(II)-Cl and Pt(IV)-Cl complexes by naked MIONs follows the order Au>Pt>Pd.

3.4.1.3 Effect of initial metal concentration on sorption of Au(III), Pd(II), and Pt(IV) complexes

The effect of initial concentration on sorption of Au(III)-Cl species by naked MIONs was studied by varying the initial concentration of Au(III)-Cl in solution as follows: 10 mg/L, 26 mg/L and 51 mg/L. The experiment was carried out at room temperature (25±2 °C), the amount of naked MIONs was 10.3 mg, the volume of the aqueous phase was 10 mL, and the pH of the solution was 2.5. The results are presented in **Figure 3.9**. Increasing the initial Au(III)-Cl concentration in the solution resulted in a decrease in percentage removal of Au(III)-Cl from solution. For instance, 10 mg/L of naked MIONs removed 100 % of Au(III)-Cl. Furthermore, batch adsorption experiments where initial Au(III)-Cl complex concentration of 51 mg/L was used, did not reach equilibrium.

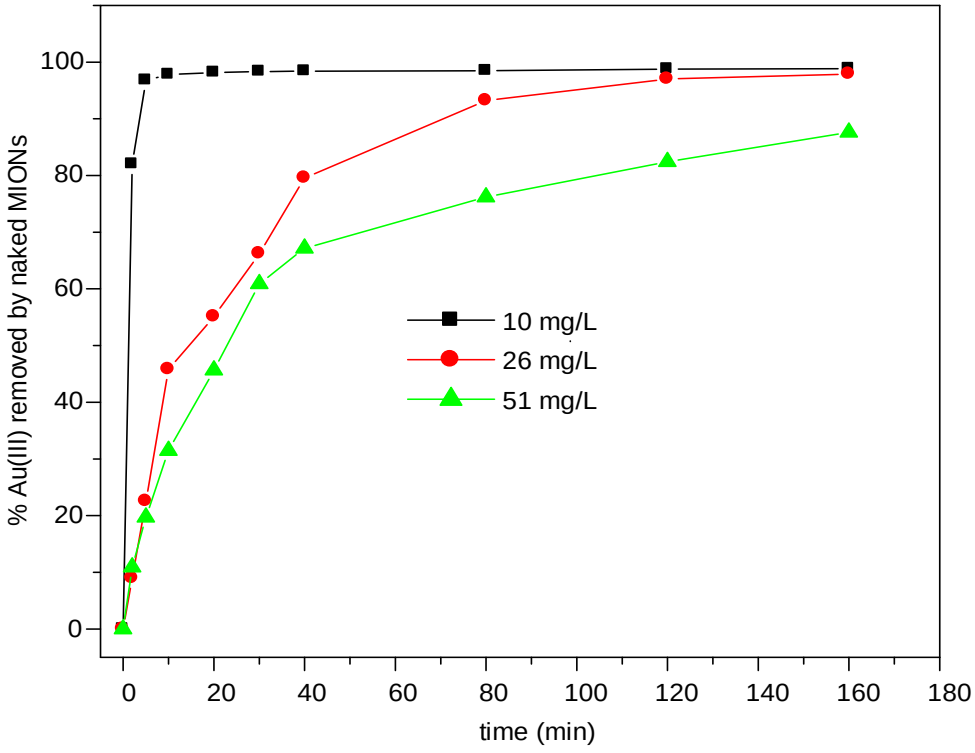

Figure 3.9: Effect of initial Au(III)-Cl concentration on sorption of Au(III)-Cl complexes by naked MIONs from acidic aqueous solution. Experimental conditions: a mass of naked MIONs: 10.3 mg, total aqueous phase: 10 mL, pH: 2.5, temperature: 25±2 °C and shaker speed: 150 rpm.

Stellenbosch University https://scholar.sun.ac.za

Increasing the Au(III)-Cl concentration to 26 mg/L and 51 mg/L but keeping the other conditions achieved Au(III)-Cl removal efficiencies of 100 % and 82 % respectively. Furthermore, the initial Au(III)-Cl concentration also had a significant effect on sorption equilibrium. For instance, 100 % of 10 mg/L Au(III)-Cl was removed from solution within less than 2 minutes of contact time, while 100 % of 26 mg/L Au(III)-Cl solution was removed from the solution after 160 min. Therefore, the initial Au(III)-Cl concentration plays a role in sorption equilibrium. To determine the effect of initial concentration on removal of Pd(II)-Cl by naked MIONs from acidic solutions, the sorption experiments were performed using the following initial concentrations: 10 mg/L, 21 mg/L, and 32 mg/L. The sorption was carried out at room temperature (25±2 °C) and pH (2.5). The results are portrayed in **Figure 3.10**. Increasing the Pd(II)-Cl concentration resulted into a decrease in removal percentages. This indicated that the initial Pd(II)-Cl concentration plays a role in the sorption of Pd(II)-Cl by naked MIONs. However, sorption equilibrium was reached within a very short time irrespective of the concentration of Pd(II)-Cl from solution.

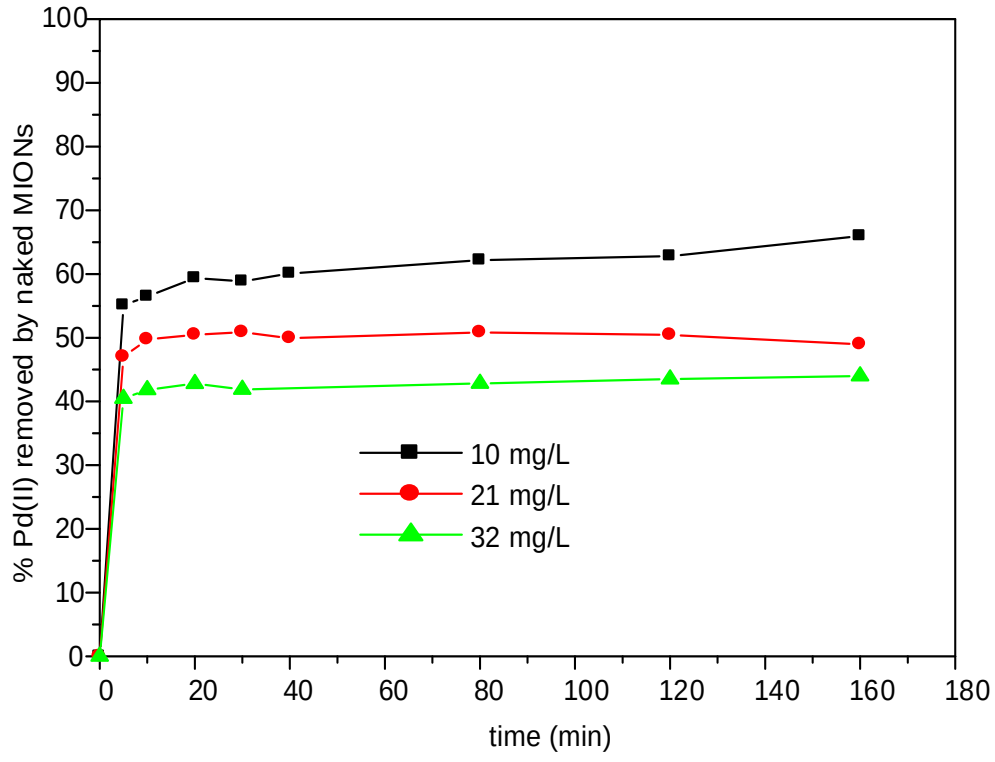

Figure 3.10: Effect of initial Pd(II)-Cl concentration on sorption of Pd(II)-Cl by naked MIONs from acid aqueous solution. Experimental conditions: a mass of naked MIONs: 90.6 mg, total aqueous phase: 10 mL, pH: 2.5, temperature: 25±2 °C and shaker speed: 150 rpm.

Stellenbosch University https://scholar.sun.ac.za

The effect of metal ion in sorption of Pt(IV)-Cl by naked MIONs from acid aqueous solution was carried out by varying Pd(II)-Cl concentration as follows: 10 mg/L, 21 mg/L and 31 mg/L. Other sorption conditions were as follows: mass of naked MIONs: 90.4 mg, total aqueous phase: 10 mL, pH: 2.5, temperature: 25±2 °C and shaker speed: 150 rpm. The results are shown in **Figure 3.11**. Increasing Pt(IV)-Cl concentration resulted in a decrease in the removal efficiencies. Compared to the results obtained for Pd(II)-Cl, the decrease in removal percentages was less pronounced.

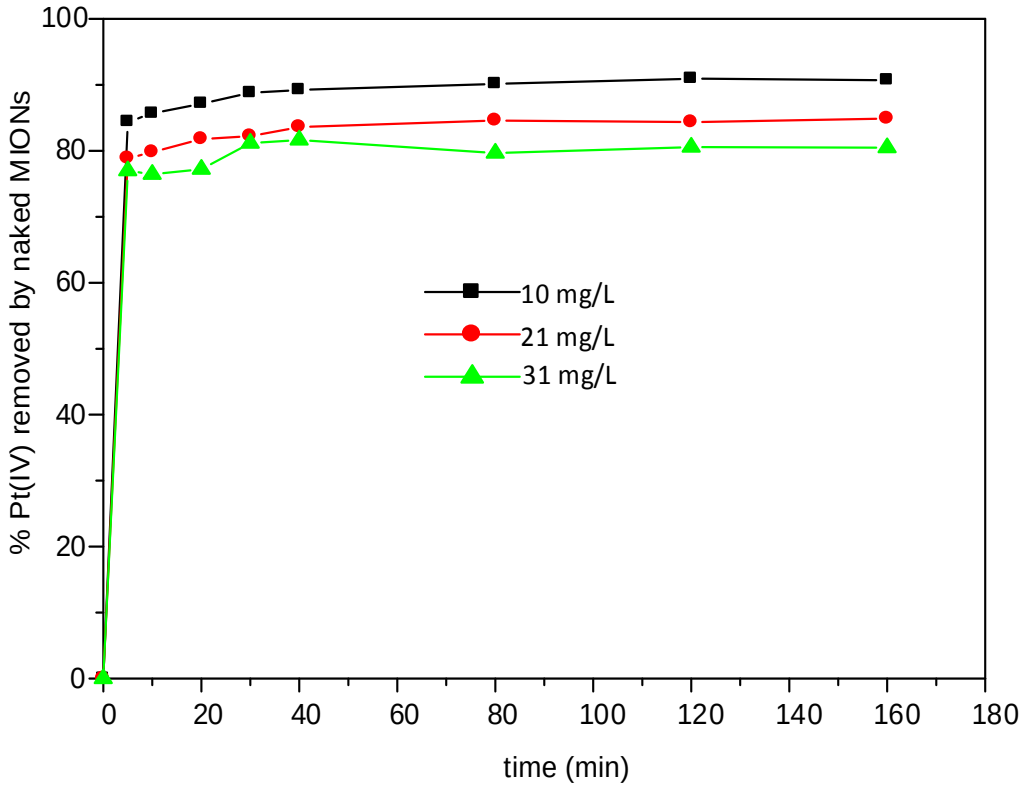

Figure 3.11: Effect of initial Pt(IV)-Cl concentration as a function of time on sorption of Pt(IV)-Cl by naked MIONs from aqueous solution. Experimental conditions: mass of naked MIONs: 90.4 mg, total aqueous phase: 10 mL, pH: 2.5, temperature: 25±2 °C and shaker speed: 150 rpm.

3.4.1.4 Effect of pH on sorption of Au(III), Pd(II) and Pt(IV) complexes

The pH of the solution plays a vital role in the sorption of Au(III)-Cl, Pd(II)-Cl, and Pt(IV)-Cl complexes by iron oxide adsorbents. The surface of naked MIONs contains hydroxyl groups symbolised as ≡FeOH in this work. The point of zero charge (pH_{ZPC}) of the adsorbents can be used to explain the effect of pH in sorption of these precious metal chloro species. At $pH<pH_{ZPC}$, the surface of naked MIONs is positively charged, whereas at a $pH>pH_{ZPC}$, the

Stellenbosch University https://scholar.sun.ac.za

surface of naked MIONs is negatively charged. The pH_{ZPC} of naked MIONs is in the range of 6.0 to 8.2.[143]

3.4.1.4.1 Effect of pH on sorption of Au(III) complexes by naked MIONs

The effect of pH on sorption of Au(III)-Cl complexes by naked MIONs was studies by carrying out batch experiments at pH 1.0, pH 3.0, and pH 5.0. Other experimental conditions were as follows: initial Au(III)-Cl concentration; 51 mg/L, amount of naked MIONs; 30.4 mg, aqueous volume; 10 mL and the temperature; 25±2 °C. The results are shown in **Figure 3.12**.

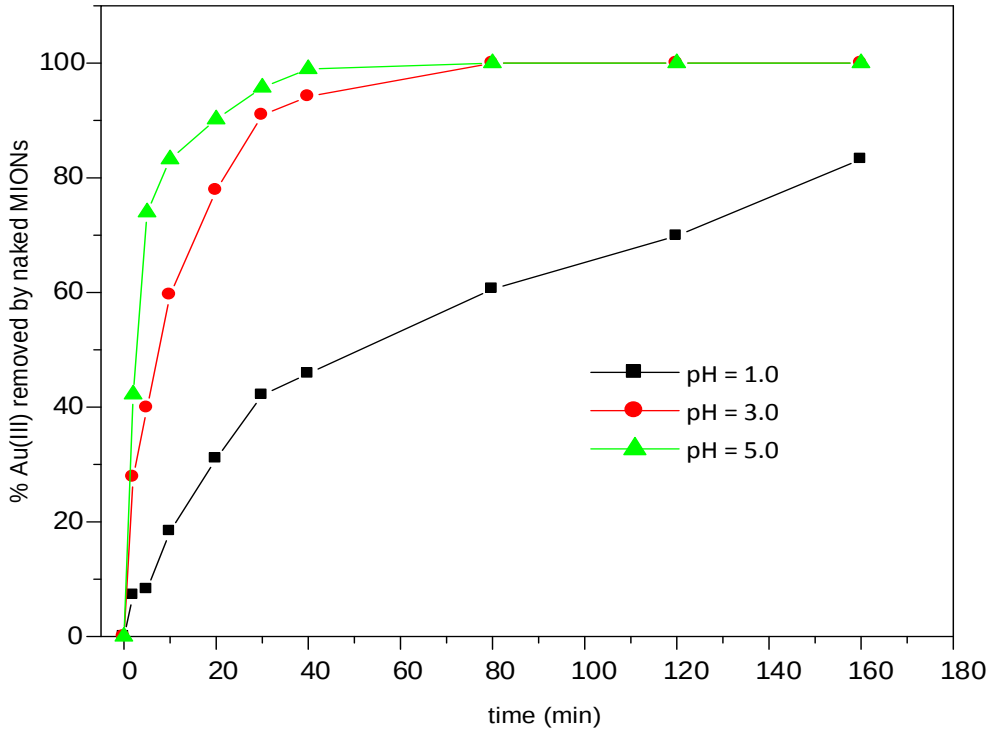

Figure 3.12: Effect of pH on sorption of Au(III)-Cl by naked MIONs from acidic aqueous solutions. Experimental conditions: mass of MIONs 30.4 mg, [Au(III)]: 51 mg/L total aqueous phase: 10 mL, shaker speed: 150 rpm, temperature: 25±2ºC.

All three sorption batch experiments show a general trend of an increase in removal percentages with time. Again, Au(III)-Cl percentage removal increased with solution Ph. At pH 1.0, about 82 % of Au(III)-Cl was removed from solution after 160 min. However, at pH 3.0 and pH 5.0, 100 % of Au(III)-Cl was removed from solution.

Stellenbosch University https://scholar.sun.ac.za

At pH<4.0 and high Cl^- concentration, Au(III)-Cl exist as $AuCl_4^-$. Increasing the pH to pH>4.0, the Au(III)-Cl exist as negatively charged anions ($AuCl_3OH^-$, $AuCl_2(OH)_2^-$, $AuCl(OH)_3^-$ *etc*). [15,143,144] Therefore, sorption of Au(III)-Cl at the pH 1.0, pH 3.0 and pH 5.0 can be attributed to the electrostatic attraction between the anionic Au(III)-Cl complexes and the protonated surface of naked MIONs. High sorption percentage at the pH of 5.0 compared to sorption percentages at pH 1.0 and pH 3.0, confirms the results of Rose and co-workers who postulated that Au(III)-Cl species with fewer than four Cl atoms are preferentially adsorbed by metal oxide surfaces.[10] The low sorption percentage exhibited at pH 1.0 can also be ascribed to the dissolution of naked MIONs at very low pH's which is discussed later in **Section 3.4.1.4.2.**

3.4.1.4.2 Stability of naked MIONs at different pH

Stability of naked MIONs during sorption of Au(III)-Cl complexes by naked MIONs was determined by measuring the concentration of iron leached into the solution during adsorption. Three batch sorption experiments were analysed at pH 1.0, pH 2.5, and pH 5.0. Other conditions were as follows: mass of MIONs 30.4 mg, [Au(III)]: 51 mg/L total aqueous phase: 10 mL, shaker speed: 150 rpm, temperature: 25±2ºC.

The mass and percentage of Fe released into solution were calculated using **Equation 3.6** and **Equation 3.7** respectively.

Equation 3.6 $$mass\ of\ Fe\ released\ (g) = C_{Fe} \times V \times 1000$$

Equation 3.7 $$\%\ \text{Fe dissolution} = \frac{\text{g Fe released}}{\text{g } Fe_3O_4} * 100\ \%$$

In **Equation 3.6**, C_{Fe} is the concentration as determined by ICP-OES and V is the total volume. The plot showing the percentage of Fe released into solution with time, is shown in **Figure 3.13**. As depicted by the figure, at pH 1.0, percentage dissolution of Fe from naked MIONs is about 2.5 % as recorded. This confirms several reports in the literature that magnetite nanoparticles are unstable in high concentration of HCl acid.[117,145] However, increasing to pH 2.5 resulted in rapid decrease in Fe dissolution percentages. The percentage of Fe released into the solution was around only 0.2 %. However, at the pH of 5.0, Fe was not leached into the solution, showing that naked MIONs are stable at higher pH. Uheida *et al*.[15]

Stellenbosch University https://scholar.sun.ac.za

carried out adsorption of Pd(II), Rh(III) and Pt(IV) complexes acidic aqueous solution at pH 2.5, and the percentage of Fe released into solution was less than 1 %.

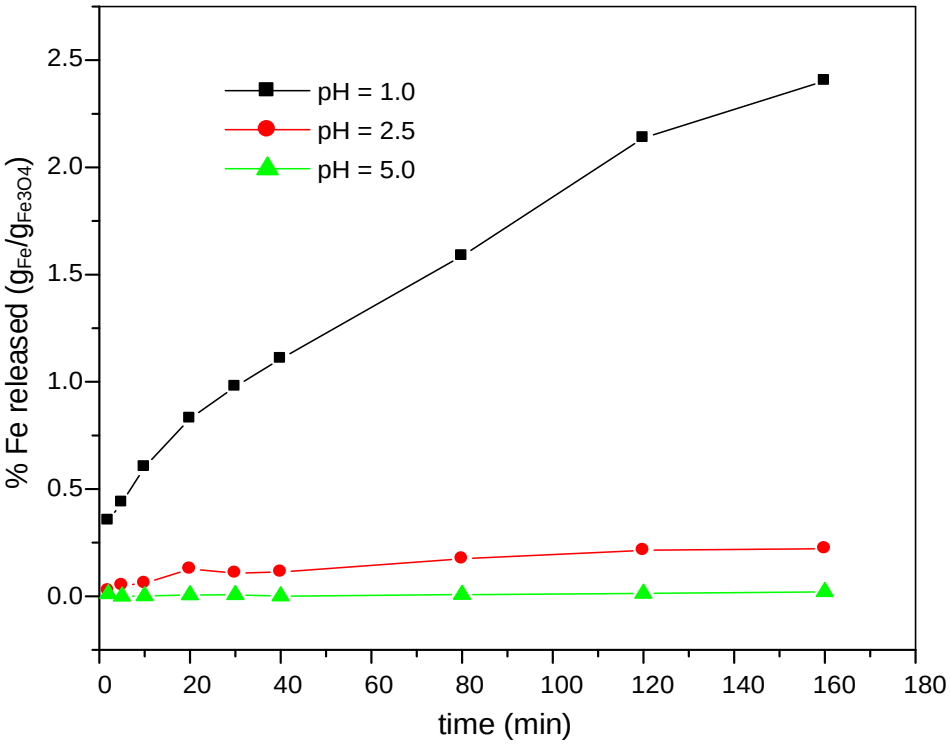

Figure 3.13: Stability of MIONs in acidic solutions. Experimental conditions: mass of MIONs 30.4 mg, [Au(III)]: 51 mg/L total aqueous phase: 10 mL, shaker speed: 150 rpm, temperature: 25±2ºC.

3.4.1.4.3 Effect of pH on sorption of Pd(II) complexes by naked MIONs

The effect of pH on sorption of Pd(II)-Cl complexes by naked MIONs was investigated by running batch experiments at pH 2.5, pH 3.0, and pH 5.0. Other experimental conditions were as follows: initial Pd(II)-Cl concentration; 10 mg/L, amount of naked MIONs; 90.4 mg, aqueous volume; 10 mL and the temperature; 25±2 °C. The results exhibited are as shown in **Figure 3.14**. Removal percentages of Pd(II)-Cl increase with an increase in the pH of the solution.

At the pH<3.5, the predominant species of Pd(II)-Cl in aqueous solutions is $PdCl_4^{2-}$. However, increasing the pH of the solution from 3.5 to basic conditions causes hydrolysis of $PdCl_4^{2-}$ to $PdCl_3(H_2O)$-, $PdCl_2(H_2O)_2$ and $Pd(OH)_2$.[125] Therefore, sorption of Pd(II)-Cl complex by naked MIONs under the experimental conditions was dominated by electrostatic attraction between Pd(II)-Cl anionic complexes with the positively charged surface of naked MIONs.

Stellenbosch University https://scholar.sun.ac.za

Again, just like Au(III)-Cl, naked MIONs have a higher sorption affinity for hydrolysis products of Pd(II)-Cl complex. However, adjusting the pH of Pd(II)-Cl complex solution to pH 5.0, resulted into the formation of the precipitate that settled at the bottom of the volumetric flask overtime. Therefore, the high sorption percentages observed at the pH of 5.0 might have also been due to Pd(II)-Cl precipitation.

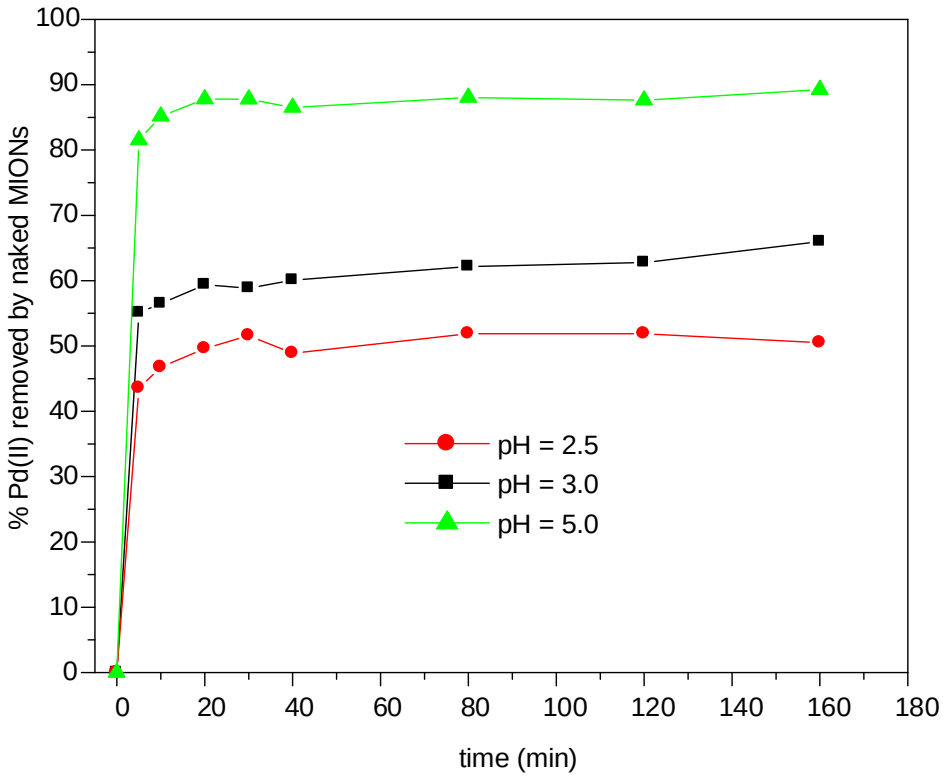

Figure 3.14: Effect of pH on sorption of Pd(II)-Cl by naked MIONs from acidic solutions. Experimental conditions: mass of MIONs 90.4 mg, [Pd(II)]: 10 mg/L total aqueous phase: 10 mL, shaker speed: 150 rpm, temperature: 25±2ºC.

3.4.1.4.4 Effect of pH on sorption of Pt(IV) complexes by naked MIONs

Subsequently, the effect of pH on sorption of Pt(IV)-Cl complexes by naked MIONs was studied by running batch experiments at pH 2.5, 3.0, and 5.0. Other experimental conditions which were kept constant were as follows: mass of naked MIONs 90.1 mg, [Pt(IV)]: 10 mg/L total aqueous phase: 10 mL, shaker speed: 150 rpm, temperature: 25±2ºC. The results are shown in **Figure 3.15**. The removal percentages for sorption of Pt(IV)-Cl complex by naked MIONs at pH 2.5, 3.0, and 5.0 were 85 %, 97 % and 98 % for the first 20 min of sorption. However, at pH 5.0, there was a slight decrease in removal percentages after 40 min.

Stellenbosch University https://scholar.sun.ac.za

At solution pH<3.5, Pt(IV)-Cl complex exist as $PtCl_6^{2-}$. Increasing the solution pH to pH>3.5, results into hydrolysis of $PtCl_6^{2-}$ as shown in **Equation 3.8** and **Equation 3.9**.[146]

Equation 3.8 $$PtCl_6^{2-} + H_2O \rightarrow PtCl_5(H_2O)^- + Cl^-$$

Equation 3.9 $$PtCl_5(H_2O)^- \leftrightarrow PtCl_5(OH)^{2-} + H_2O$$

The decrease in removal percentages of Pt(IV)-Cl at pH 3.0 and pH 5.0 might have been caused by the formation of hydroxyl complexes. As seen in **Figure 3.15**, the decrease was more pronounced than at pH 3.0.

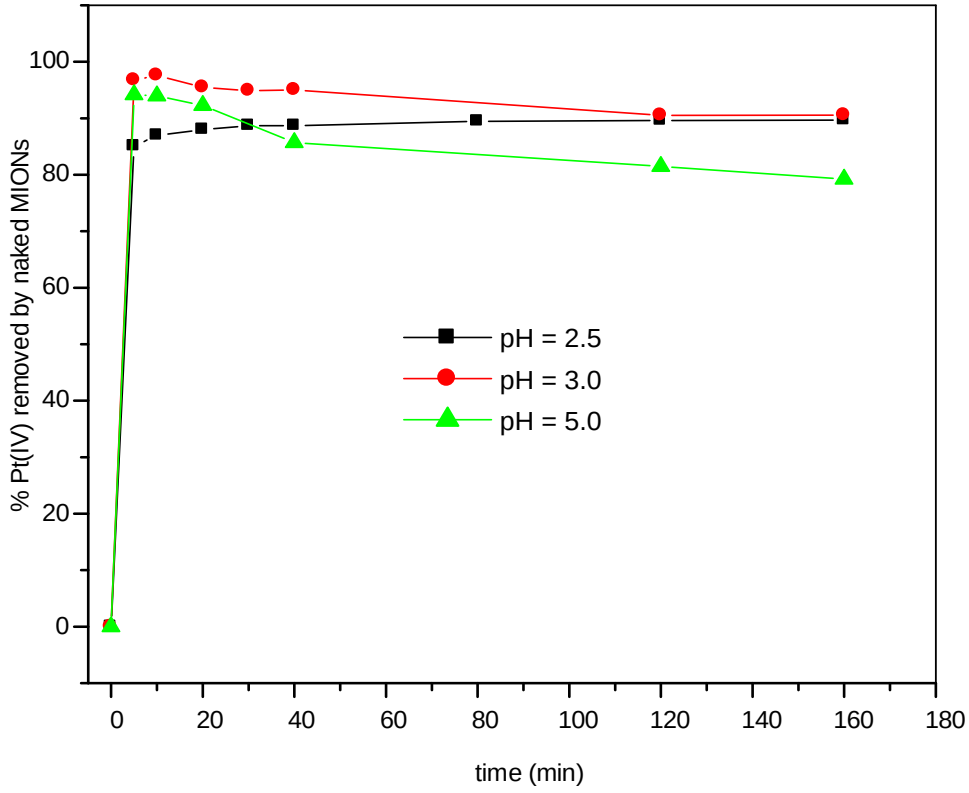

Figure 3.15: Effect of pH on sorption of Pt(IV)-Cl by naked MIONs from acid aqueous solutions. Experimental conditions: mass of naked MIONs 90.1 mg, [Pt(IV)]: 10 mg/L total aqueous phase: 10 mL, shaker speed: 150 rpm, temperature: 25±2ºC.

Stellenbosch University https://scholar.sun.ac.za

3.4.2 UV-VIS spectroscopy studies on Sorption of Au(III), Pd(II) and Pt(IV) complexes by naked MIONs

Speciation of Au(III)-Cl, Pd(II)-Cl, and Pt(II, IV)-Cl complexes have been studied extensively in the literature, using Raman vibration, UV-Vis and NMR spectroscopy. [147–149] The efficiency of metal ion sorption from aqueous solution by iron oxide materials is governed by their speciation.[129,147] In this work, the effect of pH on sorption of Au(III)-Cl, Pd(II)-Cl, and Pt(IV)-Cl complexes by naked MIONs was investigated using UV-Vis spectroscopy by carrying out batch experiments at pH 1.0, 2.5, 3.0, and 5.0.

Speciation of these metal complexes have been well studied in the literature by spectroscopic techniques such as Raman and UV-Vis spectroscopy.[125,143,150] For this reason, UV-Vis experiments were conducted for the identification of species of Au(III), Pd(II), and Pt(IV) complexes before and after contact with naked MIONs in aqueous solutions. This was done by observing spectra shift and the decrease in the intensity of the peaks. The UV-Vis spectra of Au(III)-Cl, Pd(II)-Cl and Pt(IV)-Cl complexes are dominated by ligand-to-metal charge transfer (LMCT) transitions. Such transitions involve the transfer of electrons from the ligand orbitals to the metal upon sorption of a photon. The intensity of these bands is governed by the concentration of the metal ion in solution according to Beer Lamberts law. Monitoring and recording spectra shifts and peak intensity changes with time makes it possible to study sorption of metal ions from solution by UV-Vis spectroscopy.

The pH_{ZPC} for magnetite has been reported to be in the range of 6.0 to 8.2.[7, 20] At a pH less than the pH_{ZPC}, the ≡FeOH on the surface of naked MIONs become protonated and become ≡Fe-OH_2^+. Thus, under the experimental conditions used for this work, the surface of naked MIONs was positively charged (≡Fe-OH_2^+) and, hence facilitating the initial attraction and subsequent sorption of anionic complexes of Au(III)-Cl, Pd(II)-Cl and Pt(IV)-Cl respectively.

3.4.2.1 Sorption of Au(III) complexes by naked MIONs

The effect of pH (pH 1.0, pH 3.0 and pH 5.0) on sorption of Au(III)-Cl complexes was studied by analysing solution of Au(III)-Cl before and after their contact with the naked MIONs. Experimental conditions were as follows: mass of naked MIONs 30.4 mg, [Au(III)]: 51 mg/L total aqueous phase: 10 mL, shaker speed: 150 rpm, temperature: 25±2ºC. At pH<4, Au(III)-Cl exist as a square planar complex: $AuCl_4^-$.[14,147,150] The UV-Vis spectra of Au(III)-Cl

Stellenbosch University https://scholar.sun.ac.za

complex at the pH of 1.0 before and after various contact time with naked MIONs is shown in **Figure 3.16**.

The UV-Vis spectrum of Au(III)-Cl before sorption shows two sorption maxima at λ_{max} = 229 nm and 315 nm. The two band are called ligand to metal charge transfer (LMCT).[127] As can be seen in **Figure 3.16**, with increasing contact time, there is an increase in the sorption maximum at λ = 229 nm while the sorption maximum λ = 315 nm migrates to a higher wavelength (λ = 334 nm) suggesting the formation of new species with higher molar absorptivity than Au(III)-Cl species. Leaching experiments showed that there was a large amount of iron leached into solution at the pH of 1.0. Hence, the increase and shift of the bands can most likely be attributed to the formation of $Fe^{III}Cl_n^{(3-n)}$ species (for n = 3, 4, 5, 6). Since there is an excess amount of Fe^{3+} and chloride ions in the solution, this was favourable for the formation of the iron(III) chloride complex.

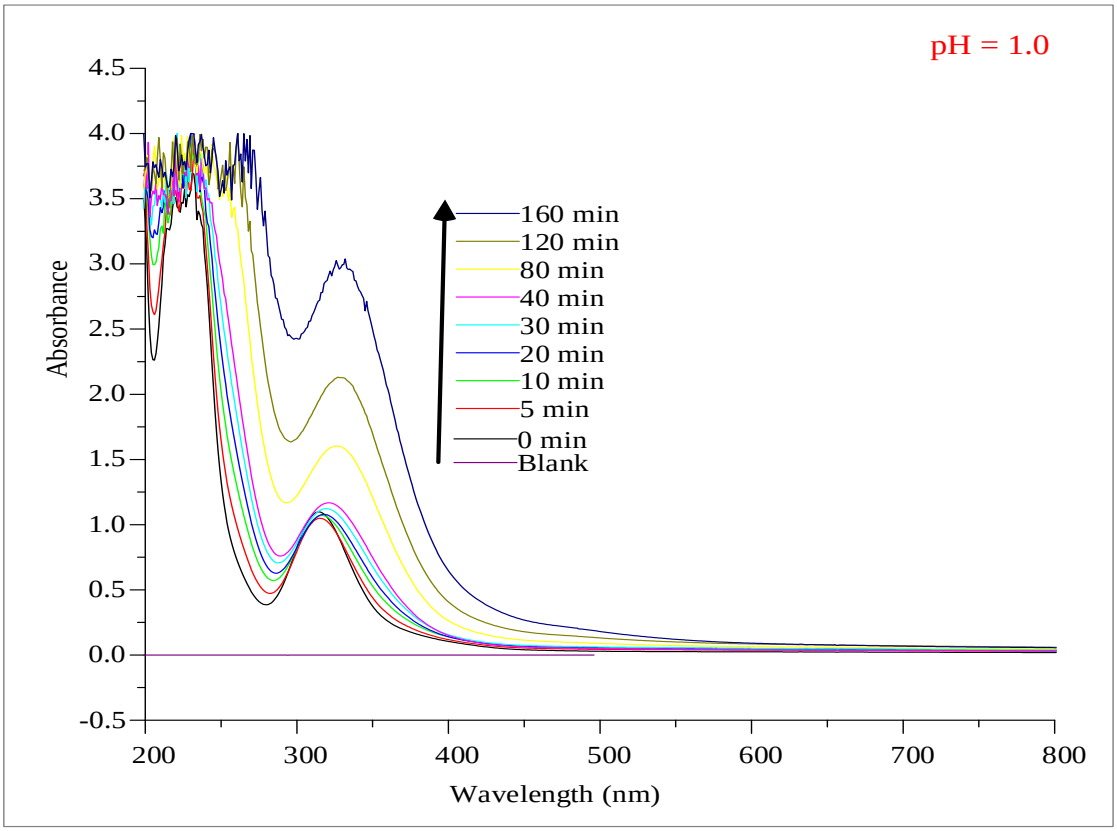

Figure 3.16: UV-Vis spectra of the individual time dependent experiments for the batch sorption of Au(III) from aqueous solution at pH 1.0. Experimental conditions: mass of MIONs 30.4 mg, [Au(III)]: 51 mg/L total aqueous phase: 10 mL, shaker speed: 150 rpm, temperature: 25±2ºC.

Stellenbosch University https://scholar.sun.ac.za

The UV-Vis spectra of Au(III)-Cl complex in aqueous solution at pH 3.0, before and after contact times with naked MIONs at various time intervals are shown in **Figure 3.17**. The spectrum of Au(III)-Cl before sorption, shows two sorption maximum at λ_{max} = 229 nm and 315 nm, corresponding to $AuCl_4^-$ species. As depicted in the figure, the UV-Vis spectra of Au(III)-Cl after contact with naked MIONs shows decreased intensities of the absorbance maxima at λ_{max} = 229 nm and 315 nm, respectively. This is true for the spectra recorded from 2 min to 80 min. The results indicated that Au(III)-Cl was removed from solution. However, from 120 min to 160 min, both absorbance maxima at λ = 315 nm and λ = 229 nm disappeared indicating formation of new species.

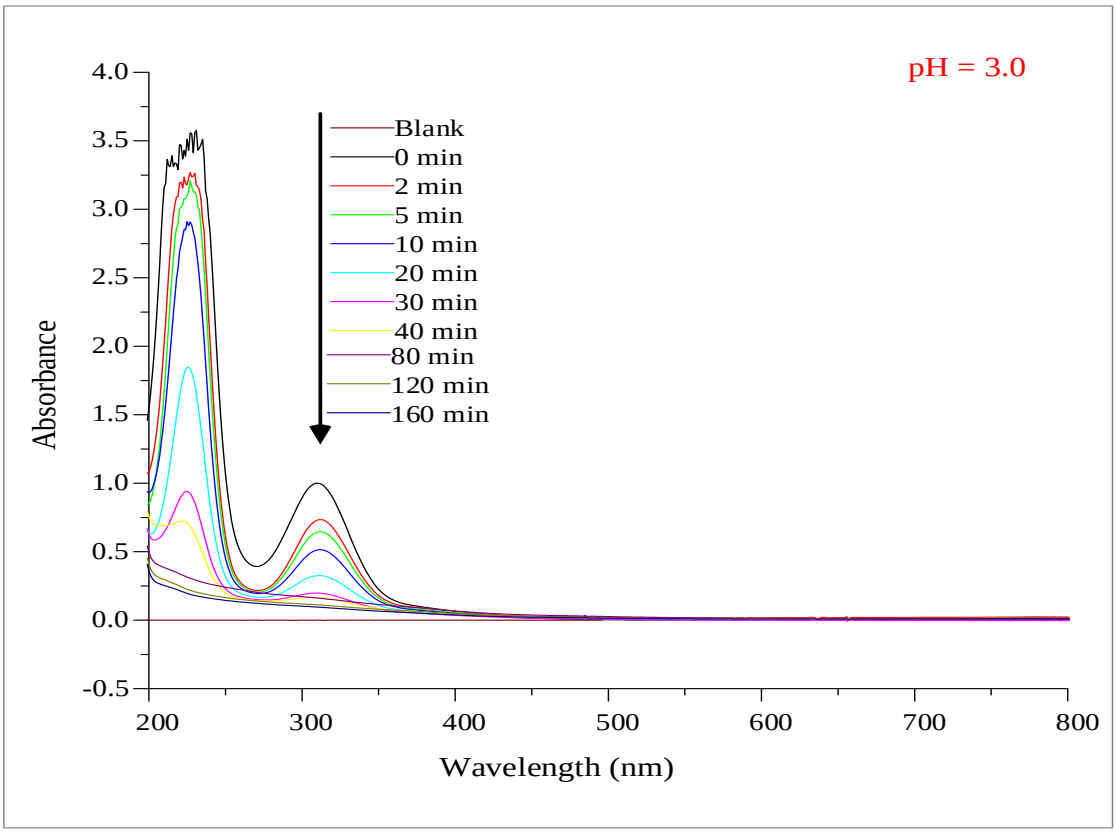

Figure 3.17: UV-Vis spectra of the individual time dependent experiments for the batch Sorption of Au(III)-Cl from aqueous solution at pH 2.5. Experimental conditions: mass of MIONs 30.4 mg, [Au(III)]: 51 mg/L total aqueous phase: 10 mL, shaker speed: 150 rpm, temperature: 25±2ºC.

The UV-Vis spectra of Au(III)-Cl solution at pH = 5.0 after various contact times with naked MIONs is presented in **Figure 3.18**. The spectra collected from 0 min to 20 min show absorption peaks with absorption maximum at λ_{max} = 229 nm and 315 nm. Comparing this with the UV-Vis spectra recorded for Au(III)-Cl after contact with naked MIONs at pH 3.0

Stellenbosch University https://scholar.sun.ac.za

in **Figure 3.18**, there was a rapid decrease in Au(III)-Cl concentration at pH 5.0, as compared to pH 3.0. As explained earlier, sorption of Au(III)-Cl by naked MIONs increase with pH.

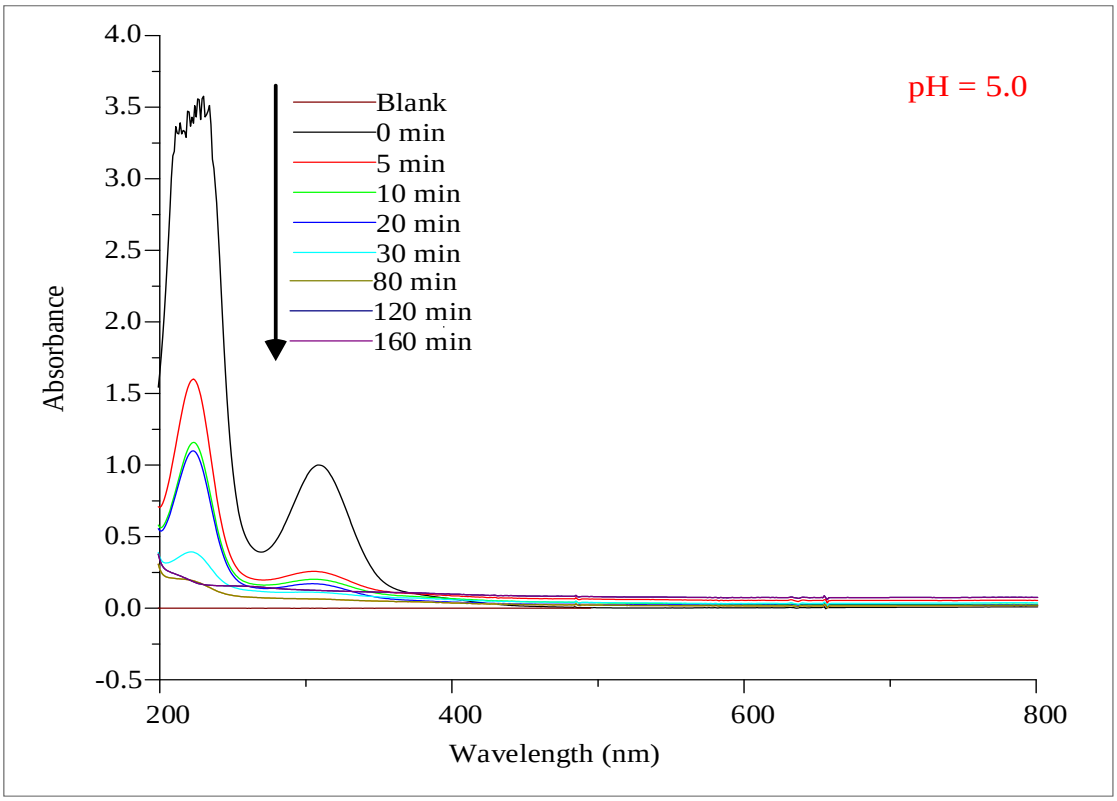

Figure 3.18: UV-Vis spectra of the individual time dependent experiments for the batch sorption of Au(III)-Cl from aqueous solution at pH 5.0. Experimental conditions: mass of MIONs 30.4 mg, [Au(III)]: 51 mg/L total aqueous phase: 10 mL, shaker speed: 150 rpm, temperature: 25±2ºC.

As pH increases from pH 4.0 to pH 7.0, $AuCl_4^-$ dominance gives away to the intermediate hydrolysis product species as $AuCl_2OHH_2O$, $AuCl_3(H_2O)$, $AuCl_3OH^-$, $AuCl_2(OH)_2^-$ and $AuCl(OH)_3^-$, which may account for the increase in sorption of Au(III)-Cl by naked MIONs as pH increases. Thus, these findings support the hypothesis that Au(III)-Cl species with fewer than four Cl atoms are preferentially adsorbed by oxide surfaces.

Consequently, UV-Vis studies for sorption of Au(III)-Cl by naked MIONs at pH 3.0 and pH 5.0 showed a decrease and ultimately the disappearance of the LMCT bands. This observation suggests that $AuCl_4^-$ loses one or two chlorides ions to adsorb or "coordinate" to the surface of naked MIONs. Presumably, these excess chloride ions were exchanged for the OH ligands present as hydroxyl groups on the surface of naked MIONs. Therefore, sorption of Au(III)-Cl supports an inner sphere sorption coordination. Another example for inner-sphere

Stellenbosch University https://scholar.sun.ac.za

complexation was studied by Machesky *et al.*[18] and they found that during sorption $AuCl_4^-$ by goethite, one to two chloride ions are released per adsorbed Au.

3.4.2.2 Sorption of Pd(II) complexes by naked MIONs

Sorption of Pd(II)-Cl by naked MIONs as a function of pH (pH 2.5, pH 3.0 and pH 5.0) was performed using the following experimental conditions: mass of MIONs 90.4 mg, [Pd(II)]: 10 mg/L total aqueous phase: 10 mL, shaker speed: 150 rpm, temperature: 25±2ºC. The UV-Vis spectra of Pd(II)-Cl solutions at pH 2.5 after various contacts time with naked MIONs are shown in **Figure 3.19**.

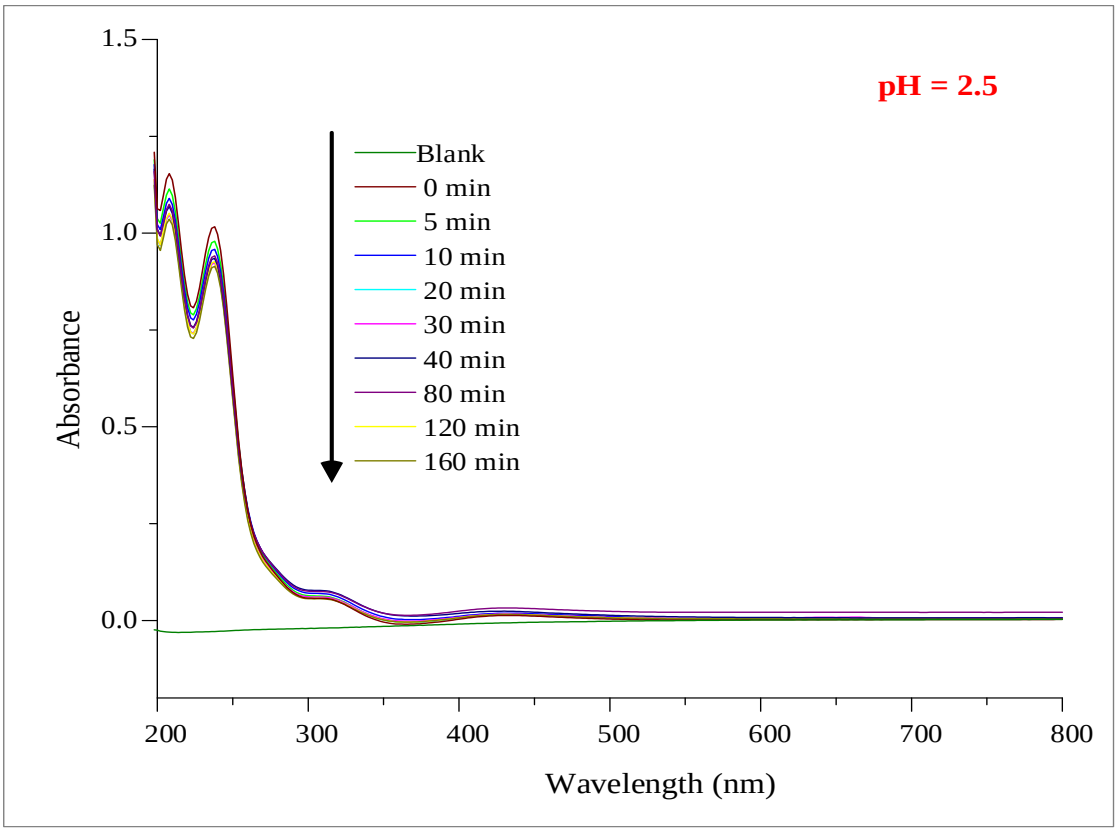

Figure 3.19: UV-Vis spectra of the individual time dependent experiments for the batch Sorption of Pd(II) from aqueous solution at pH 2.5. Experimental conditions: mass of MIONs 90.4 mg, [Pd(II)]: 10 mg/L total aqueous phase: 10 mL, shaker speed: 150 rpm, temperature: 25±2ºC.

The UV-Vis spectrum of Pd(II)-Cl before contact with naked MIONs exhibits sorption maximum at λ_{max} = 220 nm and 245 nm, corresponding to ligand to metal charge transfer bands. At pH<3.5, the predominant species of Pd(II)-Cl is $PdCl_4^{2-}$. However, the chloride of $PdCl_4^{2-}$ hydrolyses to form the following species: $PdCl_2(H_2O)_2$ (60 %), $PdCl(H_2O)_3^+$, and

Stellenbosch University https://scholar.sun.ac.za

$PdCl_3(H_2O)^-$.[15,132] As can be seen from **Figure 3.19**, there is a slight decrease in the LMCT bands of Pd(II)-Cl with time, indicating poor sorption of Pd(II)-Cl by naked MIONs.

The UV-Vis spectra of Pd(II)-Cl solutions at pH 3.0 after various contact times with naked MIONs are shown in **Figure 3.20**. The spectrum of Pd(II)-Cl before sorption exhibited LMCT bands at λ_{max} = 220 nm and 245 nm. Compared to the UV-Vis studies of Pd(II)-Cl conducted at pH 2.5, **Figure 3.20**. shows a rapid decrease in LMCT bands of Pd(II)-Cl. Note that the amount of naked MIONs used for this batch sorption was around 90.4 mg. Hence, a significant difference observed cannot be only attributed to the change in pH. But it confirms the removal of Pd(II)-Cl from solution.

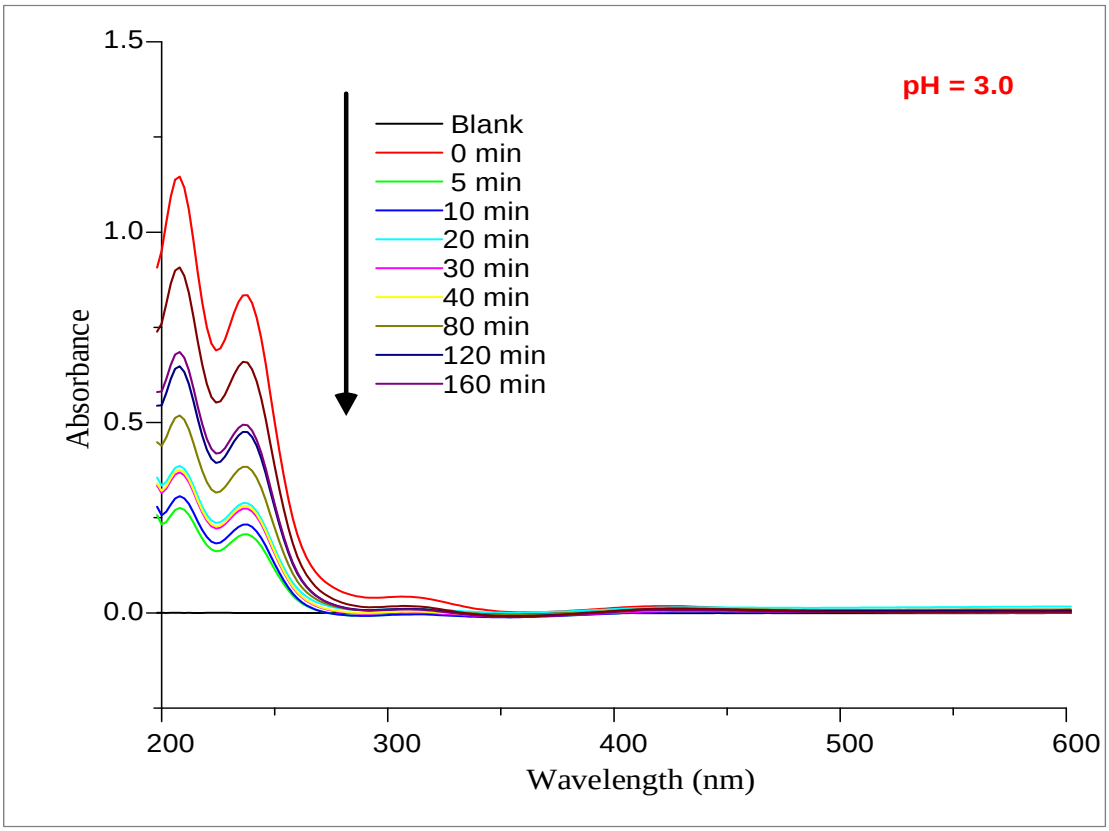

Figure 3.20: UV-Vis spectra of the individual time dependent experiments for the batch sorption of Pd(II) from aqueous solution at pH 3.0. Experimental conditions: mass of MIONs 90.4 mg, [Pd(II)]: 10 mg/L total aqueous phase: 10 mL, shaker speed: 150 rpm, temperature: 25±2ºC.

The UV-Vis spectra of Pd(II)-Cl species recorded before and after contact with the naked MIONs at pH 2.5 and pH 3.0 (**Figure 3.19** and **Figure 3.20**) corresponds to the following species: $PdCl_2(H_2O)_2$ and $PdCl_3(H_2O)^-$.[15,132]

Stellenbosch University https://scholar.sun.ac.za

The UV-Vis spectra of Pd(II)-Cl solutions at pH 5.0 after various contact times with naked MIONs is shown in **Figure 3.21**. It is worth mentioning that during pH adjustment of the solutions with 0.1 M HCl and 0.1 M NaOH, at pH 5.0, the colour of the solution changed from a clear yellow to brown colour with a precipitate that settled at the bottom of the volumetric flask.

As shown in **Figure 3.21**, the spectra of Pd(II)-Cl before and after contact with naked MIONs exhibits broad sorption bands from 250 nm tailing to 600 nm. These featureless spectra are consistent with scattering from a suspended precipitate rather than true sorption. The precipitate might be due to the formation of hydroxide species. From these equations, one can conclude that with decreasing pH of the solutions, the hydrolysis process is reversed and Pd(II)-Cl species are more stable. The chloride ion concentration also plays an important role in hydrolysis of Pd(II)-Cl species. Therefore, the dominating species at the pH of 5.0 is $Pd(OH)_4^{2-}$. Therefore, UV-Vis spectroscopy was limited in this case.

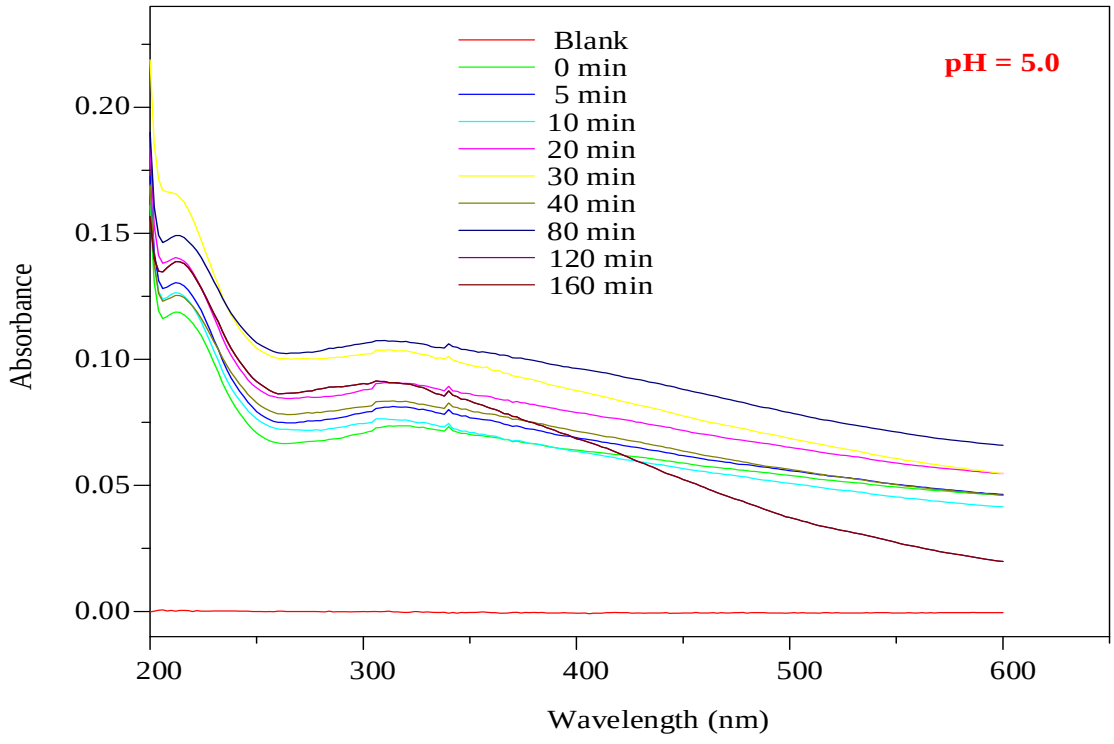

Figure 3.21: UV-Vis spectra of the individual time dependent experiments for the batch sorption of Pd(II)-Cl from aqueous solution at pH 5.0. Experimental conditions: mass of MIONs 90.4 mg, [Pd(II)]: 10 mg/L total aqueous phase: 10 mL, shaker speed: 150 rpm, temperature: 25±2ºC.

Stellenbosch University https://scholar.sun.ac.za

3.4.2.3 Sorption of Pt(IV) complexes by naked MIONs

The effect of pH on sorption of Pt(VI)-Cl by naked MIONs was studied by UV-Vis spectroscopy. Batch sorption experiments were carried out at pH 2.5, pH 3.0, and pH 5.0. The spectra of Pt(IV)-Cl before and after contact time were recorded. **Figure 3.22** shows the UV-Vis spectra of Pt(IV)-Cl solutions at pH 2.5 after various contact times with naked MIONs.

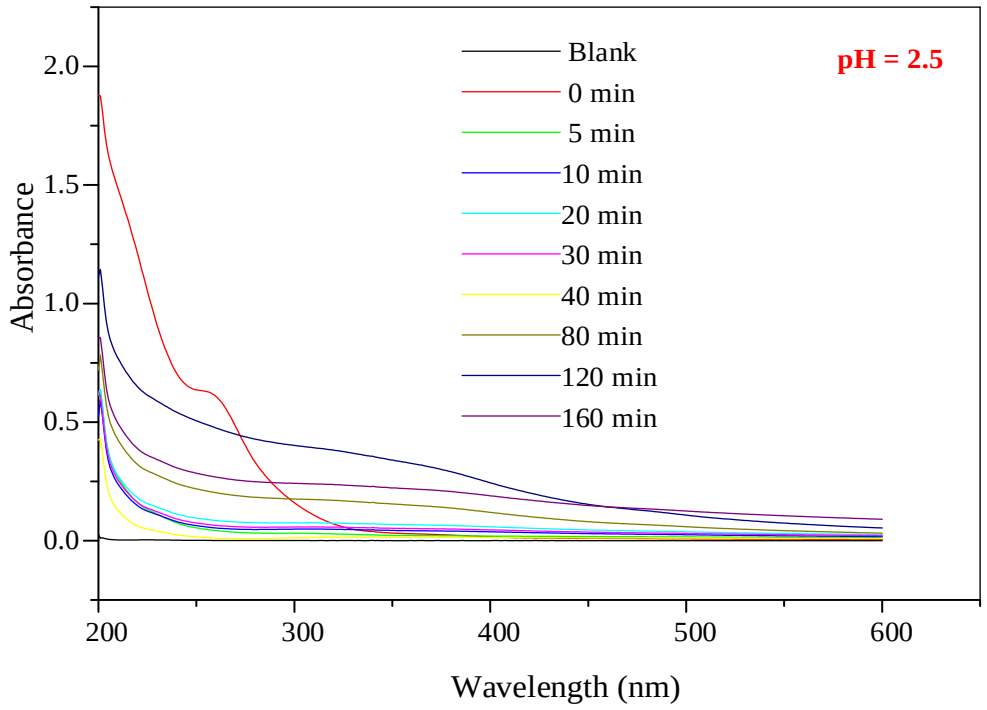

Figure 3.22: UV-Vis spectra of the individual time dependent experiments for the batch sorption of Pt(IV) from aqueous solution at pH 2.5. Experimental conditions: mass of naked MIONs 90.1 mg, [Pt(IV)]: 10 mg/L total aqueous phase: 10 mL, shaker speed: 150 rpm, temperature: 25±2ºC.

At pH < 3, the dominant species of Pt(IV)-Cl is $PtCl_6^{2-}$. As shown in **Figure 3.22**, the spectrum of $PtCl_6^{2-}$ exhibits a shoulder at $\lambda = 260$ nm. However, the spectra of Pt(IV)-Cl recorded after their contact with naked MIONs do not show any sorption bands. The spectra of Pt(IV)-Cl at pH 3.0 before and after contact with naked MIONs is as shown in **Figure 3.23**. These spectra are like those exhibited for the batch sorption at pH 2.5.

At pH<3, the chloride of the Pt(IV)-Cl is exchanged/replaced by H_2O species as shown in **Equation 3.8** and **Equation 3.9**. **Figure 3.24** show the UV-Vis spectra of Pt(IV)-Cl solutions at pH 5.0 after various contact times with naked MIONs. However, the spectra collected after sorption do not show any sorption peaks but rather a featureless spectrum.

Stellenbosch University https://scholar.sun.ac.za

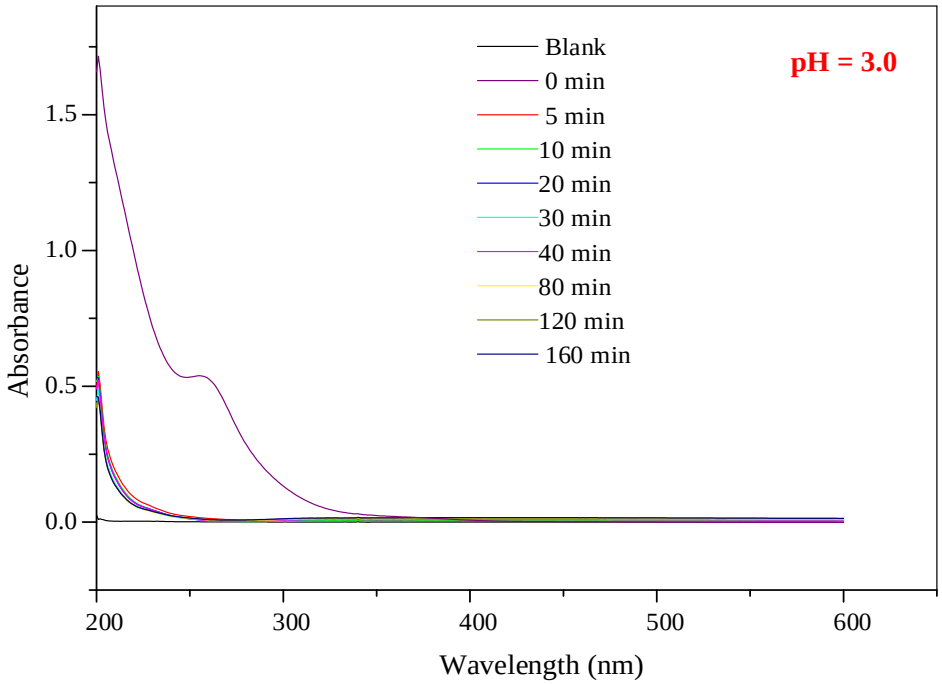

Figure 3.23: UV-Vis spectra of the individual time dependent experiments for the batch sorption of Pt(IV)-Cl from aqueous solution at pH 3.0. Experimental conditions: mass of naked MIONs 90.1 mg, [Pt(IV)]: 10 mg/L total aqueous phase: 10 mL, shaker speed: 150 rpm, temperature: 25±2ºC.

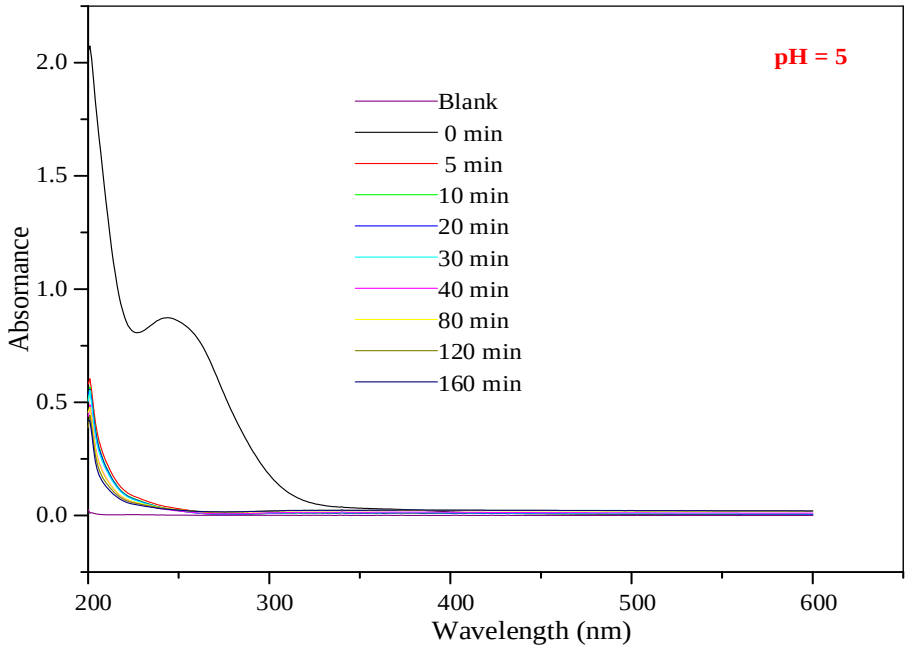

Figure 3.24: UV-Vis spectra of the individual time dependent experiments for the batch sorption of Pt(IV) from aqueous solution at pH 5.0. Experimental conditions: mass of naked MIONs 90.1 mg, [Pt(IV)]: 10 mg/L total aqueous phase: 10 mL, shaker speed: 150 rpm, temperature: 25±2ºC.

Stellenbosch University https://scholar.sun.ac.za

It is worth mentioning that studying the speciation of Pt(IV)-Cl complexes with UV-Vis was not as informative as the Pd(II)-Cl and Au(III)-Cl species study. As seen in **Figure 3.22**, **Figure 3.23** and **Figure 3.24**, the LMCT bands of Pt(IV)-Cl species are well resolved like the LMCT bands of Pd(II)-Cl and Au(III)-Cl species. It is also reported that visible spectrum for $PtC1_5OH^{2-}$ is very similar to that for $PtCl_6^{2-}$.[146]

3.4.3 Sorption kinetics of Au(III), Pd(II), and Pt(IV) complexes

It is often incorrect to apply a simple kinetics model such as first-order or second-order rate equations for sorption on solid surfaces as they are rarely homogeneous. Again, the effects of transport phenomena and chemical reactions are often experimentally inseparable.[104] Furthermore, sorption kinetics describe the rate of metal ion uptake during the sorption experiments and define the efficiency of sorption. For this reason, batch sorption kinetics are necessary when designing columns used in separation techniques such as HPLC and GC.[6,141,151,152]

3.4.3.1 Sorption kinetics of Au(III) complexes

The batch sorption kinetics of Au(III)-Cl by naked MIONs as a function of the amount of naked MIONs, initial Au(III)-Cl concentration and the pH was assessed using three kinetics models: *pseudo*-first-order, *pseudo*-second-order, and the intraparticle diffusion kinetic model.

3.4.3.1.1 *Pseudo*-first-order kinetic model

The *pseudo*-first-order kinetics model assumes that the rate of occupation of sorption sites is proportional to the number of unoccupied sites. The rate of the adsorptive interactions can be calculated by using the Lagergren equation shown in **Equation 3.10**.

Equation 3.10

$$\frac{dq}{dt} = K_1(q_e - q_t)$$

where q_e and q_t are the amounts of adsorbed metal ions (mg/g) on the adsorbent at equilibrium and at any time t, respectively, and k_1 (min^{-1}) is the *pseudo*-first-order rate constant. Integrating the equation between the limits $t = 0$ to $t = t$ and $q = 0$ to $q = q_e$ gives a linear equation shown in **Equation 3.11**.

Stellenbosch University https://scholar.sun.ac.za

Equation 3.11 $$\log(q_e - q_t) = \log q_e - \frac{k_1}{2.303} t$$

Sorption of Au(III)-Cl by different amounts of naked MIONs showed rapid sorption in the early stages, followed by a gradual decrease until equilibrium was reached. In the first step, the sorbate molecules are sorbing onto the surface where there are no other such molecules and consequently the sorbate-sorbate interactions are negligible. The *pseudo*-first order plot for *log* (q_e-q_t) *versus* time for 10.3 mg, 20.3 mg, and 30.4 mg of naked MIONs is shown in **Figure 3.25** and **Figure 3.26**. The data points were fitted for the first 10 minutes, **Figure 3.25**, and for whole sorption period, **Figure 3.26**.

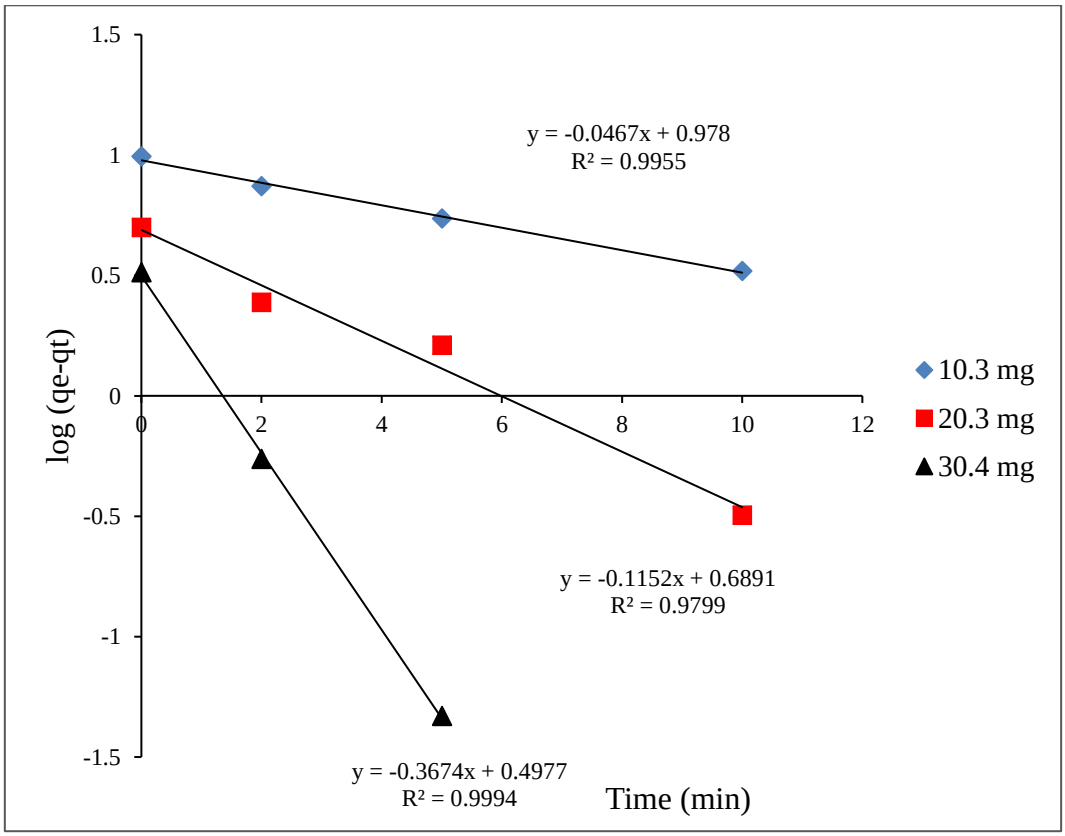

Figure 3.25: *Pseudo*-first-order kinetic plot for the sorption of Au(III)-Cl by different amounts of naked MIONs fitted for the first 10 min of sorption. Experimental conditions: [Au(III)]: 10 mg/L, total aqueous phase: 10 mL, pH: 2.5, temperature: 25±2 °C and shaker speed: 150 rpm.

As shown in the figure, the correlation coefficients (R^2) for the first 10 min is in the range of 0.9799 – 0.9994 but the R^2 for the entire sorption period are in the range of 0.5224 – 0.6466. This suggests that sorption of Au(III)-Cl by naked MIONs may follow a *pseudo*-first-order kinetics in the early stages of sorption process and adopts another mechanism as it reaches

Stellenbosch University https://scholar.sun.ac.za

equilibrium. However, the q_e values extrapolated for the *pseudo*-first-order kinetic plot which are 8.27 mg.g^{-1}, 3.08 mg.g^{-1}, and 0.37 mg.g^{-1} does not match to the experimental q_e values. For this reason, the kinetics sorption data for Au(III)-Cl by naked MIONs cannot be described using *pseudo*-first order kinetics model.

The sorption kinetics for sorption of Au(III)-Cl by naked MIONs as a function of the amount of naked MIONs, initial metal anion concentration and pH were also analysed by *pseudo*-first order-kinetics models. The kinetics parameters are listed in **Table 3.1**. The R^2 values for the kinetic linear plots for sorption of Au(III)-Cl by naked MIONs for the initial 10 min of sorption are in the range (0.9955-0.9994). These high R^2 values shows that sorption of Au(III)-Cl by naked MIONs probably followed the *pseudo*-first-order kinetics model during the initial stage of sorption. However, fitting data for entire sorption period decrease the R^2 values suggesting that sorption might be following another mechanism. The calculated q_e values are also generally lower than the experimental q_e values. Therefore, *pseudo*-first-order kinetic model is not suitable for describing sorption of Au(III)-Cl by naked MIONs.

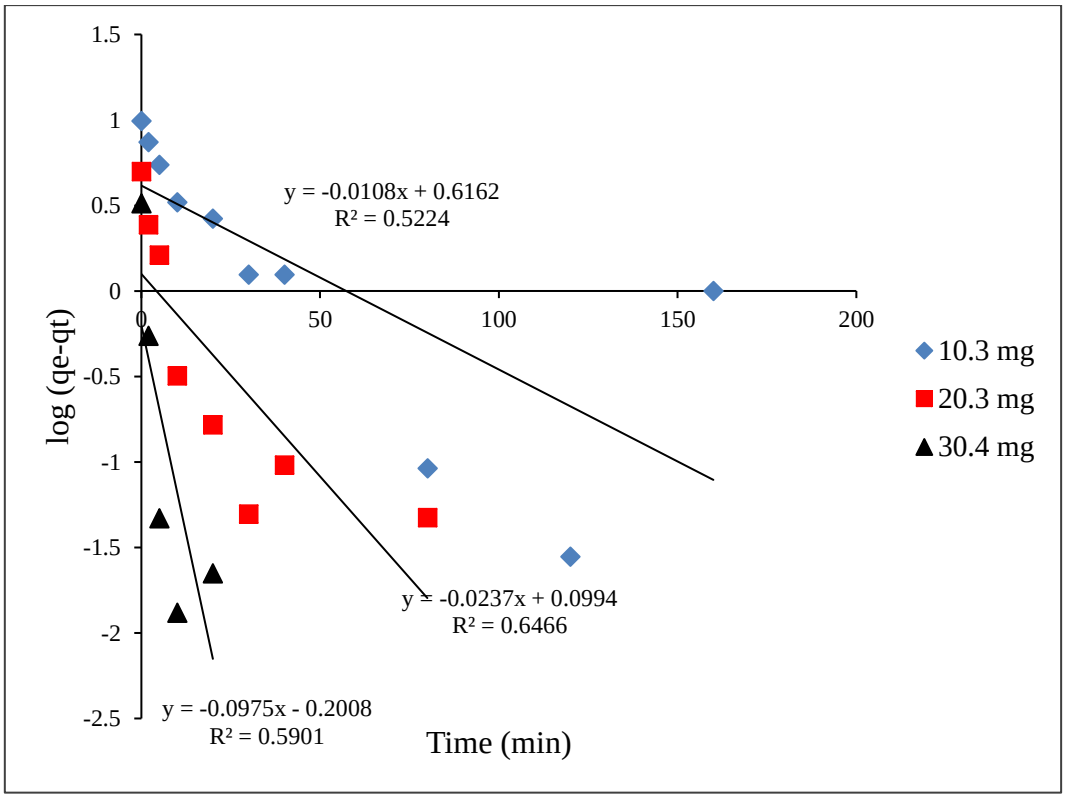

Figure 3.26: *Pseudo*-first-order kinetic plot for the sorption of Au(III)-Cl by different amounts of naked MIONs fitted for the entire sorption period (160 min). Experimental conditions: [Au(III)]: 10 mg/L, total aqueous phase: 10 mL, pH: 2.5, temperature: 25±2 °C and shaker speed: 150 rpm.

Stellenbosch University https://scholar.sun.ac.za

Table 3.1: Coefficients of *pseudo*-first-order and *pseudo*-second-order kinetic parameters and intraparticle diffusion model for sorption of Au(III)-Cl by naked MIONs

Parameters		$q_{e(exp)}$ $mg \cdot g^{-1}$	*pseudo*-first-order kinetics			*pseudo*-second-order kinetics				Intraparticle diffusion	
			k_1 min^{-1}	$q_{e(cal)}$ $mg \cdot g^{-1}$	R^2	k_2 $gmg^{-1}min^{-1}$	h $mg.g^{-1}min^{1}$	$q_{e(cal)}$ $mg.g^{-1}$	R^2	k_{id} $mg.g^{-1}min^{-0.5}$	R^2
Amount of naked MIONs (mg)	10.3	10.2	0.055	8.27	0.9955	0.018	1.88	10.2	0.9983	0.72	0.7756
	20.3	5.1	0.14	3.08	0.9799	0.174	4.43	5.0	0.9997	0.28	0.5109
	30.4	3.3	0.72	0.37	0.9994	0.872	9.56	3.3	0.9998	0.13	0.2907
Au(III)-Cl conc. (mg/L)	10.3	10.2	0.055	8.27	0.9955	0.018	1.88	10.2	0.9983	0.72	0.7756
	*25.6	24.9	0.12	24.40	0.9998	0.0060	4.14	25.5	0.9958	1.86	0.8008
	*51.1	42.2	0.043	37.88	0.9998	0.0010	2.53	41.7	0.9983	3.40	0.8091
pH	*1.0	13.9	0.023	13.74	0.9947	0.0019	0.40	14.6	0.9977	1.14	0.9797
	3.0	16.9	0.070	14.95	0.9778	0.0097	2.92	17.4	0.9988	2.58	0.8960
	5.0	16.9	0.18	14.22	0.9294	0.0388	11.21	17.0	0.9997	0.66	0.7073

* Note that the experiments marked with a star did not reach equilibrium.

Stellenbosch University https://scholar.sun.ac.za

3.4.3.1.2 *Pseudo*-second-order kinetic model

The sorption kinetics for sorption of Au(III)-Cl by naked MIONs as a function of the amount of naked MIONs, initial Au(III)-Cl concentration and pH were further evaluated using *pseudo*-second-order kinetics. This model assumes that the sorption mechanism depends on the adsorbate and adsorbent, and the rate limiting step may be chemisorption involving valence forces through the sharing or exchange of electrons between adsorbate and adsorbent.

This model can be described using **Equation 3.12**, which on integration becomes **Equation 3.13**.

Equation 3.12
$$\frac{dq}{dt} = K_2(q_e = q_t)^2$$

Equation 3.13
$$\frac{t}{q_t} = \frac{1}{K_2 q_e^2} + \frac{1}{q_e} t$$

where k_2 (g/mg min) is the rate constant of *pseudo*-second-order kinetics, q_e and q_t are the amount of metal ion adsorbed (mg/g) at equilibrium and time t respectively. The slope and intercept of the linear plot *t/qt versus t* yielded the values of *qe* and k_2. Again, the initial sorption rate (h) can be determined from k_2 and *qe* values using $h = k_2 q_e^2$.

The *pseudo*-second-order kinetics plot for sorption of 10 mg/L Au(III)-Cl by 10.3 mg, 20.3 mg, and 30.4 mg of naked MIONs is presented in **Figure 3.27**. The corresponding kinetics parameters are shown in **Table 3.1**. As seen in **Figure 3.27**, data points exhibited linearity for the whole sorption time (160 min) of the three batch experiments. The correlation coefficients, R^2 values are above 0.9980. The q_e values extrapolated from **Equation 3.13** are 10.22 $mg.g^{-1}$, 5.04 $mg.g^{-1}$, and 3.31 $mg.g^{-1}$ and are close to the experimental q_e values (**Table 3.1**). Therefore, the high R^2 values and the agreement between the q_e values suggest that the sorption of Au(III)-Cl by different amounts of naked MIONs followed *pseudo*-second-order kinetic model.

The sorption data obtained by varying the initial Au(III)-Cl concentration and pH were also analysed using the *pseudo*-second-order kinetics model. The corresponding kinetics parameters are shown in **Table 3.1** The R^2 values for all the experiments are in the range of 0.9977 – 0.9997. The calculated q_e values also match with the experimental q_e values. Hence, sorption of Au(III)-Cl by naked MIONs for all the batch experiments best fitted the *pseudo*-second-

Stellenbosch University https://scholar.sun.ac.za

order kinetics model. The sorption of metal ions on solid nano-sorbent materials has been reported as a *pseudo*-second-order process by many authors.[42,142,153]

Since a good fit was achieved with the pseudo-second-order kinetics model and the correlation between the q_e values and the high R^2 values qualifies k_2 as the suitable parameter to estimate the rates for sorption of Au(III)-Cl by naked MIONs. The k_2 values were recorded in **Table 3.1**. The sorption rates (k_2 values) is usually dependent on initial metal ion concentration.[154] As seen in the table, increasing the initial Au(III)-Cl concentration resulted in a decrease in k_2 values. The higher the initial metal ion concentration, the longer time is required to reach an equilibrium. This behaviour can be attributed to the fact that, at lower Au(III)-Cl concentration, the number of available active binding sites on the surface of the naked MIONs is higher and this facilitates the sorption process. Ho and Mckay reported the same relationship between k_2 and initial metal ion concentration for their study on kinetics of sorption of divalent metal ions using sphagnum moss peat at different initial metal ion concentrations.[104]

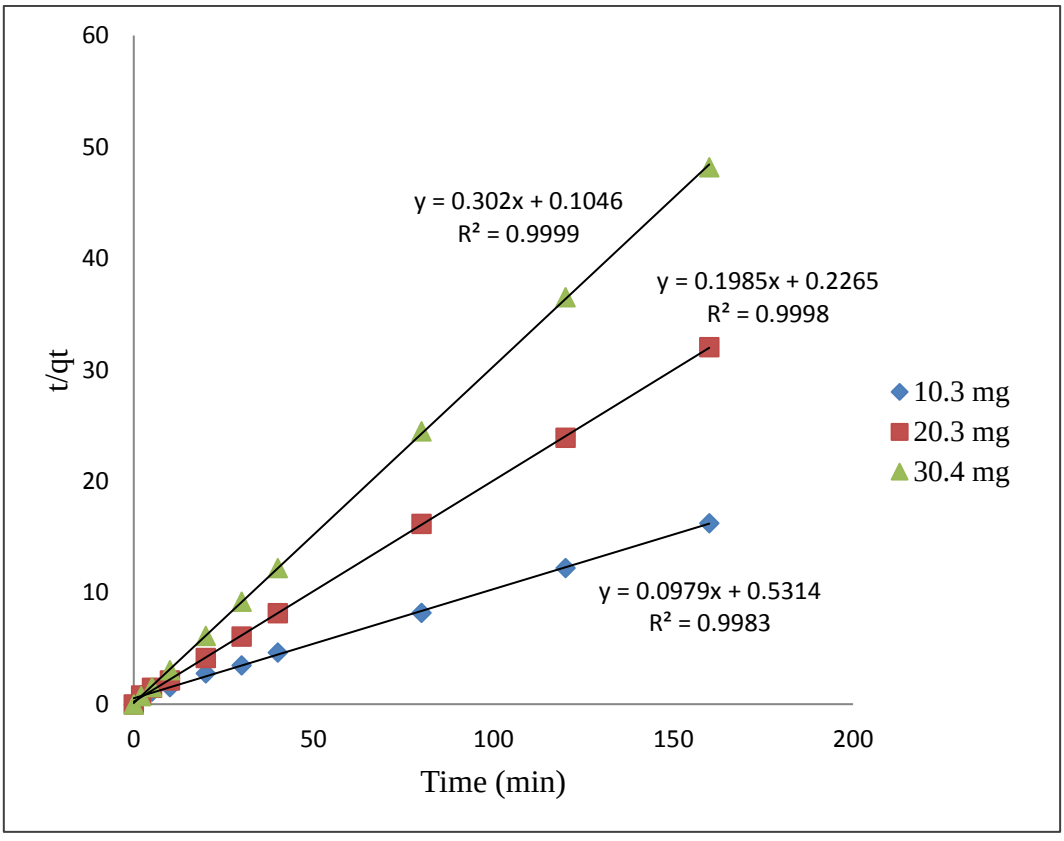

Figure 3.27: *Pseudo*-second-order kinetic model for the sorption of Au(III)-Cl by different amounts of naked MIONs. Experimental conditions: [Au(III)]: 10 mg/L, total aqueous phase: 10 mL, pH: 2.5, temperature: 25±2 °C and shaker speed: 150 rpm.

Stellenbosch University https://scholar.sun.ac.za

The influence of k_2 on adsorbent doses shows opposite effect to that of initial metal ion concentration, *i.e.* increasing the amount of adsorbent results in an increase in k_2 values. Obviously, increasing the amount of the adsorbent but keeping the initial metal ion concentration constant results in increasing of sorption binding sites. Therefore, these predictions match with the results shown in **Table 3.1**, where the k_2 values increases with an increase in amount of naked MIONs. Unlike these two parameters (effect of the amount of naked MIONs and the initial metal ion concentration), the effect of solution pH on k_2 is more complex and differs for every system. The k_2 values recorded in **Table 3.1** for the effect of pH on sorption of Au(III)-Cl by naked MIONs, shows that k_2 increases with increasing solution pH. As mentioned earlier, this can be attributed the high sorption affinity of naked MIONs for hydrolysis products of Au(III)-Cl.

3.4.3.1.3 Intraparticle diffusion kinetic model

The third model is also used as a basis to study whether the intraparticle diffusion is the rate determining step during the sorption process. This model assumes that the movement of sorbate molecules into the interior of sorbent particles is the rate determining step in the sorption process.[141] According to the model, the mass transfer rate can be expressed as a function of the square root of time and can be described using **Equation 3.14**

Equation 3.14 $$q_t = k_{id} t^{0.5}$$

where k_{id} ($mg \cdot g^{-1} \cdot min^{-0.5}$) is the intraparticle diffusion rate constant, which can be obtained from the slope of the plot q_t *versus* $t^{0.5}$. If the plot is linear and passes through the origin, then intraparticle diffusion is the sole rate-limiting step. **Figure 3.28** shows the intraparticle diffusion kinetics linear plot for sorption of Au(III)-Cl by three doses of naked MIONs.

As seen in **Figure 3.28**, the data points showed multi-linearity with two different stages of sorption, suggesting intraparticle diffusion kinetics model is not a limiting step. Liu *et al.*[42] observed similar results for sorption of Au(III)-Cl, Pd(II)-Cl and Pt(IV)-Cl complexes on graphene oxide, and assigned the initial sorption stage to the external surface sorption, second sorption stage was attributed to exchange of electrons between graphene oxide and metal ions and the final sorption stage to equilibrium stage. All the kinetics parameters extrapolated from the intraparticle diffusion equation are shown in **Table 3.1**. However, based on the poor

Stellenbosch University https://scholar.sun.ac.za

correlation coefficients, it can be concluded that the intraparticle diffusion kinetic model does not describe the sorption of Au(III)-Cl by naked MIONs.

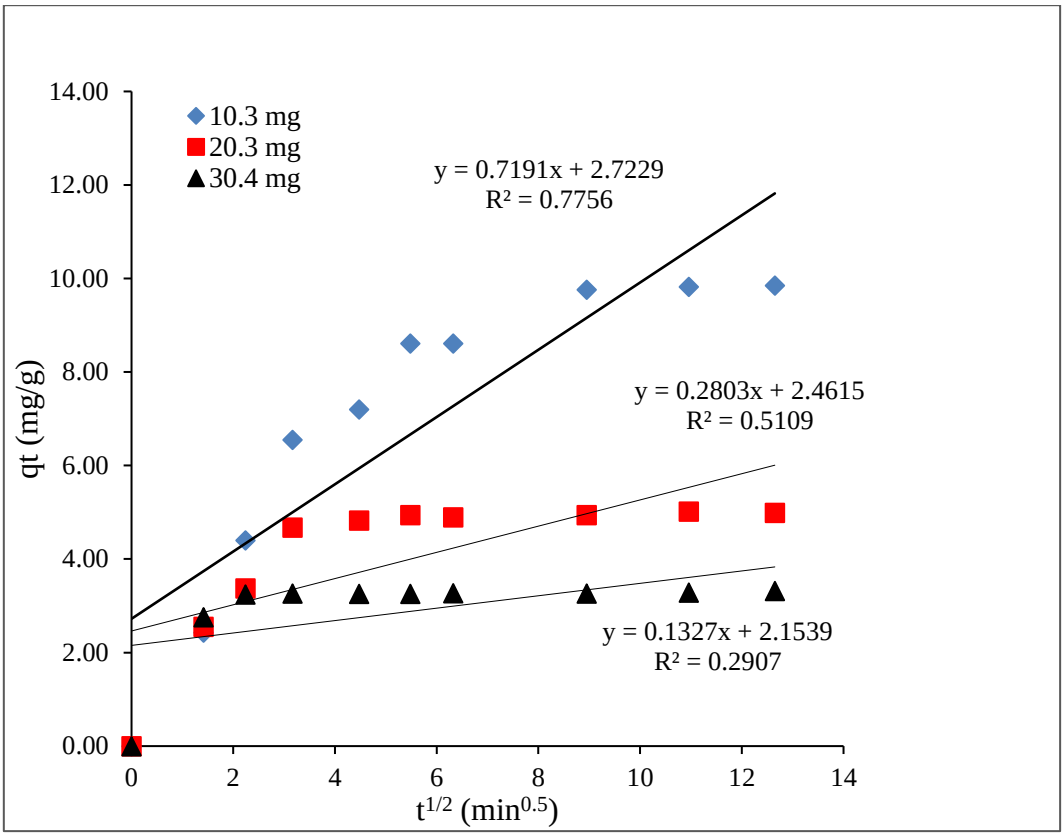

Figure 3.28: Intraparticle diffusion kinetic model for the sorption of Au(III)-Cl by different amounts of naked MIONs. Experimental conditions: [Au(III)]: 10 mg/L, total aqueous phase: 10 mL, pH: 2.5, temperature: 25±2 °C and shaker speed: 150 rpm.

3.4.3.2 Sorption kinetics of Pd(II) complexes

Sorption of Pd(II)-Cl complex by naked MIONs was analysed using *pseudo*-first-order and *pseudo*-second-order, and intraparticle diffusion kinetic models. All the corresponding kinetics parameters for sorption of Pd(II)-Cl are as listed in **Table 3.2**.

3.4.3.2.1 *Pseudo*-first-order kinetic model

The sorption kinetics of Pd(II)-Cl by different doses of naked MIONs was also fitted using the *pseudo*-first-order kinetic model. **Figure 3.29** shows the linear *pseudo*-first-order kinetic plot of sorption of Pd(II)-Cl by different amounts of naked MIONs: 30.6 mg, 60.4 mg, and 90.3 mg. The figure shows that the plot of $log(q_e-q_t)$ versus time did not exhibit a linear relationship.

Stellenbosch University https://scholar.sun.ac.za

Table 3.2: Coefficients of *pseudo*-first-order and *pseudo*-second-order kinetic parameters and intraparticle diffusion model for sorption of Pd(II) by naked MIONs

Parameters		$q_{e(exp)}$ mg·g^{-1}	*pseudo*-first-order kinetics			*pseudo*-second-order kinetics				Intraparticle diffusion	
			k_1 min^{-1}	$q_{e(cal)}$ mg·g^{-1}	R^2	k_2 gmg^{-1}min^{-1}	h mg.g^{-1}min^{-1}	$q_{e(cal)}$ mg.g^{-1}	R^2	k_{id} mg.g^{-1}min$^{-0.5}$	R^2
Amount of MIONs (mg) pH = 2.5	30.6	1.14	0.013	0.15	0.1817	1.14	1.41	1.11	0.9966	0.054	0.3779
	60.4	0.91	0.056	0.24	0.4724	1.71	1.46	0.92	0.9997	0.045	0.3871
	90.3	0.77	0.0021	0.11	0.0113	0.62	0.36	0.76	0.9986	0.038	0.4483
Pd(II) conc. (mg/L), pH = 2.5	10	0.77	0.0021	0.11	0.0113	0.62	0.36	0.76	0.9986	0.038	0.4483
	21	1.15	0.050	0.22	0.3727	1.94	2.43	1.12	0.9995	0.051	0.3116
	32	1.55	0.020	0.087	0.7826	0.90	2.16	1.55	0.9998	0.071	0.3569
Pd(II) conc. (mg/L), pH = 5.0	10	1.04	1.18	0.91	0.8026	3.70	4.05	1.05	0.9998	0.050	0.3652
	17	1.72	0.13	0.89	0.8597	0.99	2.94	1.73	0.9998	0.091	0.4385
	26	2.35	0.055	0.89	0.8476	0.45	2.54	2.38	0.9997	0.13	0.4674
pH	2.5	0.77	0.0021	0.11	0.0113	0.62	0.36	0.76	0.9986	0.038	0.4483
	3.0	0.99	0.020	0.090	0.3423	2.01	1.96	0.99	0.9998	0.0004	0.4193
	5.0	1.05	0.15	0.40	0.8698	3.70	4.05	1.05	0.9997	0.0005	0.3101

Stellenbosch University https://scholar.sun.ac.za

This was applied for intial sorption stage and the final sorption stages. The R^2 value for all the batch experimets are in the range of 0.011 to 0.47. The experimental q_e values which are 0.15 mg/g, 0.24 mg/g and 0.11 mg/g does not agree with the theoretical q_e values. Hence, sorption of Pd(II)-Cl by different amount of naked MIONs cannot be described using the *pseudo*-first-order kinetics model.

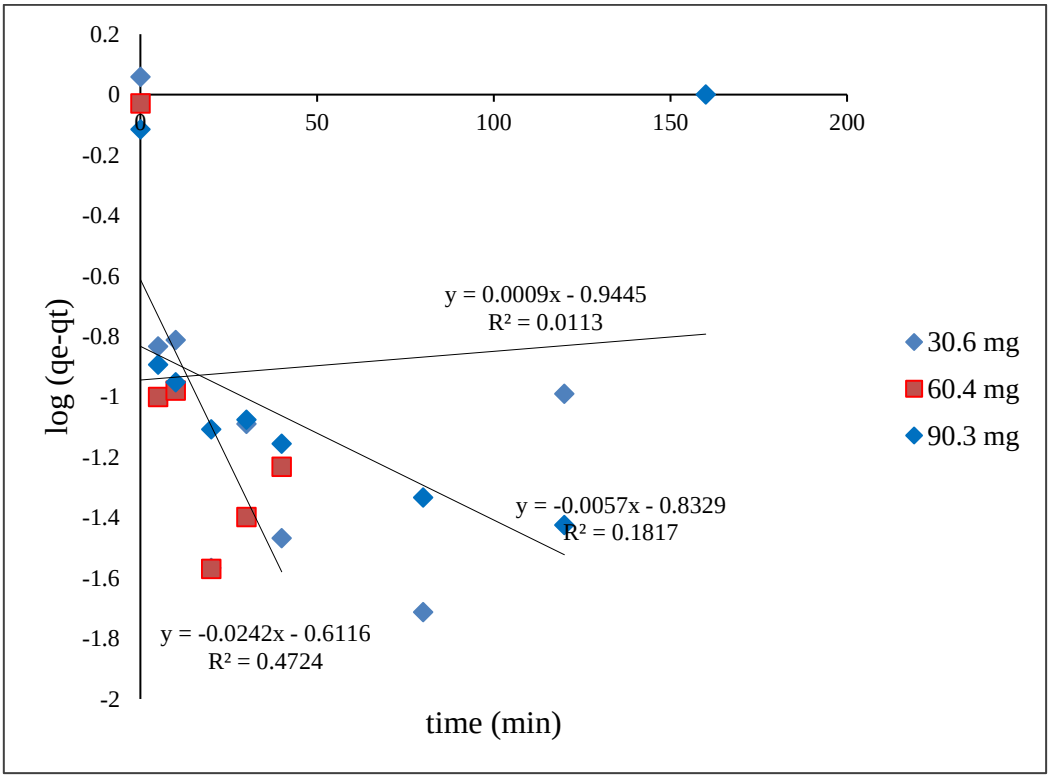

Figure 3.29: *Pseudo*-first-order kinetic model for sorption of Pd(II)-Cl by different amounts of naked MIONs Experimental conditions: [Pd(II)]: 10 mg/L, total aqueous phase: 10 mL, pH: 2.5, temperature: 25±2 °C and shaker speed: 150 rpm.

The kinetic parametes for sorption kinetics of Pd(II)-Cl by naked MIONs when varying the solution pH and initial Pd(II)-Cl concentration are also displayed in **Table 3.2**. The R^2 values which are on the range of 0.011 to 0.87 and calculated q_e values are not congruent with the experiment q_e values which suggest that the sorption of Pd(II)-Cl by naked MIONs cannot be described by *pseudo*-first-order-kinetics model. Therefore, the sorption rates for sorption of Pd(II)-Cl by naked MIONs cannot be measured using k_1 recorded in **Table 3.2**.

Stellenbosch University https://scholar.sun.ac.za

3.4.3.2.2 *Pseudo*-second-order kinetic model

The sorption of Pd(II)-Cl as a function of adsorbent doses, pH, and the initial Pd(II) concentration was further analysed using the *pseudo*-second-order kinetic model by plotting the *t/qt versus t* for the three batch sorption experiments. For instance, **Figure 3.30** shows *pseudo*-second-order linear plot for various amounts of naked MIONs used for sorption of Pd(II). As shown in **Figure 3.30**, the R^2 values are 0.9966 and higher. The calculated q_e values for sorption of Pd(II)-Cl by 30.6 mg, 60.4 mg, and 90.3 mg of naked MIONs which are 1.11 $mg.g^{-1}$, 0.92 $mg.g^{-1}$, and 0.76 mmg^{-1}, respectively, also match with the experimental values. The high R^2 values and the aggrement in *qe* values indicate that the sorption of Pd(II)-Cl by naked MIONs can be described by the *pseudo*-second-order kinetics model.

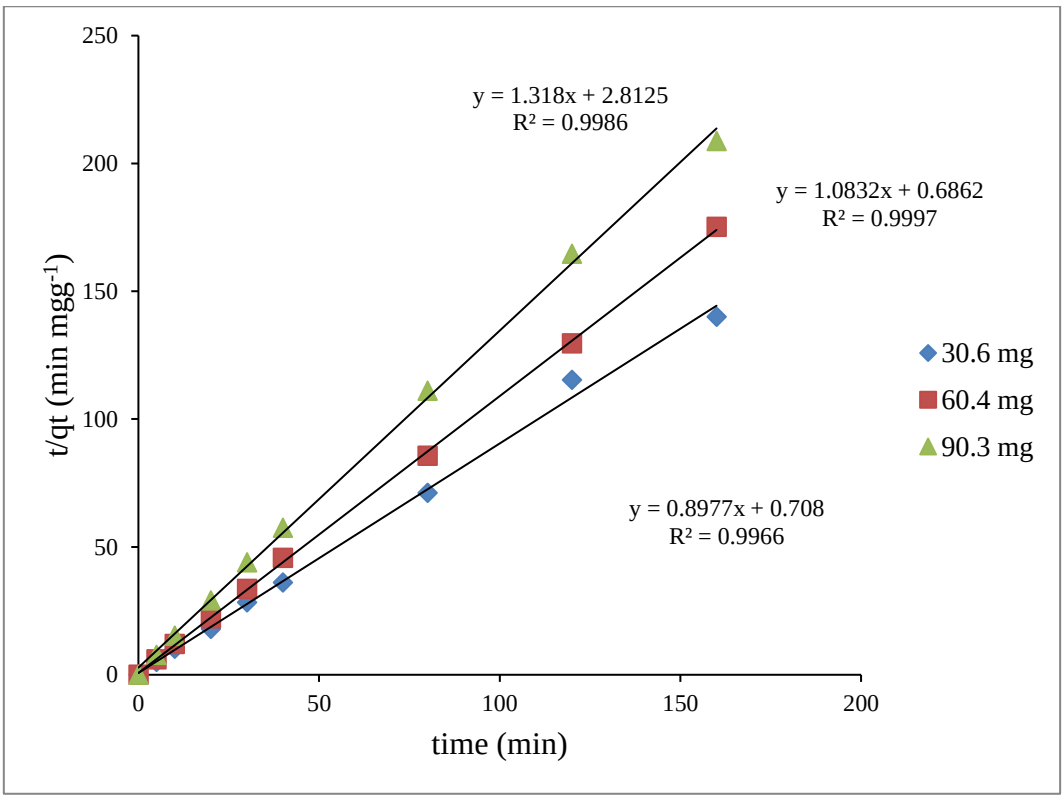

Figure 3.30: *Pseudo*-second-order kinetic model for the sorption of Pd(II)-Cl by different amounts of naked MIONs Experimental conditions: [Pd(II)]: 10 mg/L, total aqueous phase: 10 mL, pH: 2.5, temperature: 25±2 °C and shaker speed: 150 rpm.

As shown in **Table 3.2** R^2 values for sorption of Pd(II)-Cl by naked MIONs as a function of pH are greater than 0.9986. In addition, the R^2 values for sorption of Pd(II)-Cl by naked MIONs

Stellenbosch University https://scholar.sun.ac.za

as a function of initial Pd(II)-Cl concentration at pH 2.5 and pH 5.0 in the range of (0.9986 – 0.9998) and (0.9997 – 0.9998), respectively.

Beside the high R^2 values, the calculated q_e values for the sorption of Pd(II)-Cl as a function of pH which are as follows: 0.76 $mg.g^{-1}$, 0.99 $mg.g^{-1}$, and 1.05 $mg.g^{-1}$ are congruent with the experimental values. Furthermore, the calculated q_e values for the sorption of Pd(II)-Cl as a function of the initial Pd(II)-Cl concentrations (at pH 2.5 and pH 5.0) are also in agreement with the experimental q_e values. Furthermore, the q_e values for the batch sorption at pH 2.5 and pH 5.0 increase with the intial Pd(II)-Cl concentration *i.e*, the large q_e values correspond to high concentration.

Considering the above discussions, it is reasonable to postulate that sorption of Pd(II)-Cl by naked MIONs followed *pseudo*-second-order kinetics models. Therefore, the sorption rates can be explained using k_2. All the k_2 values for sorption of Pd(II)-Cl by naked MIONs as a function of adsorbent amount, pH and initial Pd(II)-Cl concentration (at pH 2.5 and pH 5.0) are shown in **Table 3.2**. The k_2 values decrease with an increasing initial Pd(II)-Cl concentration at pH 5.0 as expected. However, the k_2 values for the batch sorption carried at pH 2.5 did not show any trend due to low sorption affinity exhibited by naked MIONs for Pd(II)-Cl at low pH.

3.4.3.2.3 Intraparticle diffusion kinetic model

Batch sorption experiments of Pd(II)-Cl by 30.6 mg, 60.4 mg, and 90.3 mg naked MIONs were also analysed using intraparticles diffusion kinetic model. **Figure 3.31** shows the intraparticle diffusion plot for different doses of naked MIONs. As seen in the figure, a linear relationship was not achieved. Hence, this model was not a rate liming step

Stellenbosch University https://scholar.sun.ac.za

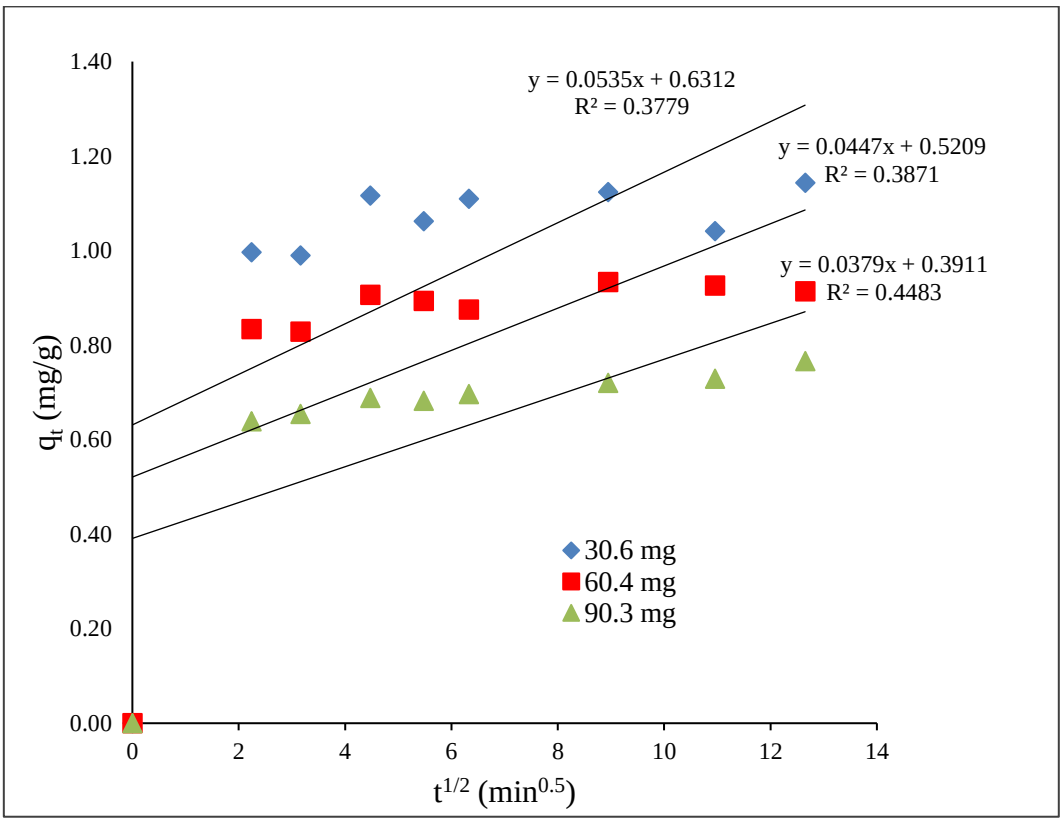

Figure 3.31: Intraparticle diffusion for the sorption of Pd(II)-Cl by different amounts of naked MIONs. Experimental conditions: [Pd(II)]: 10 mg/L, total aqueous phase: 10 mL, pH: 2.5, temperature: 25±2 °C and shaker speed: 150 rpm.

3.4.3.3 Sorption kinetics of Pt(IV) complexes

Sorption of Pt(IV)-Cl by naked MIONs was analysed using *pseudo*-first and second-order kinetics model, and intraparticle diffusion. All the corresponding kinetics parameter are listed in **Table 3.3**.

3.4.3.3.1 *Pseudo*-first-order kinetic model

Figure 3.32 shows the plot of $log(q_e-q_t)$ versus time for sorption of Pt(IV) as a function of the amount of naked MIONs (30.1 mg, 60.1 mg, and 90.1 mg). As seen from **Figure 3.32** and **Table 3.3**, a linear relationship was not achieved and the R^2 values are in the range of 0.6314-0.7268. The q_e values which are 0.54 $mg.g^{-1}$, 0.38 $mg.g^{-1}$, and 0.24 $mg.g^{-1}$ are low compared to the experimental q_e values. The batch sorption results for Pt(IV)-Cl by naked MIONs as a function of pH and initial concentration were also fitted onto the *pseudo*-first-order kinetic model and the kinetics parameters are listed in **Table 3.3**. The low R^2 values and the calculated

Stellenbosch University https://scholar.sun.ac.za

q_e values which do not match with the experimental q_e values suggest that sorption of Pt(IV)-Cl by naked MIONs cannot be described by the *pseudo*-first-order kinetics model.

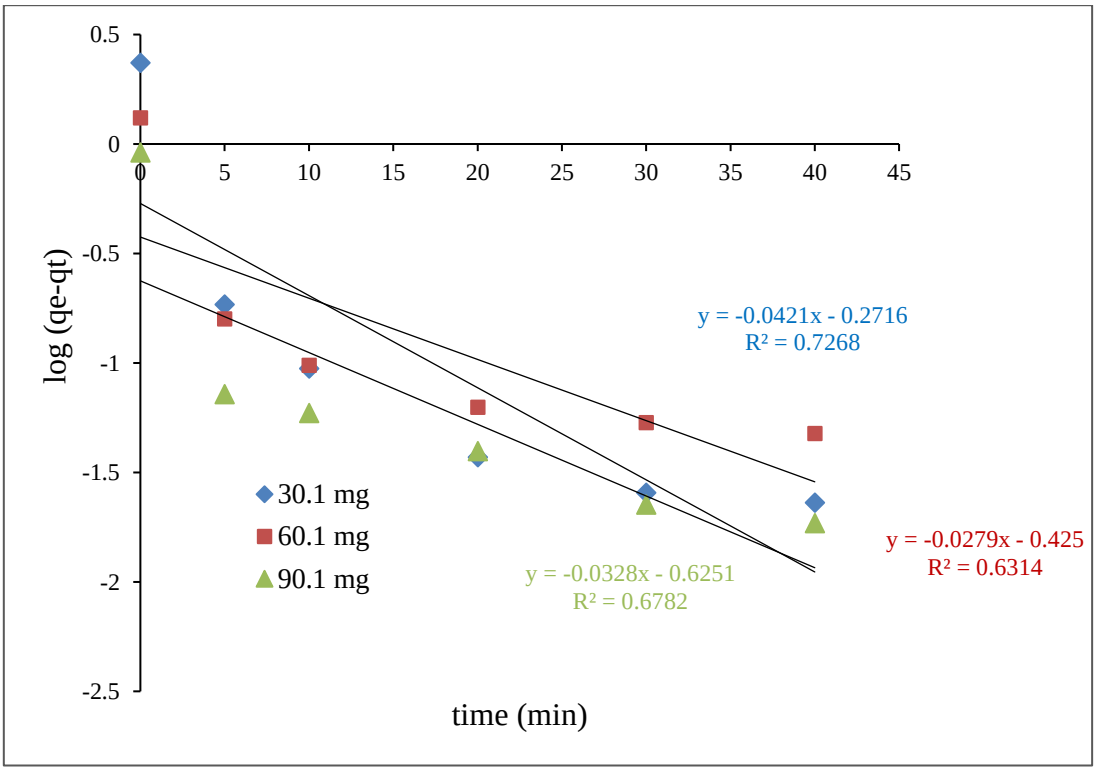

Figure 3.32: *Pseudo*-first-order kinetic model for the sorption of Pt(IV)-Cl by different dosages of naked MIONs. Experimental conditions: [Pt(IV)]: 10 mg/L, total aqueous phase: 10 mL, pH: 2.5, temperature: 25±2 °C and shaker speed: 150 rpm.

3.4.3.3.2 *Pseudo*-second-order kinetic model

The batch sorption of Pt(IV)-Cl by naked MION as a function of the amount of naked MIONs, pH and the initial Pt(IV)-Cl concentration were fitted on linear *pseudo*-second-order kinetic equation. If the second order kinetics is applicable, the plot of t/q_t versus time should give a linear relationship from which the kinetics parameters q_e, h, and k_2 can be determined. All the extrapolated kinetic parameters are as shown in **Table 3.3**.

All the *pseudo*-second-order kinetics plots for the sorption of Pt(IV) as a function of the amount of naked MIONs, pH and the initial Pt(IV) concentration exhibited a linear relationship with the R^2 of 0.9998. For instance, **Figure 3.33** shows the plot of *t/qt versus t* for batch sorption of Pt(IV)-Cl by different amount of naked MIONs: 30.1 mg, 60.1 mg, and 90.1 mg display linear

Stellenbosch University https://scholar.sun.ac.za

relationship with the R^2 value of 0.9998. Also, as shown in **Figure 3.33**, the calculated q_e values agree with the experimental q_e values for all the batch sorption carried out.

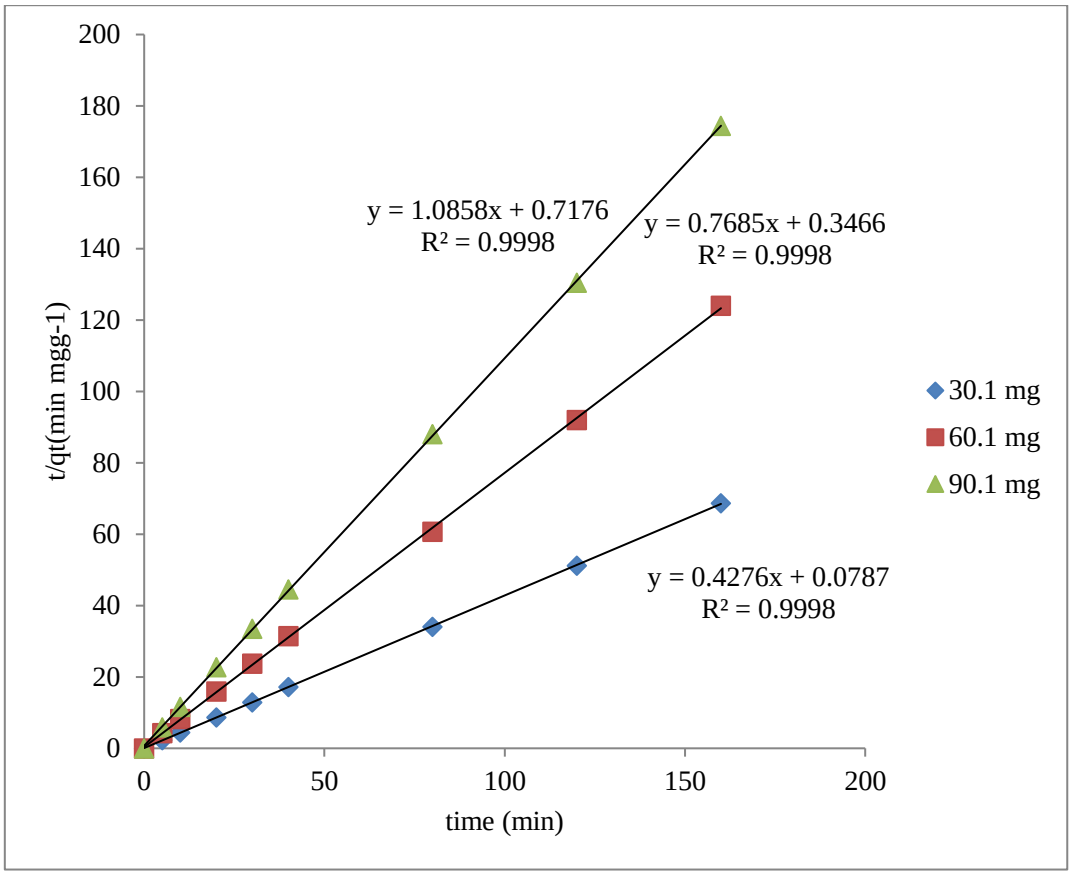

Figure 3.33: *Pseudo*-second-order kinetic model for the sorption of Pt(IV)-Cl by different dosages of naked MIONs. Experimental conditions: [Pt(IV)]: 10 mg/L, total aqueous phase: 10 mL, pH: 2.5, temperature: 25±2 °C and shaker speed: 150 rpm.

Logically, the q_e values increases with increasing initial Pt(IV)-Cl concentration. This trend is also observed in **Table 3.3**. as the calculated q_e values for sorption of 10 mg/L, 21 mg/L and 31 mg/L using 90.4 mg of naked MIONs are 0.92 $mg.g^{-1}$, 1.96 $mg.g^{-1}$ and 2.75 $mg.g^{-1}$, respectively. Based on the higher R^2 values, and the agreement between the calculated q_e values the experimental q_e values, the sorption kinetics of Pt(IV)-Cl by naked MIONs can be well described by the *pseudo*-second-order kinetic model. Therefore, sorption rates for the uptake of Pt(IV)-Cl by naked MIONs can be predicted using k_2. Theoretically, k_2 and initial metal ion concentration are inversely proportional. As shown in **Table 3.3**., the k_2 values for sorption of 10 mg/L, 21 mg/L and 31 mg/L of Pt(IV)-Cl by naked MIONs decreased with an increase in Pt(IV) concentration.

Stellenbosch University https://scholar.sun.ac.za

Table 3.3: Coefficients of *pseudo*-first-order and *pseudo*-second-order kinetic parameters and intraparticle diffusion model for sorption of Pt(IV) by naked MIONs

Parameters		$q_{e(exp)}$	*pseudo*-first-order kinetics			*pseudo*-second-order kinetics				intraparticle diffusion	
			k_1	$q_{e(cal)}$	R^2	k_2	H	$q_{e(cal)}$	R^2	k_{id}	R^2
		mg·g^{-1}	min^{-1}	mg·g^{-1}		gmg^{-1}min^{-1}	mg.g^{-1}min^{-1}	mg.g^{-1}		mg.g^{-1}min$^{-0.5}$	
Amount of MIONs (mg)	30.1	2.34	0.097	0.54	0.7268	2.32	12.71	2.34	0.9998	0.11	0.3458
	60.1	1.32	0.064	0.38	0.6314	1.70	2.89	1.30	0.9998	0.063	0.3809
	90.1	0.92	0.041	0.24	0.6782	1.64	1.39	0.92	0.9998	0.044	0.3698
Pt(IV) conc. (mg/L)	10	0.92	0.041	0.15	0.6075	1.64	1.39	0.92	0.9998	0.0072	0.8788
	21	1.95	0.033	0.11	0.6763	0.79	3.01	1.96	0.9997	0.016	0.7269
	31	2.75	0.004	0.31	0.0261	0.15	1.12	2.75	0.9999	0.014	0.4810
pH	2.5	0.92	0.041	0.15	0.6075	1.64	1.39	0.92	0.9998	0.0072	0.8788
	3.0	0.90	0.018	0.69	0.0127	3.81	3.00	0.89	0.9999	0.019	0.6294
	5.0	1.03	0.018	0.50	0.3946	1.12	1.16	1.02	0.9998	0.0078	0.7036

Stellenbosch University https://scholar.sun.ac.za

3.4.3.3.3 Intraparticle diffusion kinetics model

Figure 3.34 shows intraparticle diffusion kinetic linear plot for sorption of Pt(IV)-Cl by 30.1 mg, 60.1 mg, and 90.1 mg of naked MIONs. The data point does not pass through the origin and the correlation coefficients are very low suggesting that sorption of Pt(IV)-Cl naked MIONs is not governed by intraparticle diffusion kinetic models.

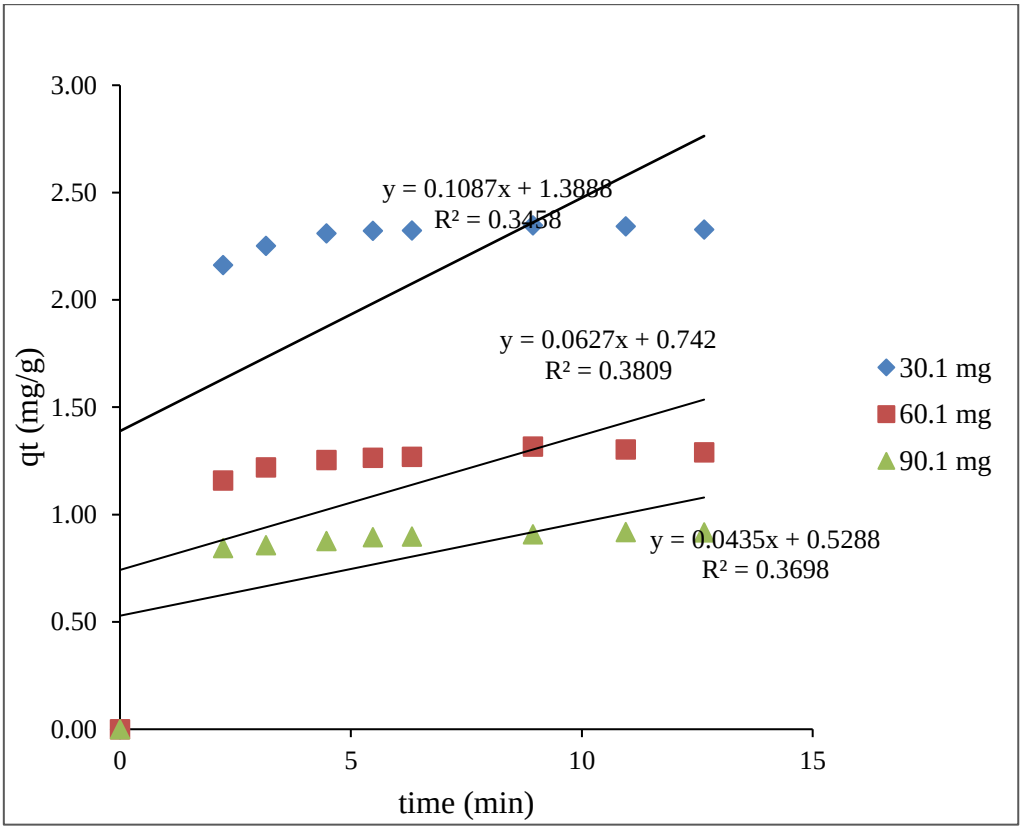

Figure 3.34: Intraparticle diffusion kinetic model for the sorption of Pt(IV)-Cl by different dosages of naked MIONs. Experimental conditions: [Pt(IV)]; 10 mg/L, total aqueous phase; 10 mL, pH; 2.5, temperature; 25±2 °C and shaker speed; 150 rpm.

The batch sorption kinetic for Pt(IV)-Cl by naked MIONs as a function of the solution pH and the initial Pt(VI)-Cl concentration was also analysed using intraparticle diffusion kinetic model. When the plot of q_t *versus* $t^{0.5}$ is linear and passes thorough the origin (0.0) then the intraparticle diffusion is the rate limiting step. The intraparticle diffusion parameters are listed in **Table 3.3**.

Stellenbosch University https://scholar.sun.ac.za

3.4.4 Sorption isotherms

Sorption is a physical and/or chemical process in which a substance is accumulated at an interface between phases. Several different equations can be used to predict theoretical sorption capabilities for different adsorbents. For this study, the Freundlich isotherm and Langmuir isotherm equations have been used to predict sorption capabilities of Au(III)-Cl complexes by naked MIONs from acidic aqueous solutions. These models are the most frequently used for explaining equilibrium sorption of metal ions/complexes by various adsorbents.[13-15] The Langmuir model is based on monolayer sorption on the active sites of the adsorbent. Furthermore, the Langmuir model assumes that there is no interaction between adsorbate species and that once a species occupies a site, no further sorption can take place at that site. Theoretically, therefore, a saturation value is reached, beyond which no further sorption can take place.

The linear form of Langmuir sorption model is given as **Equation 3.15**.

Equation 3.15

$$\frac{C_e}{q_e} = \frac{1}{q_{max} K_L} + \frac{C_e}{q_{max}}$$

where q_e is the amount of adsorbed metal ion per unit weight of adsorbent (mg/g), C_e is the concentration of the free metal ion in solution (mg/L), q_{max} the maximum adsorbed metal ion per unit weight of the adsorbed (mg/g), and k_L is the Langmuir constant (L/mg) which are related to the energy of sorption. This constant can be calculated from the intercept and slope of the linear plot, with C_e/q_e *versus* C_e.

The plot of C_e/q_e *versus* C_e for sorption of Au(III)-Cl by naked MIONs as function of pH is shown in **Figure 3.35**. The R^2 values as shown in **Figure 3.35** and **Table 3.4** are as follows: 0.9992, 0.9999 and 0.9995 for sorption at pH 1.0, pH 3.0 and pH 5.0, respectively. As depicted by this figure, Langmuir model represents a good fit of the experimental data and was considered adequate for estimating the loading capacity of Au(III)-Cl by naked MIONs. This observation suggested that the sorption process was dominated by a monolayer sorption process rather than a multiple one.

The other Langmuir parameters along with corresponding coefficients of correlation are listed in **Table 3.4**. The high K_L value indicates the binding strengths of the hydroxyl groups on the

Stellenbosch University https://scholar.sun.ac.za

surface of MIONs. As shown in **Table 3.4**, the maximum Au(III) loading capacities at pH 1.0, 3.0 and 5.0 are 10.44 mg/g, 18.98 mg/g and 27.25 mg/g respectively. Hence, the q_{max} values increased with increasing solution pH. The calculated q_e values extrapolated from the *pseudo*-second-order kinetic linear plot also increased with solution pH. Therefore, the Langmuir sorption isotherm and the *pseudo*-second-order kinetic models best described sorption of Au(III)-Cl by naked MIONs. Hence, sorption of Au(III)-Cl by naked MIONs is a chemical process.

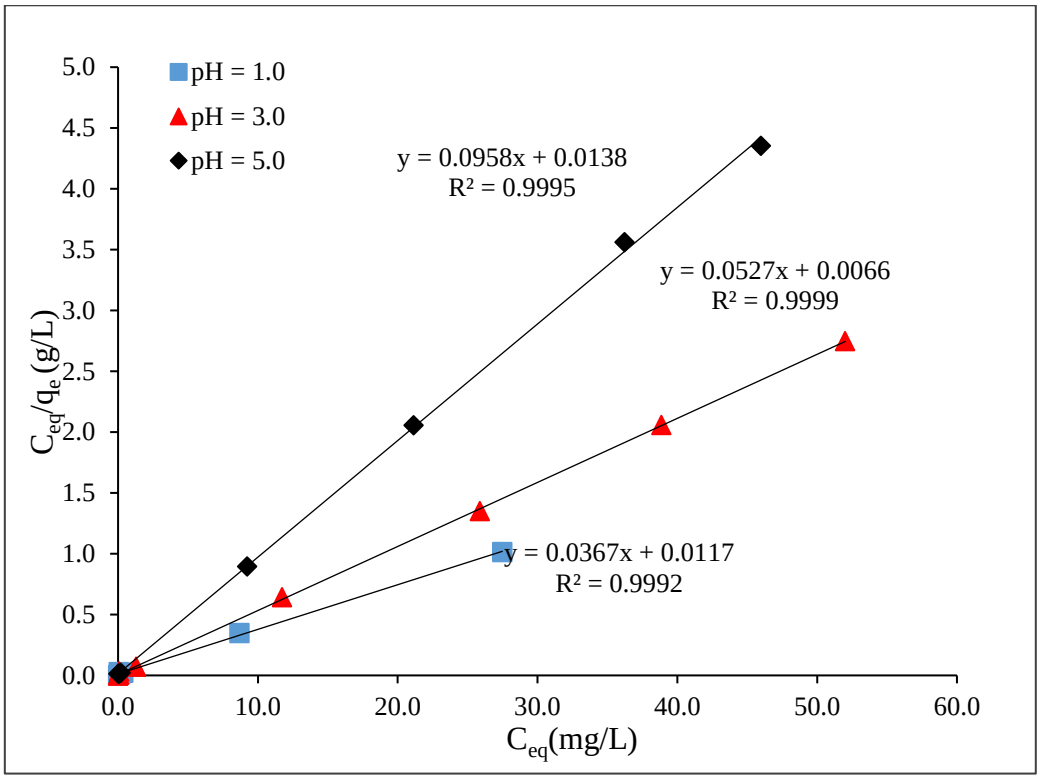

Figure 3.35: Langmuir sorption isotherm linear plot for equilibrium sorption of Au(III)-Cl by naked MIONs at pH 1.0, pH 3.0 and pH 5.0. Other experimental conditions: [Au(III)]: 1.00 to 110 mg/L, mass of MIONs 30.4 mg, total aqueous phase: 10 mL, shaker speed: 150 rpm, temperature: 25±2ºC.

Table 3.4: Langmuir parameters for the sorption of Au(III)-Cl by naked MIONs from acidic aqueous solutions

Metal ions	pH	Langmuir		
		K_L (L/mmg)	q_{max} (mg/g)	R^2
Au(III)	1.0	3.14	10.44	0.9992
	3.0	7.98	18.98	0.9998
	5.0	6.94	27.25	0.9995

Stellenbosch University https://scholar.sun.ac.za

The *Freundlich model* [15] explains the sorption on a heterogeneous (multiple layers) surfaces with uniform energy. This model can be represented using the linearized equation (**Equation 3.16**).

Equation 3.16

$$\log q_e = \log K_F + \frac{1}{n} \times \log C_e$$

where q_e is, the equilibrium loading capacity (mg/g), C_e is the equilibrium metal concentrations in the aqueous phase (mg/L), K_F is the Freundlich constant (L/mmg), and n is the heterogeneity factor associated with the Freundlich model. k_F and n are related to the sorption capacity and intensity, respectively. These constants can be calculated from the slope and intercept of the linear plot, with $logq_e$ *versus* $logC_e$. **Figure 3.36** shows Freundlich sorption isotherm linear plot. The R^2 values shown in **Figure 3.36** and **Table 3.5** are less than 0.90 suggesting that Freundlich sorption isotherm is not the best model to describe sorption of Au(III)-Cl by naked MIONs.

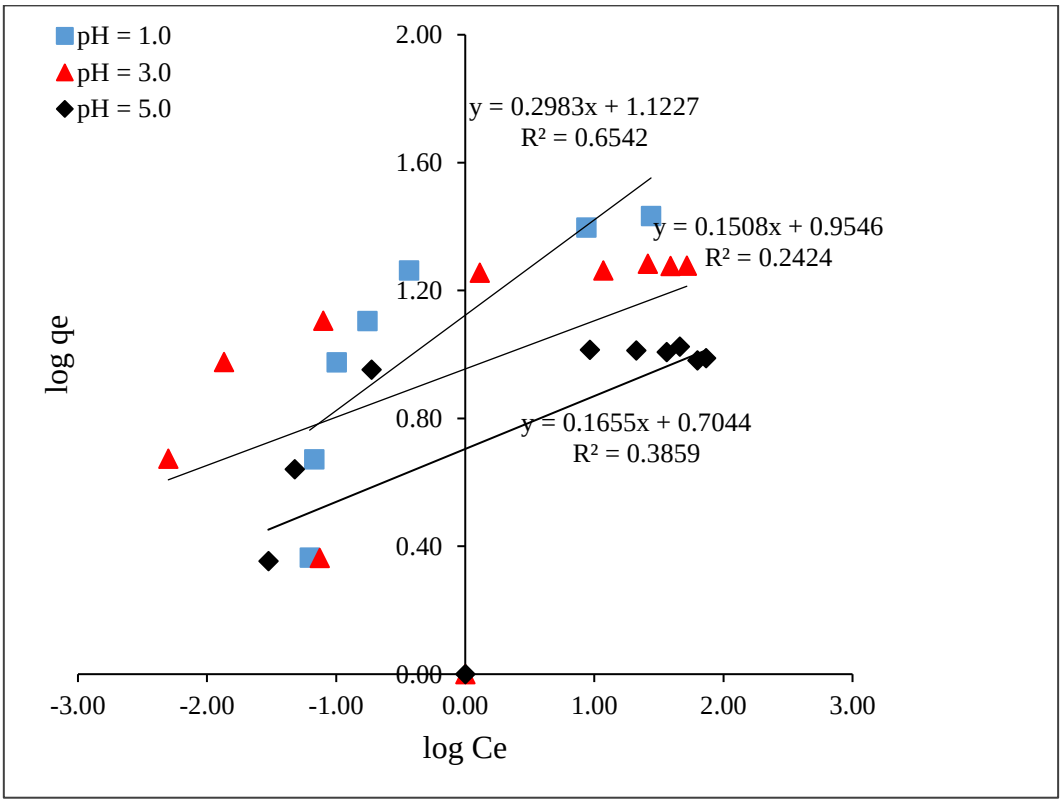

Figure 3.36: Freundlich sorption isotherm linear plot for equilibrium sorption of Au(III)-Cl by naked MIONs at pH 1.0, pH 3.0 and pH 5.0. Other experimental conditions: [Au(III)]: 1.00 to 110 mg/L, mass of MIONs 30.4 mg, total aqueous phase: 10 mL, shaker speed: 150 rpm, temperature: 25±2ºC.

Stellenbosch University https://scholar.sun.ac.za

Table 3.5: Freundlich parameters for the sorption of Au(III)-Cl by naked MIONs from acidic aqueous solutions

Metal ions	pH	Freundlich		
		K_F	*n*	R^2
Au(III)-Cl	1.0	13.27	3.35	0.6542
	3.0	9.01	6.63	0.2424
	5.0	5.06	6.04	0.3859

3.4.5 Characterisation of naked MIONs after sorption

The power X-ray diffraction was carried to analyse the crystalline structure of the MIONs after sorbing Au(III)-Cl complexes at pH 1.0, pH 3.0 and 5.0. **Figure 3.37** shows a diffractogram of naked MIONs and recovered MIONs after adsorption. The diffraction peaks of naked MIONs not used for adsorption corresponded to magnetite. Comparing the diffractogram of the naked MIONs to the recovered MIONs after sorption, some additional diffraction peaks corresponding to the metal gold can be seen in the diffractogram of the recovered MIONs at pH 3.0 and pH 5.0.

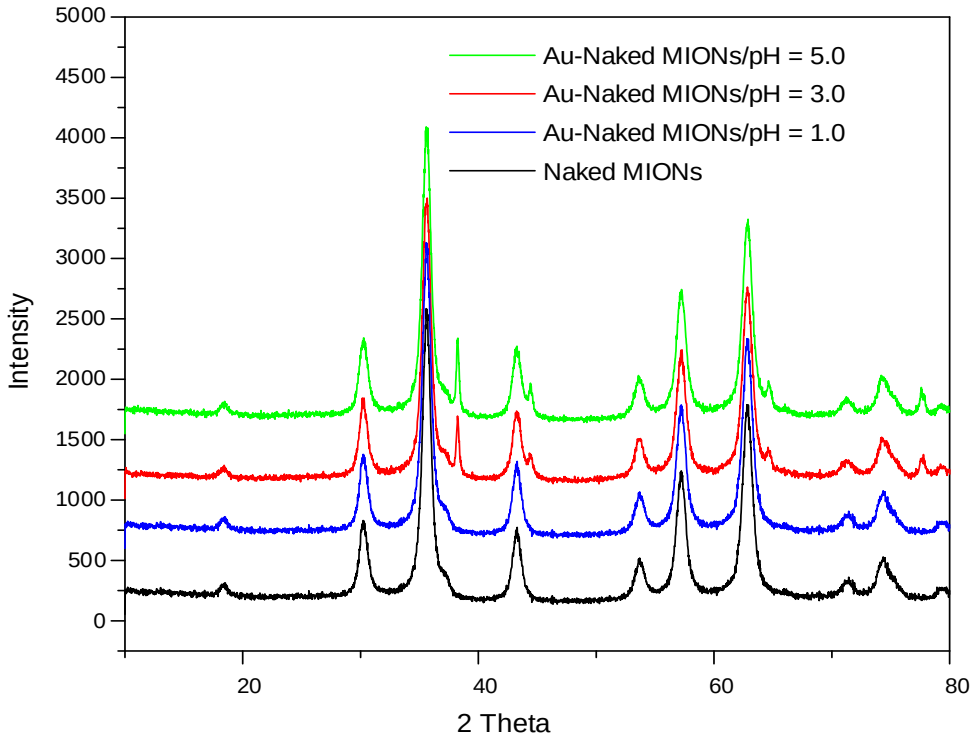

Figure 3.37: Powder XRD analysis of naked MIONs (±30 mg) and Au loaded MIONs subjected to 50 mg/L of Au(III)-Cl solutions at pH 1.0, pH 3.0, and 5.0.

Stellenbosch University https://scholar.sun.ac.za

Magnetite is a semiconductor and hence, the oxidation of magnetite transfers electrons both within the solid phase and across the solid-aqueous interface elucidates that the electrical conductivity in magnetite is responsible for heterogeneous electron transfer between the solid state and redox sensitive species in solution.[149] The presence of metallic gold on naked MIONs shows that the redox reaction of Au(III)-Cl took place on the surface of naked MIONs. Alorro *et al*.[139] used electrochemistry to investigate the adsorption mechanism of Au(III)-Cl species on magnetite. The results of the electrochemical experiments suggested that Au(III)-Cl are reduced to metallic Au on the surface of magnetite. This study also revealed that Fe^{3+} ions released from magnetite into the solution, suppressed the gold uptake at the acidic pH region.

Naked MIONs recovered after sorption of Pd(II)-Cl and Pt(IV)-Cl were characterised by powder XRD. **Figure 3.38** and **Figure 3.39** shows the powder XRD analysis of Pd loaded naked MIONs and Pt loaded naked MIONs respectively. As seen in **Figure 3.38** and **Figure 3.39**, the diffractograms show only diffraction peaks corresponding to naked MIONs. The primary reason for these observations might be due to the limitation of this technique to detect these elements at very low concentration.

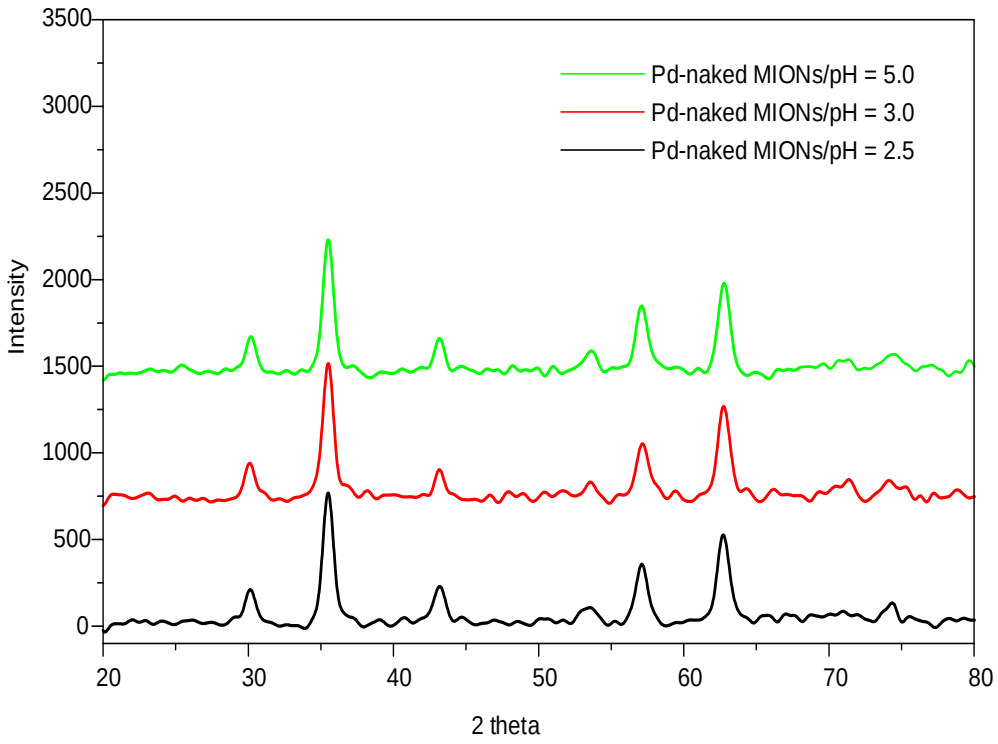

Figure 3.38: Powder XRD analysis of Pd loaded naked MIONs (±90 mg) subjected to 10 mg/L of Pd(II)-Cl solutions at pH 2.5, pH 3.0 and pH 5.0.

Stellenbosch University https://scholar.sun.ac.za

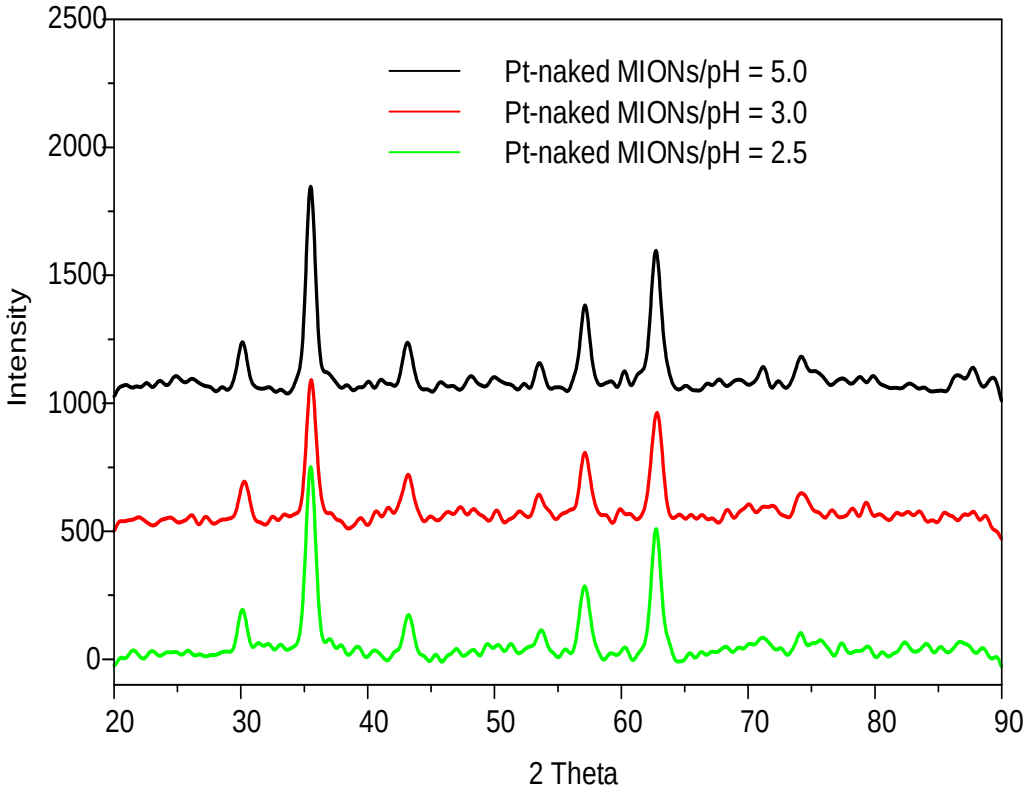

Figure 3.39: Powder XRD analysis of Pt loaded naked MIONs (±90 mg) subjected to 10 mg/L of Pt(IV)-Cl solutions at pH 2.5, pH 3.0 and pH 5.0.

3.5 PROPOSED MECHANISM FOR SORPTION of Au(III), Pd(II) and Pt(IV) COMPLEXES BY NAKED MIONs

The surface of naked MIONs contains hydroxyl groups (≡FeOH) that can either be negatively or positively charged depending on the pH of the solution (**Equation 3.2** and **Equation 3.3)**. The PZC for magnetite has been reported to be in the range of 6.0 to 8.2.[7, 20] At a pH less than the PZC, the ≡Fe-OH_2^+ groups on the surface of the naked MIONs predominate. Thus, under the experimental conditions used (pH 1.0 to pH 5.0) in these studies (solution pH<PZC), the naked MIONs surface is essentially protonated and positively charged. Alorro *et al.*[139] carried out electrochemical sorption studies of Au(III)-Cl by magnetite nanoparticles and proposed a four stage mechanism depicted in **Figure 3.40** and outlined below.

Step 1: Mass transport of $AuCl_4^-$ from the aqueous phase to the magnetite surface.
Step 2: Electrostatic and/or chemical sorption of $AuCl_4^-$ on the surface of magnetite
Step 3: Reduction of $AuCl_4^-$ to elemental gold, Au.

Stellenbosch University https://scholar.sun.ac.za

Step 4: Mass transport of the reacted or soluble species, such as released Cl^-, from the surface of the magnetite to the bulk solution.

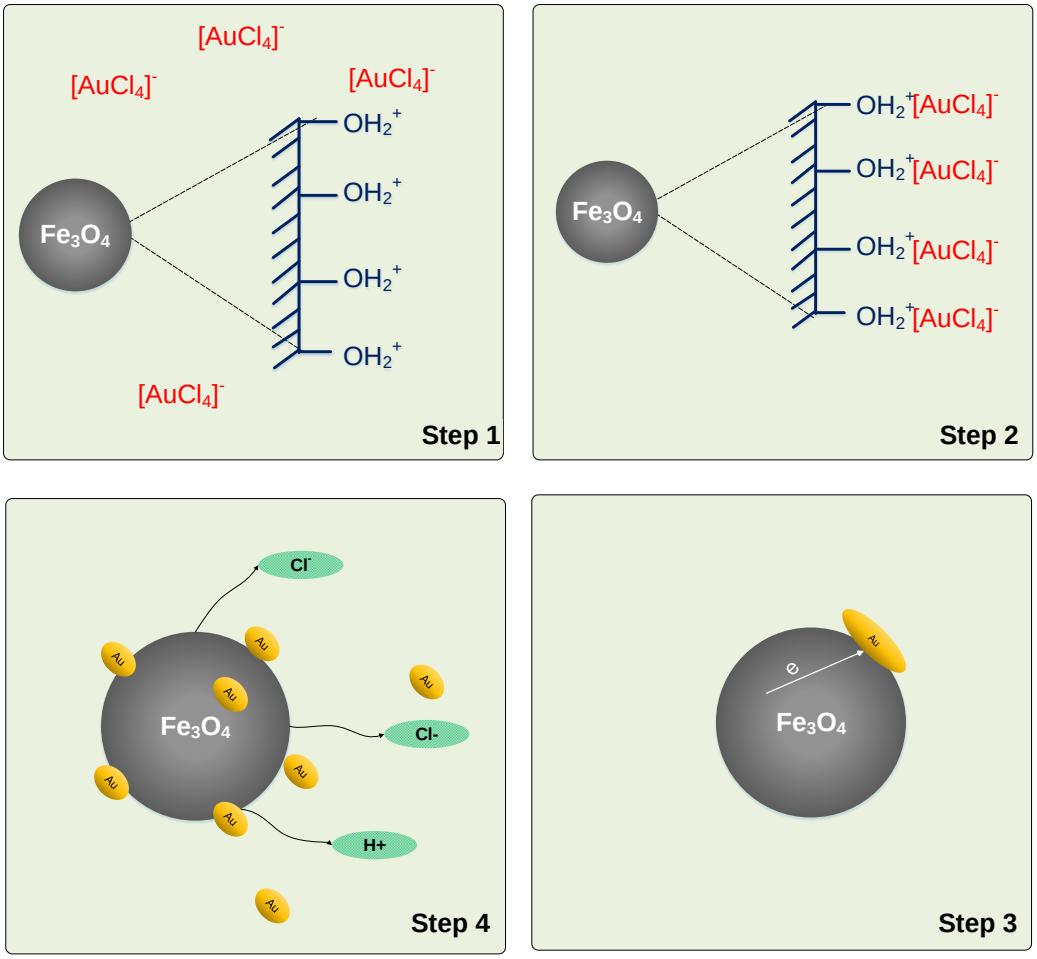

Figure 3.40: Schematic representation of steps involved in sorption of Au(III)-Cl by naked MIONs

In this work, this mechanism is used to explain the sorption of Au(III), Pd(II), and Pt(IV) complexes by naked MIONs. The first two steps (step 1 and 2) of the proposed reaction mechanism are governed by the surface electric charge or zeta potential of magnetite. Under the experimental conditions, naked MIONs were protonated. On the other hand, Au(III)-Cl Pd(II)-Cl, and Pt(IV)-Cl complexes species hydrolyses to form species with the general formula $[AuCl_n(OH)_{4-n}]^-$, $[PdCl_4(H_2O)_{4-n}]^{2-}$, and $[PtCl_n(H_2O)_{6-n}]^{2-}$respectively. For this reason, electrostatic interaction between the $\equiv Fe\text{-}OH_2^+$ and the anionic species of Au(III), Pd(II) and Pt(IV) complexes was favoured. The batch sorption experiments in **Section 3.2.1** for Pd(II) and Pt(IV) complexes were very fast and reached equilibrium within a very short time compared to Au(III) complexes, indicating that an outer-sphere mechanism was dominating the adsorption of Pd(II)-Cl and Pt(IV)-Cl complexes.

Stellenbosch University https://scholar.sun.ac.za

In Step 3, either the adsorbate diffuses inwards and adsorbs to the inner sites of the adsorbent or there is electron transfer between the adsorbent and the adsorbate. Previous studies showed that sorption of Au(III)-Cl and Pt(IV)-Cl complexes by naturally occurring magnetite suggested that these metal complexes are reduced during sorption.[137,147] For reduction of these metal complexes to happen, there has to be a direct interaction between the metal complex and the surface of naked MIONs to facilitate a flow of electrons from magnetite. Free electrons cannot be transferred into aqueous solution; hence, sorption sites are on location where reduction of metal species occur.

Equation 3.17 $$2Fe_3O_4 + H_2O \leftrightarrow 3_\gamma - 3Fe_2O_3 + 2H^+ + 2e^-$$

The solid-state oxidation of Fe^{2+} to Fe^{3+} has a half-cell potential range of -0.34 V to -0.65 V, making the structural Fe a stronger reducing agent than aqueous Fe^{2+} which has an oxidation potential of -0.77 V. Consequently, the standard potentials of Au(III), Pd(II), and Pt(IV) which are 1.0 V, 0.68 V and 0.62 V, respectively, and are higher than the standard potential of Fe^{2+}/Fe^{3+} on the surface of magnetite.

Furthermore, the fact that kinetics data for sorption of Au(III), Pd(II), and Pt(IV) complexes by naked MIONs is best described by the *pseudo*-second-order kinetic model also suggest that there was a transfer of electrons from the adsorbate to adsorbent. Hence, the Fe(II) ions could provide electrons needed for the reduction process of the Au(III), Pd(II), and Pt(IV) complexes. This leads us to believe that Au(III), Pd(II) and Pt(IV) complexes could be removed from solution *via* an electrostatic attraction and subsequently a reductive sorption mechanism. However, this is still subject to further research.

3.6 CONCLUSION

Naked MIONs have proved to be an efficient adsorbent for removal of Au(III), Pd(II), and Pt(IV) complexes from acid aqueous solutions. Time dependent batch experiments were carried out to study the effect of the amount of naked MIONs, initial metal concentration and solution pH. All three parameters played a vital role in sorption of these precious metal complexes. The sorption of Au(III)-Cl and Pd(II)-Cl complexes increases as pH rises from pH 1.0 to pH 5.0. However, the effect of pH in sorption of Pt(IV)-Cl using naked MIONs was not significant.

Stellenbosch University https://scholar.sun.ac.za

The sorption of Pd(II), and Pt(IV) complexes was more rapid that the sorption of Au(III) and reached equilibrium within a very short time. The slow sorption kinetics suggests that the adsorption mechanism does not only involve physical adsorption but chemisorption as well. The kinetics data was tested using *pseudo*-first-order, *pseudo*-second-order kinetics, and the intraparticle diffusion model. The results showed that sorption of Au(III), Pd(II) and Pt(IV) complexes by naked MIONs can be described by the *pseudo*-second-order kinetics model. The equilibrium sorption data for Au(III)-Cl by naked MIONs were fitted into Langmuir and Freundlich, and the model parameters were appropriately evaluated. The sorption of Au(III)-Cl by naked MIONs is best described by Langmuir sorption isotherm model suggesting monolayer coverage of Au(III)-Cl complexes by the naked MIONs.

Again, the UV-Vis spectroscopy results, for sorption of Au(III) and Pd(II) complexes showed the disappearance of the ligand to charge transfer bands (LMCT) bands during sorption process, suggesting the formation of new species. The disappearance of the LMCT was attributed to the formation of Au, Pd and Pt nanoparticles. The sorption of Au(III), Pd(II) and Pt(IV) complexes by naked MIONs from acidic aqueous solution was postulated to be due to electrostatic interaction and reductive sorption. Therefore, the interaction between these metal anionic complexes and the surface of naked MIONs is governed by both inner- and outer-sphere coordination mechanism.

3.7 EXPERIMENTAL

3.7.1 Materials

All the chemicals were purchased either from Merck or Sigma-Aldrich and were used without further purification. Distilled deionized water (Milli-Q, 18 MΩ cm^{-1}) was deoxygenated by bubbling with pure N_2 gas for 30 min prior to use.

3.7.2 Sorption procedure

The aqueous solution of Au(III)-Cl, Pd(II)-Cl, and Pt(IV)-Cl complexes that were used for the sorption studies were prepared from solution of $HAuCl_4$, $PdCl_2$, and H_2PtCl_6 salts, respectively. $HAuCl_4$ and H_2PtCl_6 salts are soluble in water, therefore their stock solutions were prepared by dissolving the required amount of salt in distilled water. However, $PdCl_2$ salt is not soluble in water, hence to prepare its stock solution, it was first digested in few drops of *aqua regia*

Stellenbosch University https://scholar.sun.ac.za

and then diluted to the desired volume using distilled deionised water. The sorption studies were done using batch mode. All the sorption experiments were carried in a Schott bottle. Pre-weight naked MIONs were added to the Schott bottles. This was followed by addition of an aqueous solution containing with the initial metal ion concentration at a desired pH. The pH of the solutions was adjusted with 0.1 M HCl and 0.1 M NaOH before they were added into the Schott bottles. The mixture was shaken on a mechanical shaker for a prescribed period. The nanoparticles were recovered from the solution using a neodymium magnet. The remaining supernatant was transferred into a conical centrifuge tube. To ensure complete removal of the nanoparticles and to avoid blocking the ICP's nebulizer, the samples were centrifuged. Finally, sample matrix matching was done by spiking the samples with HNO_3. The concentration of the samples before and after sorption was determined by ICP-OES.

3.7.3 Characterisation techniques

3.7.3.1 pH meter

The pH measurements were carried out using Crison basic 20 plus pH meters that carries magnetic stirrer and stand for the sensor. The pH meter was used after calibration with Merck buffer solution at pH 4.01, 7.01 and 9.01. The pH of the solution was adjusted using 0.01 M NaOH and 0.01 M HCl.

3.7.3.2 Mechanical shaker

A horizontal mechanical shaker (Labcon, BR-30L) was used for constant agitation of the sample solutions for specified contact times. A strong ferrite magnet with a magnetic field strength of ~ 0.35 T was utilized as an external magnetic field for magnetic separation between the aqueous and solid phases.

3.7.3.3 UV-Vis spectroscopy

A Shimadzu UV-Vis 1800 spectrophotometer equipped with a temperature-controlled sample changer was used to produce UV- Vis spectra. All the UV- Vis analyses were carried out using 10 mm path length quartz cuvettes.

Stellenbosch University https://scholar.sun.ac.za

3.7.3.4 Inductively coupled plasma Optical emission spectroscopy

The concentration of metal ions in the supernatant solutions was determined by Inductively Coupled Plasma Optical Emission Spectroscopy (ICP-OES) with a Liberty Series II spectrometer (Varian, Australia). Standards (traceable to NIST) were matrix matched to acid concentrations of the samples. For calibration, the standard solutions containing a mixture of PGMs and Au, and a single Fe metal ion with the concentration of 1000 mg/L were used. The operation conditions are listed in **Table 3.6**.

Table 3.6: ICP-OES operating conditions used for analysis of Au(III), Pd(II), and Pt(IV)

Parameter	Setting
Generator power	1400 W
View mode	Radial
View height	15 mm
Plasma	Argon
Shear gas	Argon
Gas flow: plasma	15 ml min^{-1}
Gas flow: auxiliary	1.5 ml min^{-1}
Gas flow: nebulizer	1.5 ml min^{-1}
Sample aspiration rate	2 ml min^{-1}
Detector	PMT
Emission line: Au(III)	242.795
Emission line Pd(II)	340.46
Emission line Pt(IV)	214.42
Emission line: Fe	259.94
Rinse delay	15 s
Read	Peak area
Replicate read time	2 s
Number of replicates	3

Stellenbosch University https://scholar.sun.ac.za

CHAPTER 4 SYNTHESIS AND CHARACTERISATION OF MODIFIED MIONs

4.1 INTRODUCTION

This chapter focuses on stabilising or modifying the surface of magnetic iron oxide nanoparticles (MIONs) with various dendrimer micelles and aliphatic carboxylic acids. The modification of the MIONs with the aliphatic carboxylic acids is done using two methods: *in-situ* method whereby the MIONs are prepared in the presence of the stabilising agent and *ex-situ* method which means that MIONs are prepared in the absence of the stabilising agent. The stability of the modified MIONs is evaluated by soaking them aqueous acid solutions of different pH's. Characterisation of the modified MIONs is carryout out using various analytical techniques.

4.1.1 Dendrimer functionalised magnetic iron oxide nanoparticles

In the literature, MIONs have been successfully modified with various synthetic polymers such as poly(acrylamine), poly(ethylene glycol), as well as naturally occurring polymers such as chitosan. Dendrimers are very interesting macromolecules used as templating/stabilising hosts to produce dendrimer stabilised nanoparticles.[155–157] Different strategies are used in the literature to prepare dendrimer modified MIONs and have been summarised in **Figure 4.1**. These include (a) dendrimer-stabilised MIONs (DSNs), (b) dendrimer-assembled MIONs, (c) dendrimer-encapsulated MIONs (DENs), (d) MIONs-cored dendrimers and (e) dendron-assembled MIONs.

The synthesis of dendrimer stabilised MIONs (DSNs) shown in **Figure 4.1**(a) is achieved *via* an *in-situ* method. Meaning that the MIONs are prepared in the presence of dendrimer molecules. Several DSNs, including Au, Cu, Ag and MIONs have been prepared for various applications such as catalyst, MR contrast agents and for environmental remediation. Strable *et al*.[158] proposed the preparation of a highly soluble nanocomposite based on ferromagnetic iron oxide nanoparticles and PAMAM dendrimers. The synthesis was conducted under mild reactions conditions (pH 8.5 and 65 °C). These nanocomposite materials showed high colloidal stability and a narrow size distribution in the size range of 20 – 30 nm.

Figure 4.1(b) shows a scheme representing dendrimer-assembled MIONs (DAN). The major difference between DSNs and DANs is that DANs are produced from preformed nanoparticles,

Stellenbosch University https://scholar.sun.ac.za

while DSNs are prepared using the *in-situ* approach. The driving forces enabling dendrimers to assemble onto the preformed MIONs include covalent bonding, electrostatic interaction, hydrogen bonding or combination of any of these types of interactions.

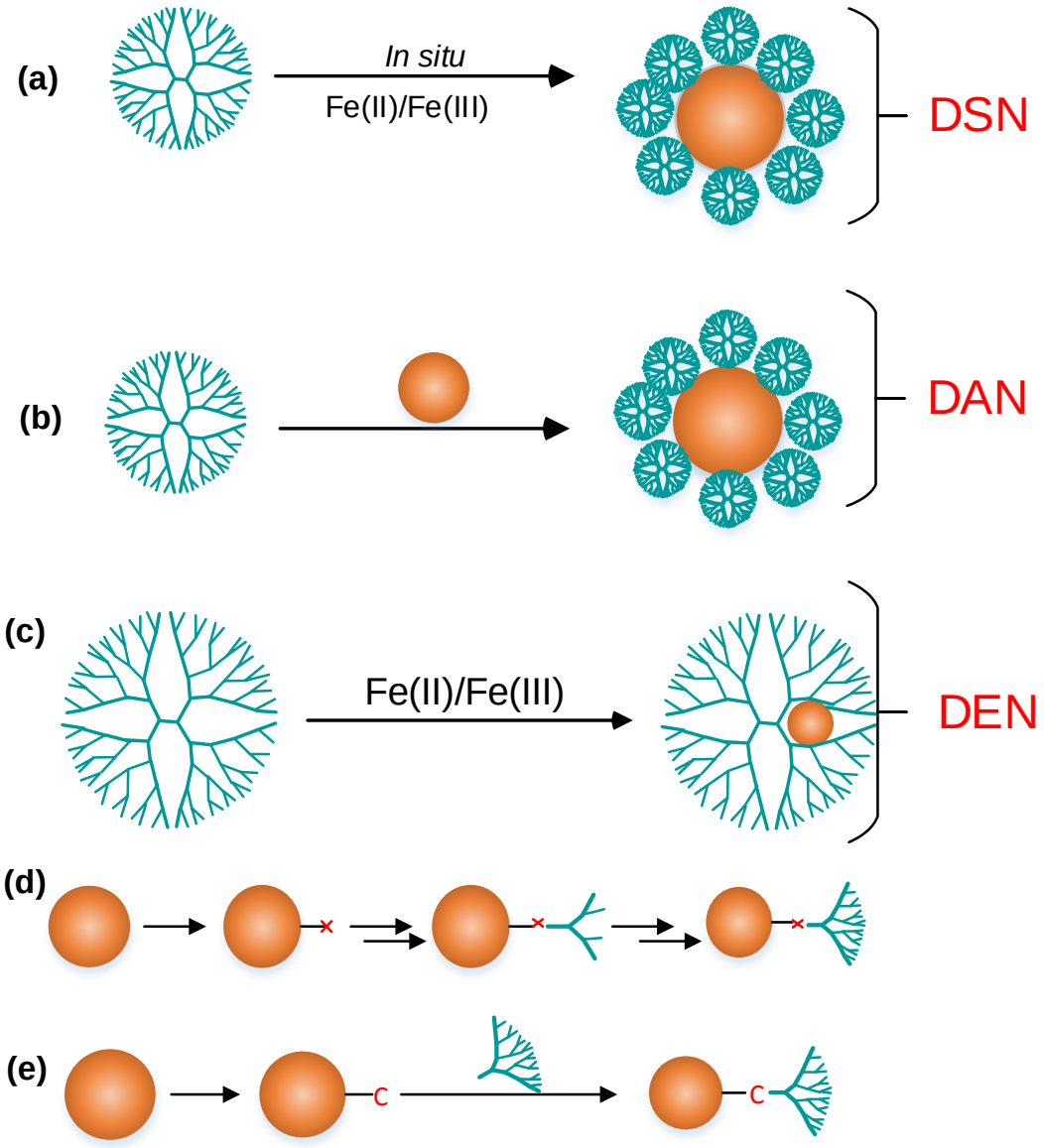

Figure 4.1: Schematic illustration of the formation of dendrimer-based magnetic iron oxide nanoparticles, including dendrimer-stabilised NPs (a); dendrimer-assembled NPS (b); dendrimer-entrapped NPs (c); MION core/dendrimer shells *via* a step-wise divergent synthesis approach (d); and Dendron-grafted MIONs (e).[88]

The cavities found in the interior structure of dendrimers allow for their use as templates to encapsulate different metal nanoparticles. **Figure 4.1**(c) shows a scheme that summarises the preparation of dendrimer encapsulated nanoparticles (DENs). Domracheva *et al.*[159] developed a convenient approach to prepare DEN of MIONs. This was achieved by first complexing

Stellenbosch University https://scholar.sun.ac.za

Fe(III) ions with liquid crystalline G2 poly(propylene imine) (PPI) dendrimers, followed by reducing the Fe(III) complexes to form Fe(II) complexes using diimide (N_2H_2). Then, the Fe(II) complex was reacted with NaOH to produce dendrimer-$Fe(OH)_2$ composite that was subsequently oxidised to form dendrimer encapsulated Fe_2O_3 nanoparticles.

Figure 4.1(d) shows another method used for the synthesis of dendrimer modified MIONs referred to as MION-core dendrimers. This method has been explored using PAMAM dendrimers. The dendrimer is grown on the surface of MIONs by repeated Michael addition reactions with methyl acrylate (MA) and amide formation with ethylenediamine (EDA). The MION-cores are usually silanized through formation of amines on their surface, followed by an alternative reaction with MA and EDA to allow the formation of dendrimers of different generations.

Finally, dendrimer modified MIONs can also be prepared using the approach shown in **Figure 4.1**(e). The MIONs prepared using this approach are called dendron-grafted MIONs. Dendron molecules, also referred to as half dendrimers are used as ligands to form a shell through a direct grafting process, a ligand exchange approach, or hydrophobic interactions. Basly *et al*.[160] obtained dendronized MIONs after simple functionalisation of MIONs coated with oleic acid with two types of PEGylated (PEG) dendrons. The first dendron has a non-functionalised PEG chain as terminal group, whereas the second dendron has PEG chain with one carboxylic group as terminal group. The dendronized MIONs showed a good colloidal stability in water.

4.2 RESULTS AND DISCUSSION

The synthesis of generation 3 dibutane poly(propylene) imine dendrimers (G3 DAB-PPI, **DM_n** where n represents the alkyl chain of the acid chloride, n = 5, 11 and 15) were synthesised by modifying commercially purchased G3 DAB-PPI dendrimers with different alkyl chlorides of different chain lengths.

The MIONs (**S4**) synthesised using the optimised reaction conditions established in **Chapter 2** were stabilised using three approaches:

(1) Stabilisation of MIONs (**S4**) with only dendrimer micelles (**DM_{15})** to give dendrimer micelle stabilised MIONs: (**S4-DM_{15} (a)**, **S4-DM_{15} (b)** and **S4-DM_{15} (c)**) where **a, b, c** represents the mass ratio between **S4** and **DM_{15}** of 1:1, 2:1 and 4:1 respectively.

Stellenbosch University https://scholar.sun.ac.za

(2) Stabilisation of naked MIONs (**S4**) with the aliphatic carboxylic acids of different chain lengths (**C_n**; hexanoic acid (n=5), lauric acid (n=11) and palmitic acid (n=15), whereby n represents the alkyl chain length of the carboxylic acid) forming carboxylic acid stabilised MIONs (**S4-C_5 (a,b,c) S4-C_{11} (a,b,c)** and **S4-C_{15} (a,b,c)** where **a,b,c** are the different ratios of C_n-acid to MIONs.

(3) Then, the **S4-C_n (b,c)**, n = 5, 11 and 15, prepared in (2) above were modified with **DM_n** forming **S4-C_n (b,c)-DM_n**, n = 5, 11 and 15. The alkyl chain groups of carboxylic acid and the dendrimer micelles intercalate with one another as shown in **Figure 4.2**.

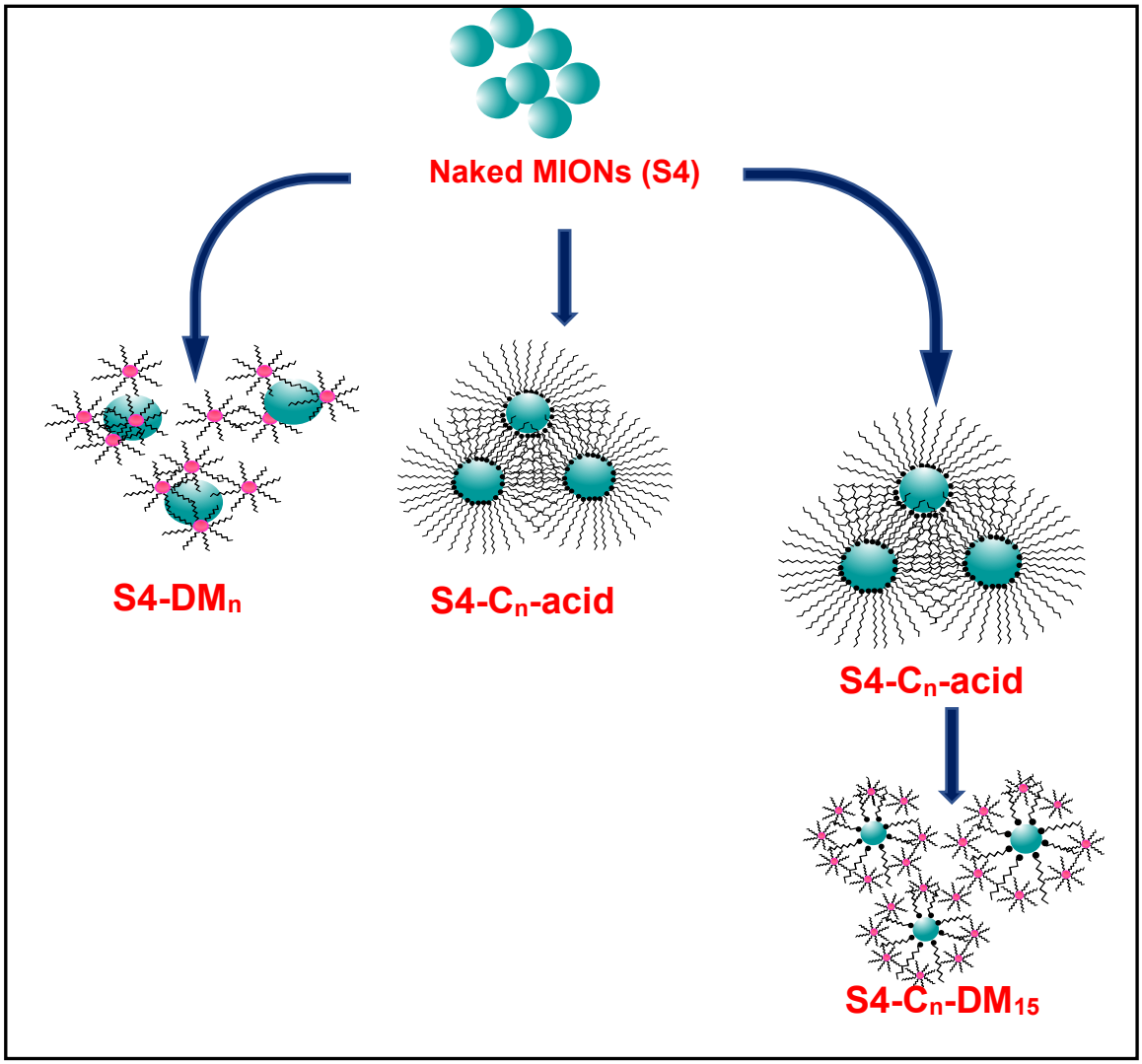

Figure 4.2: Schematic representation of the two methods used to stabilise MIONs with the aliphatic carboxylic acid and dendrimer micelles.

Stellenbosch University https://scholar.sun.ac.za

4.2.1 Synthesis G3 DAB-PPI dendrimer micelles

The synthetic procedure used for the preparation of G3 DAB-PPI dendrimer micelles (**DM_n**) was adapted from the work of Stevelmans *et al.*[161] **DM_n** were synthesised by modifying them with aliphatic acid chlorides of different chain lengths: (hexanoyl chloride (n=5), lauroyl chloride (n=11), and palmitoyl chloride (n=15)). The modification was achieved through the conversion of the primary amines located at the periphery of **DM_n** into their amide analogs. The structural representation of the three **DM_n** (n = 5, 11, 15) is summarised in **Figure 4.3**, the hydrophilic part of the dendrimer is highlighted in pink.

4.2.2 Characterisation of dendrimer micelles

Characterisation of dendrimer micelles (**DM_n**) was carried out using IR, ^{1}H NMR, and ^{13}C NMR analytical techniques and the results are discussed as follows.

4.2.2.1 Infrared spectroscopy

The combined IR spectra of G3 DAB-PPI dendrimers and **DM_n** are shown in **Figure 4.4**. The spectrum of the G3 DAB-PPI dendrimers shows broad absorption bands at 3276 cm^{-1} responsible for ν_s(N-H) vibration stretching frequencies. Other bands observed at 2936 cm^{-1} and 2798 cm^{-1}can be assigned to $\nu_{as}(CH_2)$ and $\nu_s(CH_2)$ stretching vibrations. Moreover, the band at 1568 cm^{-1} and 1464 cm^{-1} are ascribed to vibrations of the primary and secondary amine (ν(N-H) respectively. The figure also shows IR spectra of the dendrimer micelles. The IR spectra of the **DM_n** are characterised by the formation of the newly formed amide bonds (ν_s(NHC=O) vibrations). These bands are observed at 1635 cm^{-}, 1634 cm^{-1} and 1635cm^{-} for **DM_5**, **DM_{11}** and **DM_{15}** respectively. The spectra also exhibited more intense C-H bands ($\nu_{as}(CH_2)$ and $\nu_s(CH_2)$ stretches at 2936 cm^{-1} to 2848 cm^{-1} respectively) due to the increased number of the methylenes groupd at the exterior of the dendrimer than at the core.

Stellenbosch University https://scholar.sun.ac.za

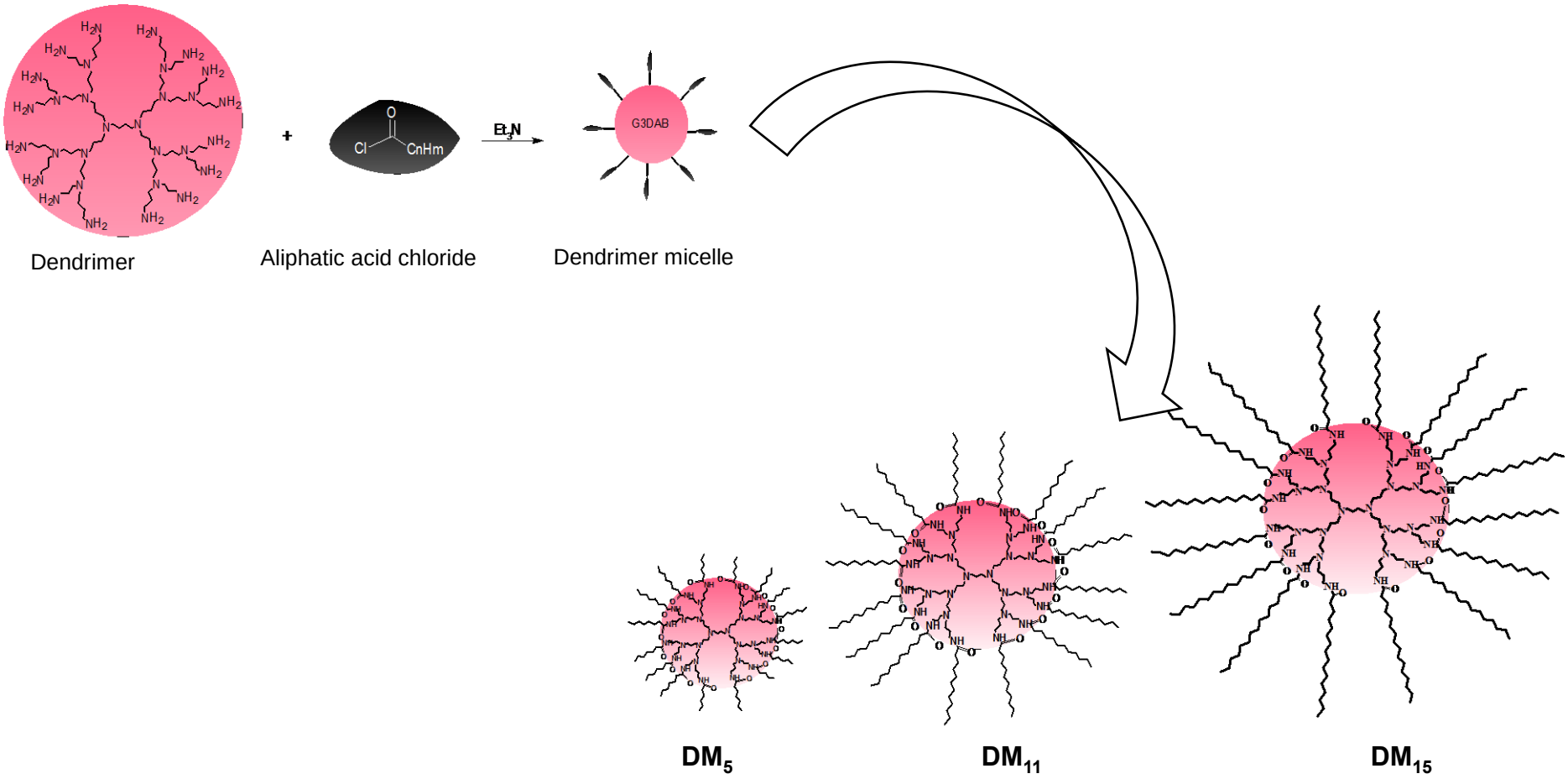

Figure 4.3: Modification of G3 DAB-PPI dendrimers with alkyl chloride of different chain lengths

Stellenbosch University https://scholar.sun.ac.za

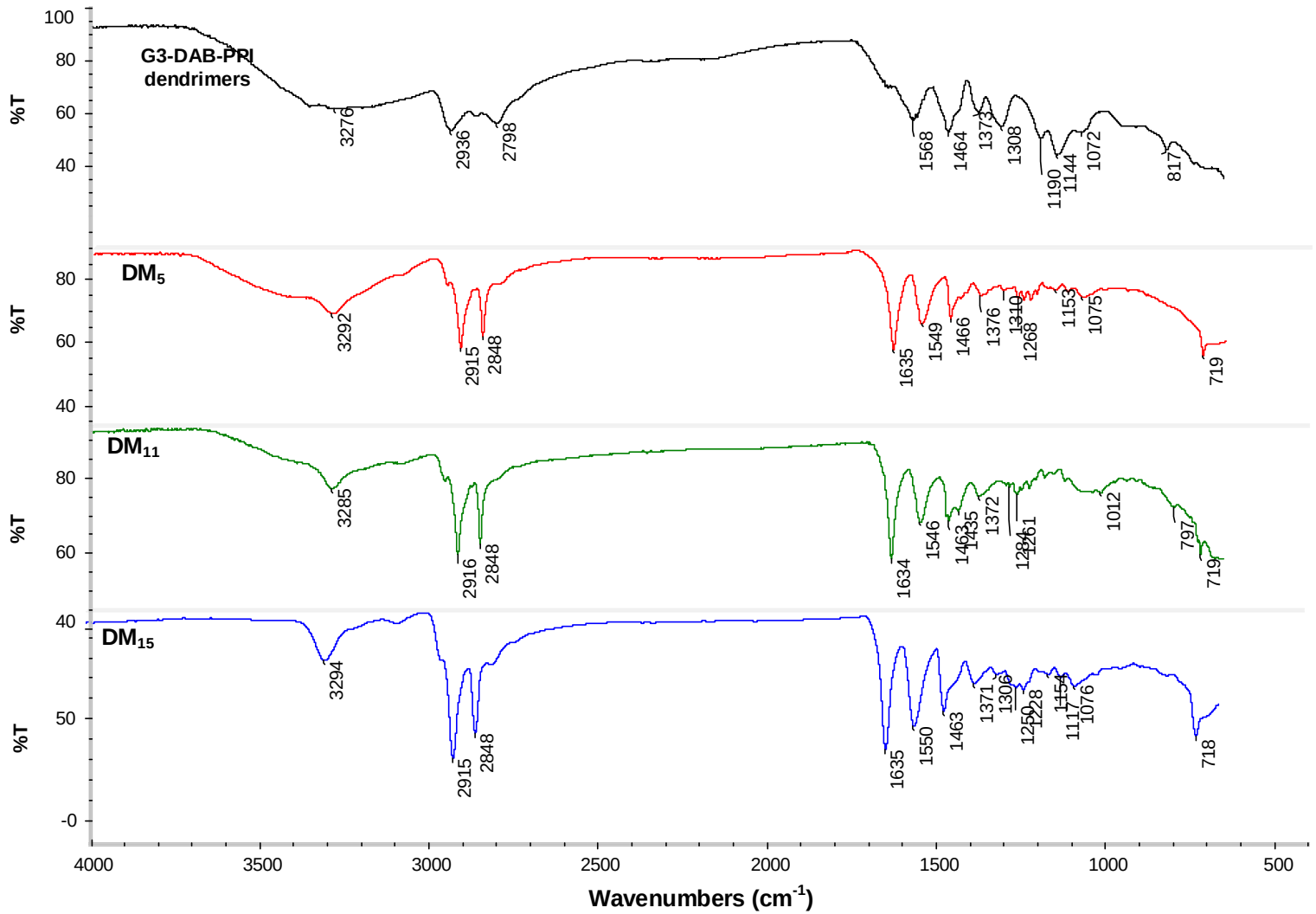

Figure 4.4: A combined FTIR spectra of the G3 DAB-PPI dendrimers and dendrimer micelles **(DM_n**; n = 5, 11 and 15).

Stellenbosch University https://scholar.sun.ac.za

4.2.2.2 ^{1}H and ^{13}C NMR spectroscopy

The ^{1}H NMR and ^{13}C NMR spectroscopy analysis of dendrimer micelles, **DM_n** where n = 5, 11, 15, were performed in d-chloroform at 25 °C. The overlaid ^{1}H NMR spectra of **DM_n** are as shown in **Figure 4.5**. The alkyl chains attached to the periphery of the dendrimer have many methylene groups at the exterior than at the core; these contribute very strong signals in the NMR spectra (signal at 0.81 ppm). The spectrum exhibits five intense $–CH_2$ multiplets around 2.31 ppm, 2.17 ppm, 1.54 ppm and 1.18 ppm. The resonances from the interior methylene's of the dendrimer produce strongly overlapping multiplets due to their similar chemical environments. The signal at 7.07 ppm is ascribed to NHCO of the newly formed amide group. The signals in the range of 3.20 ppm - 3.19 ppm represent the $-CH_2$ groups of the micelle located next to the amide bonds. The broad signal near 1.50 ppm is from the exchangeable $-NH_2$ protons.

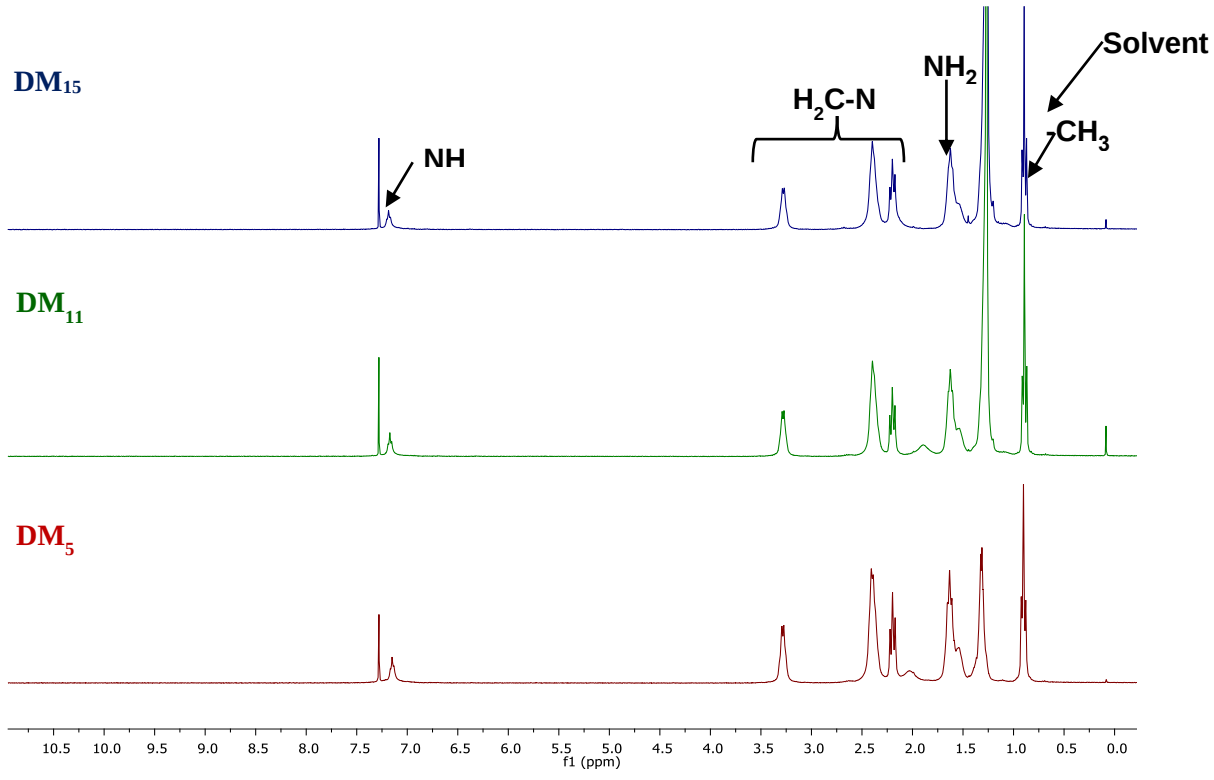

Figure 4.5: ^{1}H NMR spectra of dendrimer micelle (**DM_n**, n = 5, 11, and 15) in d-chloroform at 25±2 °C.

The purity of the dendrimer micelles (**DM_n**) was further confirmed using ^{13}C NMR spectroscopy, (**Figure 4.6**). The signal between 180 ppm – 170 ppm is assigned to the amide group (NHCO). The upfield signals between 60 ppm – 50 ppm are assigned to the C-CO-N

Stellenbosch University https://scholar.sun.ac.za

signal. The C-N signal is observed at 39 ppm, 37 ppm, 38 ppm for **DM_{15}**, **DM_{11}** and **DM_5** respectively. The signal between 35 ppm – 25 ppm are assigned to the C-H groups. The signals between 20 ppm – 10 ppm are assigned to the -CH_3 groups of the alkyl chains of the **DM_n**.

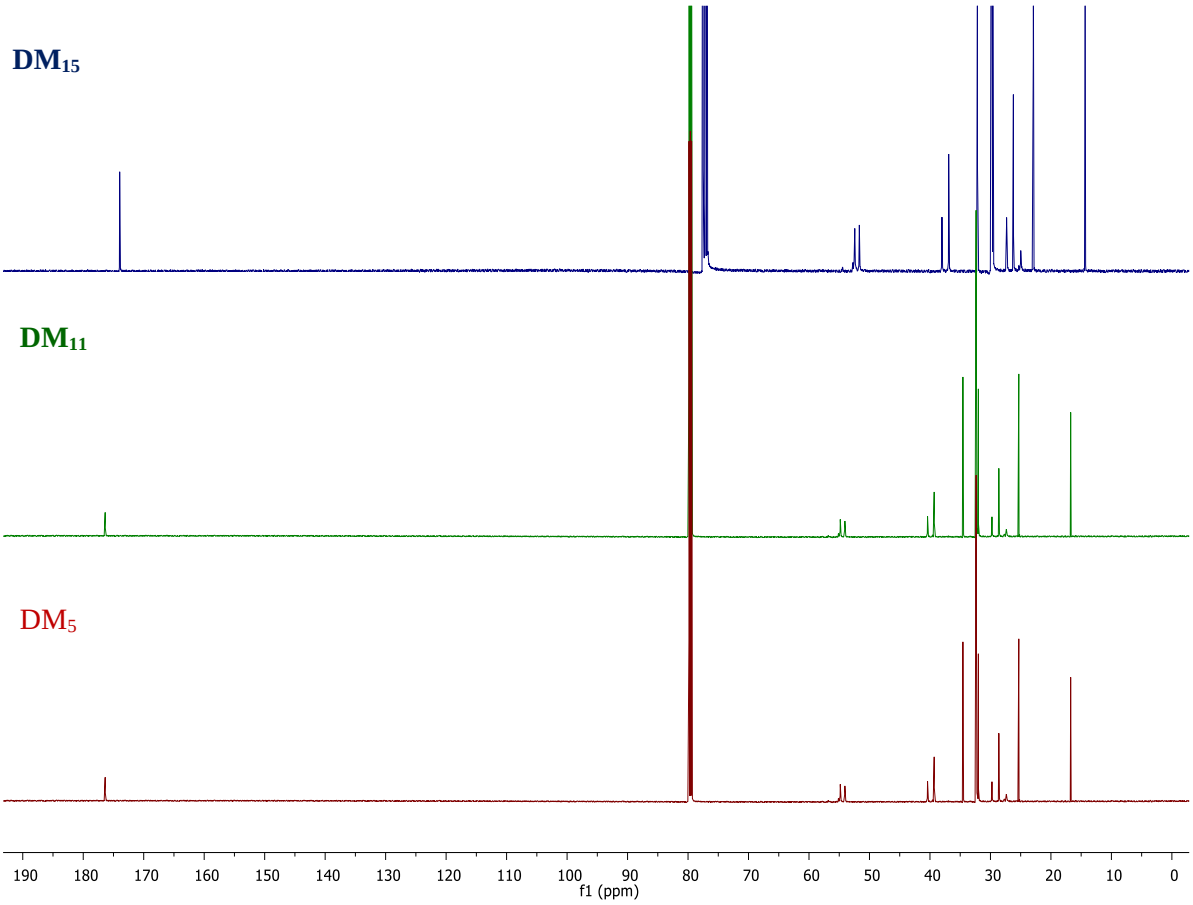

Figure 4.6: ^{13}C NMR spectra of **DM_n** (n = 5, 11, and 15) in d-chloroform at 25±2 °C.

No further characterisation of the **DM_n** was carried out because the IR and NMR results compared well with literature.[161,162]

4.2.3 Synthesis of dendrimer micelle modified MIONs

The naked MIONs (**S4**) were first prepared using the optimised reaction conditions described in **Chapter 2**. Synthesis of dendrimer micelle modified MIONs (**S4-DM_{15} (a, b, c**), whereby **a**, **b**, **c** represents the mass ratio of **S4**:**DM_{15}** of 1:1, 2:1 and 4:1 respectively) was carried out at 60 °C. The reaction conditions were optimised by varying the mass ratio between naked MIONs (**S4**) and **DM_{15}** and the reaction conditions are summarised in **Table 4.1**. The dried naked MIONs (**S4**) were dispersed in degassed chloroform solution containing **DM_{15}** and the

Stellenbosch University https://scholar.sun.ac.za

reaction mixtures were stirred for three days. **Figure 4.7** shows a schematic representation of the steps carried out in the synthesis of **S4-DM$_{15a}$(S10)**, **S4-DM$_{15b}$ (S11)** and **S4-DM$_{15c}$ (S12)**. The full synthesis procedure is given in **Section 4.5.3.4**.

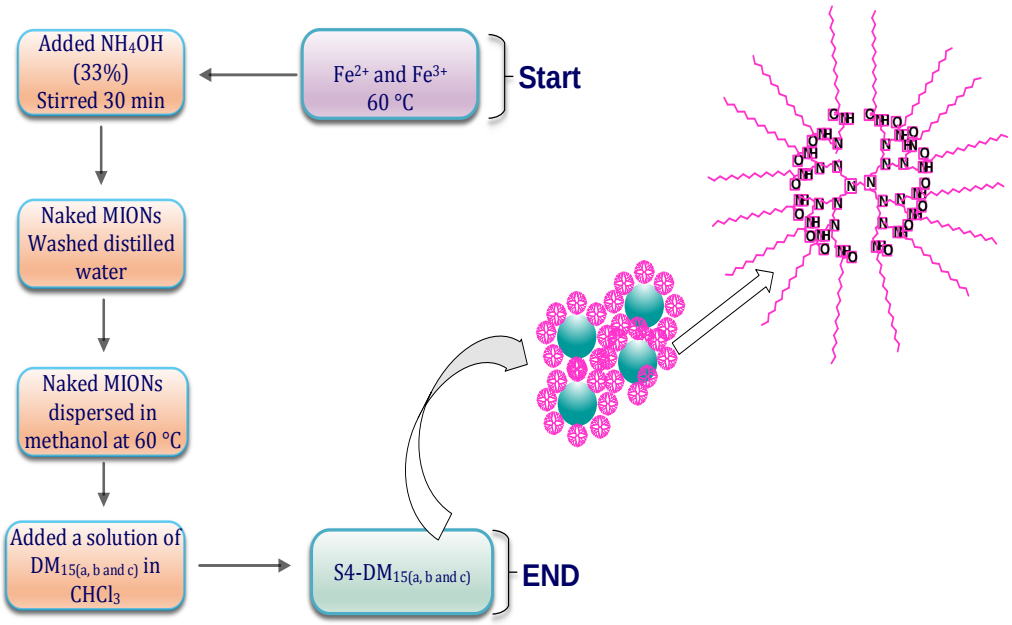

Figure 4.7: Schematic representation for synthesis of dendrimer micelle modified MIONs. The insert shows a representation of **S4-DM$_{15}$(a, b, c)**.

Table 4.1: Conditions used for the synthesis of **DM$_{15}$** stabilised MIONs

Reaction	mass ratio **S4**:**DM$_{15}$**	**S4** mass (mg)	**DM$_{15}$** mass (mg)
S10	1:1	100	100
S11	2:1	100	50
S12	4:1	100	25

4.2.4 Characterisation of dendrimer micelle modified MIONs

Characterisation of dendrimer micelle modified MIONs, **S4-DM$_{15}$ (a, b, c)** was carried out using the following analytical techniques: infrared spectroscopy (FTIR), powder X-ray diffraction (PXRD), and high-resolution transmission electron microscopy (HRTEM).

Stellenbosch University https://scholar.sun.ac.za

4.2.4.1 Infrared spectroscopy

The infrared spectroscopy analysis of **S4-DM$_{15}$ (a, b, c)** was carried out to confirm the presence of **DM$_{15}$** on the surface of the MIONs. **Figure 4.8** shows the overlaid IR spectra of naked MIONs (**S4**), **DM$_{15}$** and **S4-DM$_{15}$(a)**. The broad band observed at 3303 cm^{-1} in the spectrum of the **DM$_{15}$** is due to the O-H and N-H stretching vibrations, while the bands at 3083 cm^{-1}, 2919 cm^{-1}, and 2851 cm^{-1} correspond to $\nu_{as}(CH_2)$ and $\nu_s CH_2$) stretches. The absorption at 1378 cm^{-1} is assigned to the C-N stretching of the amine, while the series of bands from 1245 cm^{-1} to 955 cm^{-1} can be ascribed to the CH_2 wagging and twisting, as well as the C-O-C stretching vibrations.

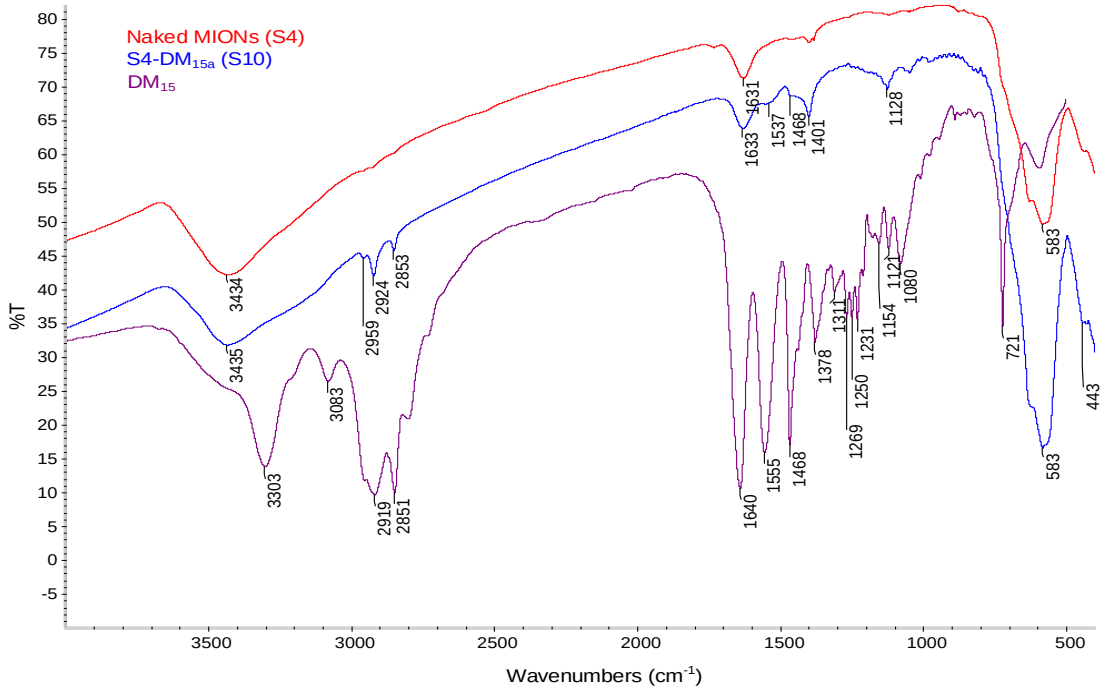

Figure 4.8: Infrared spectra of the naked MIONs, **DM$_{15}$** and **S4-DM$_{15}$(a)**.

As seen in **Figure 4.8** the absorption bands of **DM$_{15}$** are sharp and well resolved. The absorption bands of dendrimer micelle modified MIONs (**S4-DM$_{15}$(a)** are broad with fewer bands. The strong absorption band at around 583 cm^{-1} is assigned to the Fe-O stretching vibrational mode of MIONs. The absorption bands at 1640 cm^{-1} and 1555 cm^{-1} due to the C=O of the amide in the dendrimer micelle shifted to lower wavenumbers in **S4-DM$_{15}$(a)** indicating that the binding nature of the **DM$_{15}$** to the MIONs is through the C-O functionality.[163] The band broadening observed in the spectrum of **S4-DM$_{15}$** compared to the spectrum of neat **DM$_{15}$** indicates chemisorption of dendrimer micelles on the surface of the MIONs. Therefore, **DM$_{15}$**

Stellenbosch University https://scholar.sun.ac.za

formed a bond with the surface of MIONs. Due to the large density of the alkyl chains of the dendrimer micelle, MIONs were believed to have also been stabilised *by* electrostatic interactions of the alkyl chains of the dendrimer micelles. The spectrum of **S4-DM$_{15}$(a)** also shows two bands at 2924 cm^{-1} and 2853cm^{-1} corresponding to $\nu_{as}(CH_2)$ and $\nu_s(CH_2)$ stretches. **Figure 4.9** shows overlaid spectra of all the **S4-DM$_{15}$ (a, b, c)** all the spectra show new absorption bands compared to the spectrum of **S4,** confirming the presence of the **DM$_{15}$** on the surface of **S4**.

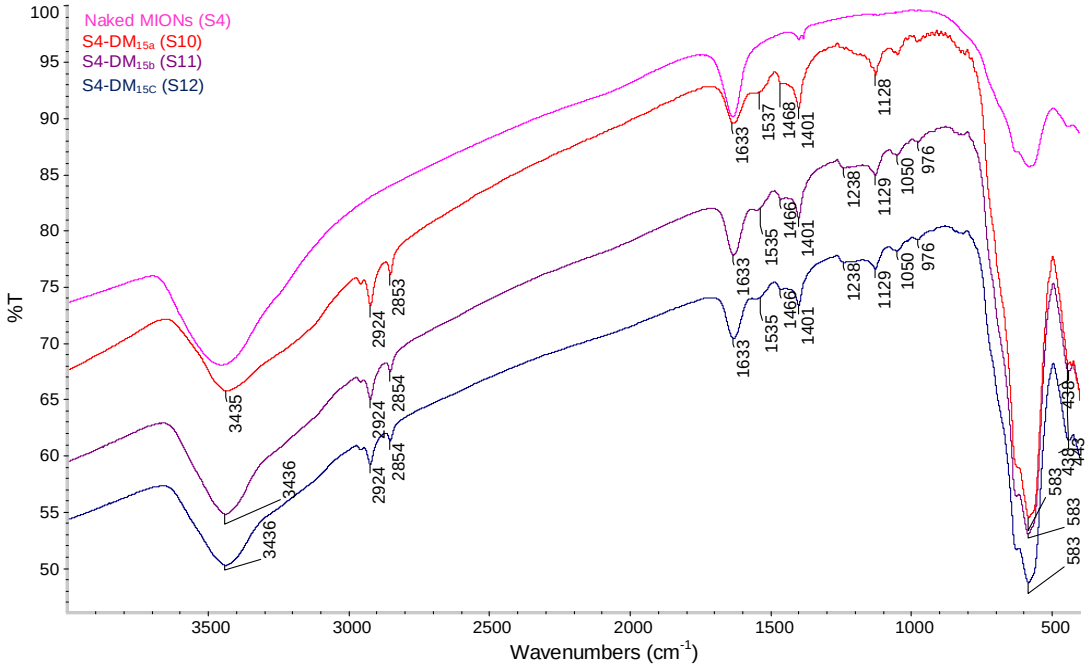

Figure 4.9: Infrared spectra of naked MIONs (**S4**) before and after modification with **DM$_{15}$**.

4.2.4.2 Thermal analysis

Thermal analysis (TGA and DTA) of **S4-DM$_{15}$(a) (S10)**, **S4-DM$_{15}$(b) (S11)** and **S4-DM$_{15}$(c) (S12)** was performed to confirm the presence of (**DM$_{15}$**) on the surface of the MIONs. The TGA and DTA curves of **S10**, **S11** and **S12** are shown in **Figure 4.10** and **Figure 4.11** respectively. For comparison, both figure also show the weight loss profile of **S4** which exhibited one significant weight loss ranging from 50 °C to 100 °C. This weight loss can be assigned to the loss of moisture absorbed by **S4** during sample preparation. However, the thermal decomposition curves of **S4-DM$_{15}$(a) (S10)**, **S4-DM$_{15}$(b)** (**S11)** and **S4-DM$_{15}$(c) (S12)** shows weight loss of temperature ranging from 250 °C to 450 °C. This weight losses can be attributed to the organic break down of **DM$_{15}$** on the surface of the MIONs.

Stellenbosch University https://scholar.sun.ac.za

The corresponding differential thermal analysis (DTA) curves of **S4**, **S10**, **S11** and **S12** shown in **Figure 4.11** clearly indicates the decomposition of **DM_{15}** in the temperature range of 250 °C to 350 °C compared to **S4** which does not show any decomposition in that temperature range. Therefore, TGA and DTA results further confirm the presence of **DM_{15}** on the surface of MIONs, complimenting the IR spectroscopy results discussed in the previous section.

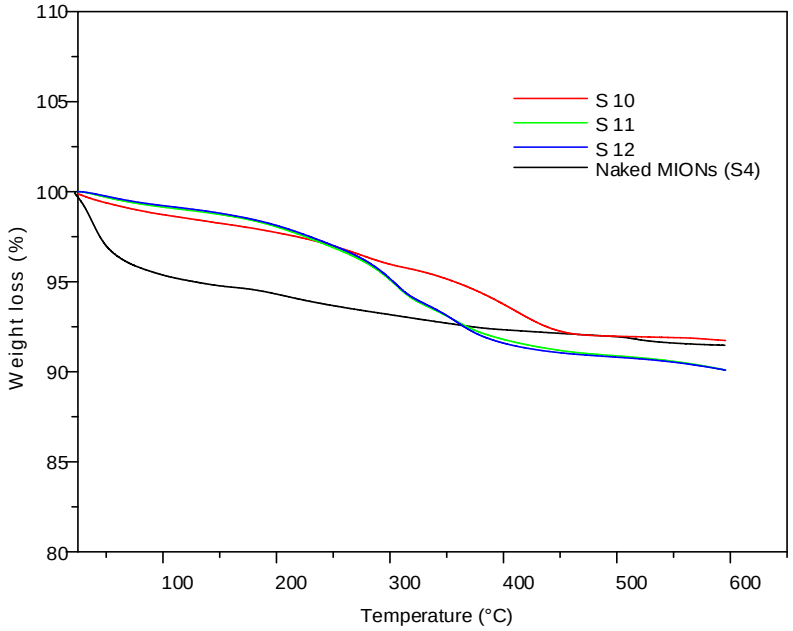

Figure 4.10: TGA curves of **S4**, **S10**, **S11** and **S12**.

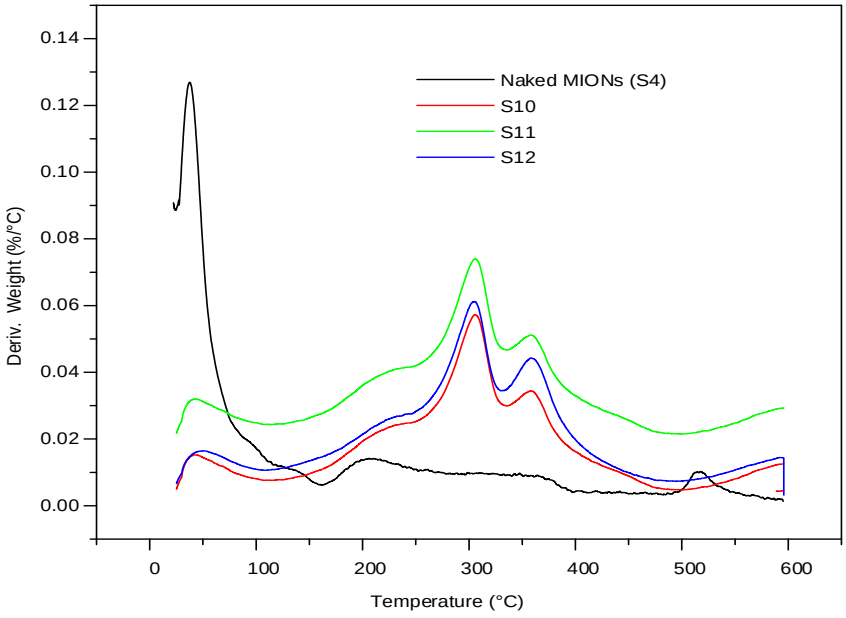

Figure 4.11: DTA curves of **S4**, **S10**, **S11** and **S12**.

Stellenbosch University https://scholar.sun.ac.za

4.2.4.3 Power X-ray diffraction

Powder XRD analysis was used to determine the crystal structure and size of **S4-DM$_{15}$ (a, b, c)**. **Figure 4.12** shows overlaid diffractograms of **S4**, **S10**, **S11** and **S12**. As seen in the figure, all the samples exhibited diffraction peaks with miller indices (*hkl*) values of (220), (311), (400), (422), (511) and (440). These diffraction peaks matched with the peaks of the standard magnetite sample, as per JCPDS cards No. 00-016-0653. The absence of other diffraction peaks, not corresponding to magnetite is an indication that all the samples were single phase with spine cubic structure. Hence, MIONs maintained their crystal structure after their functionalisation with **DM$_{15}$**.[164,165]

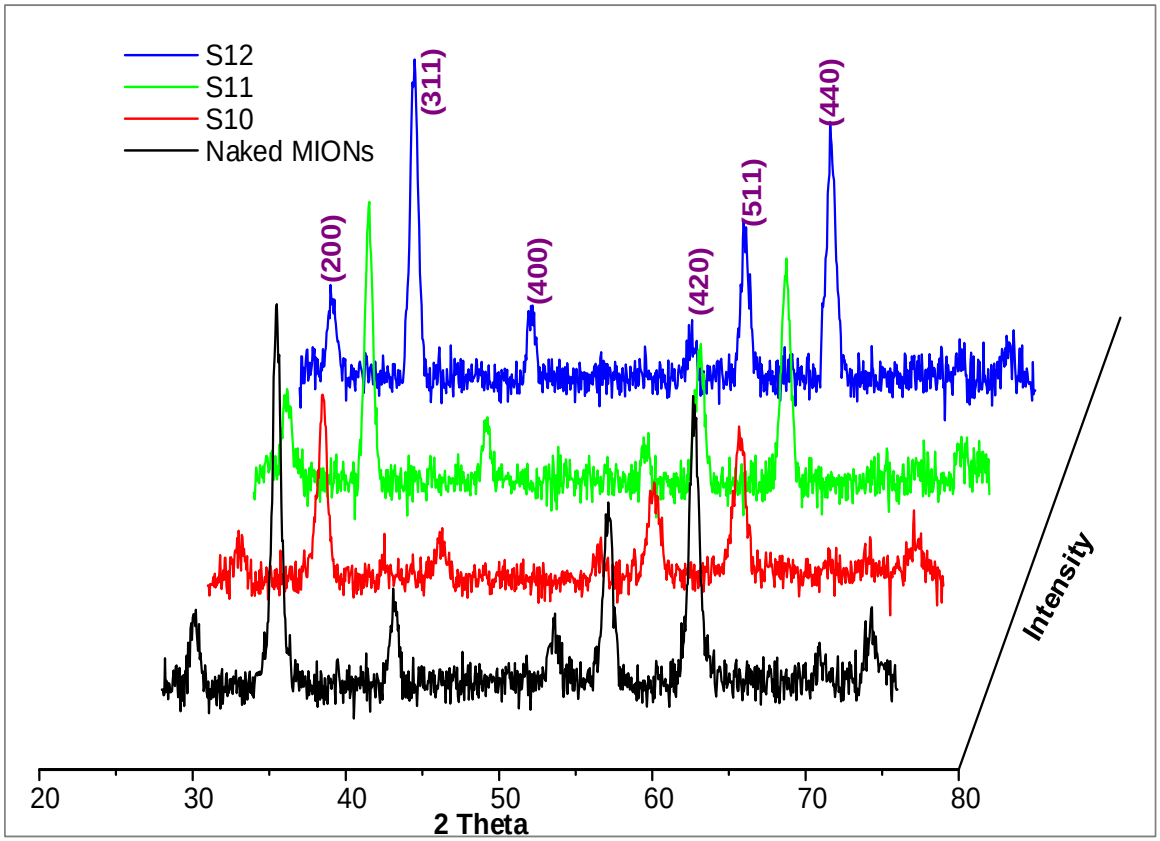

Figure 4.12: Powder XRD of naked MIONs (**S4**), **S10**, **S11** and **S12**.

The mean crystallite sizes (<D>, Å) of **S10**, **S11** and **S12** were calculated using the Debye-Scherrer equation (**Equation 4.1**). In the literature, the particle size of MIONs is calculated using the peak indexed at (311) as is more defined than other peaks and therefore believed to give a more reliable particle size. However, in this work, the particle size was determined using

Stellenbosch University https://scholar.sun.ac.za

the full width at half maximum height (FWMH) of three independent diffraction peaks indexed at (311), (511), and (440) as these diffractions peaks are also well resolved.

Equation 4.1:

$$D_{hkl} = \frac{k\lambda}{\beta\cos\theta}$$

Where D_{hkl} is the crystallite size (nm), λ is the radiation wavelength, β is the full width at half maximum height (FWHM), θ is the Bragg angle (degrees).

The particle sizes of **S10**, **S11** and **S12** determined using Scherrer equation are summarised in **Table 4.2**. Modification of naked MIONs (**S4**) with the **DM_{15}** resulted into a slight increase in particle size. This can be attributed to the high temperature used during the preparation of dendrimer micelle modified MIONs. The average particle sizes calculated using the FWMH of these independent peaks are very close to the particle size determined by using the (311) peak.

Table 4.2: Particle size of **S4**, **S10**, **S11** and **S12** determined from PXRD diffraction data using Scherrer equation

Sample	Particle size (nm)			PXRD mean particle size (nm)
	(311)	(511)	(440)	
Naked MIONs (S4)	11.40	11.47	11.26	11.38±0.11
S4-DM_{15}(a) (S10)	11.98	9.63	10.44	10.68±1.19
S4-DM_{15}(b) (S11)	13.75	12.42	12.95	13.04±0.67
S4-DM_{15}(c) (S12)	13.49	13.19	12.97	13.22±0.26

4.2.4.4 High resolution transmission electron microscopy

High resolution transmission electron microscopy (HRTEM) was used to determine the mean particle size and shape of **S4-DM_{15}(a) (S10)**, **S4-DM_{15}(b) (S11)**, and **S4-DM_{15}(c) (S12)**. The average sizes of **S4-DM_{15} (a, b, c)** were determined by counting more than 250 particles with ImageJ software. HRTEM images of **S10**, **S11** and **S12** and their corresponding particle size histograms are as shown in **Figure 2.9**. All the three images show that the MIONs were mostly spherical. The MIONs are also agglomerated and polydispered. Comparing the HRTEM images of naked MIONs (**S4** in **Figure 2.9**) with the images of the modified MIONs (**S10**, **S11** and **S12)**, the shape of the particles is the same.

Stellenbosch University https://scholar.sun.ac.za

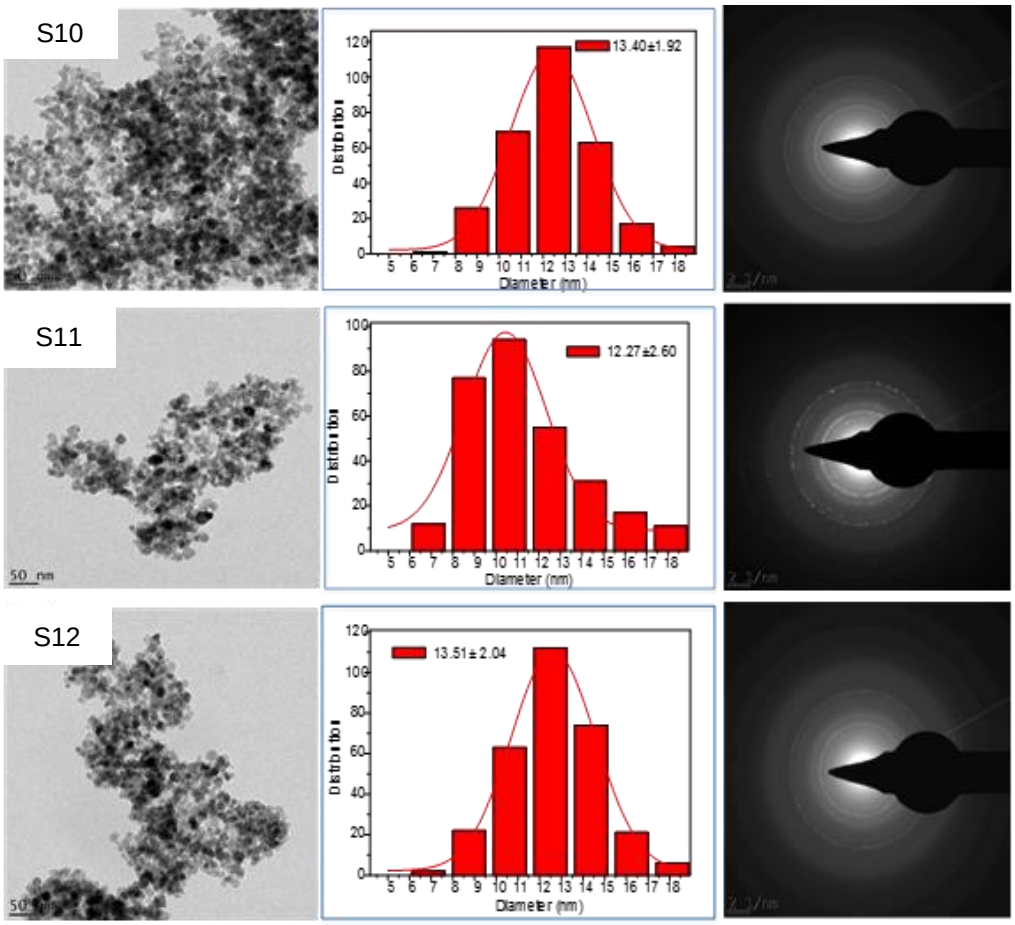

Figure 4.13: HRTEM images (scale = 50 nm), particle size histograms and SAED of **S10**, **S11** and **S12**.

The average particle sizes of **S10**, **S11** and **S12** are as follows: 13.40±1.92, 12.27±2.60, and 13.51±2.04 respectively. Comparing the average particles of **S4** which is 11.60±1.70 nm with MIONs modified with **DM$_{15}$** (**S10**, **S11** and **S12)**, the particles slightly increased in size and this is due to the high temperature of 60 °C used during the modification. The nanoparticles tend to easily interact with each other hence, agglomeration is likely to occur. Therefore, a small increase in the average size of the particle demonstrated the efficacy of **DM$_{15}$** in preventing the agglomeration of the particles. However, using different amount of **DM$_{15}$** did not have a significant effect in particle size. **Figure 4.13** also shows the selected area electron diffraction patterns (SAED) of **S10**, **S11** and **S12** shows the d-spacing's corresponding to the respective miller indices (*hkl*) (111), (220), (311), (400), (422), and (440) of a pure magnetite. These diffraction patterns agree with the PXRD results that the crystal structure of MIONs was not change during their modification.

Stellenbosch University https://scholar.sun.ac.za

The average particle sizes of **S4**, **S10**, **S11** and **S12** determined using HRTEM analysis were compared to the average particle sizes determined from the Scherrer equation. **Table 4.3** shows the average particle sizes of naked MIONs and the **S4-DM$_{15}$ (a, b, c)** determined with HRTEM and PXRD analysis. As seen in **Table 4.3**, the results obtained from both techniques shows a good correlation.

Table 4.3: Particle size of **S4-DM$_{15}$ (a, b, c)** determined from Scherrer equation and HRTEM analysis.

Sample	PXRD mean particle size (nm)	HRTEM mean particle size (nm)
Naked MIONs(S4)	11.38±0.11	11.60±1.70
S4-DM$_{15}$ (a) (S10)	10.68±1.19	13.40±1.92
S4-DM$_{1}$ (b) (S11)	13.04±0.67	12.27±2.60
S4-DM$_{15}$ (c) (S12)	13.22±0.26	13.51±2.04

4.2.5 Synthesis of carboxylic acid functionalised MIONs

Several reports in the literature proved that carboxylic acids coordinate to the surface of MIONs and effective stabilise MIONs in solution.[166,167] Therefore, the second modification of MIONs was carried out using, aliphatic carboxylic acids (**C$_n$-acid**): (hexanoic acid (**C$_5$-acid**), lauric acid (**C$_{11}$-acid**) and palmitic acid (**C$_{15}$-acid**). Schematic representation of MION stabilised with aliphatic carboxylic acid is as shown **Figure 4.14**. The resultant MIONs were referred to as carboxylic acid stabilised MIONs (**S4-C$_n$ (a**, **b**, **c))**, the letter **a**, **b**, and **c** represent the mass ratio between the naked MION and the carboxylic acids**)** (**Table 4.4**.). For simplicity, the **S4-C$_n$ (a**, **b**, **c)** will be used interchangeably with **S13, S14, S15, S16, S17, S18, S19, S20** and **S21**.

Synthesis of **S4-C$_n$(a**, **b**, **c)** was performed using first the *ex-situ* and then *in-situ* method as presented in **Figure 4.15**. However, the MIONs produced by the *ex-situ* method formed a glue-like substance (did not suspend in solution) while MIONs prepared by the *in-situ* method formed a suspension in the solution. Hence, all the **S4-C$_n$(a**, **b**, **c)** were prepared using the *in-situ* method.

Stellenbosch University https://scholar.sun.ac.za

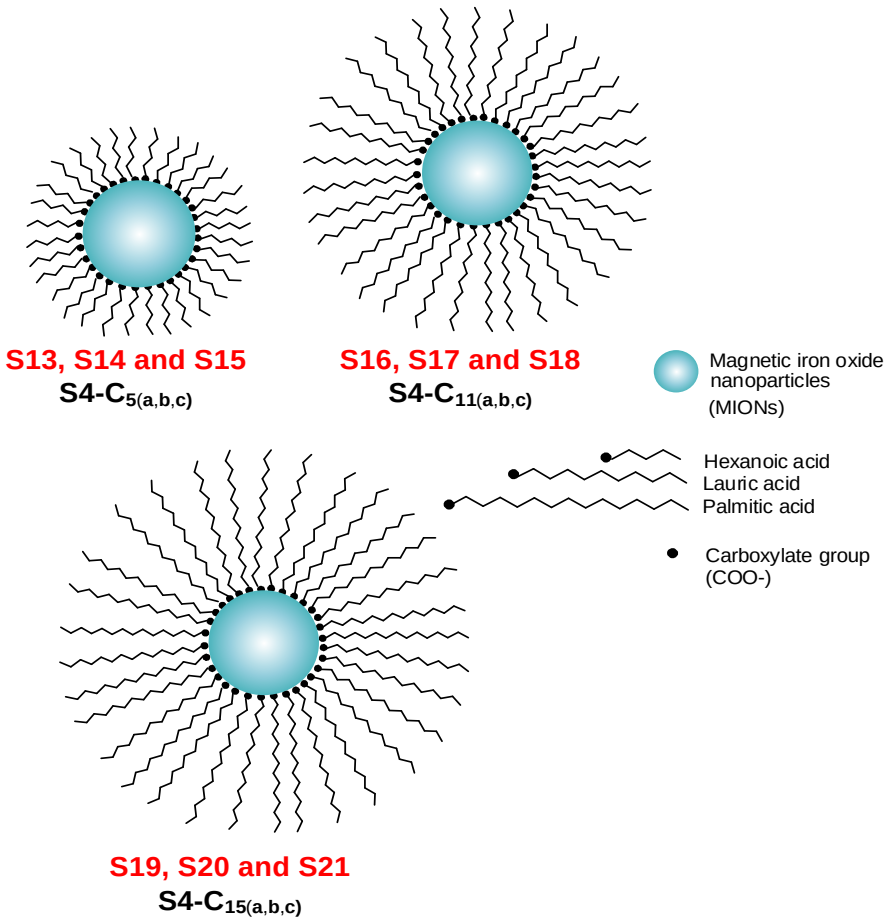

Figure 4.14: Schematic representation of aliphatic carboxylic acid modified MIONs.

Table 4.4: Conditions used for synthesis of aliphatic carboxylic acid stabilised MIONs, **S4-C$_n$ (a, b, c)**

Sample	mass ratio MIONs (**S4**):C$_n$-acid	mass (g) naked MIONs (S4)	mass (g) C$_n$-acid (n = 5, 11, 15)
S4-C$_5$(a) (S13)	4:1	0.966	0.242
S4-C$_5$(b) (S14)	2:1	0.966	0.483
S4-C$_5$(c) (S15)	1:1	0.966	0.966
S4-C$_{11}$(a) (S16)	4:1	0.966	0.242
S4-C$_{11}$(b) (S17)	2:1	0.966	0.483
S4-C$_{11}$(c) (S18)	1:1	0.966	0.966
S4-C$_{15}$(a) (S19)	4:1	0.966	0.242
S4-C$_{15}$(b) (S20)	2:1	0.966	0.483
S4-C$_{15}$(c) (S21)	1:1	0.966	0.966

Stellenbosch University https://scholar.sun.ac.za

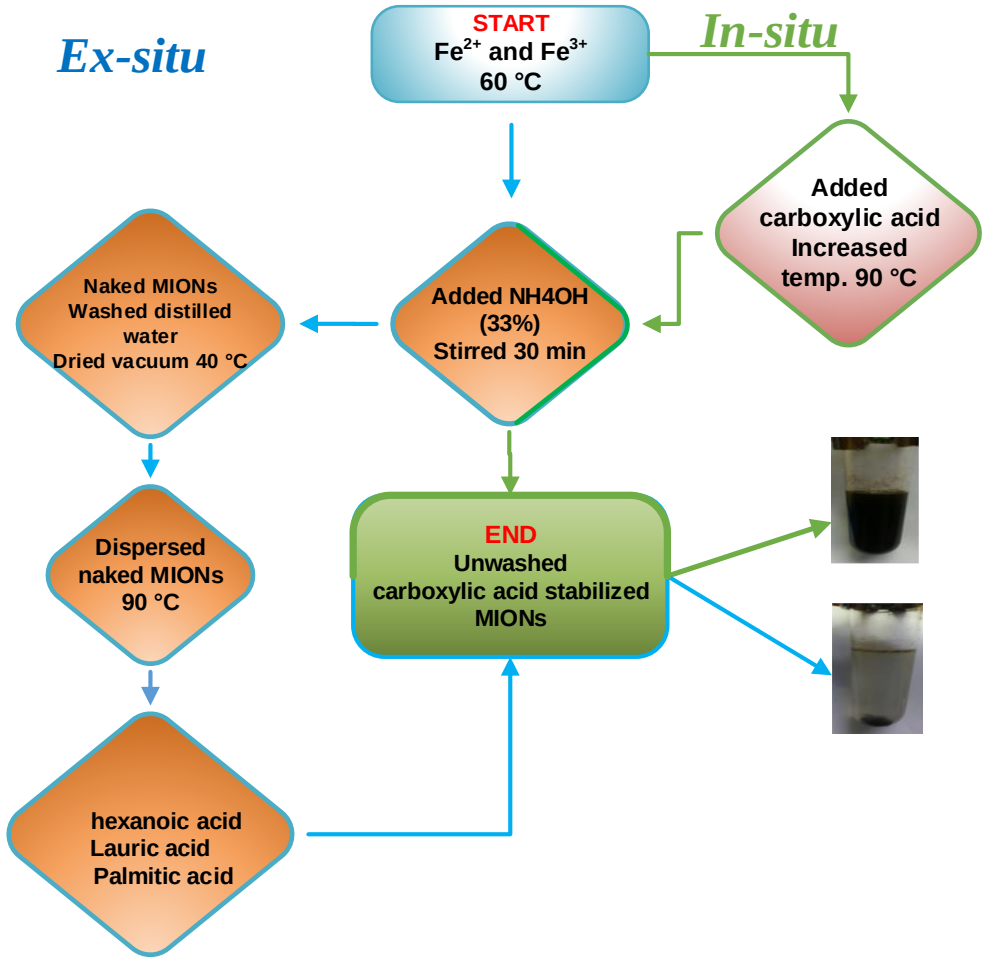

Figure 4.15: Basic flow chart summarising the synthesis of aliphatic carboxylic acid stabilised MIONs (**S4-C$_n$** (**a**, **b**, **c**)). As shown in the figure, the MIONs synthesised using the *in-situ* method "suspected" in the solution. However, the MIONs prepared by means of the *ex-situ* method did not form a suspension but rather formed a glue-like substance that adhered at the bottom of the Schleck tube.

Upon cooling, **S4-C$_n$**(**a**, **b**, **c**) behaved differently (**Figure 4.16**). All **S4-C$_5$**(**a**, **b**, **c**) (**S13**, **S14** and **S15**) precipitated out of solution and settled at the bottom of the Schlenk tube. In the case of **S4-C$_{11}$**(**a**, **b**, **c**) **(S16, S17 and S18)**, only **S16** prepared with the lowest concentration of lauric acid precipitated out of solution. The **S17** and **S18** remained suspended in the solution even after being exposed to the magnet for more than 20 min. As for **S4-C$_{15}$** (**a**, **b**, **c**) **(S19, S20** and **S21)**, **S19** and **S20** precipitated out of solution while **S21** remained suspended in the solution even after they were subjected to the magnetic field.

Stellenbosch University https://scholar.sun.ac.za

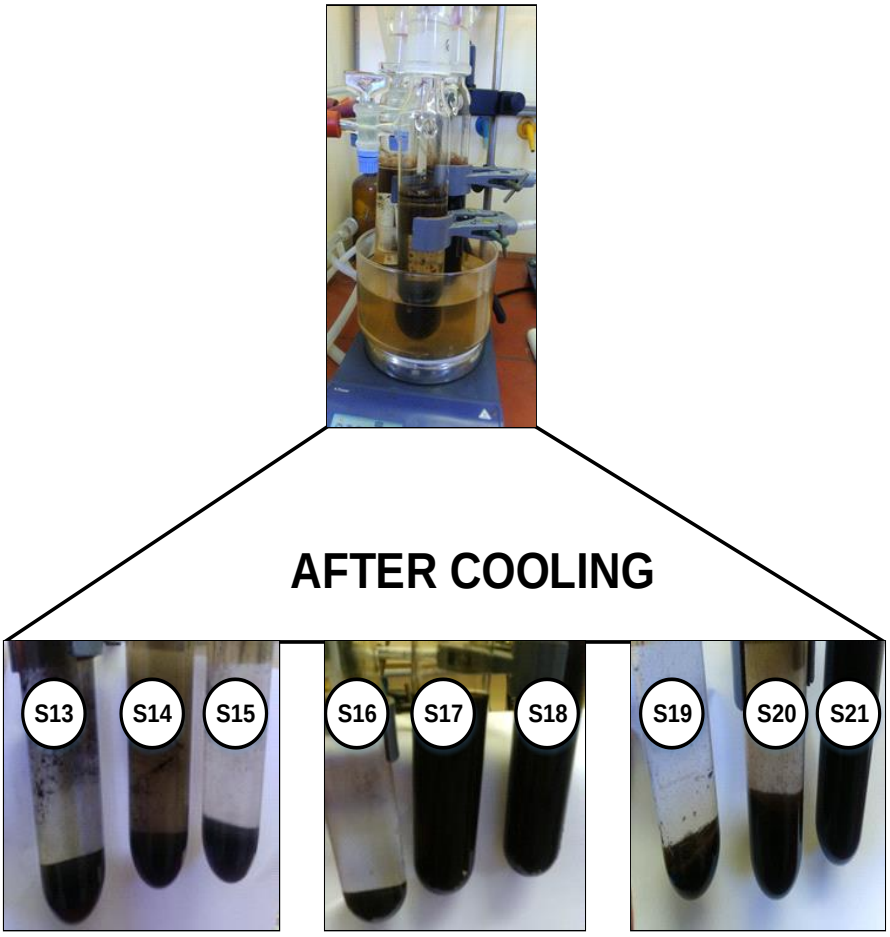

Figure 4.16: Shows that the **S4-C$_n$(a, b, c)** behave differently when cooled after the reaction. The (**S13, S14**, and **S15**) were pulled by gravity and settle at the bottom of the Schlenk tube. For **S4-C$_{11}$(a, b, c)** only **S16** precipitated out of solution and for **S4-C$_{15}$ (a, b, c)**, **S19** and **S2**0 precipitated out of the solution.

It worth mentioning that naked MIONs in solution are easily pulled by gravity and settle at the bottom of the Schlenk tube within few seconds. Therefore, formation of the stable suspensions by **S4-C$_{11}$(a, b, c)** and **S4-C$_{15}$(a, b, c)** was a clear indication that C$_{11}$-acid and C$_{15}$-acid successfully functionalised MIONs. Again, increasing the concentration of C$_{11}$-acid and C$_{15}$-acid increased the stability of the suspension as S18 and S21 MIONs could not be pulled out of the solution by the magnet. However, the suspended MIONs were later precipitated out by adding ammonium to the suspensions. The precipitated MIONs were then treated like the **S4-C$_n$(a, b, c)** that easily precipitated out of the solution. The detailed work-up procedure has been outlined in **Subsection 4.5.3**.

Stellenbosch University https://scholar.sun.ac.za

4.2.6 Characterisation of long chain carboxylic acid functionalised MIONs

Characterisation of **S4-C_n(a, b, c)** was carried out using the following analytical techniques: infrared spectroscopy (IR), thermogravimetric analysis (TGA), derivative thermal analysis (DTA), powder X-ray diffraction (PXRD), high-resolution transmission electron microscopy (HRTEM) and selected area electron diffraction (SAED).

4.2.6.1 Infrared spectroscopy

The IR spectra of the aliphatic carboxylic acids (**C_n-acids**) were contrasted with the IR spectra of **S4-C_n(a, b, c) (S13** to **S21)**. **Figure 4.17** shows overlaid infrared spectra of **C_5**-acids, **C_{11}**-acids and **C_{15}**-acids. The spectrum of **C_5**-acid exhibited absorption bands: 2927 cm^{-1}, 2931 cm^{-1} and 2861 cm^{-1} consistent with the $\nu_{as}(CH_2)$ and $\nu_s(CH_2)$ stretches. The intense band at 1703 cm^{-1}, corresponds to C=O stretches of **C_5-acid**. The spectra of **C_{11}-acid** and **C_{15}-acid** exhibited similar absorption bands with their C=O stretches observed at 1680 cm^{-1} and 1695 cm^{-1} respectively. Moreover, the $\nu_{as}(CH_2)$ and $\nu_s(CH_2)$ stretches are C_{11}-acid can be seen at 2911 cm^{-1} and 2842 cm^{-1} respectively. The $\nu_{as}(CH_2)$ and $\nu_s(CH_2)$ stretches of C_{15}-acid can be seen at 2914 cm^{-1} and 2847 cm^{-1} respectively.

The following **S4-C_n(a, b, c)** (**S15**, **S18** and **S21**) were characterised using IR spectroscopy. **Figure 4.18** Shows infrared spectra of unwashed **S15**, **S18** and **S21**. The spectra of **S18** and **S21** show a strong band at 1403 cm^{-1} and 1405 cm^{-1} respectively corresponding to C_m-$H_{23(25)}$-$COO^-NH_4^+$ of the secondary surfactant layer or free acid.[168] The absorption bands at 1112 cm^{-1} and 1100 cm^{-1} for **S18** and **S21** respectively corresponds to the vibrations of O-H bond and out-of-plane vibrations of C-H bands of CH_2-OH groups.[169] The spectrum of **S15** shows weaker bands showing that only a small fraction of the surfactant was found on the surface of MIONs.

Stellenbosch University https://scholar.sun.ac.za

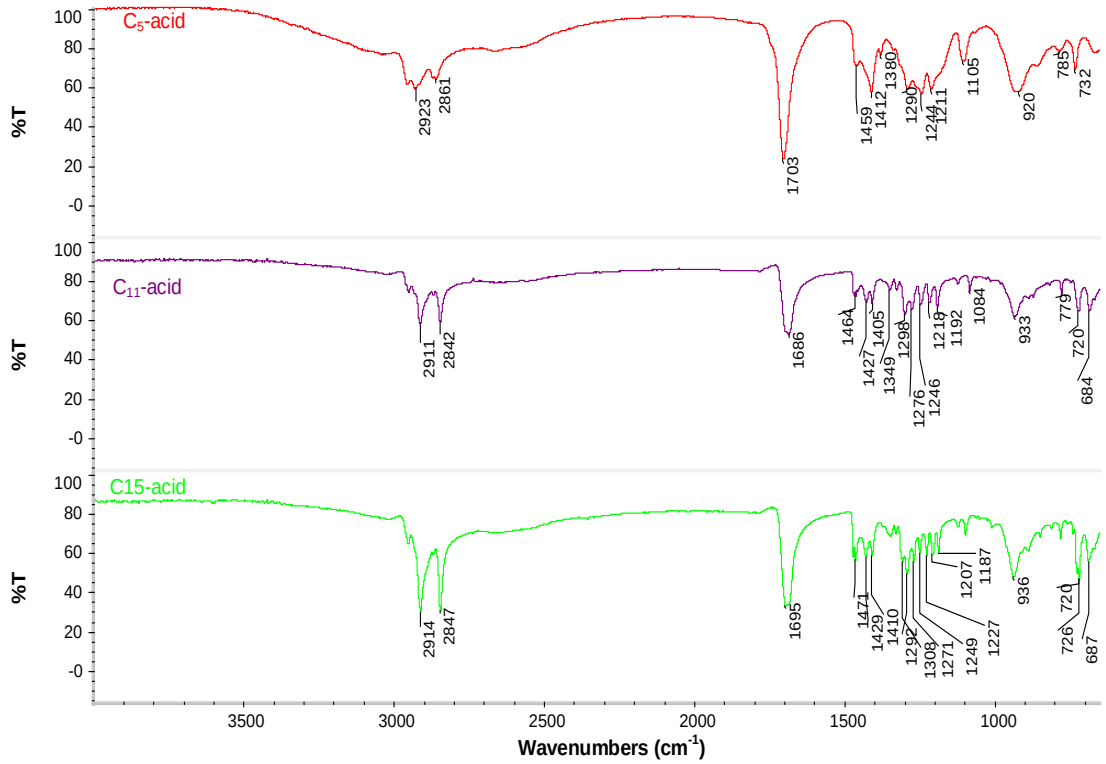

Figure 4.17: Infrared spectra of **C_5-acid**, lauric **C_{11}-acid** and palmitic **C_{15}**-acid.

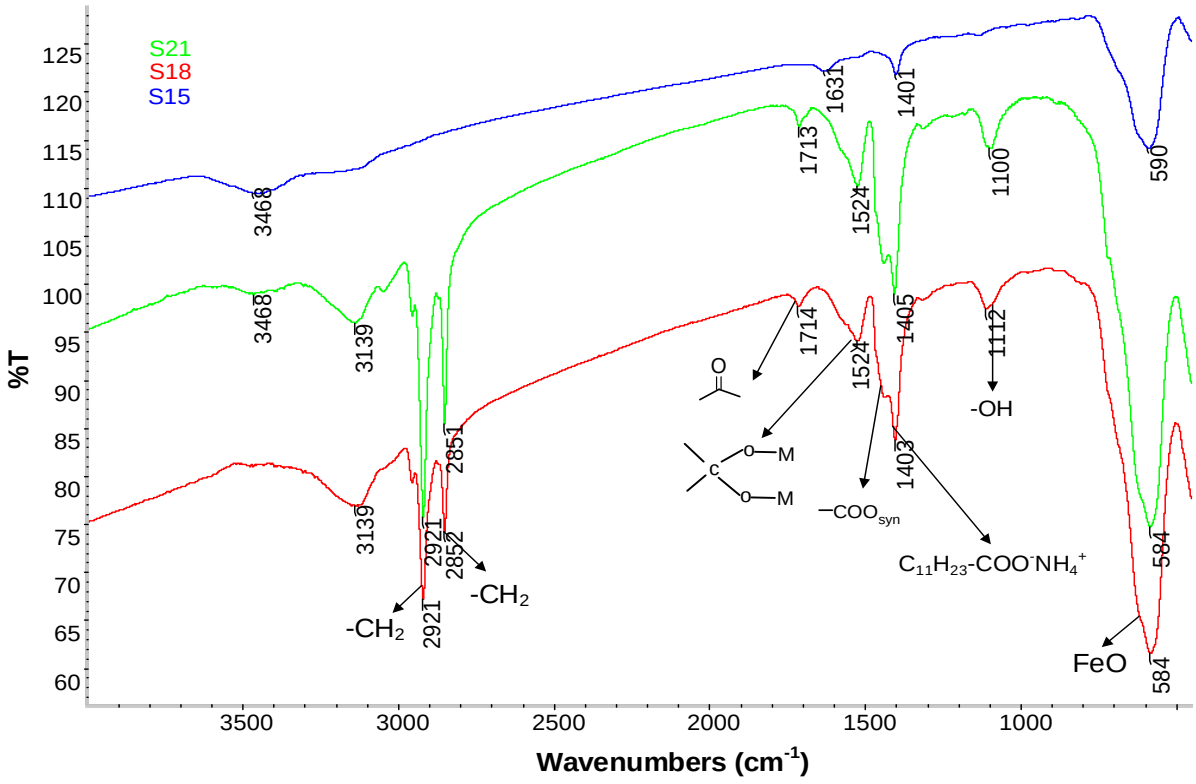

Figure 4.18: Infrared spectra of unwashed **S15, S18** and **S21.**

Stellenbosch University https://scholar.sun.ac.za

Figure 4.19 shows IR spectra of **S4-C$_5$(a, b, c)** (**S13, S14** and **S15**) after washing. Infrared spectrum of **S13**; prepared at a low concentration of **C5**-aciddoes not show new absorption bands corresponding to the **C$_5$**-acid. Some additional absorption bands corresponding to **C$_5$**-acid can however be observed in the spectrum of **S14** and **S15**. These new bands at 1632 cm^{-1}, 1513 cm^{-1}, and 1427 cm^{-1} are consistent with ν_{as}(-COO$^-$) and ν_s(-COO$^-$) absorption bands. The intensity of these bands was rather too low indicating only a small function of C$_5$-acid was found on the surface of MIONs. These results corroborated the work of Lambrick and co-workers in their preparation of short and long chain carboxylic acid stabilised MIONs that short chain carboxylic acid do not effectively stabilise MIONs.[166,167]

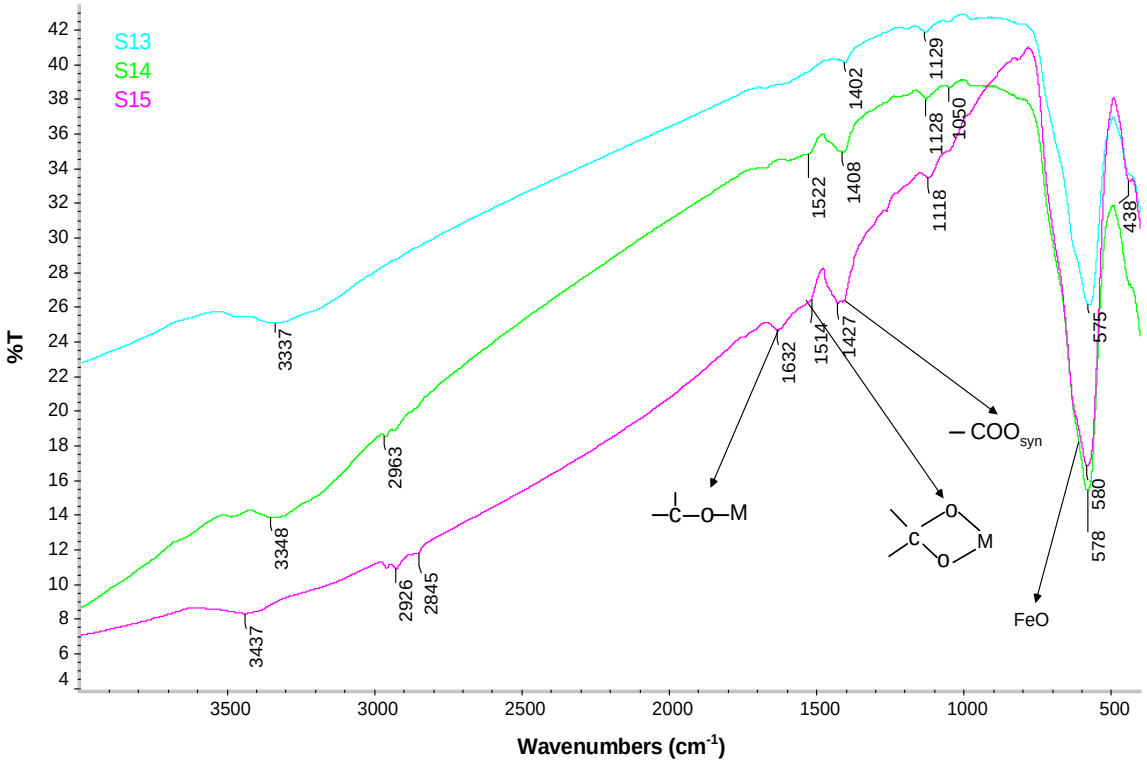

Figure 4.19: Infrared spectra of **S4-C$_5$(a, b, c)** (**S13, S14** and **S15).**

The IR spectra of **S4-C$_{11}$(a, b, c)** (**S16, S17** and **S18**) after washing are shown in **Figure 4.20**. All the spectra show new absorption bands corresponding to functional groups of the C$_{11}$-acid. For instance, the IR spectrum of **S18** shows absorption bands corresponding to the -CH$_2$ stretches at 2852 cm^{-1} and 2920 cm^{-1} respectively.[115] As seen in the figure, the intensity of these bands increases from **S16** to **S18**. Carbonyl stretch (C=O) of the free **C$_{11}$-acid** is located at 1714 cm^{-1}. As seen in **Figure 4.20**, the intensity of this band is reduced for **S4-C$_{11}$(a, b, c)**. The presence of this band designates the presence of free **C$_{11}$-acid**. The intensity of this band

Stellenbosch University https://scholar.sun.ac.za

increase from **S16** to **S18** as expected. Some literature studies postulated that the presence of this band indicates that the acid forms two layers on the surface of the MIONs.[166–168] The spectra of **S8** also shows other absorption bands corresponding to ν_{as}(-COO$^-$) and ν_s(-COO$^-$) at 1572 cm^{-1}, 1533 cm^{-1}, and 1442 cm^{-1} respectively. The absorption band at 582 cm^{-1}.is assigned to the Fe-O vibrations.[170] All these bands can be seen in the spectra of **S16** and **S17**.

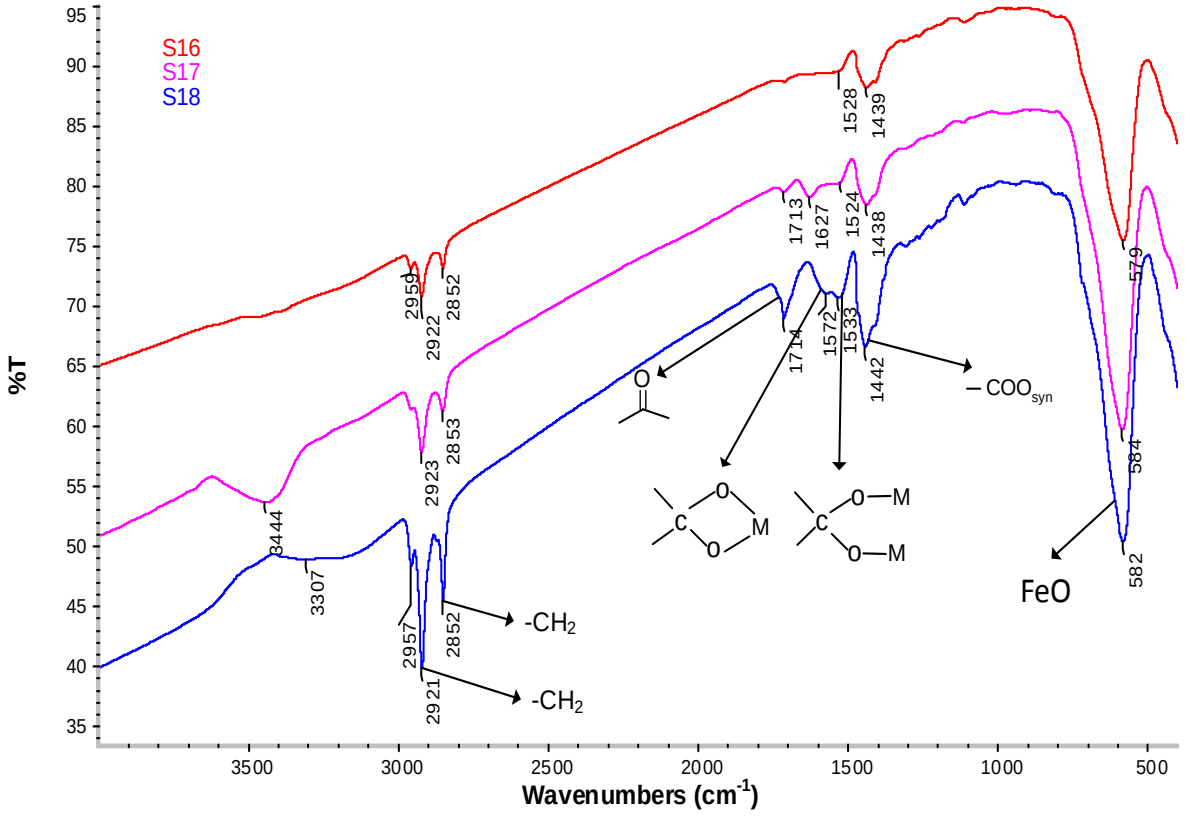

Figure 4.20: Infrared spectra of **S4-C$_{11}$(a, b, c)**, **S16, S17** and **S18**.

The spectra of **S4-C$_{15}$(a, b, c)** (**S19**, **S20** and **S21**) are shown in **Figure 4.21**. All the spectra confirmed the presence **C$_{15}$**-acid on the surface of naked MIONs. For instance, the spectrum of **S19** exhibited the following absorption bands: ν_{as} (CH$_2$) and ν_s (CH$_2$) are observed at 2918 cm^{-1} and 2850 cm^{-1}, ν_{as}(-COO$^-$) and ν_s(-COO$^-$) absorption bands can be seen at 1438 cm^{-1} and 1571 cm^{-1}, and while the Fe-O band can be observed at around 577 cm^{-1}. All the spectra show carbonyl stretching bands at 1708 cm^{-1}. This shows that during washing, not all the free of the **C$_{15}$-acid** was removed from the **S4-C1$_5$** nanoparticles.

Stellenbosch University https://scholar.sun.ac.za

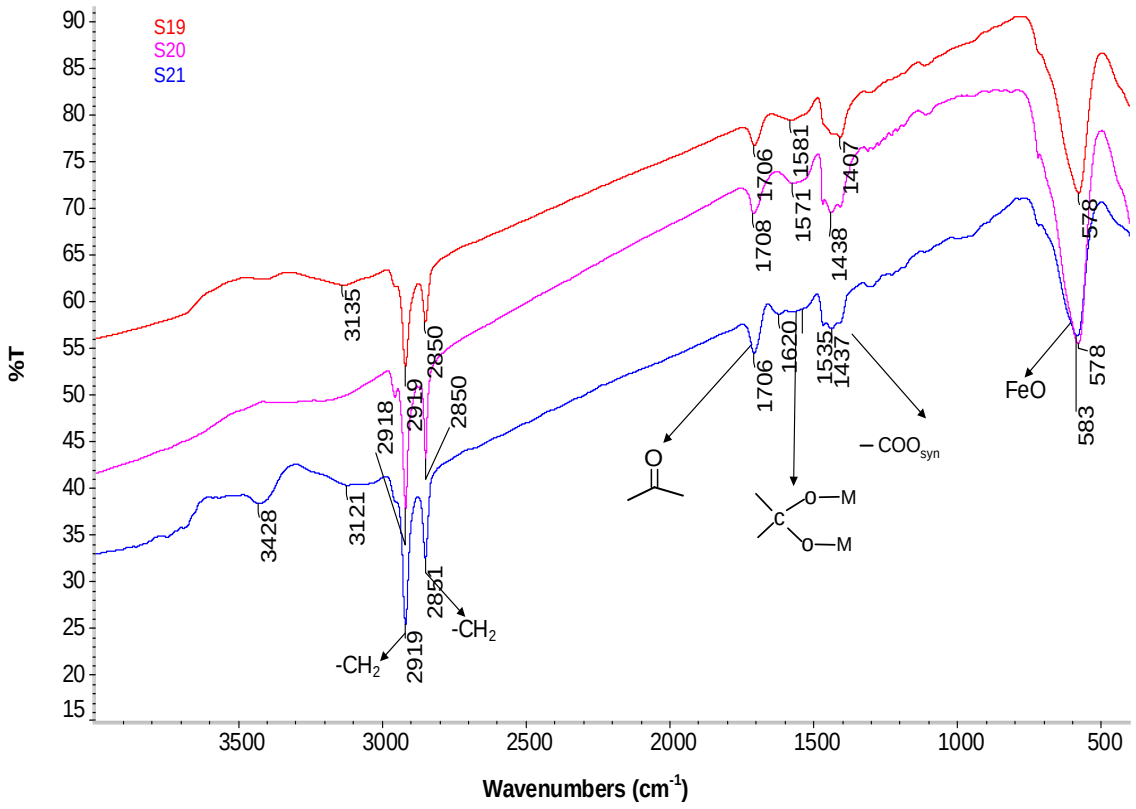

Figure 4.21: Overlaid IR spectra **S4-C15(a, b, c)** (**S19**, **S20** and **S21**).

All the **S4-Cn(a, b, c)** exhibited broad metal-carboxylate bands. The broadening of these bands indicates their adsorption to the surface of the MIONs.[82,168] This behaviour can be attributed to the complexation of the iron oxide surface by the carboxylate group (esterification).[88,115] Previous studies categorized the interaction of carboxylates with metal atoms into four types: ionic interaction, monodentate, bridging (bidentate), and chelating (bidentate).[170] The position and wavelength separation, Δ, between the $\nu_{as}(COO^-)$ and $\nu_s(COO^-)$ stretching vibration can be used to distinguish the type of the interaction between the carboxylate head and the metal atom.

Figure 4.22 shows different coordination modes of carboxylic acid head of long chain carboxylic acid with the surface of naked MIONs. The largest $\Delta\nu$ (> 200 cm^{-1}) corresponds to the monodentate interaction while the smallest $\Delta\nu$ (< 110 cm^{-1}) corresponds to the chelating bidentate coordination. The medium range $\Delta\nu$ (140 – 200 cm-^{1}) is associated with the bridging bidentate coordination. The band splitting between $\nu_{as}(COO^-)$ and $\nu_s(COO^-)$ for all **S4-Cn(a, b, c)** were recorded in **Table 4.5**. Hence, **S4-C5(b, c)** exhibited both unidentate and bidentate coordination. On the other hand, **S4-C11** and **S4-C15** exhibited both chelating and bridging bi-dentate coordination.

Stellenbosch University https://scholar.sun.ac.za

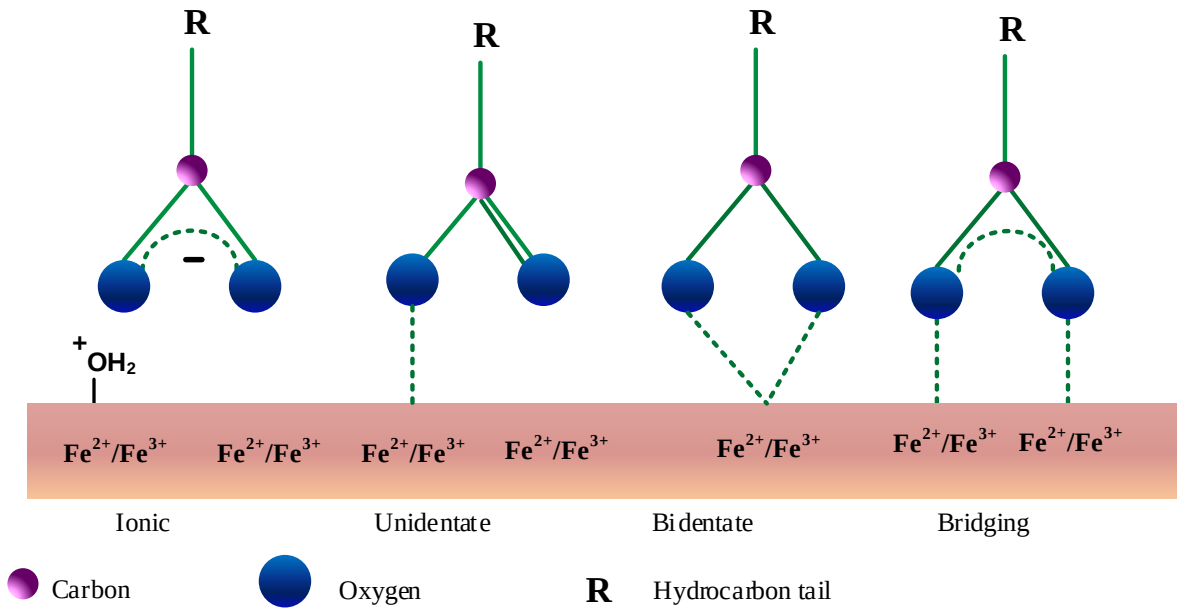

Figure 4.22: Types of coordination sites of the carboxylic acid head of long chain carboxylic acids (the monovalent metal) on the surface of magnetite nanoparticles. However, coordination can also occur in ionic coordination or through a surface hydroxyl group.

Table 4.5: Coordination modes of carboxylate group of Cn-acids with the surface MIONs

Sample	$\Delta\nu$ (cm^{-1})	Coordination
S4-C_5(a) (S13)		No band
S4-C_5(b) (S14)	79, 220	Monodentate, chelating bidentate
S4-C_5(c) (S15)	89, 225	Monodentate, chelating bidentate
S4-C_{11}(a) (S16)	93	Chelating bidentate
S4-C_{11}(b) (S17)	93, 193	Chelating bidentate, bridging bidentate
S4-C_{11}(c) (S18)	93, 142	Chelating bidentate, bridging bidentate
S4-C_{15}(a) (S19)	178	bridging bidentate
S4-C_{15}(b) (S20)	143	bridging bidentate
S4-C_{15}(c) (S21)	143	bridging bidentate

4.2.6.2 Thermal analysis

Thermogravimetric analysis (TGA) was carried out to obtain information on the amount of short and long chain carboxylic acids on the surface of these MIONs. **Figure 4.23** shows the

Stellenbosch University https://scholar.sun.ac.za

TGA profile of a neat C_{11}-acid which shows a sharp weight loss at around 200 °C. The DTA curve shows that lauric acid was pure.

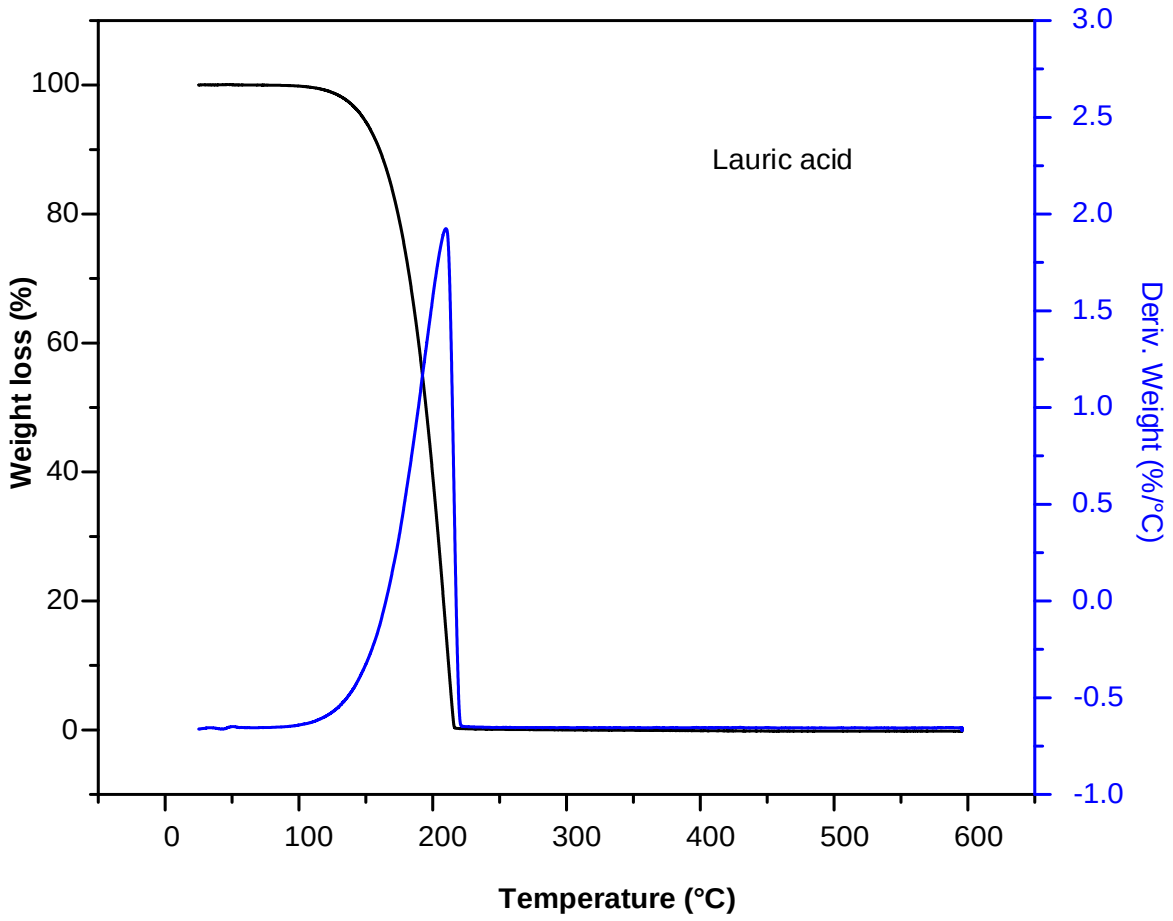

Figure 4.23: TGA and DTA curves of **C_{11}**-acid.

Figure 4.24 shows the TGA curves of **S4-C_{11}(a, b, c) (S16, S17** and **S18)** Comparing the TGA curves of **S16, S17** and **S18** to that of the neat lauric acid, their curves shows two weight losses. The first small weight loss below 100 °C can be attributed to the loss of moisture absorbed by MIONs during sample preparation. The second weight loss starting from 250 °C and extending to 400 °C can be ascribed to desorption of chemically absorbed carboxylate moiety on the surface of the nanoparticles. A third weight loss signifying secondary surfactant layer was not observed. Hence, it can be concluded that one layer of surfactant was formed on the surface of the **S16, S17** and **S18**.

Stellenbosch University https://scholar.sun.ac.za

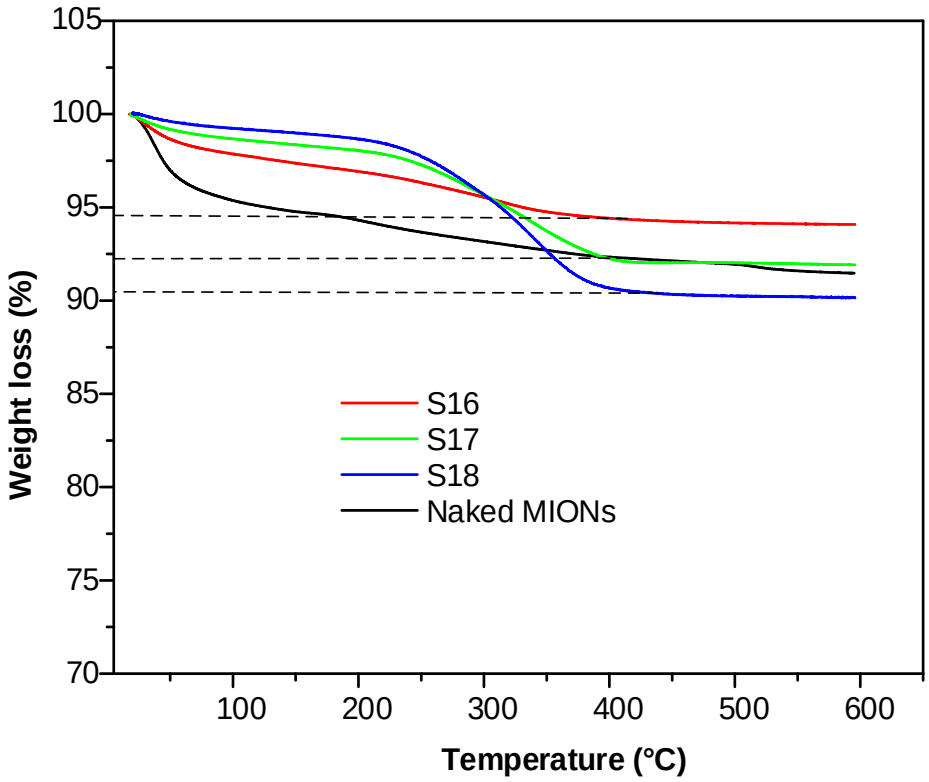

Figure 4.24: TGA curves of naked MIONs (**S4**), **S16**, **S17** and **S18**, respectively.

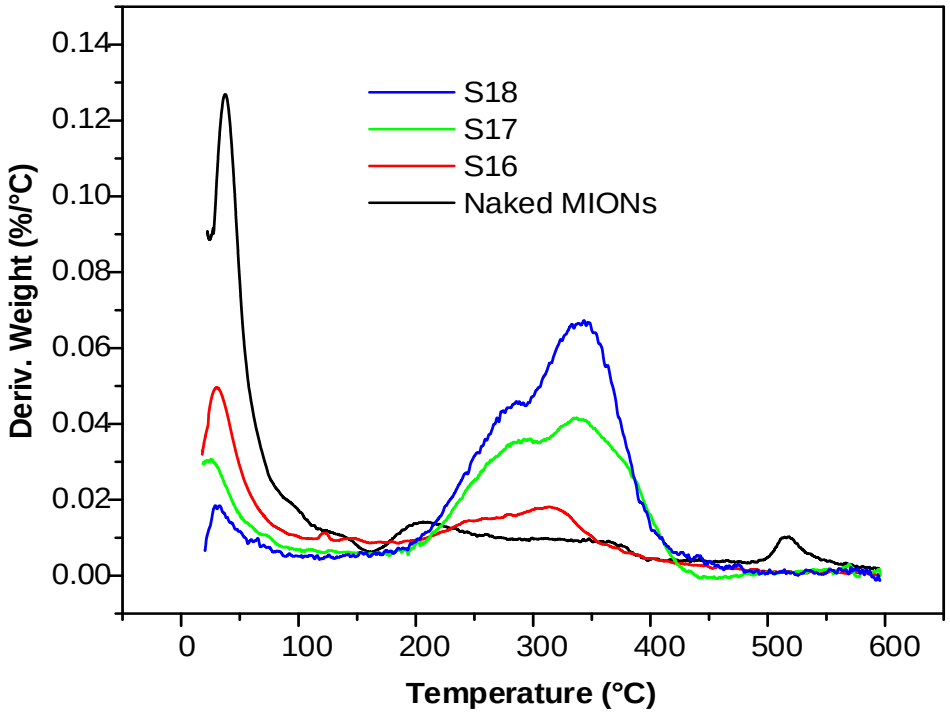

Figure 4.25: DTA curves of naked MIONs (**S4**), **S16**, **S17** and **S18**, respectively.

Stellenbosch University https://scholar.sun.ac.za

To study the adsorption effect of the surfactant chain length on the surface of the nanoparticles, thermal analysis of **S4-C$_{5c}$**, **S4-C$_{11c}$** and **S4-C$_{15c}$** (**S15**, **S18** and **S21)** was conducted. **Figure 4.26** shows their corresponding TGA curves. All the curves show broad weight losses indicating desorption, decomposition, and evaporation of the surfactant from the surface of the nanoparticles. The TGA curve of **S4-C$_{5c}$**, (**S15)** showed the smallest weight loss ascribed to the presence of **C$_5$**-acid on the surface of **S4**-MIONs. On the other hand, the TGA curve of **S4-C$_{11(c)}$** (**S18)** showed two weight losses.

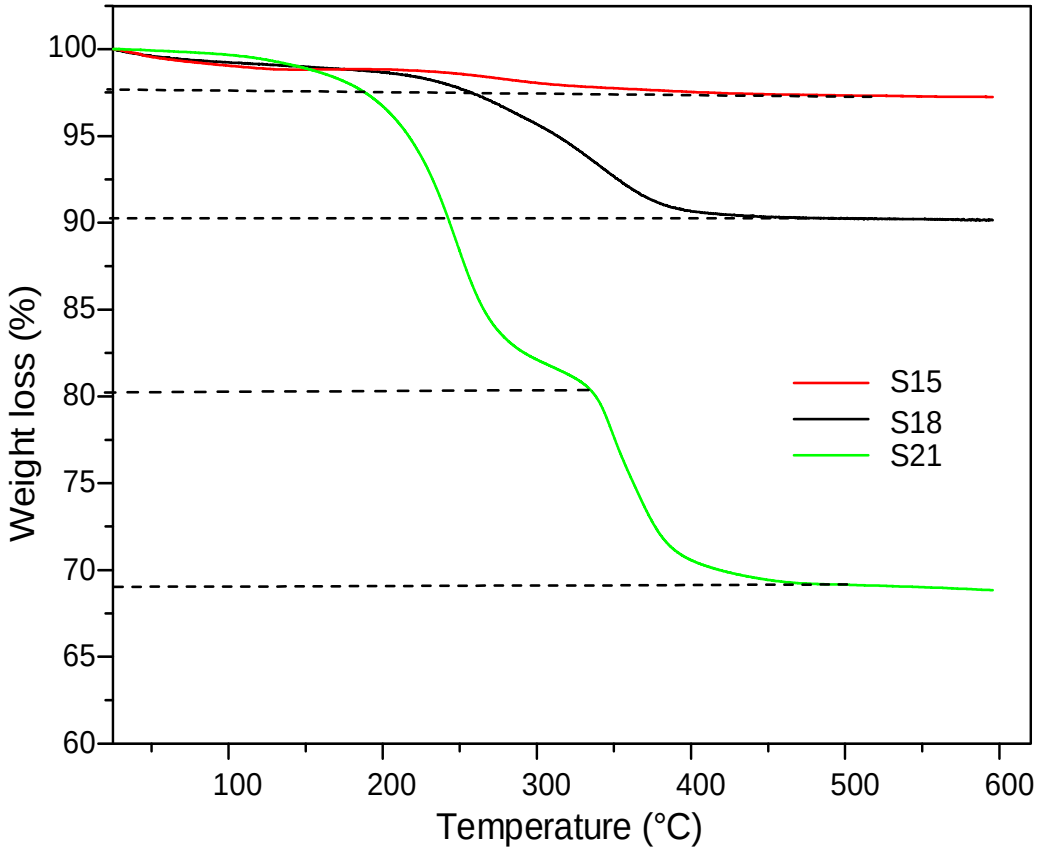

Figure 4.26: TGA analysis of **S15**, **S18** and **S21**.

The first weight loss below 100 °C can be attributed to moisture absorbed by the samples during the sample preparation. The second weight loss was due to desorption of chemically adsorbed **C$_{11}$**-acid on the surface of the nanoparticles. Then, the TGA curve of **S4-C$_{11(c)}$** (**S21)** shows three weight losses. The first weight loss below 100 °C can be assigned to water molecules or moisture. The second weight loss was due to physically adsorbed surfactant while the third weight loss was due to the chemically adsorbed surfactant molecules on the surface of the nanoparticles. Note that the samples were washed with a mixture of methanol and acetone;

Stellenbosch University https://scholar.sun.ac.za

lauric acid is soluble in both solvents while palmitic acid is not. Therefore, even though the samples were washed three times, it is possible that some of the uncoordinated **C15-acid** was still trapped in the sample. The DTA curves shown in **Figure 4.27** are in good correlation with the TGA analysis of **S15**, **S18** and **S21.**

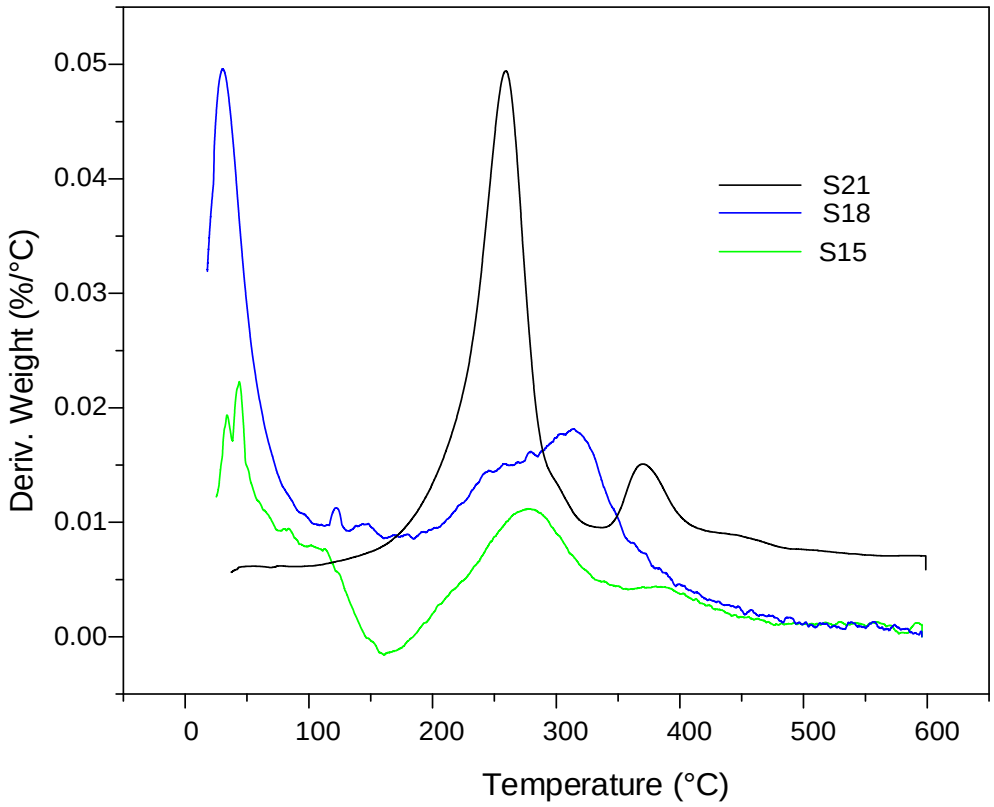

Figure 4.27: DTA analysis of **S15**, **S18** and **S21**.

4.2.6.3 Powder X-ray diffraction

The **S4-C(a, b, c)** were further characterised by powder X-ray diffraction (PXRD). **Figure 4.28**, **Figure 4.29**, and **Figure 4.30** show PXRD patterns of **S4-C$_n$ (a, b, c)**. The diffraction peaks of all the of **S4-C$_n$(a, b, c)** were indexed at the following diffraction patterns (220), (311), (400), (422), (511) and (440) respectively and matched to standard magnetite sample, as per JCPDS cards No. 00-016-0653. Therefore, **S4-C$_n$(a, b, c)** exhibited the cubic spinel structure. It has been reported in the literature that magnetite can be easily oxidised in air to form maghemite at the temperature 110 °C – 230 °C and can be further transformed to the hematite at the temperature above 250 °C.[115] Generally, diffraction patterns of hematite can be indexed

Stellenbosch University https://scholar.sun.ac.za

at (113), (210), (213), and (210).[115] These diffraction peaks were not observed in the diffractograms of **S4-Cn(a, b, c)** The diffractogram of all **S4-Cn(a, b, c)** shows high intensity and sharp peaks showing that coating naked MIONs (**S4**) with long chain carboxylic acid did not alter their crystallinity.

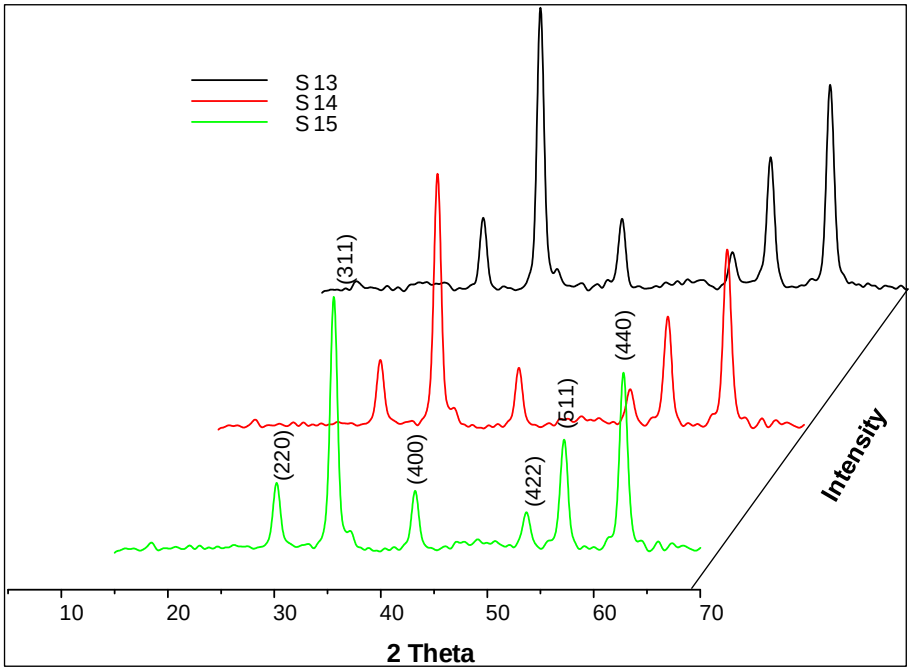

Figure 4.28: Powder XRD analysis of **S13**, **S14**, **S15**.

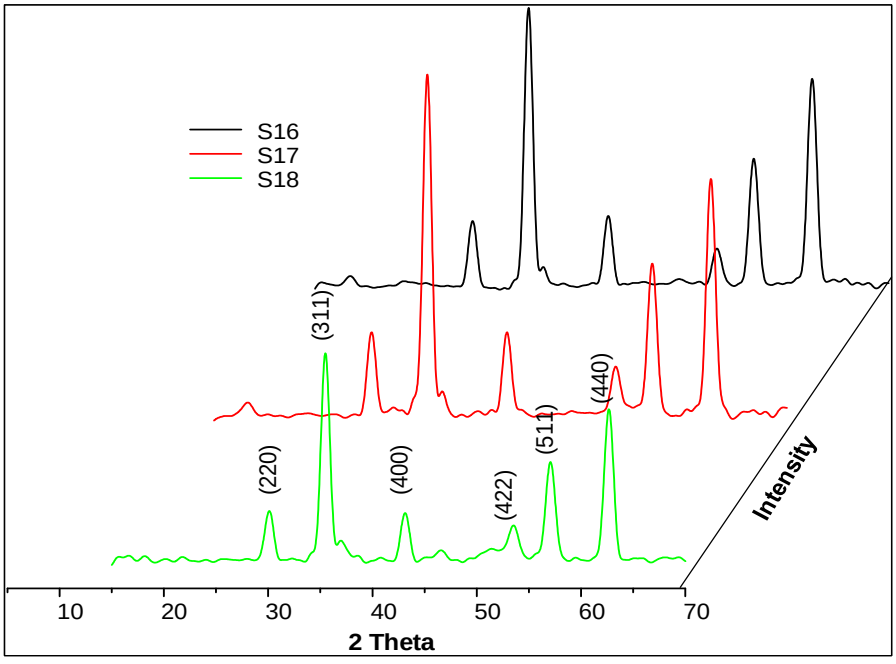

Figure 4.29: Powder XRD analysis of **S16**, **S17**, **S18**.

Stellenbosch University https://scholar.sun.ac.za

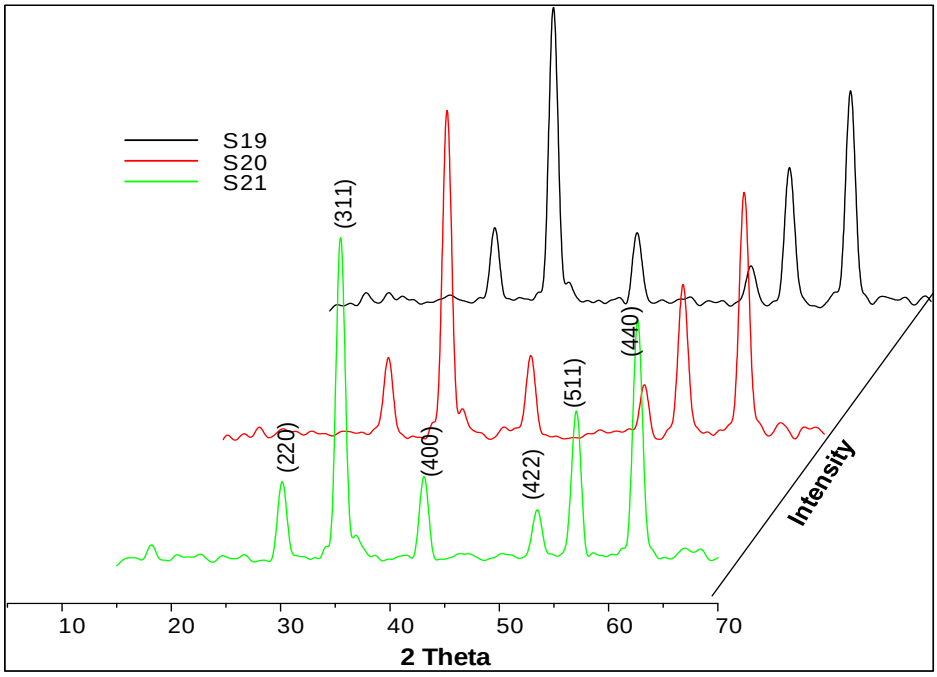

Figure 4.30: Powder XRD analysis of **S19**, **S20**, **S21**.

Table 4.6: Particle size of long chain carboxylate stabilised MIONs determined PXRD analysis by Scherrer equation

Sample	Particle size (nm)			Average size (nm)
	(311)	(511)	(440)	
S4-C_5(a) (S13)	13.6	12.98	13.78	13.45±0.34
S4-C_5(b) (S14)	13.57	14.06	13.88	13.84±0.20
S4-C_5(c) (S15)	13.47	14.14	13.3	13.64±0.36
S4-C_{11}(a) (S16)	13.55	12.67	12.36	12.86±0.50
S4-C_{11}(b) (S17)	13.89	13.23	12.79	13.30±0.45
S4-C_{11}(c) (S18)	14.29	14.07	13.83	14.21±0.19
S4-C_{15}(a) (S19)	14.54	14.27	13.82	14.21±0.30
S4-C_{15}(b) (S20)	13.80	13.25	13.35	13.47±0.24
S4-C_{15}(c) (S21)	13.29	12.89	13.75	13.45±0.34

The average crystallite size (<D>, nm) was calculated from line broadening analysis using the Debye-Scherrer formula. [1, 2] The particle crystal size was calculated using FWMH of the three diffraction peaks, and results were tabulated in **Table 4.6**. Comparing the average particle size of all **S4-C_n(a, b, c)** to those of naked MIONs, particle sizes of **S4-C_n(a, b, c)** were bigger in size as expected. The size of the nanoparticles might have increased when the reaction

Stellenbosch University https://scholar.sun.ac.za

temperature was increased to 90 °C. However, the change was not drastic as the nanoparticles increased by only 2 nm. This result confirms that long chain carboxylic acids successfully minimised the particles agglomeration.

4.2.6.4 High resolution transmission electron microscopy

The long chain carboxylic acid functionalised MIONs **S4-C$_n$(a, b, c)** were further studied by HRTEM analysis. **Figure 4.31** shows the HRTEM image and corresponding histogram of C5-acid functionalised MIONs (**S4-C$_n$(a, b, c)**). The HRTEM image of **S4-C$_5$(a)** (**S13**); prepared with 4:1, MIONs to **C$_5$-acid** mass ratio produced agglomerated and polydispered nanoparticles. However, changing the mass ratio of MIONs to **C$_5$-acid** to 1:2 slightly improved the dispersion of the nanoparticles as shown by the HRTEM image of **S15**.

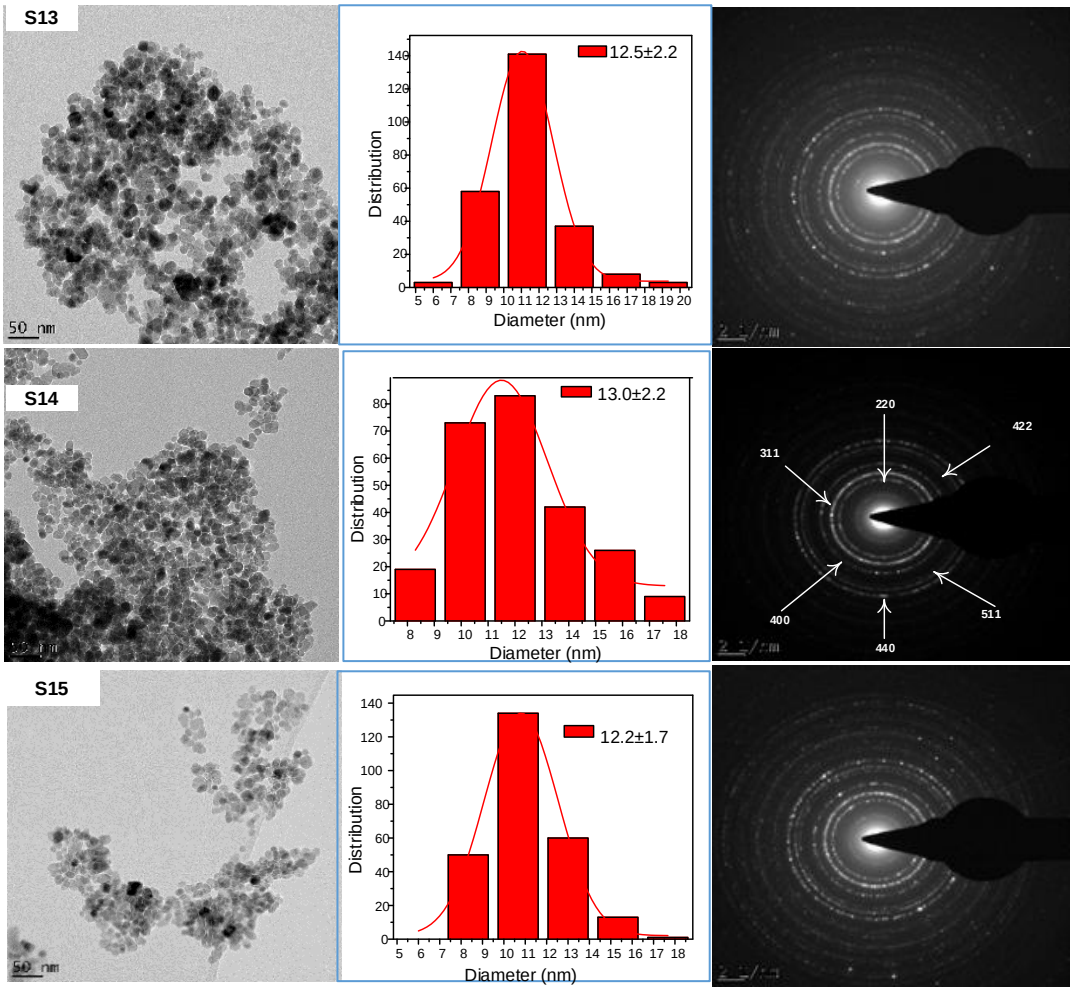

Figure 4.31: HRTEM images, SAED, and corresponding histograms of C5-MIONs_**X**, **Y**, and **Z**: **S13**, **S14**, and **S15**.

Stellenbosch University https://scholar.sun.ac.za

Figure 4.32 shows HRTEM images of **S4-C$_5$(a, b, c)** and their corresponding particle size histograms. The images of **S16** and **S17** shows agglomerated particles. However, increasing the concentration of C11-acid improved the dispersing of the nanoparticles (**S18**). The HRTEM analysis of **S4-C$_{15}$(a, b, c)** also followed a similar trend: at low surfactant concentration, the nanoparticles agglomerated. Increasing the concentration, the surfactant concentration improved the dispersity of the nanoparticles. The average sizes of **S4-C$_n$(a, b, c)** were determined by counting more than 250 particles with ImageJ software and the histograms are shown **Figure 4.32**.

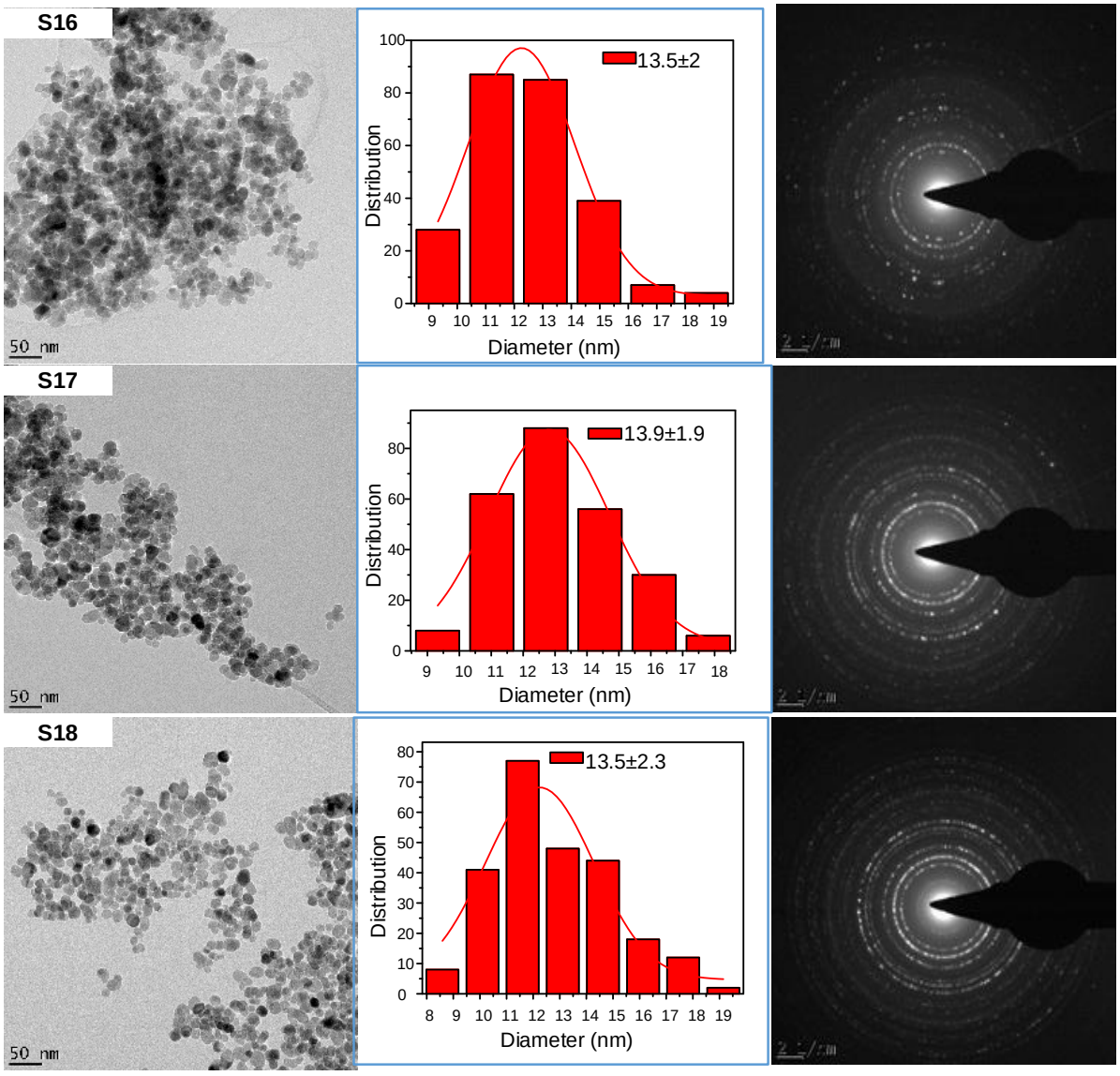

Figure 4.32: HRTEM images, SAED, and corresponding histograms of **S4-C$_{11}$(a, b, c)** (**S16**, **S17**, and **S18)**.

Stellenbosch University https://scholar.sun.ac.za

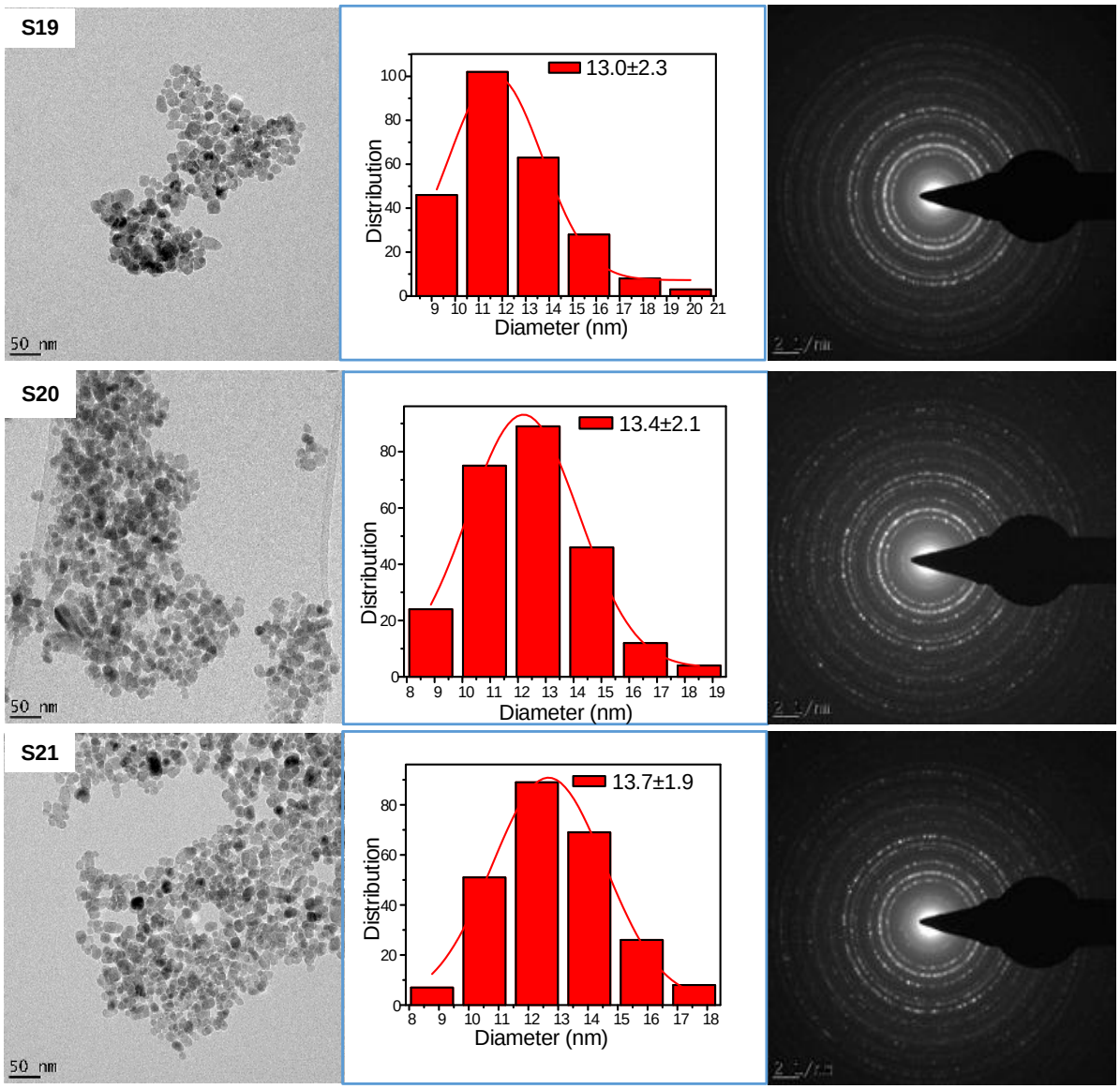

Figure 4.33: HRTEM images, SAED, and corresponding histograms of **S4-C$_{15}$(a, b, c)** (**S19**, **S20**, and **S21)**.

The average particle size of all **S4-C$_n$(a, b, c)** determined by ImageJ and Sherrer calculation from PXRD data are shown in **Figure 4.34**. The average particle sizes of **S4-C$_n$(a, b, c)** which were determined by counting 250 particles from their HRTEM images correlated well with the particle sizes determined using Sherrer's equation.

Stellenbosch University https://scholar.sun.ac.za

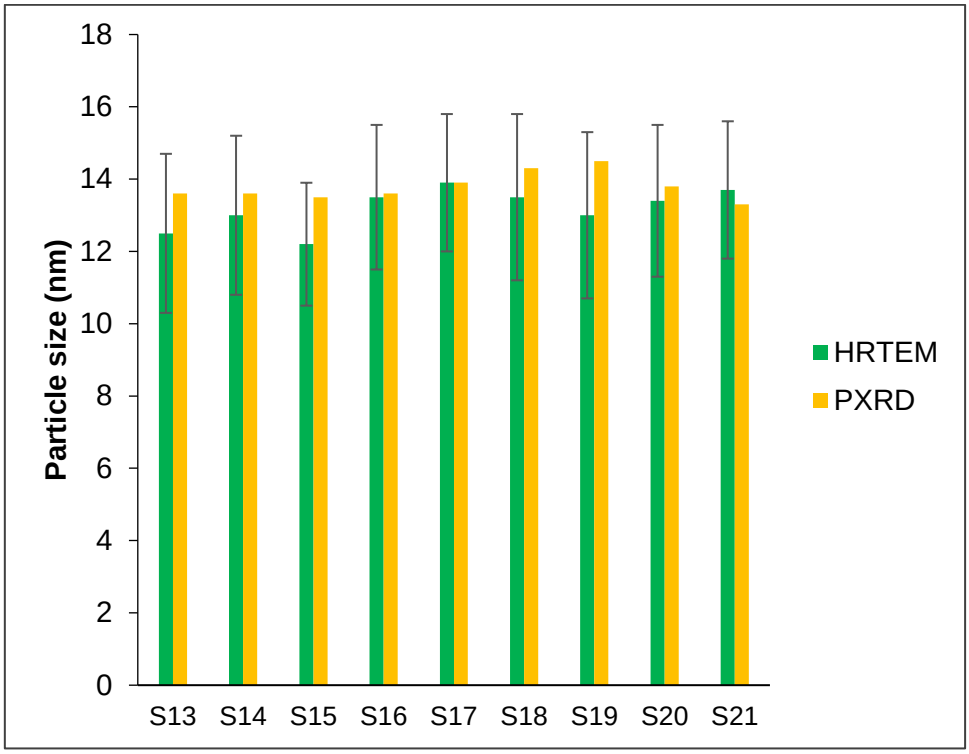

Figure 4.34: Particle size analysis of **S4-C$_n$(a, b, c)** using HRTEM and PXRD.

4.2.7 Synthesis of dendrimer micelle (DM$_n$) modified S4-C$_n$(b, c)

Freshly made and washed **S4-C$_5$(b, c)**, **S4-C$_{11}$(b, c)** and **S4-C$_{15}$(b, c)** were prepared using the procedure explained in **Section 4.2.5** They were then dispersed in a mixture of methanol and chloroform and heated to 35 °C. A solution of dendrimer micelles (**DM$_n$**) was added dropwise to the slurry and the reaction mixture was run overnight under nitrogen. The reaction conditions were varied as shown in **Table 4.7**. The resultant MIONs were referred to as **S4-C$_n$(b, c)-DM$_n$** where n = 5, 11 and 15 (**S22** to **S27**). The synthetic procedure was summarised using **Figure 4.35** and the full synthesis method is given in **Section 4.5.3.**

Table 4.7: Conditions used for the synthesis of dendrimer micelle modified **S4-C$_n$(b, c)-DM$_n$**

Sample	**S4-C$_n$(a, b, c)** mass (g)	**DM$_n$** mass (mg)
S4-C$_5$(b)-DM$_5$ (S22)	1.00	200
S4-C$_5$(c)-DM$_5$ (S23)	1.00	200
S4-C$_{11}$(b)-DM$_{11}$ (S24)	1.00	200
S4-C$_{11}$(c)-DM$_{11}$ (S25)	1.00	200
S4-C$_{15}$(b)-DM$_{15}$ (S26)	1.00	200
S4-C$_{15}$(c)-DM$_{15}$ (S27)	1.00	200

Stellenbosch University https://scholar.sun.ac.za

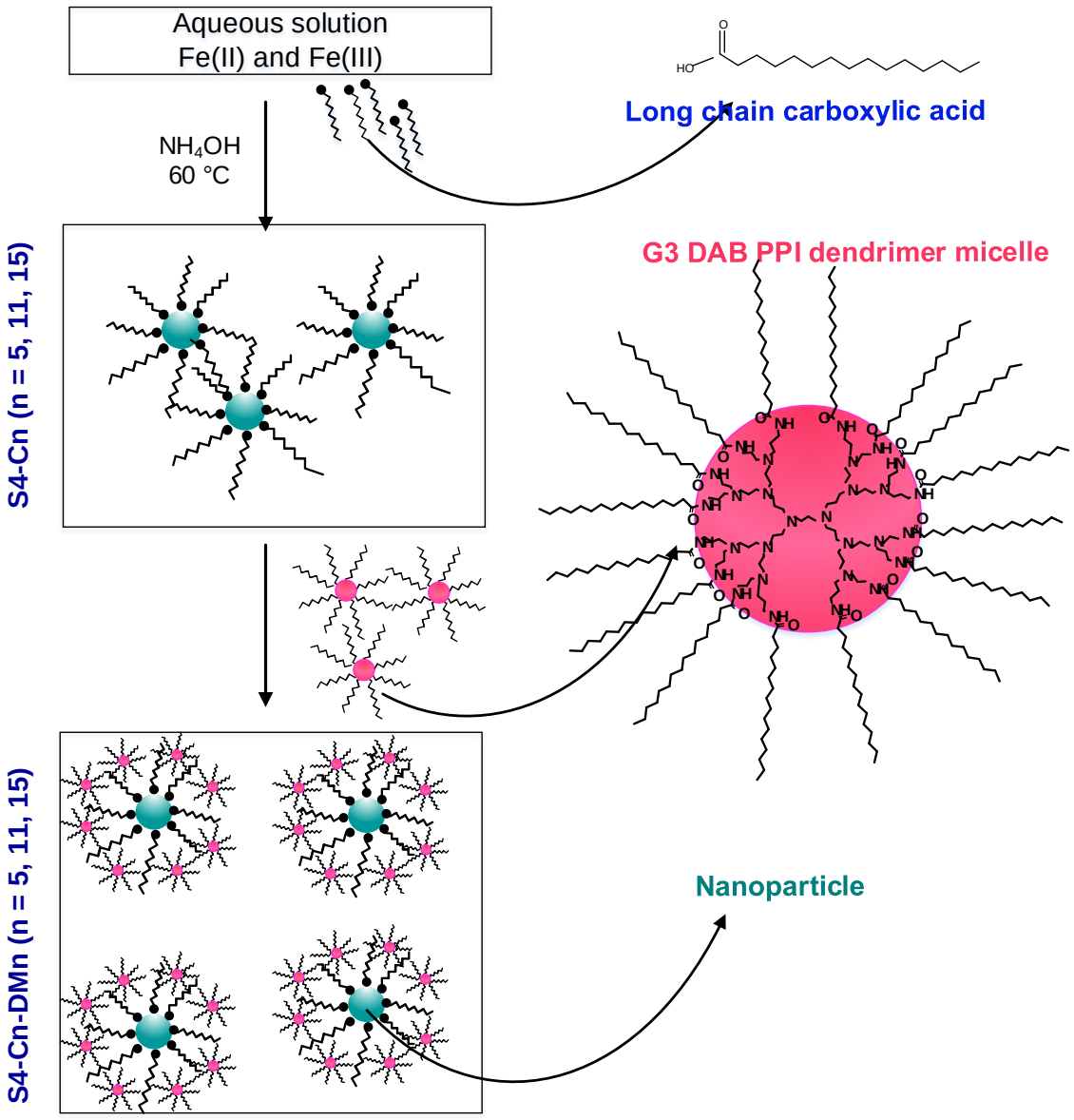

Figure 4.35: Schematic representation of the synthesis of dendrimer micelle modified **S4-C$_n$** (**S4-C$_n$-DM$_n$**).

4.2.8 Characterisation of DM$_n$ modified S4-C$_n$(a, b, c)

Characterisation of **S4-C$_n$(b, c)-DM$_n$** (**S22** to **S27**) was carried out using the following analytical techniques: IR, PXRD, and HRTEM.

4.2.8.1 Infrared spectroscopy

Infrared analysis **S4-C$_5$(b)–DM$_5$ (S22)**, **S4-C$_{11}$(b)-DM$_{11}$ (S24)** and **S4-C$_{15}$(b)-DM$_{15}$** (**S26**) was used to study the interaction between dendrimer micelle (**DM$_n$(b, c)**) and **S4-C$_n$** (where n = 5,

Stellenbosch University https://scholar.sun.ac.za

11 and 15). **Figure 4.37 s**hows overlaid spectra of **S22**, **S24** and **S26** subjected to the same concentration of each respective dendrimer micelles (**DM_n**).

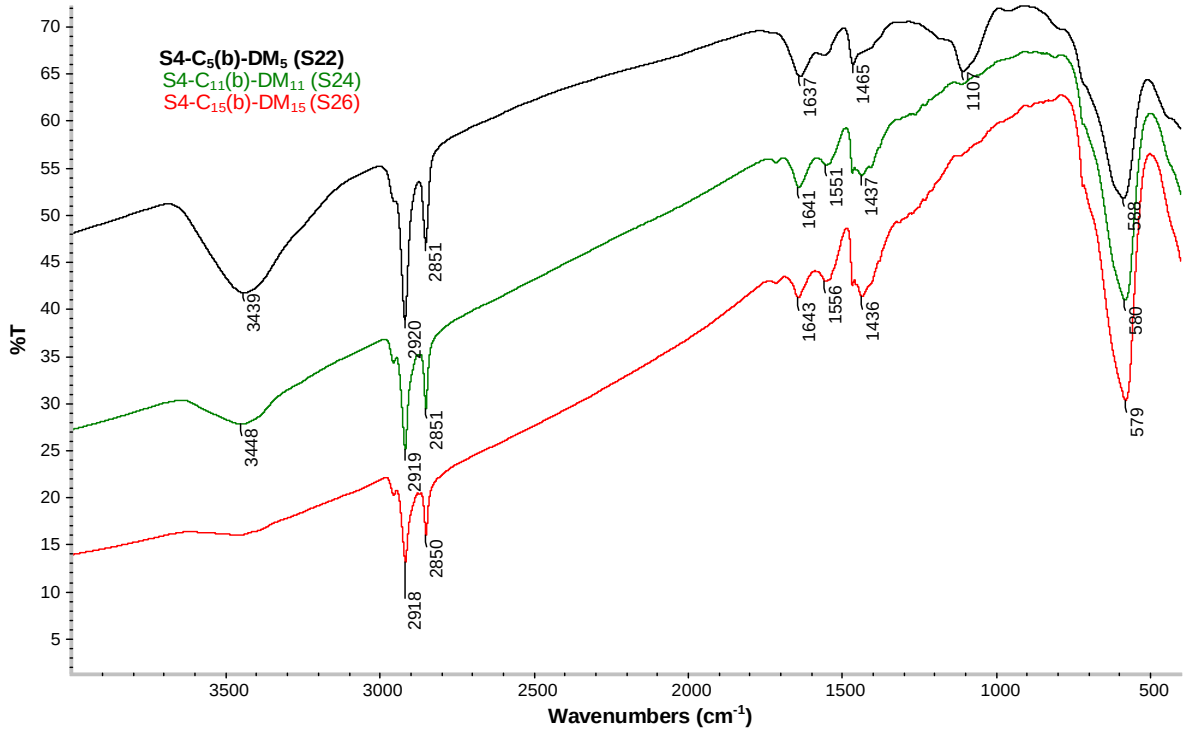

Figure 4.36: Infrared spectroscopy analysis of **S22**, **S24** and **S26**.

The spectrum of **S4-C_5(b)–DM_5** (**S22**) exhibited the following absorption bands at 1641 cm^{-1} and 1643 cm^{-1} consistent with carbonyl amide groups and the 1560 cm^{-1} which is attributed to C-N stretches of dendrimer micelles (**DM_n**). The absorption band 1465 cm^{-1} represent ν_s(-COO^-), 1107 cm^{-1} corresponds to –O-H out of plane vibrations and λ = 587 cm^{-1} corresponds to Fe-O vibration modes. The IR spectra of **S4-C_{11}(b)–DM_{11} (S24)** and **S4-C_{15}(b) –DM_{15}** (**S26**) also showed additional absorption bands ascribed to both the surfactant and **DM_n**. These bands are slightly shifted from the bands of the pure dendrimer micelles (**DM_n**) (1635 cm^{-1} and 1549 cm^{-1}, respectively). Furthermore, comparing the shapes of the absorption bands of the neat **DM_n** to those displayed in the spectra of modified MIONs, the absorption bands of the neat **DM_n** are sharp. The C=O stretching band observed in the spectrum of **S24** and **S26** at around 1715 cm^{-1} shows that the dendrimer did not replace the **C_{11}** or the **C_{15}** chemisorbed onto the surface of the MIONs but rather formed a second layer.

Stellenbosch University https://scholar.sun.ac.za

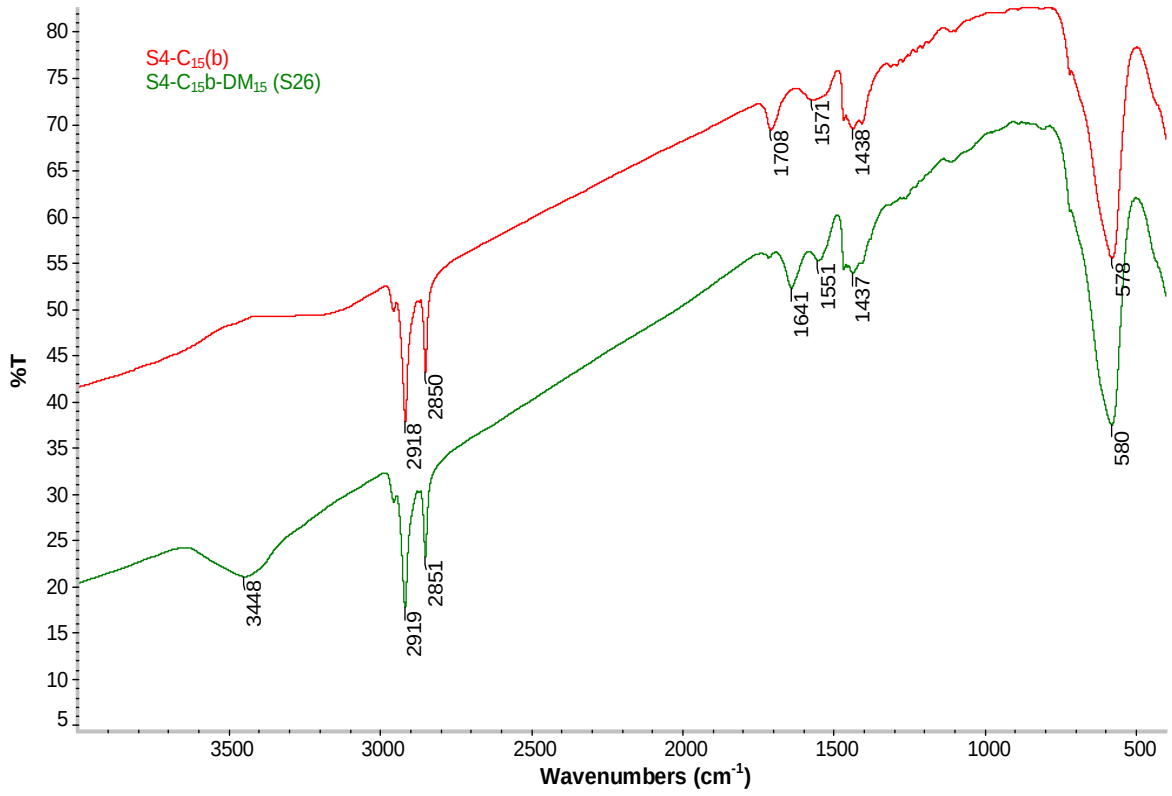

Figure 4.37: Infrared spectroscopy analysis of **S4-C$_{15}$(b) (S20)** and **S4-C$_{15}$(b)–DM$_{15}$ (S26)**.

4.2.8.2 Thermal analysis

Thermal analysis of **S4-C$_{15}$(b)–DM$_{15}$** (**S26**), and **S4-C$_{15}$(c)–DM$_{15}$** (**S27**) to further get information about the dendrimer micelles on the MIONs. **Figure 4.38** shows the TGA curves of naked MIONs (**S4**), **S4-C$_{15}$(b)–DM$_{15}$** (**S26**), and **S4-C$_{15}$(c)–DM$_{15}$** (**S27**). The weight loss of naked MIONs (**S4**) only shows one weight loss. On the contrary, TGA curves of **S26** and **S27** shows two distinct losses. The first weight loss can be attributed to the loss of palmitic acid adsorbed on the surface of the nanoparticles. The second weight loss can be attributed to the loss of **C$_{15}$-acid** and dendrimer micelles which forms the second surfactant layer on the surface of the nanoparticles. **Figure 4.39** shows the corresponding DTA curves of the **S4-C$_{15}$(b)–DM$_{15}$**. The TGA and DTA shows that the nanoparticles were stabilised by a double layer of palmitic acid (**C$_{15}$-acid**) and the dendrimer micelle (**DM$_{15}$**).

Stellenbosch University https://scholar.sun.ac.za

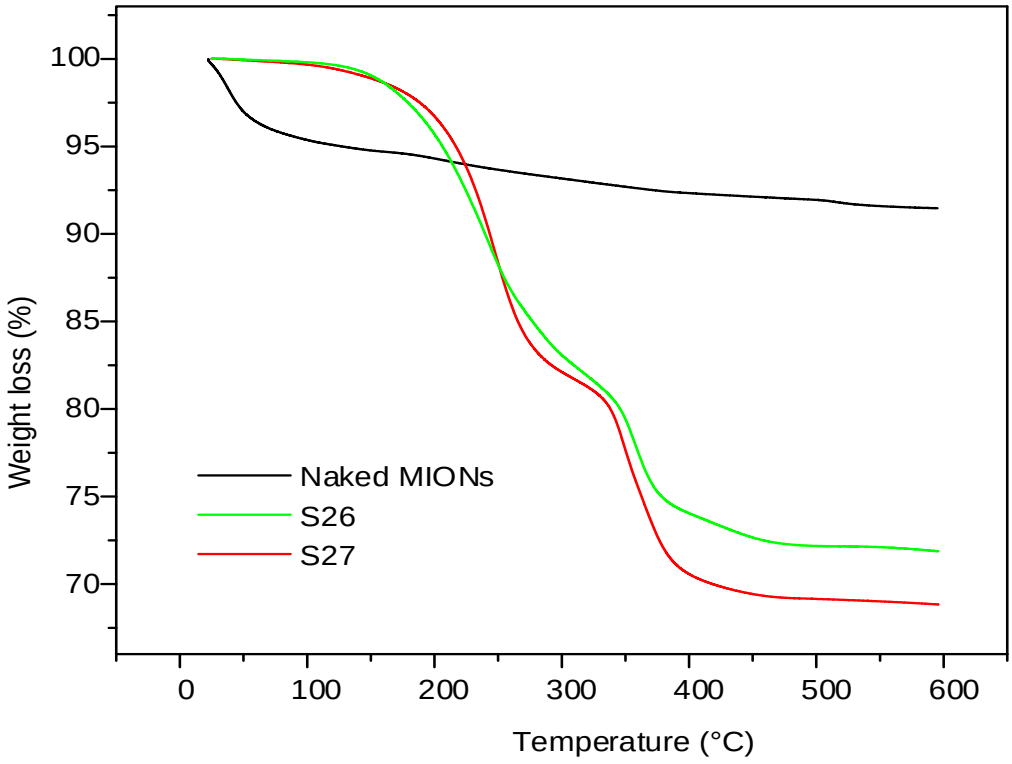

Figure 4.38: TGA curves of **S4**, **S26** and **S27**.

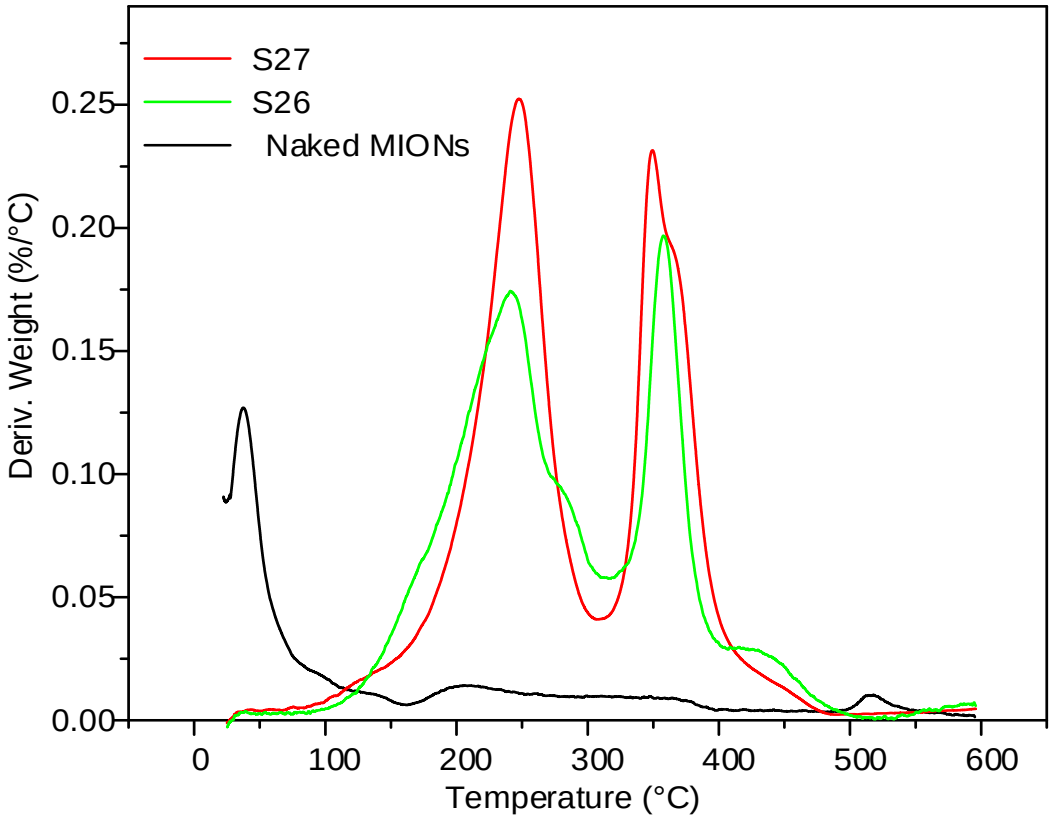

Figure 4.39: DTA analysis of **S4**, **S26** and **S27**.

Stellenbosch University https://scholar.sun.ac.za

4.2.8.3 Power X-ray diffraction

The **S4-C_n(b, c)–DM_n** (**S22** to **S27**) were also characterised using PXRD. The diffraction peaks of all the **S4-C_n(b, c)–DM_n** were indexed at the following diffraction patterns (220), (311), (400), (422), (511) and (440) respectively and matched to standard magnetite sample as per JCPDS cards No. 00-016-0653. Hence modification of **S4-C_n(b, c)** with dendrimer micelle did not change the crystallinity of the nanoparticles. The absence of other diffraction peaks shows that the nanoparticles were in one phase which is magnetite. In addition, the diffractogram of all dendrimer micelle modified **DM_n** showed high intensity and sharp peaks showing that the nanoparticles were crystalline. Particle size was determined using Scherrer equation and the results were tabulated in **Table 4.8**. The particle size was determined using the diffraction peaks indexed at (311), (511), and (440). The average particle sizes were between 10 nm and 13 nm.

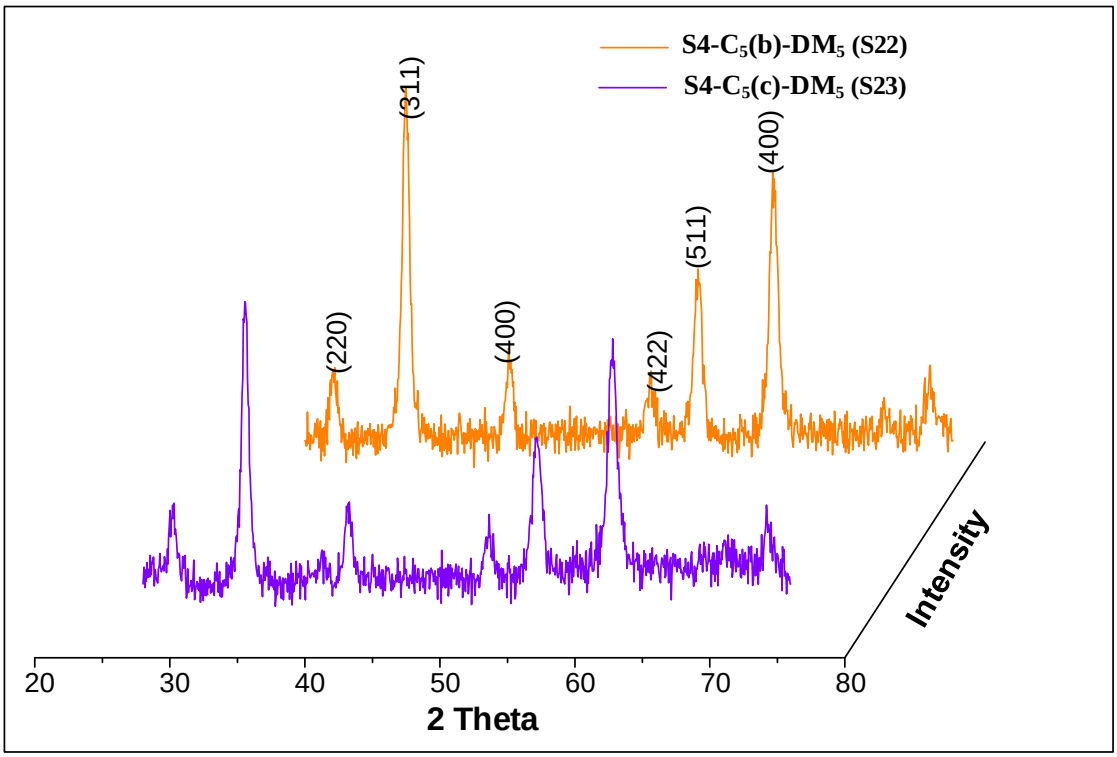

Figure 4.40: Powder XRD analysis of **S22** and **S23**.

Stellenbosch University https://scholar.sun.ac.za

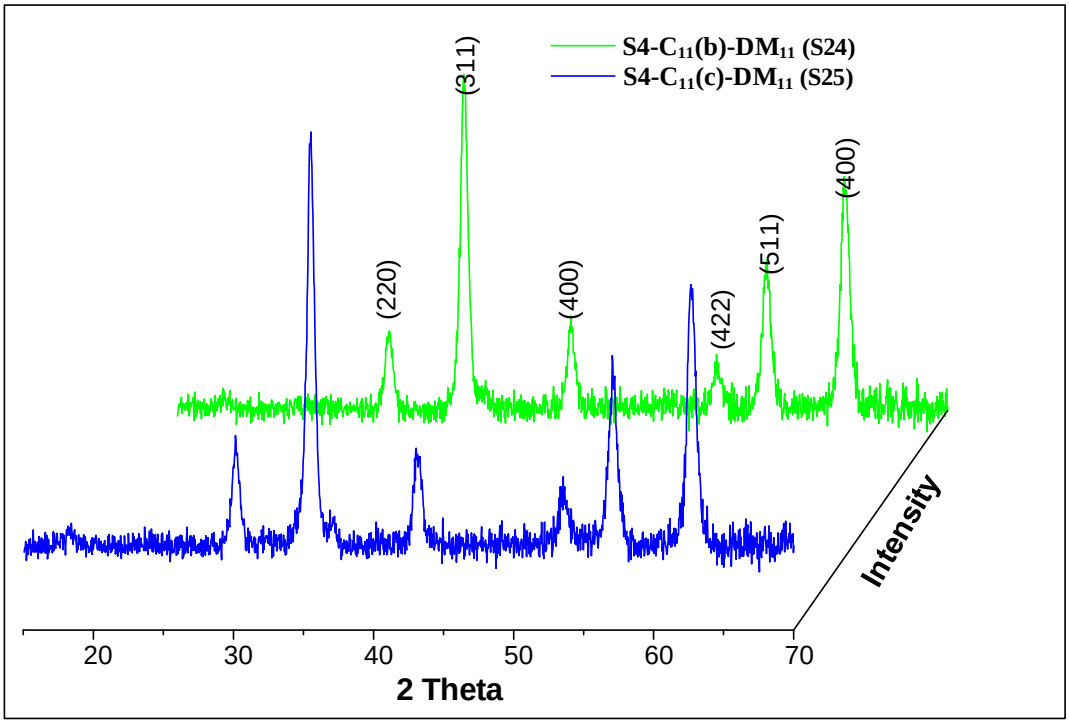

Figure 4.41: Powder XRD analysis of **S24** and **S25**.

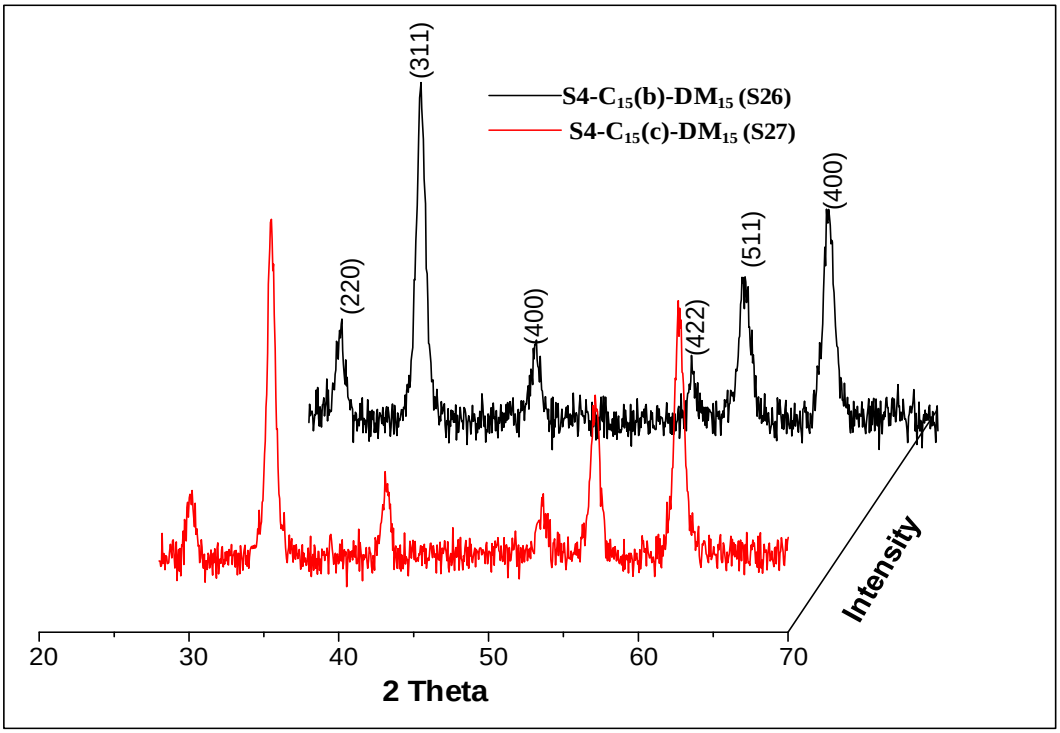

Figure 4.42: Powder XRD analysis of **S26** and **S27**.

Stellenbosch University https://scholar.sun.ac.za

Table 4.8: Particle size of **S4-C_n(a, b, c)** modified with **DM_n** determined using Scherrer equation

Sample	Particle size (nm)			Average size (nm)
	(311)	(511)	(440)	
S4-C_5(b)-DM_5 (S22)	13.31	12.20	12.40	12.64±0.48
S4-C_5(c)-DM_5 (S23)	13.17	10.58	10.61	11.45±1.21
S4-C_{11}(b) -DM_{11} (S24)	13.08	9.98	10.34	11.13±1.38
S4-C_{11}(c) -DM_{11} (S25)	10.16	10.00	9.99	10.05±0.08
S4-C_{15}(b) -DM_{15} (S26)	11.31	9.82	10.67	10.60±0.61
S4-C_{15}(c) -DM_{15} (S27)	10.81	9.66	10.56	10.34±0.49

4.2.8.4 High resolution transmission electron microscopy

Figure 4.43 shows the HRTEM image of **S4-C_{11}(b, c)-DM_{11} (S24)** (**S24** and **S25**). Both images show small nanoparticles trapped in a mesh-like material forming multi-core micro-clusters. The HRTEM images of **S4-C_{15}(b, c)-DM_{15} (S24)** (**S26** and **S27**) exhibited similar characteristics (**Figure 4.44**). The HRTEM image of **S25** and **S27** clearly shows small nanoparticles trapped within this mesh-like material. Presumably, this mesh-like material was formed by the intercalation of the alkyl chains of the dendrimer micelle and the long chain carboxylic acids. For this reason, these results confirm the IR spectroscopy and TGA results that the **S4-C(b, c)** were successfully modified with dendrimer micelles, forming a double layer of surfactant on the surface of **S4**.

As mentioned earlier, the average particle sizes of **S4-C_n(a, b, c)** from HRTEM analysis is determined by counting more than 250 nanoparticles with ImageJ software. However, due to the entrapment of the nanoparticle, it was almost impossible to count them. Therefore, the particle size of these trapped MIONs was determined solely by PXRD.

Stellenbosch University https://scholar.sun.ac.za

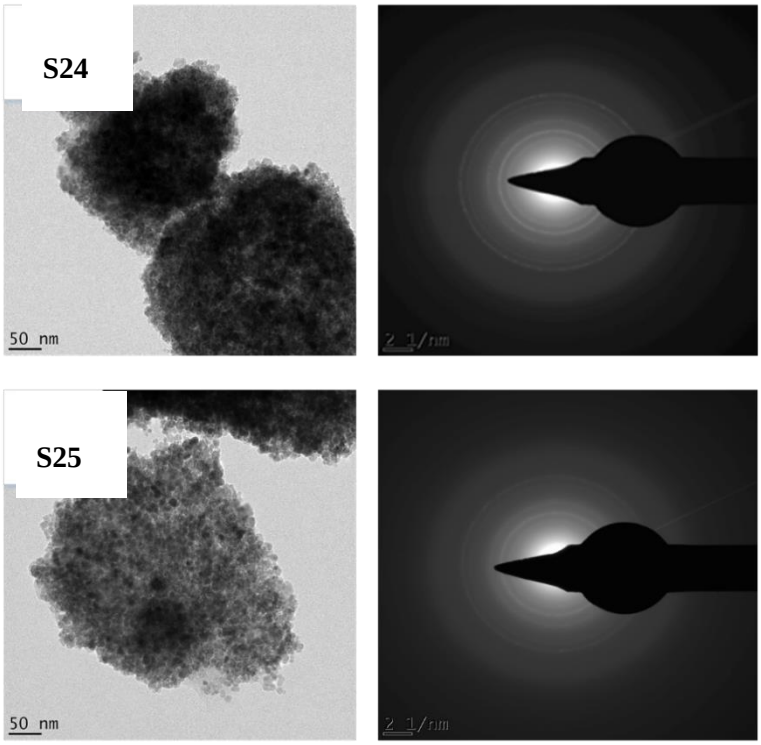

Figure 4.43: HRTEM images of **S24** and **S25**.

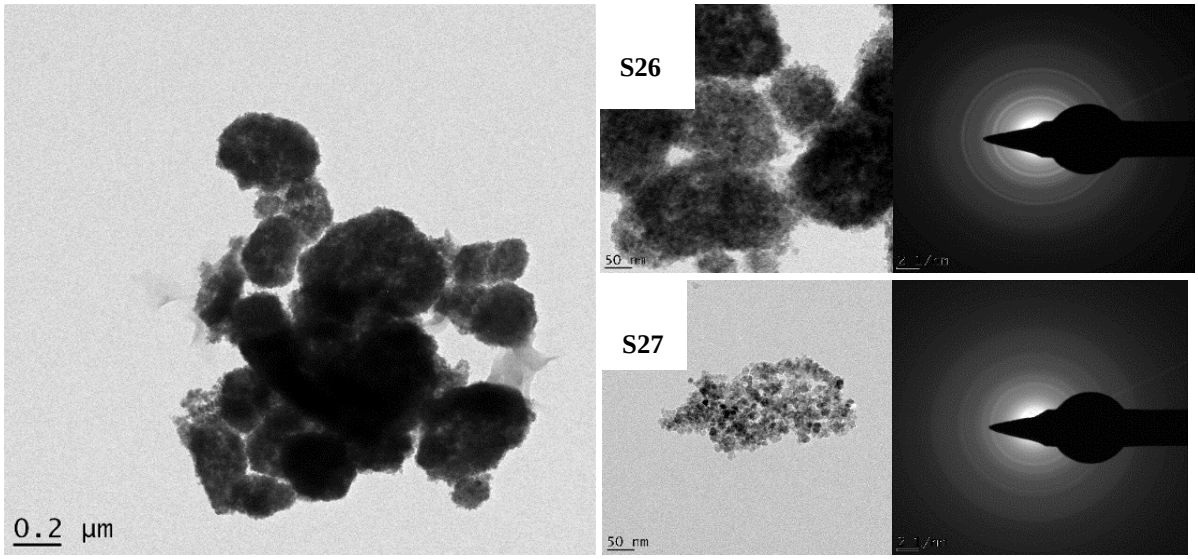

Figure 4.44: HRTEM images of **S26** and **S27**.

4.3 STABILITY OF THE NANOPARTICLES

Stability of **S4** and functionalised MIONs in acidic solutions was investigated by conducting leaching experiments in aqueous HCl solutions of various pH's. The naked MIONs (**S4**), **S4-DM_{15}(c)** (**S12**), **S4-C_{15}(c)** (**S21**), and **S4-C_{15}(c)-DM_{15}** (**S27**) were dispersed in water at pH 1.0,

Stellenbosch University https://scholar.sun.ac.za

3.0 and 5.0. The mixture was then shaken at 150 rpm for 2 h. The concentration of Fe leached into solution was determined by ICP-OES. The results obtained are as shown in **Figure 4.45**. From the figure, it was clear that, high concentration of Fe was leached into the solution at the pH of 1.0 for all the adsorbents except for **S27**, demonstrating its stability at very low pH's. However, at the pH of 2.0 and 3.0, the dissolution of all the four materials, including naked MIONs (**S4**) was significantly reduced. Vatta *et* al.[171] also reported that the stability of MIONs was improved after their functionalisation with silica.

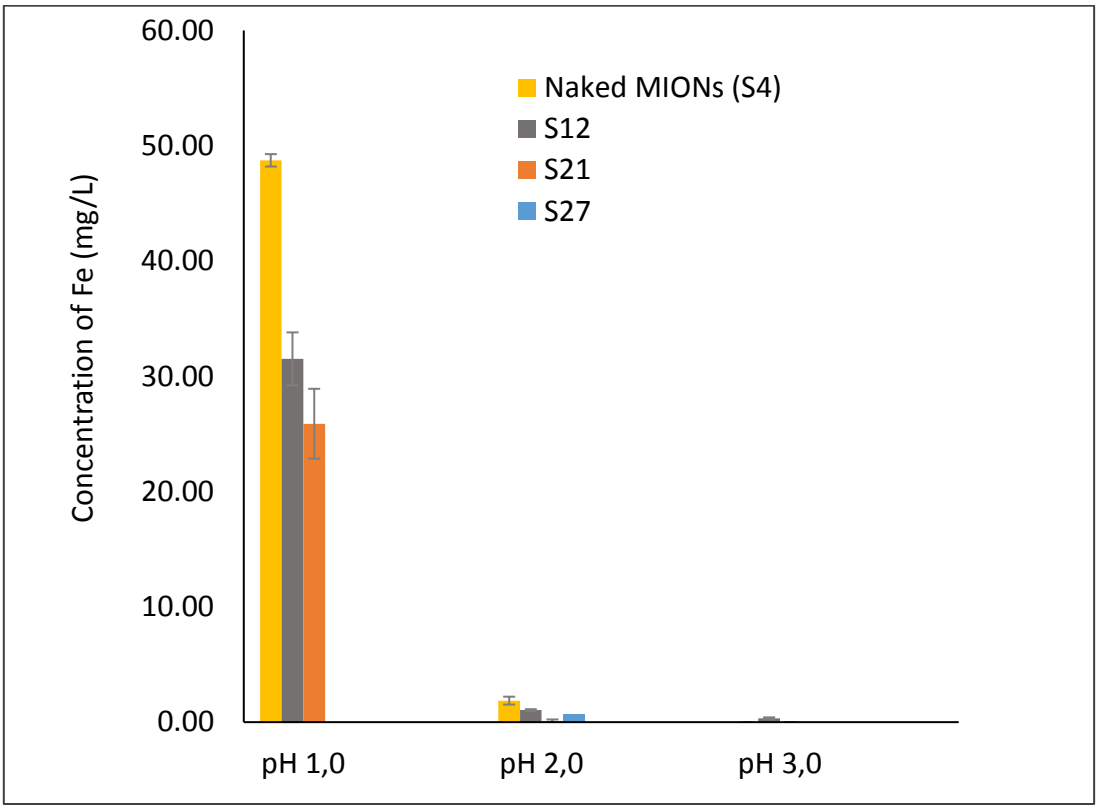

Figure 4.45: The concentration of iron leached from **S4**, **S12**, **S21** and **S27** at pH 1.0, 3.0, and 5.0.

4.4 CONCLUSION

The surface of naked MIONs (**S4**) were successfully modified with different organic compounds: aliphatic carboxylic acids and G3 DAB PPI dendrimer micelles. The **DM_n (n = 5, 11, 15)** were successfully prepared by modifying commercially purchased G3 DAB PPI dendrimer with hexanoyl chloride, lauryl chloride, and palmitoyl chloride while the aliphatic carboxylic acids were used without modification. The **DM_n** were characterised with the following analytical techniques by FT-IR, ^{1}H NMR and ^{13}C NMR spectroscopy which confirmed the amidation of the end-groups of the dendrimer.

Stellenbosch University https://scholar.sun.ac.za

These **DM_{15}** were used as stabilising agents for the naked MIONs (**S4**) and the resultant MIONs were referred to as **S10**, **S11** and **S12**. The presence of **DM_{15}** on the surface of **S10**, **S11** and **S12** was characterised by IR and TGA analysis. HRTEM, Powder XRD and SAED analysis confirmed that **S4** were still magnetite nanoparticles after their modification. HRTEM and PXRD determined the particle size of **S10**, **S11** and **S12** to be in the range of 12 nm to 14 nm. The particle sizes analysis of MIONs modified with **DM_{15}** by both HRTEM and PXRD techniques were in good agreement.

The MIONs were further stabilised using hexanoic acid (**C_5-acid**), lauric acid (**C_{11}-acid**) and palmitic acid (**C_{15}-acid**) and the products of were called **S4-C_n(a, b, c)**, n = 5, 11,15. IR spectroscopy and TGA results showed that MION (**S4**) have a higher binding affinity for long chain carboxylic acids **C_{11}-acid** and **C_{15}-acid** than the short chain **C_5-acid**. The average particle size of the **S4-C_n(a, b, c)** as determined by HRTEM and PXRD was the range of 10 nm to 15 nm. The **S4-C_n(b, c)** were also further stabilised with **DM_n** producing doubly stabilised MIONs referred to as **S4-C_n(b,c)-DM_n**. It was postulated that the MIONs were stabilised by the intercalation of the alkyl chains of the **DM_n** and the aliphatic acids (**C_{11}** acid and **C_{15}** acid). Successful modification of **S4-C_n(b,c)** with the **DM_n** was confirmed by IR spectroscopy and HRTEM analysis.

Leaching experiments in aqueous HCl solutions at the pH range of 1.0 to 3.0 confirmed that modified MIONs are more stable than naked MIONs, showing the efficacy of using both **C_{15}-acids** and **DM_{15}** as stabilised for MIONs.

4.5 EXPERIMENTAL

4.5.1 Materials

All the chemicals were purchased either from Merck or Sigma-Aldrich and were used without further purification. Distilled deionized water (Milli-Q, 18 MΩ cm) was deoxygenated by bubbling with pure N_2 gas for 30 min prior to use.

4.5.2 Characterisation techniques

Infrared spectra were recorded using PerkinElmer spectrum Two IR spectrometer. A very small amount of dried **S4**-MIONs were mixed with dried KBr salt finely ground and pressed into a

Stellenbosch University https://scholar.sun.ac.za

pellet. A sample of finely crushed pure KBr was used as the background. The spectra were collected between 4000 and 400 cm^{-1} using 32 scans at a nominal resolution of 4.0 cm^{-1} and were presented without background correction.

For TGA measurements, samples were dried at 40 °C overnight in the oven. The mass loss from 5 – 15 mg of dried sample was monitored under N_2 at a temperature from 25 °C to 600 °C at the rate of 10 °C/min.

Structural properties of the **S4**-MIONs obtained were investigated by Powder X-ray diffraction (XRD) with a Siemens D8 Advance diffractometer using Cu Kα radiation (λ = 1.540 Å) operated at 40 kV and 30 mA. XRD patterns were recorded in the range 10 º – 90º (2θ) with a scan step of 0.02°. The average crystallite size (<D>, nm) was calculated from line broadening analysis using the Debye-Scherrer formula.[1, 2]

Particle size, morphology and selected area electron diffraction patterns (SAED) were determined using JEOL-1200EXII electron microscope, high resolution transmission electron microscopy (HRTEM). An accelerating voltage of 250 KV was used throughout. A drop of sample was placed on a carbon-coated 200 mesh copper grid. The sample was dried under UV lamp and attached to the sample holder. The average particle size was determined by counting more than 250 individual particles using ImageJ software.

4.5.3 Synthetic procedures

4.5.3.1 Synthesis of hexanoyl chloride modified dendrimer micelles, **DM_5**

The hexanoyl chloride modified generation 3 poly(propyl imine)dendrimer micelles were prepared using a literature procedure reported by Stevelmans and co-workers.[161] In summary, a solution of (0.182 g, 0.108 mmol) in THF (20 ml), triethylamine (3 mL) and hexanoyl chloride (0.256 g, 1.90 mmol) were added to a 100 mL round bottom flask. The mixture was stirred for 72 hrs at 25±2 °C and the solvent was evaporated using a rotary evaporator at 65 °C. The solid collected was then heated under reflux in 50 mL of diethyl ether for 30 min and filtered to remove excess hexanoyl chloride. To the residue, a solution of Na_2CO_3 (0.25 g) in H_2O (50 mL) was added, and the mixture was heated under reflux for 16 hrs, to remove residual ammonium salts and to deprotonate the dendrimers. The product was a yellow oil and was recovered by decanting off the solution. The IR and NMR spectroscopy results compared well

Stellenbosch University https://scholar.sun.ac.za

with that found in the literature.[172] IR (cm^{-1}): amide N-H stretch (3292), saturated C-H (2915, 2848), sec. amide NHC=O (1635), N-H bend (1549). ^{1}H NMR (300 MHz, $CDCl_3$): δ 0.82 (t, *J* = 6.7 Hz), 1.24 (d, *J* = 3.4 Hz), 1.53 (dd, *J* = 20.1, 13.4 Hz), 1.87 – 1.68 (m), 2.42 – 1.96 (m), 3.20 (d, *J* = 5.6 Hz), 3.22 (s), 7.07 (t, NHCO). ^{13}C NMR (101 MHz, $CDCl_3$) δ 14.27 (s), 22.84 (s), 25.08 (d,), 26.14 (s), 27.26 (s), 29.97 – 29.40 (m), 32.08 (s), 36.83 (s), 37.95 (s), 51.61 (s), 52.52 (d, *J* = 31.7 Hz), 173.90 (s).

4.5.3.2 Synthesis of lauryl chloride modified dendrimer micelles with, **DM_{11}**

The lauroyl chloride modified generation G3 DAB-PPI dendrimer micelles (**DM_{11}**) was prepared using a similar method used for the synthesis of **DM_5**. A solution of G3 DAB-PPI dendrimer (0.543 g, 0.322 mmol) in THF (20 ml), triethylamine (3 mL) and lauroyl chloride (1.24 g, 5.67 mmol) were added to a 100 mL round bottom flask. The mixture was stirred for 72 hrs at 25±2 °C and the solvent was evaporated using a rotary evaporator at 65 °C. The solid collected was then heated under reflux in 50 mL of diethyl ether for 30 min and filtered to remove excess lauroyl chloride. To the residue, a solution of Na_2CO_3 (0.5 g) in H_2O (50 mL) was added, and the mixture was heated under reflux for 16 hrs, to remove residual ammonium salts and to deprotonate the dendrimers. The product (white-yellow solid) was recovered by filtration. IR (cm^{-1}): amide N-H stretch (3285), saturated C-H (2916, 2848), sec. amide NHC=O (1634), N-H bend (1546). ^{1}H NMR (300 MHz, $CDCl_3$) 0.81 (t, *J* = 6.7 Hz, 3H), 1.27 (d, *J* = 53.9 Hz, 14H), 3.20 (d, *J* = 5.7 Hz, 5H), 3.31 – 0.75 (m, 35H), 3.20 (d, *J* = 5.7 Hz, 3H), δ 7.56 – 7.23 (m, 1H), ^{13}C NMR (151 MHz, $CDCl_3$)δ 14.27 (s), 22.94 – 22.76 (m), 26.15 (s), 24.91 (s), 29.53 (s), 27.28 (s), 30.02 – 29.57 (m), 32.09 (s), 36.84 (s), 37.93 (s), 51.60 (s), 52.36 (s), 173.91 (s).

4.5.3.3 Synthesis of palmitoyl chloride modified dendrimer micelles with, **DM_{15}**

The palmitoyl chloride modified generation G3 DAB-PPI dendrimer micelles, **DM_{15}** were prepared using a similar method used for the synthesis of the **DM_5**. A solution of G3 DAB-PPI (0.473 g, 0.280 mmol) in THF (20 ml), triethylamine (3 mL) and palmitoyl chloride (1.36 g, 4.94 mmol) were added to a 100 mL round bottom flask. The mixture was stirred for 72 hrs at 25±2 °C and the solvent was evaporated using a rotary evaporator at 65 °C. The solid collected was then heated under reflux in 50 mL of diethyl ether for 30 min and filtered to remove excess palmitoyl chloride. To the residue, a solution of Na_2CO_3 (0.5 g) in H_2O (50 mL) was added,

Stellenbosch University https://scholar.sun.ac.za

and the mixture was heated under reflux for 16 hrs, to remove residual ammonium salts and to deprotonate the dendrimers. The product (white-yellow solid) was recovered by filtration. IR (cm^{-1}): amide N-H stretch (3294), saturated C-H (2915, 2848), sec. amide NHC=O (1635), N-H bend (1550). ^{1}H NMR (300 MHz, $CDCl_3$) 0.81 (t, J = 6.7 Hz, 16H), 1.87 – 0.46 (m), 2.60 – 1.87 (m), 3.19 (d, J = 5.7 Hz, 16H), 7.20 (s, 2H). ^{13}C NMR (151 MHz, $CDCl_3$) δ 14.27 (t), 22.94 – 22.66 (m), 25.22 (s), 24.91 (s), 26.15 (s), 27.28 (s), 30.02 – 29.57 (m), 32.09 (s), 36.84 (s), 51.60 (s), 52.52 (d), 173.91 (s).

4.5.3.4 Synthesis of MIONs modified with **DM_{15}** (**S4-DM_{15}**)

The **S4-DM_n** were prepared by dispersing a recommended amount of naked MIONs (**S4**) in a degassed chloroform solution containing dendrimer micelles (**DM_{15}**). The mixture was stirred for three days at 60 °C. The modified MIONs were separated *via* magnetic decantation and dried in the oven at 40 °C.

4.5.3.5 Synthesis of aliphatic carboxylic acid stabilised MIONs (**S4-C_n**)

The synthesis of long chain carboxylate stabilised MIONs ((**S4-C_n** where n = 5, 11 and 15) was performed using the method adapted from Hatton and co-workers.[173] Three modifications were made: (I) precipitation temperature of 60 °C was used instead of 90 °C, (ii) NH_4OH was only added once off, for precipitation of the nanoparticles, and (iii) furthermore, a solution of long chain carboxylic acid was added to the reaction mixture once off. In a typical synthesis to obtain 0.966 g of naked MIONs, $FeCl_3{\cdot}6H_2O$ (2.255 g) and $FeSO_4{\cdot}7H_2O$ (1.16 g) (molar ratio of 2:1, the total iron concentration was 0.125 M) were dissolved in 100 ml of degassed deionised water. A solution of a neat long chain carboxylic acid in 10 mL acetone was added to the solution of Fe^{2+} and Fe^{3+} salts. Then, an excess amount of NH_4OH (33%) was added to the pre-warmed mixture at 60 °C and the reaction temperature increased to 90 °C. Formation of a black precipitate was observed. The reaction mixture was further stirred for 60 minutes and finally slowly cooled to room temperature. This was followed by washing the resultant nanoparticles with distilled water until the pH of the water was 7 (to remove unreacted salts). To remove an excess of the unreacted carboxylic acid, the product was further washed with a mixture of methanol and acetone (3 x 5 mL). Lastly, the resulted nanoparticles were dried in the oven at 40 °C.

Stellenbosch University https://scholar.sun.ac.za

4.5.3.6 Synthesis of dendrimer micelle (**DM_n**) modified **S4-C_n(b,c)**

Freshly prepared and washed **S4-C_n(b, c)** (n = 5, 11, 15) were dispersed in 50 ml of degassed methanol/chloroform and the mixture was heated to 35 °C. A solution of **S4-C_n** was added drop wise to the slurry and the reaction mixture was stirred overnight under nitrogen. The resultant nanoparticles were recovered using magnetic-decantation. These **S4-C_{15}** modified with dendrimer micelles were called **S4-C_{15}-DM_{15}**.

Stellenbosch University https://scholar.sun.ac.za

CHAPTER 5 : COMPETITIVE SORPTION OF Au(III), Pd(II) AND Pt(IV) COMPLEXES WITH MODIFIED MIONs

5.1 INTRODUCTION

Some of the modified MIONs prepared in **Chapter 4** (**S4-DM$_{15}$(c)**, (**S12)**, **S4-C$_{15}$(c)** (**S21**) and **S4-C$_{15}$(c)-DM$_{15}$** (**S27)** and naked MIONs (**S4**) were used in competitive adsorption of Au(III)-Cl, Pd(II)-Cl, and Pt(IV)-Cl complexes from acidic aqueous solutions. **Figure 5.1** shows schematic representation of these four adsorbents: **S4**, **S12**, **S21** and **S27**, their synthesis and characterisation are discussed in **Chapter 4**. The influences of experimental conditions on adsorption such as the effect of pH and contact time were studied. Three kinetics models used to analyse the data were: *pseudo*-first-order, *pseudo*-second-order, and intraparticle diffusion. The equilibrium adsorption data were analysed by Langmuir and Freundlich adsorption isotherms. The preliminary desorption studies were performed using 1 M HNO_3, 0.5 M thiourea and 1 M HNO_3/0.5 M thiourea.

In the literature, adsorption of metal ions from aqueous solutions has been performed using MIONs stabilised/functionalised with PAMAM dendrimers.[157,174] As mentioned earlier in **Chapter 4**, MIONs were modified with G3 DAB PPI dendrimer micelles. Therefore, it is important to discuss some few similarities and distinctions between PAMAM and PPI dendrimers (**Figure 5.2**). Both dendrimers are commercially available and can be prepared by either divergent or convergent method. As depicted in **Figure 5.2**, the nature of the repeating units results in the interior of a PPI dendrimer are less hydrophilic than that of a PAMAM dendrimer; the less polar $(–CH_2-)_3$ repeating units rendering the PPI dendrimer more hydrophobic compared to the more polar, oxygen containing repeating units of the PAMAM dendrimer. Furthermore, PPI is smaller than PAMAM for equivalent generations. This is illustrated in **Figure 5.3** which shows that a PPI dendrimer must reach generation 5 to have an equivalent radius to a generation 3 PAMAM dendrimer (≈ 1.8 nm). As is further illustrated in **Figure 5.3**, this is due to the PPI dendrimer having a shorter repeating unit ($-CH_2CH_2CH_2-$) compared to a PAMAM dendrimer repeating unit ($-CH_2CH_2COCH_2CH_2-$).

Stellenbosch University https://scholar.sun.ac.za

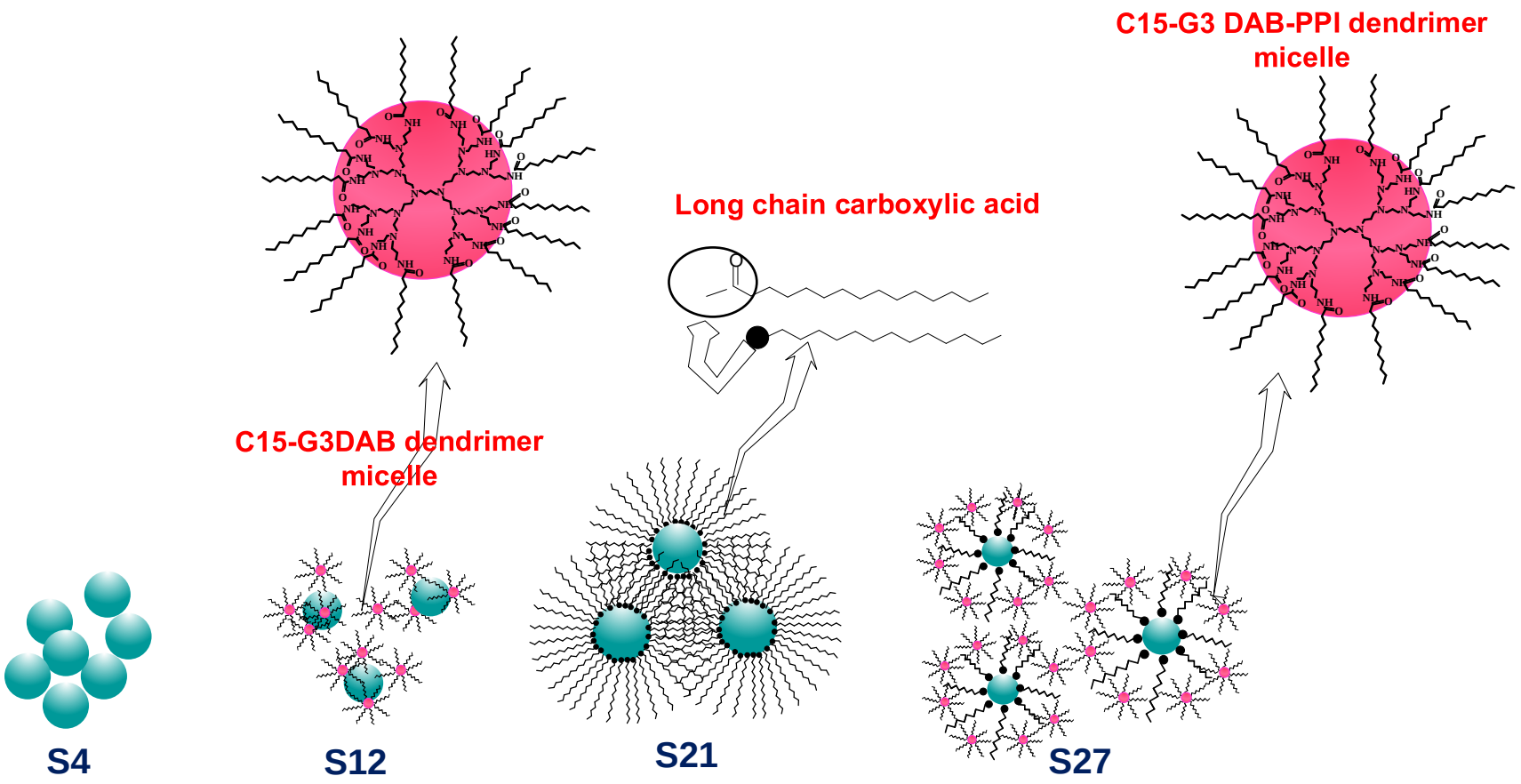

Figure 5.1: Schematic representation of adsorbents (**S4, S12, S21** and **S27**) used for competitive adsorption of Au(III)-Cl, Pd(II)-Cl and Pt(IV)-Cl from acid aqueous solutions

Stellenbosch University https://scholar.sun.ac.za

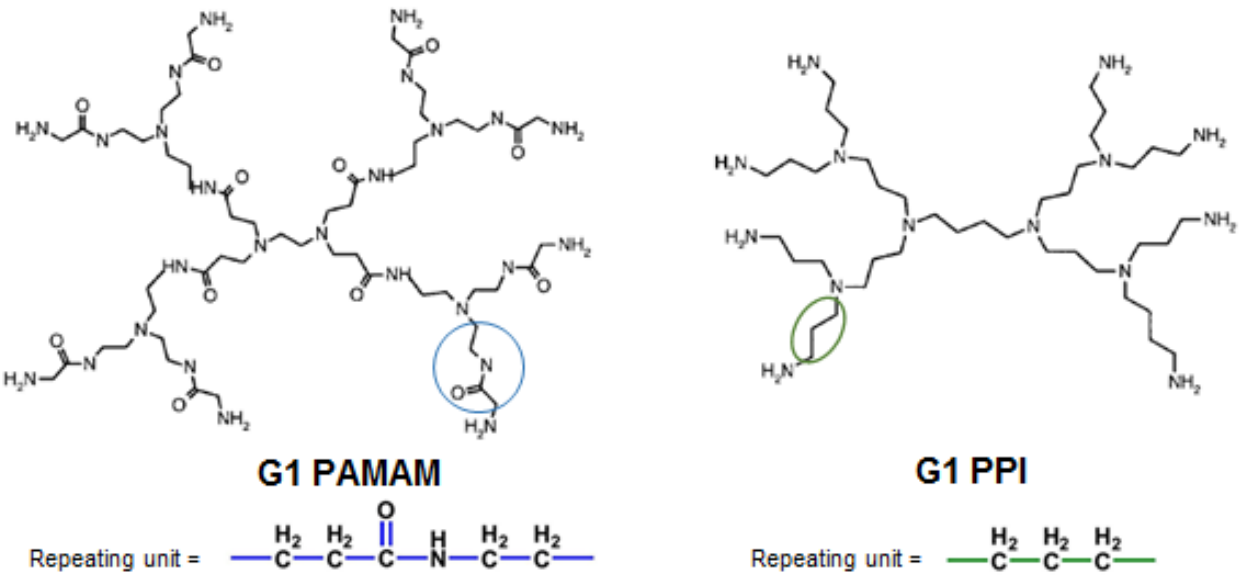

Figure 5.2: Structures of G1 PAMAM and G1 PPI dendrimers.

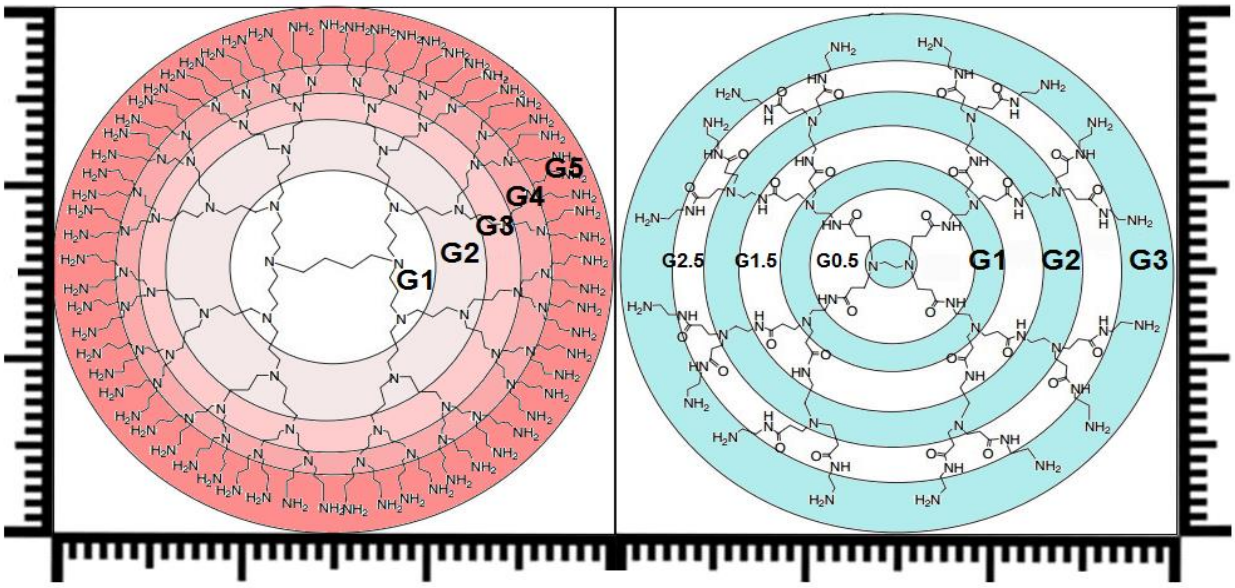

Figure 5.3: Comparison of equivalent dendrimer generation radii of PPI (left) and PAMAM (right).

Several reports in the literature have shown that Poly(amido amine) (PAMAM) and poly(propylene imine) (PPI) dendrimers can bind to metal ions.[96,175,176] Compared to traditional chelating agents such as triethylene tetraamine, dendrimers have higher binding capacity.[83,175] Furthermore, their binding capacity can be improved by using high generation dendrimers. For

Stellenbosch University https://scholar.sun.ac.za

instance, Diallo and co-workers,[177] who first reported the chelating binding affinities of PAMAM dendrimers to Cu(II) ions from an aqueous solution showed that generation 2,3, and 6 hydroxyl-terminated PAMAM bind 4,8, and 64 Cu(II) ions in aqueous solutions, respectively.

5.1.1 Dendrimer functionalised MIONs for recovery of metal ions

The binding affinity of metal ions to PAMAM dendrimers indicates that dendrimers can be used as chelating agents to remove metal ions from wastewater solutions.[157,177–179] The bound metal ions can be released by protonation of the primary and tertiary amine groups on dendrimer scaffolds and the dendrimer recovered for reuse.[157] Diallo *et al*.[177] reported the recovery of Cu^{2+} from aqueous solutions using a PAMAM dendrimer enhanced ultrafiltration (DEUF) systems. The system achieved almost complete removal of Cu^{2+} ions with initial concentration of 10 ppm and Cu^{2+} to PAMAM dendrimer-NH_2 ratio of 0.2. After adsorption, the metal ion loaded dendrimers were recovered by ultrafiltration and re-generated by decreasing the pH to 4.0. Although studies showed that the PAMAM dendrimers have low tendencies to foul cellulose membranes, fouling is still one of the main problems in any membrane separation.[157,180]

Dendrimers supported on solid material are efficient alternatives for DEUF in the removal of metal ions from aqueous solutions.[174,178] For example, silica gel supported dendrimers have been used as an adsorbent for the adsorption of heavy metals such as Hg(II) and other base metals in water.[81,89,174] Zhang *et al*.[83] employed generation 3 polyamidoamine dendronized hollow fibre membrane (G3-HFM) in the recovery of heavy metal ions (Cu^{2+}, Pb^{2+}, and Cd^{2+}) from solutions. G3-HFM were selective towards Cu^{2+} with binding capacity of 583.8 µmol/g of dry G3 HFM which Pb^{2+} and Cd^{2+} have 263.6 µmol/g of dry G3 HFM and 255.6 µmol/g dry G3 HFM respectively. About 80 %, 76 %, and 78 % of the bound Cu^{2+}, Pb^{2+}, and Cd^{2+} ions, respectively, were desorbed from G3-HFM using HCl solution with pH of 2.0. However, these materials are normally collected by centrifugation or filtration process which presents many challenges for practical purposes.

In the literature, PAMAM and PPI dendrimers have been used as templating agents for the synthesis of dendrimer encapsulated metal nanoparticles (DENs).[158,181,182] To prepare DENs, metal ions coordinate with the interior functional group of the dendrimer which are then reduced with an

Stellenbosch University https://scholar.sun.ac.za

appropriate reducing agent from the nanoparticles. Schematic representation of the synthesis of DENs is shown in **Figure 5.4**. This method is considered as the best method for synthesising monodispersed nanoparticles.[96,175,181,182] PAMAM and PPI dendrimers and their derivatives are now commercially available. Although high cost is involved with these promising polymers, recently developed click chemistry allows the synthesis of high-generation PAMAM dendrimers within a couple of days, which significantly reduce the synthesis time and costs.[83]

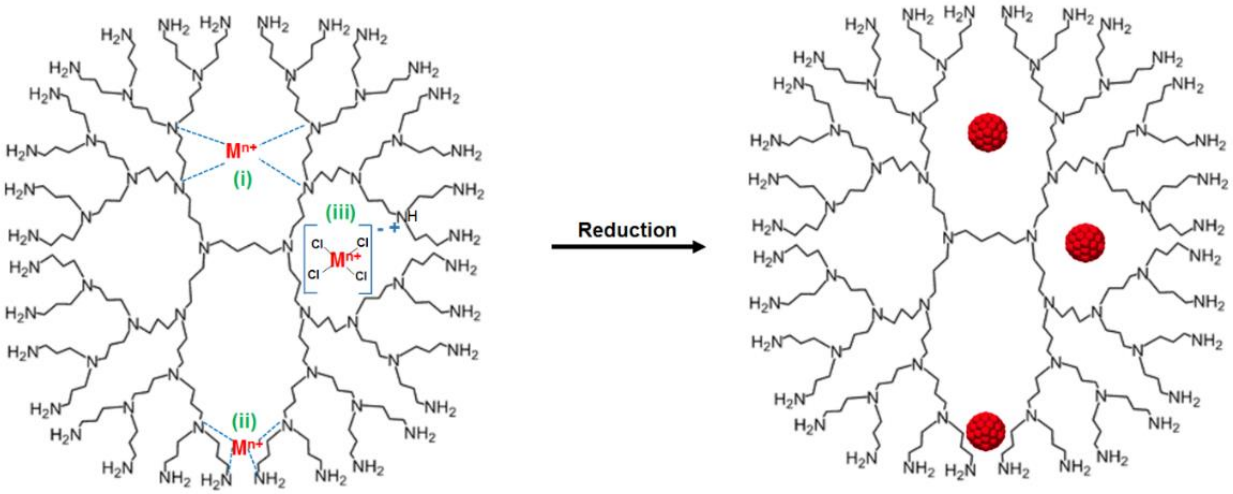

Figure 5.4: Schematic representation of the possible coordination sites of metal ions and formation of DEN within the dendrimer scaffold.

Recently, some researchers have studied the use of dendrimers immobilised on magnetic nanoparticles for removal of metal ions. For instance, Chou and Lien used PAMAM dendrimer-conjugated magnetic nanoparticles (Gn-MNPs) for removal of Zn(II) from aqueous solutions.[157] The Gn-MNPs effectively removed Zn(II) from aqueous solutions, and more than 75 % of the total Gn-MNPs were recovered after 10 consecutive cycles. The repetitive adsorption and desorption studies indicated that Zn(II) was rapidly removed by G3-MNPs in each cycle, and the recovery of Zn(II) had an average greater than 90 % in 10 cycles.

Lien *et al.*[81] reported adsorption of precious metals (Pt(IV)-Cl, Pd(II)-Cl, Au(III)-Cl and Ag(I) from water samples using dendrimer modified magnetic nanoparticles (MNP-G3) and MNP-G3 modified by ethylenediaminetetraacetic acid (EDTA) (MNP-G3-EDTA). The maximum adsorption capacity determined by the linear Langmuir model for Pt(IV)-Cl, Au(III)-Cl, Pd(II)-Cl

Stellenbosch University https://scholar.sun.ac.za

and Ag(I) were 3.60 mg/g, 3.58 mg/g, 2.75 mg/g, and 2.84 mg/g respectively. The metal loaded MNP-G3 was regenerated using 1.0 % HCl. The recyclability of MNP-G3 was tested by running repetitive adsorption and desorption of Pt(IV)-Cl for 6 cycles, and the adsorbent achieved around 90 % - 95 % in each cycle, suggesting that the adsorption ability of reused MNP-G3 remains relatively stable.

5.2 RESULTS AND DISCUSSIONS

5.2.1 Batch sorption experiments

The competitive adsorption studies of Au(III)-Cl, Pd(II)-Cl and Pt(IV)-Cl complexes using the four adsorbents naked MIONs (**S4**), **S4-DM$_{15}$(c)**, (**S12)**, **S4-C$_{15}$(c)** (**S21**) and **S4-C$_{15}$(c) DM$_{15}$ (S27)** respectively were carried out using batch experiments. The effect of pH and contact time in adsorption were investigated. The concentration of Au(III)-Cl, Pt(II) and Pd(IV) complexes were determined before and after adsorption by inductively coupled plasma optical emission spectroscopy (ICP-OES). At the end of each run, the adsorbents were separated from the solution magnetically and supernatant decanted into a 10 mL or 15 mL conical centrifuge tube. The adsorption capacities and removal efficiency of Au(III)-Cl, Pt(II) and Pd(IV) complexes from the aqueous acidic solution was defined by **Equation 3.4** and **Equation 3.5** shown in **Chapter 3**.

5.2.1.1 Effect of pH in adsorption

The effect of pH on competitive adsorption of Au(III)-Cl, Pd(II)-Cl, and Pt(IV)-Cl complexes by naked MIONs (**S4**), **S4-DM$_{15}$(c)**, (**S12)**, **S4-C$_{15}$(c)** (**S21**) and **S4-C$_{15}$(c)-DM$_{15}$** (**S27)** respectively was evaluated by conducting competitive batch adsorption experiments at pH ranging from 1.0 to 6.0. The experiments were carried out at room temperature 25±2 °C. The aqueous phase and the shaking speed for all the experiments were 10mL and 150 rpm respectively. The solution pH was adjusted by adding very small quantities of 0.1 M HCl or 0.1 M NaOH to the solution containing the mixture of these metals with the desired initial metal complex concentration.

Stellenbosch University https://scholar.sun.ac.za

5.2.1.1.1 Naked MIONs (**S4**)

The results for competitive adsorption of Au(III)-Cl, Pd(II)-Cl and Pt(IV)-Cl using 30.30±0.0015 mg naked MIONs (**S4**) has been presented in **Figure 5.5**. As seen this figure, a high removal percentage of Au(III)-Cl was recorded compared to the removal percentages of Pd(II)-Cl and Pt(IV)-Cl. **S4** has a high adsorption affinity towards Au(III)-Cl. This result corroborated the results obtained in **Chapter 3**, where single-component batch adsorption of Au(III)-Cl, Pd(II)-Cl, and Pt(IV)-Cl chloro- anions using **S4** was performed. Another important observation is that, at pH of 1.0, **S4** selectively sorbed Au(III)-Cl.

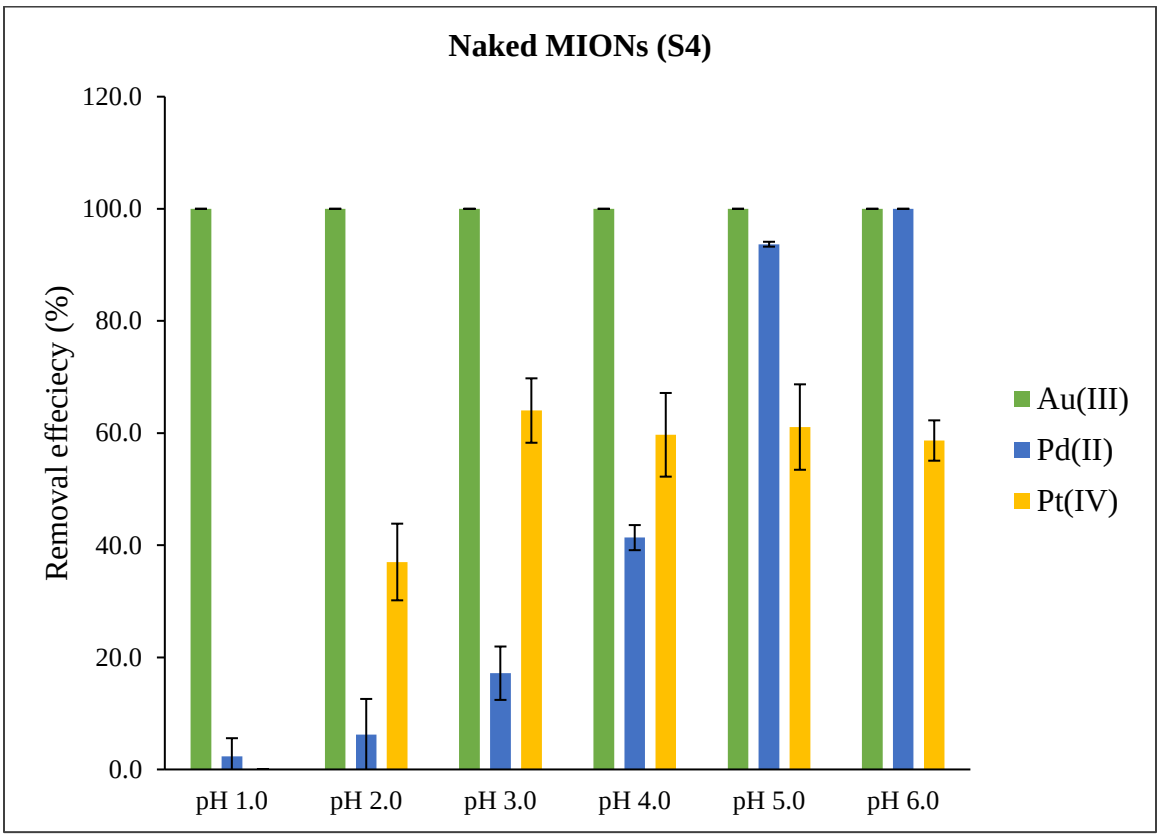

Figure 5.5: Effect of pH on sorption of Au(III)-Cl, Pd(II)-Cl, and Pt(IV)-Cl from aqueous solutions using 30.30±0.0015 mg of **S4** for 160 min at room temperature (25±2 °C). Initial metal ion concentrations ((Au(III)-Cl: 9.78±0.20 ppm, Pd(II)-Cl: 10.61±0.59 ppm, Pt(IV)-Cl: 10.24±0.059 ppm). The volume of the samples was 10mL and were shaken at 150 rpm.

Stellenbosch University https://scholar.sun.ac.za

On the other hand, removal efficiencies of Pd(II)-Cl increased significantly with an increase in pH. However, during the sample preparation, a precipitate of Pd(II)-Cl was observed at pH>4.0. Therefore, the high percentage removal observed at pH 5.0 and pH 6.0 cannot be attributed solely to adsorption of Pd(II)-Cl onto naked MIONs. Possibly, some of the Pd(II)-Cl might sit at the Schott bottle when the supernatant was transferred to the ICP tube. The adsorption efficiencies for Pt(IV)-Cl by **S4** reached a maximum of about 60 % at pH 3.0 and remained constant to pH 6.0. Therefore, the optimum adsorption of Pt(IV)-Cl using **S4** was pH 3.0.

In **Chapter 3**, it was noted that these metal chloro anions lose their chloride during adsorption and ultimately get reduced on the surface of the **S4**. However, it is worth mentioning that since adsorption was carried out using very low metal concentration, the entire surface of **S4** was not covered by the reduced species of these precious metals. Therefore, a full coverage of the **S4** was not possible.

5.2.1.1.2 **S4-DM$_{15}$(c)**, (**S12)**

The effect of pH on competitive adsorption of Au(III)-Cl, Pd(II)-Cl, and Pt(IV)-Cl using 30.15±0.055 mg of **S12** was also studied by carrying out batch adsorption studies. The results are as shown in **Figure 5.6**. As shown in this figure, **S12** shows higher adsorption affinities towards Au(III)-Cl than Pd(II)-Cl and Pt(IV)-Cl. However, the figure also shows improved adsorption percentages for Pd(II)-Cl and Pt(IV)-Cl. Therefore, an increase in removal percentages of Pd(II)-Cl and Pt(IV)-Cl suggests that the dendrimer micelle found on the surface of **S4** plays a vital role in adsorption of these precious metal chloro- species. As stated earlier, dendrimers are used as templates for the synthesis of DENs. This method has proven that various metal ions including Au(III)-Cl, Pd(II)-Cl, and Pt(IV)-Cl can be coordinated to the interior amines of the dendrimer.[181,183]

As explained earlier in **Chapter 3**, these precious metals form anionic complexes in the presence of hydrochloric acid. In acidic solution, although amine groups may contribute to metal chelation, their protonation significantly reduces their ability to react with Au(III)-Cl, Pd(II)-Cl, and Pt(IV)-Cl and it appears that most of the metal sorption can be explained by electrostatic attraction of anion metal complexes by protonated amine groups.[142,152] Based on the above findings, in HCl

Stellenbosch University https://scholar.sun.ac.za

solutions at pH<3.0, the adsorption mechanism of Au(III)-Cl, Pd(II)-Cl, and Pt(IV)-Cl using **S12** is assumed to be electrostatic attraction and ion exchange. The interaction between Au(III)-Cl, Pd(II)-Cl and Pt(IV)-Cl complexes and protonated sites of the dendrimer micelles are shown in **Equation 5.1**, **Equation 5.2**, **Equation 5.3** and **Equation 5.4**.[142]

Equation 5.1 $$R - NH_2 + H^+Cl^- \rightarrow RNH_3^+Cl^-$$

Equation 5.2 $$RNH_3^+Cl^- + AuCl_4^- \leftrightarrow RNH_3^+AuCl_4^- + Cl^-$$

Equation 5.3 $$2RNH_3^+Cl^- + PdCl_4^{2-} \leftrightarrow RNH_3^+PdCl_4^{2-} + Cl^-$$

Equation 5.4 $$2RNH_3^+Cl^- + PtCl_6^{2-} \leftrightarrow RNH_3^+PtCl_6^{2-} + Cl^-$$

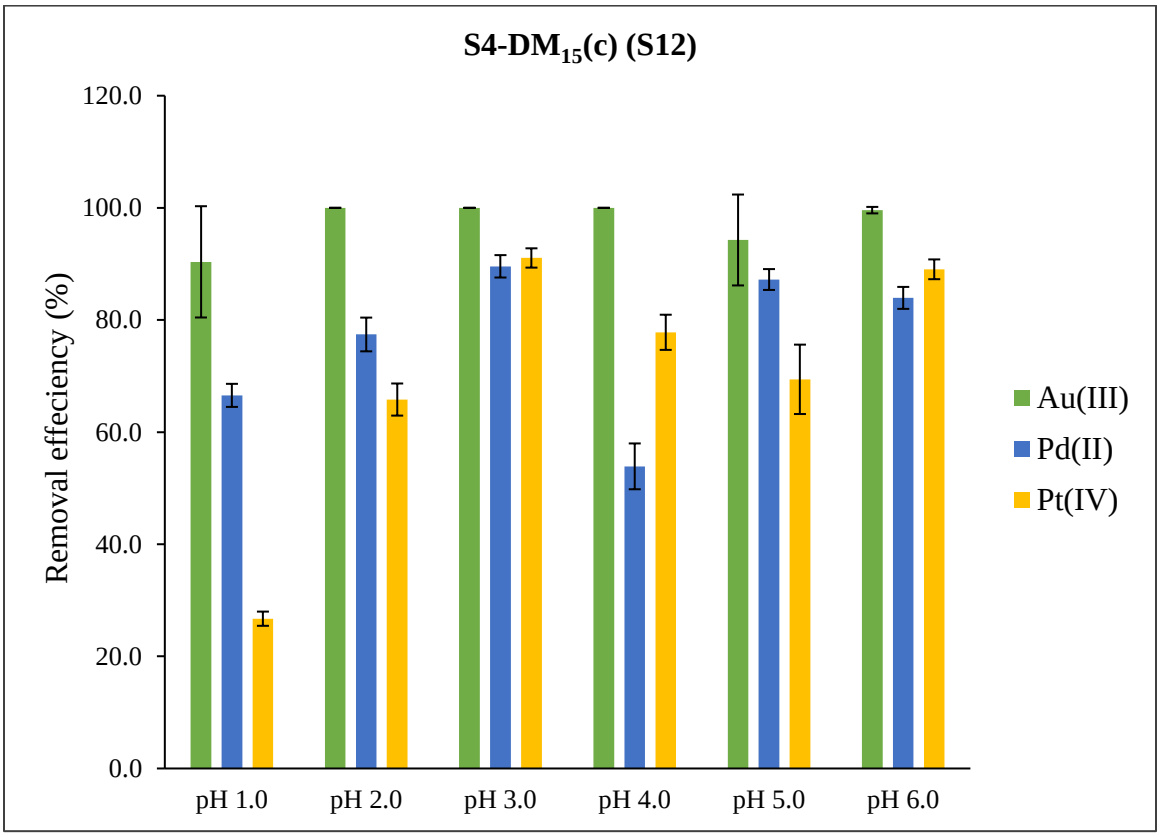

Figure 5.6: Effect of pH on sorption of Au(III)-Cl, Pd(II)-Cl, and Pt(IV)-Cl from acid aqueous solutions using 30.15±0.055 mg of **S12** at room temperature (25±2 °C). Initial metal ion concentration ((Au(III)-Cl: 9.78±0.20 ppm, Pd(II)-Cl: 10.61±0.59 ppm, Pt(IV)-Cl: 10.24±0.059 ppm). The volume of the samples was 10mL and were shaken at 150 rpm.

Stellenbosch University https://scholar.sun.ac.za

5.2.1.1.3 **S4-C$_{15}$(c)** (**S21**)

Figure 5.7 shows the results for competitive adsorption of Au(III)-Cl, Pd(II)-Cl, and Pt(IV)-Cl chloro species using 30.23±0.075 mg **S4-C$_{15}$(c)** (**S21**). Due to the large amount of alkyl chain groups of palmitic acid on the surface of **S21**, this material did not entirely disperse in solution. Therefore, the interaction between the adsorbent of the metal chloro species was limited as only a small fraction of **S21** dispersed into the aqueous phase.

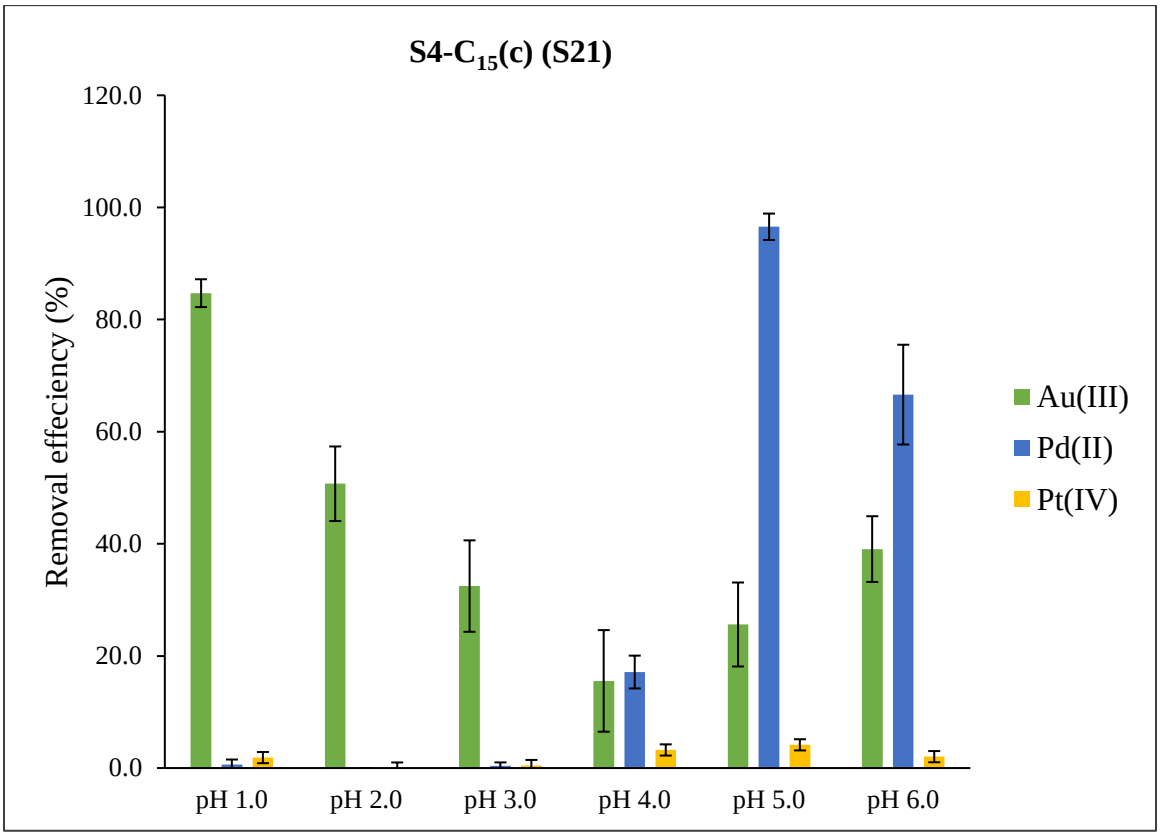

Figure 5.7: Effect of pH in adsorption of Au(III)-Cl, Pd(II)-Cl, and Pt(IV)-Cl using 30.23±0.075 mg of **S21** from acidic aqueous solutions at room temperature; 25±2 °C. Initial metal ion concentrations ((Au(III)-Cl: 9.78±0.20 ppm, Pd(II)-Cl: 10.61±0.59 ppm, Pt(IV)-Cl: 10.24±0.059 ppm). The volume of the samples was 10mL and were shaken at 150 rpm.

Adsorption results are very interesting in that **S21** is selective to Au(III)-Cl at low pH (pH 1.0 to pH 3.0). Furthermore, the removal percentage for Au(III)-Cl decreased with increasing pH (from pH 1.0 to pH 4.0). The studies of Peck and co-workers shows that at pH<4.0, the dominating

Stellenbosch University https://scholar.sun.ac.za

species of Au(III)-Cl is $AuCl_4^-$.[127] Therefore, increasing solution pH from pH 4.0 introduces hydrolysis products of Au(III)-Cl into the system. Hydrolysis products of Au(III)-Cl include $AuCl_2OHH_2O$, $AuCl_3OH^-$, $AuCl_2(OH)_2^-$ and $AuCl(OH)_3^-$. Based on these observations, it is reasonable to postulate that **S21** has a better adsorption affinity towards $AuCl_4^-$ species than its hydrolysed products.

The adsorption removal percentages of Pd(II)-Cl and Pt(IV)-Cl were very low at lower pH's. At pH>3.5, both Pd(II)-Cl and Pt(IV)-Cl hydrolyse to form hydroxy species. For Pd(II)-Cl, at the pH of 5.0, these hydroxy species form a precipitate that fall out of the solution. In summary, **S21** only sorbed Au(III)-Cl in the pH range of 1.0 to 6.0 and showed high adsorption percentages at very low pH.

5.2.1.1.4 **S4-C_{15}(c)-DM_{15} (S27)**

To further explore the efficacy of dendrimer micelle modified MIONs in competitive adsorption of Au(III)-Cl, Pd(II)-Cl, Pt(IV)-Cl, batch adsorption experiments of these metal chloro species using 30.57±0.086 mg **S27** was performed. As mentioned earlier, PAMAM dendrimers functionalised MIONs have been used by several researchers for adsorption of some heavy and precious metals.[81,157,174,178] However, the dendrimers were not sterically hindered, *i.e.* their periphery was not modified with alkyl groups as in this case.

Figure 5.8 shows the results for competitive adsorption of Au(III)-Cl, Pd(II)-Cl, and Pt(IV)-Cl using adsorbent **S27** at pH 1.0 to pH 6.0. As seen in **Figure 5.8**, **S27** shows a higher adsorption affinity for Au(III)-Cl over Pd(II)-Cl and Pt(IV)-Cl, as 100 % Au(III)-Cl was recovered at pH 1.0 to pH 6.0. Compared to adsorption efficacy of **S21**, **S27** shows improved adsorption for Au(III)-Cl as 100 % removal efficiencies were achieved at all the pH values and improved adsorption percentages for Pd(II)-Cl and Pt(IV)-Cl are seen. This improvement in adsorption percentages of Au(III) by **S27** as compared to **S21** indicates that C15 dendrimer micelles played a crucial part in competitive adsorption of these three precious metal complex anions.

At the pH range of pH 1.0 to pH 3.0, adsorption of the three metal complex anions can be ascribed to electrostatic attraction between the protonated amines and the negatively charged Au(III)-Cl,

Stellenbosch University https://scholar.sun.ac.za

Pd(II)-Cl and Pt(IV)-Cl anions as discussed earlier. However, adsorption percentages of Pd(II)-Cl using **S27** increased with an increase in solution pH. This can be attribute to precipitation of Pd(II)-Cl at pH>4.0. It is worth noting that adsorption percentages recorded for **S21** were higher than the adsorption percentages achieved with **S27**. This can be attributed to steric hindrance since **S27** had the higher density of the alkyl groups from the palmitic acid and the C15 dendrimer micelles.

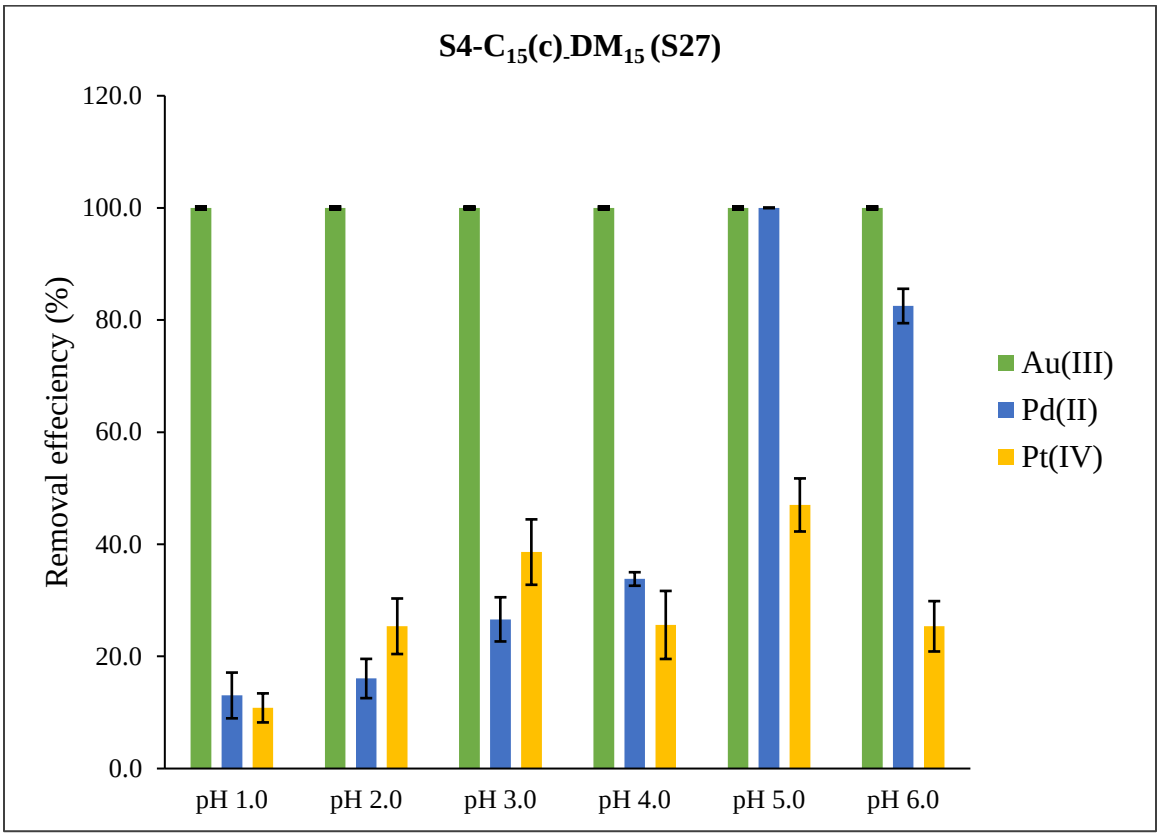

Figure 5.8: Effect of pH in adsorption of Au(III)-Cl, Pd(II)-Cl, and Pt(IV)-Cl using 30.57±0.086 mg **S27** from acidic aqueous solutions at room temperature 25±2 °C. Initial metal ion concentrations ((Au(III)-Cl: 9.78±0.20 ppm, Pd(II)-Cl: 10.61±0.59 ppm, Pt(IV)-Cl: 10.24±0.059 ppm). The volume of the samples was 10mL and were shaken at 150 rpm.

5.2.1.2 Effect of time

The effect of contact time is another important parameter when describing adsorption of metal ions from solution using the adsorbent materials. Batch adsorption experiments were carried out to study the effect of contact time (5 min to 160 min) in adsorption of Au(III)-Cl, Pd(II)-Cl, and

Stellenbosch University https://scholar.sun.ac.za

Pt(IV)-Cl using **S4**, **S12**, **S21** and **S27**. All the experiments were carried out at pH 3.0. Initial metal ion concentrations ((Au(III)-Cl: 12.01±0.50 mg/L, Pd(II)-Cl: 12.50±0.59 mg/L, Pt(IV)-Cl: 12.03±0.40 mg/L).

5.2.1.2.1 Naked MIONs (**S4**)

The effect of contact time in competitive adsorption of Au(III)-Cl, Pd(II)-Cl, and Pt(IV)-Cl chloro-anions using 30.15±0.005 mg of **S4** was performed at pH 3.0. At pH<4.0, these metal chloro-anions exist as $AuCl_4^-$, $PdCl_4^{2-}$, and $PtCl_6^{2-}$, respectively. Therefore, adsorption has been ascribed to electrostatic attraction between the positively charged naked MIONs and negatively charged metal complex anions. However, in **Chapter 3**, it was proposed that these metal complex anions might also be reduced during the adsorption process. The contact time was varied from 5 min to 160 min and the results are shown in **Figure 5.9**. As seen in the figure, adsorption percentages of each respective metal complex anions increase with time.

Nonetheless, the adsorption equilibrium for adsorption of Au(III)-Cl using naked MIONs was reached after 80 min, while adsorption equilibrium for Pd(II)-Cl and Pt(IV)-Cl was reached within 5 min. Furthermore, naked MIONs achieved 100 % removal of Au(III)-Cl indicating that naked MIONs have a high affinity for Au(III)-Cl. On the contrary, adsorption percentages of Pd(II)-Cl and Pt(IV)-Cl only reached a maximum removal percent of 30. This result corroborates our findings for single-component batch adsorption of Au(III)-Cl, Pd(II)-Cl and Pt(IV)-Cl using naked MIONs described in **Chapter 3**.

5.2.1.2.2 **S4-DM$_{15}$(c)**, (**S12)**

The effect of contact time in competitive adsorption of Au(III)-Cl, Pd(II)-Cl and Pt(IV)-Cl using 30.23±0.007 mg of **S12** was also studied at pH 3.0. The results are shown in **Figure 5.10**. As depicted in the figure, adsorption percentages increase with time. The adsorption equilibria for three metal chloro- anions was reached after 120 min. As seen in the figure, **S12** is more selective towards Au(III)-Cl than Pd(II)-Cl and Pt(IV)-Cl as 100 % of Au(III)-Cl was adsorbed compared to about 70 % adsorption percentages for Pd(II)-Cl and Pt(IV)-Cl.

Stellenbosch University https://scholar.sun.ac.za

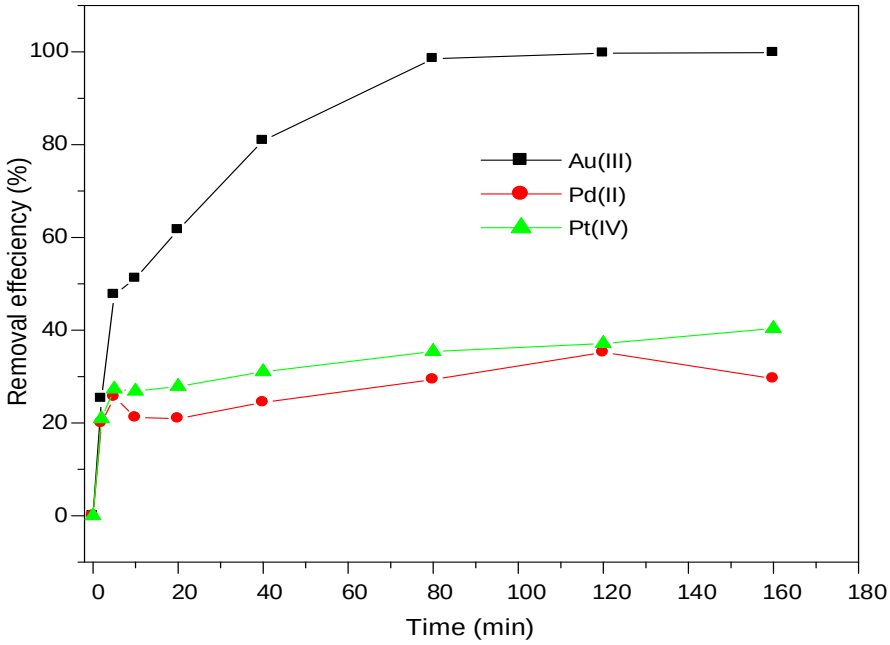

Figure 5.9: Effect of contanct time on adsorption of Au(III)-Cl, Pd(II)-Cl, and Pt(IV)-Cl using 30.15±0.005 mg of naked MIONs (**S4**) at room teperature (25±2 °C). Initial metal ion concentrations ((Au(III)-Cl: 12.01±0.50 ppm, Pd(II)-Cl: 12.50±0.59 ppm, Pt(IV)-Cl: 12.03±0.40 ppm), aqueous phase 10 mL, shaking speed 150 rpm.

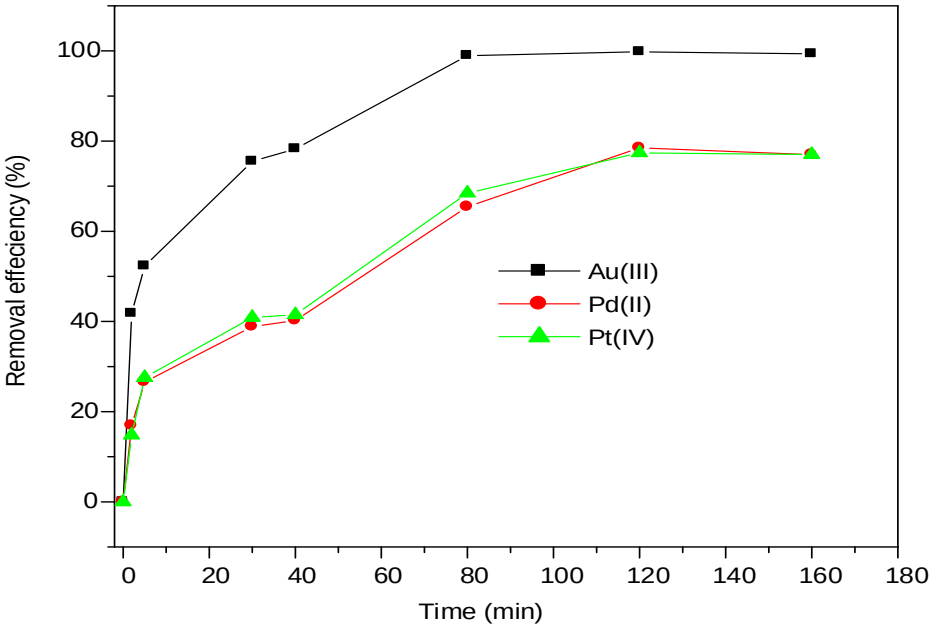

Figure 5.10: Effect of contanct time on adsorption of Au(III)-Cl, Pd(II)-Cl, and Pt(IV)-Cl using 30.23±0.007 mg of **S12** at room teperature (25±2 °C). Initial metal ion concentrations ((Au(III)-Cl: 12.01±0.50 ppm, Pd(II)-Cl: 12.50±0.59 ppm, Pt(IV)-Cl: 12.03±0.40 ppm), aqueous phase 10 mL, shaking speed 150 rpm.

Stellenbosch University https://scholar.sun.ac.za

5.2.1.2.3 **S4-C$_{15}$(c)** (**S21**)

The results for investigating the effect of contact time in adsorption of Au(III)-Cl, Pd(II)-Cl and Pt(IV)-Cl using 30.40±0.006 mg C15-MIONs_Z(**S21**) are shown in **Figure 5.11**. As seen in the figure, **S21** exhibited lower adsorption percentages for these metal chloro- anions. As mentioned earlier, this can be attributed to poor interaction between the adsorbent and the metal ion solution.

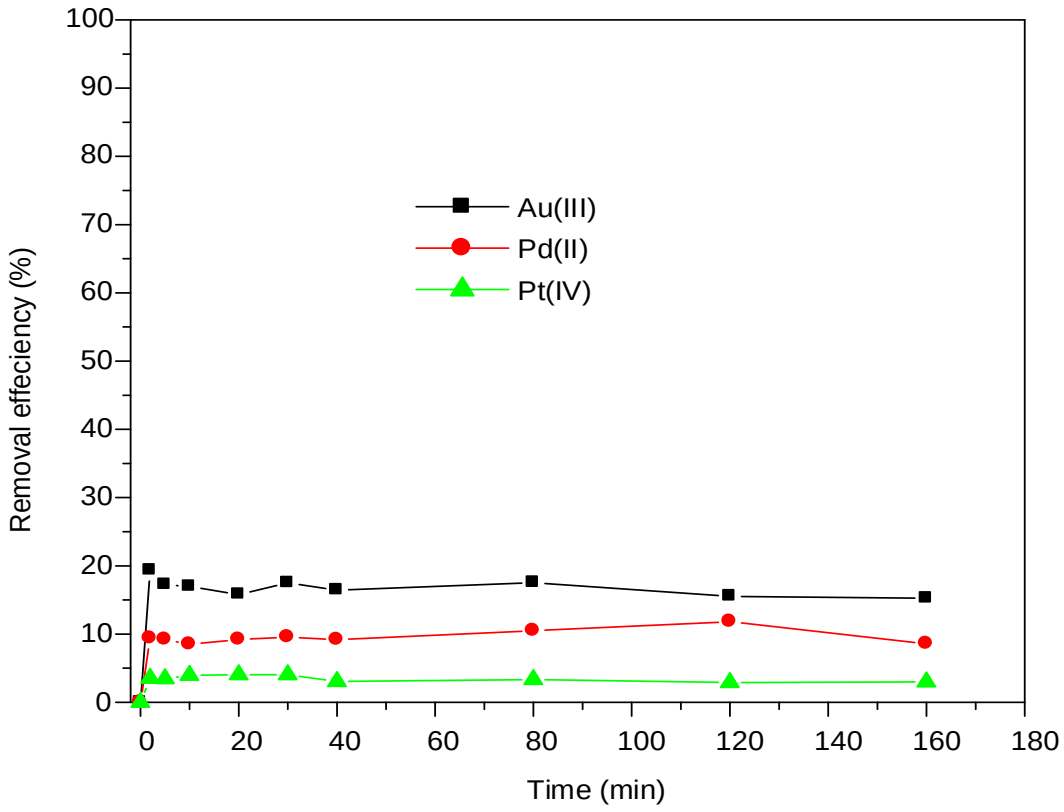

Figure 5.11: Effect of contact time on sorption of Au(III)-Cl, Pd(II)-Cl, and Pt(IV)-Cl using 30.40±0.006 mg of C15-MIONs_Z (**S21**) at room temperature (25±2 C°). Initial metal ion concentrations ((Au(III)-Cl: 12.01±0.50 ppm, Pd(II)-Cl: 12.50±0.59 ppm, Pt(IV)-Cl: 12.03±0.40 ppm) aqueous phase 10 mL, shaking speed 150 rpm.

5.2.1.2.4 **S4-C$_{15}$(c)-DM$_{15}$ (S27)**

In comparison, competitive adsorption of Au(III)-Cl, Pd(II)-Cl and Pt(IV)-Cl was carried out using 30.30±0.008 mg **S4-C$_{15}$(c)-DM$_{15}$ (S27)** at pH 3.0. Adsorption results are shown in **Figure 5.12**. As seen in the figure, **S27** showed improved adsorption percentages and selectivity to Au(III)-Cl.

Stellenbosch University https://scholar.sun.ac.za

However, less than 100 % adsorption percentages were recorded. This might be caused by the high concentration of the alkyl chains of the palmitic acid and the dendrimer micelles, obscuring the tertiary amines of the dendrimer responsible for removal of these metal ions from solution. Adsorption equilibrium for adsorption of Au(IIII) was reached after 120 min while adsorption equilibrium for adsorption of Pd(II)-Cl and Pt(IV)-Cl was reached after 40 min.

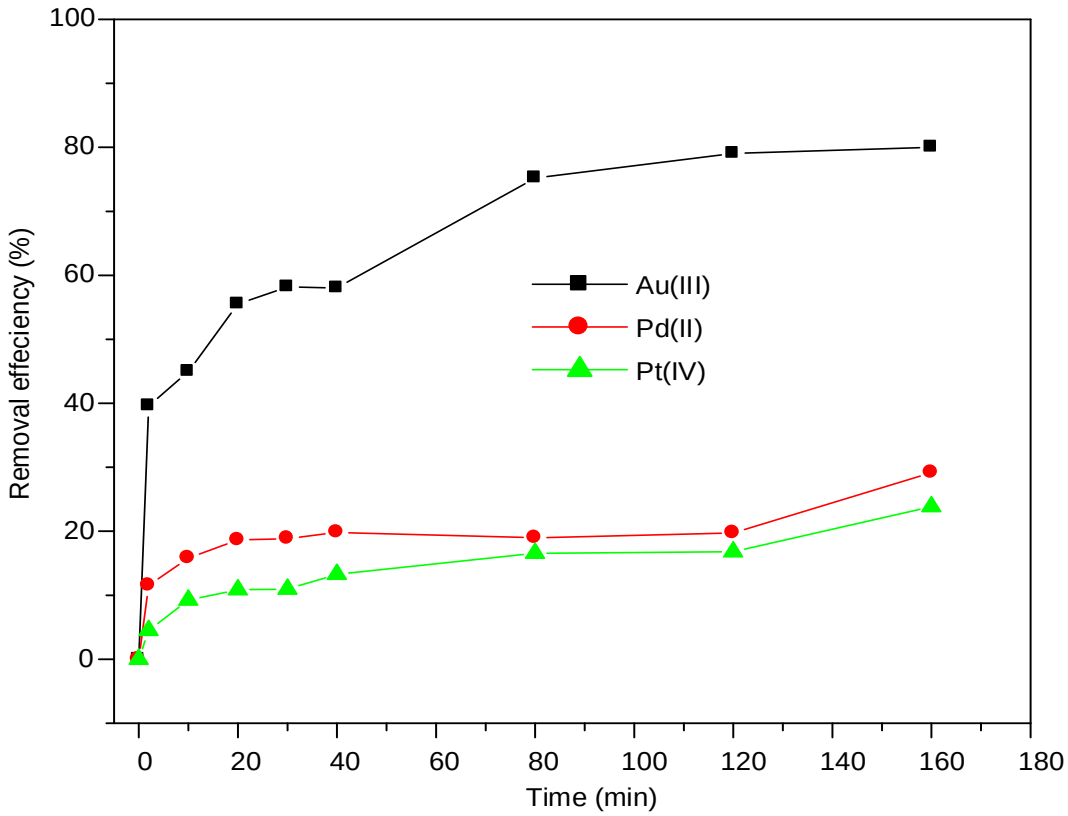

Figure 5.12: Effect of contact time in sorption of Au(III)-Cl, Pd(II)-Cl, and Pt(IV)-Cl using 30.30±0.008 mg of **S27** at room temperature (25±2 °C), Initial metal ion concentrations ((Au(III)-Cl: 12.01±0.50 ppm, Pd(II)-Cl: 12.50±0.59 ppm, Pt(IV)-Cl: 12.03±0.40 ppm). aqueous phase 10 mL, shaking speed 150 rpm.

5.2.2 Adsorption kinetics

Adsorption of the Au(III)-Cl, Pd(II)-Cl, and Pt(IV)-Cl using naked MIONs was fitted using three kinetic models which are *pseudo*-first-order, *pseudo*-second-order and intraparticle diffusion kinetic model. These kinetic models are normally used to describe the adsorption of metal ions using different solid supports.[42,153,178,184]

Stellenbosch University https://scholar.sun.ac.za

5.2.2.1 *Pseudo*-first-order kinetics model

The *pseudo*-first-order kinetics model assumes that the rate of occupation of adsorption sites is proportional to the number of unoccupied sites. The rate of the adsorptive interactions can be calculated by using the Lagergren equation shown **Equation 3.3** and **Equation 3.4** in **Section 3.2.2 (Chapter 3).** The *pseudo*-first-order plot of *log* (q_e-q_t) *versus time* for Au(III)-Cl, Pt(IV)-Cl and Pd(II)-Cl using naked MIONs as shown in **Figure 5.13**. The data points were fitted for the whole sorption period and the correlation coefficients (R^2) were 0.8329, 0.8277 and 0.4060 for Au(III)-Cl, Pt(IV)-Cl and Pd(II)-Cl, respectively. This suggests that adsorption of Au(III)-Cl, Pd(II)-Cl and Pt(IV)-Cl using naked MIONs does not follow the *pseudo*-first-order kinetics model. The R^2 values and other *pseudo*-first-order kinetics model parameters for adsorption with the four adsorbents are as shown in **Table 5.1**.

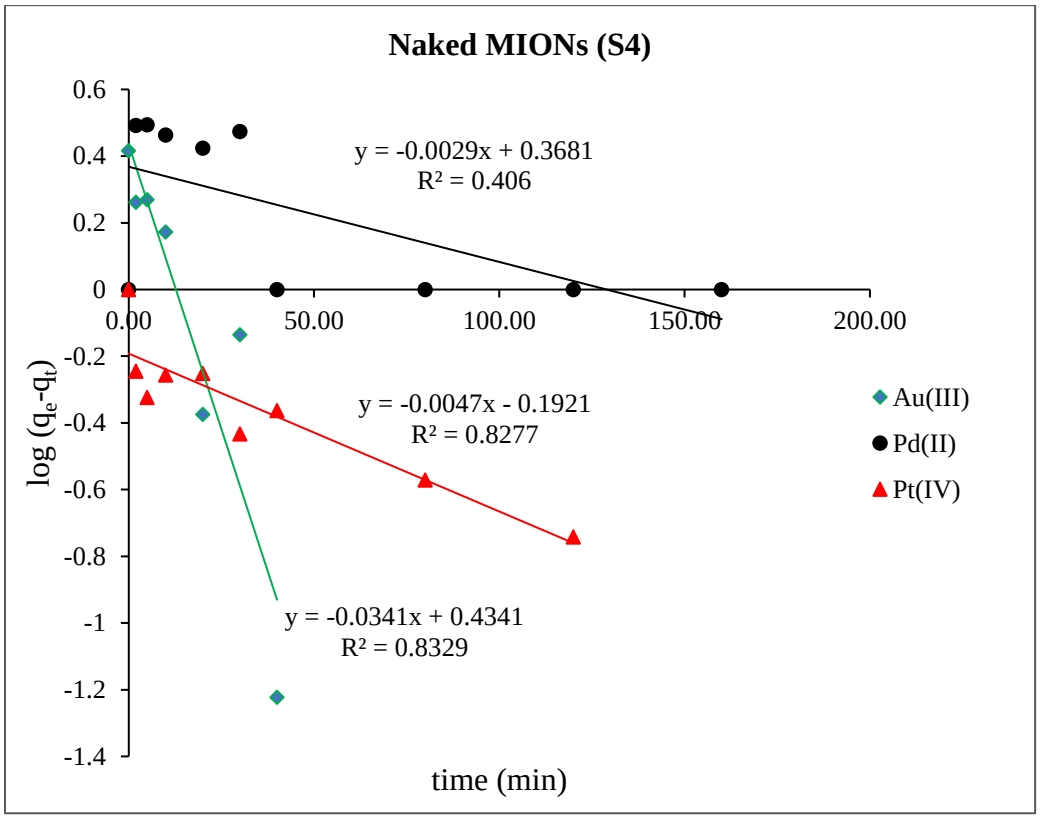

Figure 5.13: *Pseudo*-first-order kinetic plots for adsorption of Au(III)-Cl, Pd(II)-Cl, and Pt(IV)-Cl using 30.15±0.005 mg of naked MIONs at room teperature (25±2 °C). Initial metal ion concentrations ((Au(III)-Cl: 12.01±0.50 ppm, Pd(II)-Cl: 12.50±0.59 ppm, Pt(IV)-Cl: 12.03±0.40 ppm) aqueous phase 10 mL, shaking speed 150 rpm.

Stellenbosch University https://scholar.sun.ac.za

Table 5.1: Parameters of *pseudo*-first-order, *pseudo*-second-order and intraparticle diffusion kinetic models for competitive extraction of Au(III), Pd(II) and Pt(IV).

Adsorbent	Metal ions	$q_{e(exp)}$ $mg \cdot g^{-1}$	*pseudo*-first-order kinetics			*pseudo*-second-order kinetics				Intraparticle diffusion	
			k_1 min^{-1}	$q_{e(cal)}$ $mg \cdot g^{-1}$	R^2	k_2 $gmg^{-1}min^{-1}$	h $mg.g^{-1}min^{-1}$	$q_{e(cal)}$ $mg.g^{-1}$	R^2	k_{id} $mg.g^{-1}min^{-}_{0.5}$	R^2
S4	Au(III)	3.98	0.039	2.182	0.8329	0.004	0.65	4.13	0.9950	0.282	0.8088
	Pd(II)	1.23	0.080	0.506	0.406	0.25	0.18	0.85	0.9912	0.0572	0.5802
	Pt(IV)	1.49	0.022	0.506	0.8277	0.21	0.46	1.49	0.9946	0.0518	0.8869
S12	Au(III)	3.98	0.03	1.48	0.5173	0.08	1.23	4.03	0.9994	0.291	0.6694
	Pd(II)	2.72	0.04	2.58	0.8543	0.07	0.55	2.81	0.9982	0.255	0.8220
	Pt(IV)	5.45	0.02	3.74	0.7346	0.04	1.23	5.66	0.9977	0.514	0.8979
S21	Au(III)	0.69	0.004	0.064	0.0212	3.12	1.48	0.69	0.9983	-0.025	0.5364
	Pd(II)	0.48	0.001	0.210	0.0083	0.74	0.15	0.46	0.9927	-0.001	0.0031
	Pt(IV)	0.07	0.014	0.064	0.4493	0.48	0.07	0.06	0.9927	0.0025	0.0376
S27	Au(III)	3.89	0.024	3.940	0.8268	0.05	0.68	3.79	0.9814	0.560	0.8014
	Pd(II)	0.91	0.046	1.023	0.8203	0.88	0.76	0.93	0.9959	0.142	0.6026
	Pt(IV)	0.66	0.020	1.118	0.0864	0.44	0.20	0.68	0.9890	0.140	0.8726

Stellenbosch University https://scholar.sun.ac.za

As can be seen in the table, the R^2 values for competitive adsorption of Au(III)-Cl, Pd(II)-Cl, and Pt(IV)-Cl using **S12**, **S21**, and **S27**, are in the range of (0.5173 to 0.8543), (0.0212 to 0.4493), and (0.0864 to 0.8268) respectively. Furthermore, calculated q_e values do not match the experimental q_e values. For instance, the calculated q_e values for the adsorption of Au(III)-Cl, Pd(II)-Cl, and Pt(IV)-Cl using naked MIONs which were 2.182 $mg.g^{-1}$, 0.506 mg^{-1}, and 0.506 $mg.g^{-1}$, and do not match the experimental values. Therefore, the low R^2 values and disagreement between the calculated q_e values and experimental q_e values suggest that adsorption of these three metal ions cannot be described by the *pseud*o-first-order kinetics model.

5.2.2.2 *Pseudo*-second-order kinetics model

The adsorption of Au(III)-Cl, Pd(II)-Cl, and Pt(IV)-Cl using four adsorbents was fitted using *pseudo*-second-order kinetics model. Assuming the *pseudo*-second-order kinetics, the rate of the adsorptive interactions can be calculated by using **Equation 3.6**, in **Chapter 3**.The *pseudo*-second-order kinetics plot for competitive adsorption of Au(III)-Cl, Pd(II)-Cl, and Pt(IV)-Cl using naked MIONs (**S4**) is as shown in **Figure 5.14**. The R^2 values for Au(III)-Cl, Pd(II)-Cl, and Pt(IV)-Cl were 0.9950, 0.9912, and 0.9946 respectively. Other *pseud*o-second-order kinetics parameters for adsorption of naked MIONs were presented in **Table 5.1**. The calculated q_e values which are 4.13 $mg.g^{-1}$, 0.85 $mg.g^{-1}$, 1.49 $mg.g^{-1}$ agree with the experimental q_e values (3.98 $mg.g^{-1}$, 1.23 $mg.g^{-1}$ and 1.49 $mg.g^{-1}$).

The *pseudo*-second-order kinetics parameter for adsorption of these three metals using **S12**, **S21**, and **S27** are also presented in **Table 5.1**. The R^2 values for *pseudo*-second-order kinetics linear plot are in the following ranges: (0.9977 – 0.9994), (0.9927 – 0.9983), and (0.9814 – 0.9959) for adsorption using **S12**, **S21**, and **S27**, respectively. The calculated q_e values correlated well with the experimental q_e values. For example, the calculated q_e values for adsorption of Au(III)-Cl, Pd(II)-Cl, and Pt(IV)-Cl using **S21** were 0.69 $mg.g^{-1}$, 0.46 $mg.g^{-1}$, and 0.06 $mg.g^{-1}$ corresponds with the experimental q_e which are as follows 0.69 $mg.g^{-1}$, 0.48 $mg.g^{-1}$, and 0.07 $mg.g^{-1}$.

The *pseudo*-second-order kinetics model seems to be the best kinetic model used to describe adsorption of metal ions using various nano-materials.[42,131,141] Liu *et al*.[42] studied adsorption of Au(III)-Cl, Pd(II)-Cl, and Pt(IV)-Cl using graphene oxide. The influence of experimental

Stellenbosch University https://scholar.sun.ac.za

parameters such as pH, initial concentration, contact and temperature were investigated. The adsorption kinetics of Au(III)-Cl, Pd(II)-Cl, and Pt(IV)-Cl using graphene oxide (GO) could be described by the *pseudo*-second-order kinetic model.

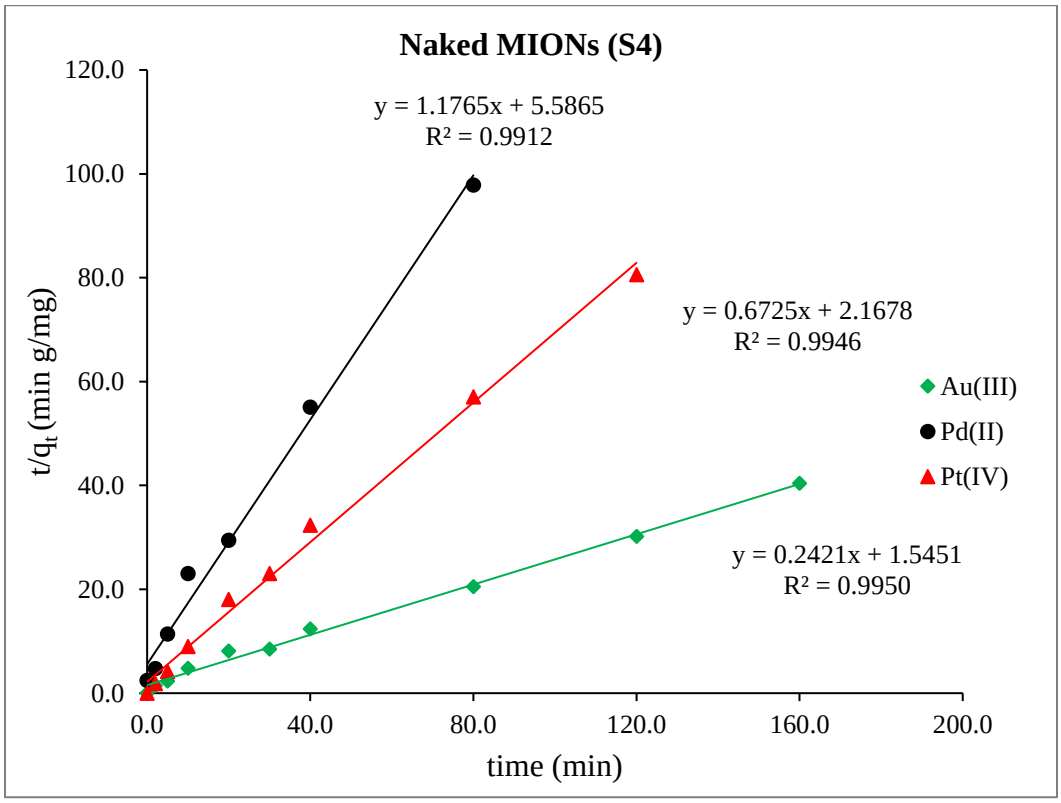

Figure 5.14: *Pseudo*-second-order kinetic plots for adsorption of Au(III)-Cl, Pd(II)-Cl, and Pt(IV)-Cl using 30.15±0.005 mg of **S4** at room teperature (25±2 °C). Initial metal ion concentrations ((Au(III)-Cl: 12.01±0.50 ppm, Pd(II)-Cl: 12.50±0.59 ppm, Pt(IV)-Cl: 12.03±0.40 ppm) aqueous phase 10 mL, shaking speed 150 rpm.

In another study, Kraus *et al.*[185] studied adsorption of Au(III)-Cl using cobalt ferrite ($CoFe_2O_4$) modified with (3-mercaptopropyl)trimethoxysilane (MPTS). The adsorption efficacy as a function of the pH, contact time, and initial Au(III)-Cl concentration was evaluated. The Co-MPTS nanoparticles showed maximum adsorption in the pH range from 1.0 to 4.0. The adsorption kinetics data best fitted the *pseudo*-second-order kinetic model with correlation coefficients higher than 0.999. *Pseudo*-second-order kinetics model assumes that there is transfer of electrons between adsorbent and adsorbate.

Stellenbosch University https://scholar.sun.ac.za

5.2.2.3 Intraparticle diffusion kinetic model

The adsorption kinetics model for adsorption of Au(III)-Cl, Pd(II)-Cl, and Pt(IV)-Cl was also fitted on intraparticle diffusion equation. This kinetic model can be written as shown in **Chapter 3. Figure 5.15** shows intraparticle diffusion kinetics linear plot for adsorption of Au(III)-Cl, Pd(II)-Cl and Pt(IV)-Cl using 30.00±0.005 mg of **S4**. As seen in the figure, the data points showed multi-linearity with two different stages of adsorption, suggesting intraparticle diffusion kinetics model is not a limiting step. All the kinetics parameters extrapolated from the intraparticle diffusion equation are shown in **Table 5.1**.

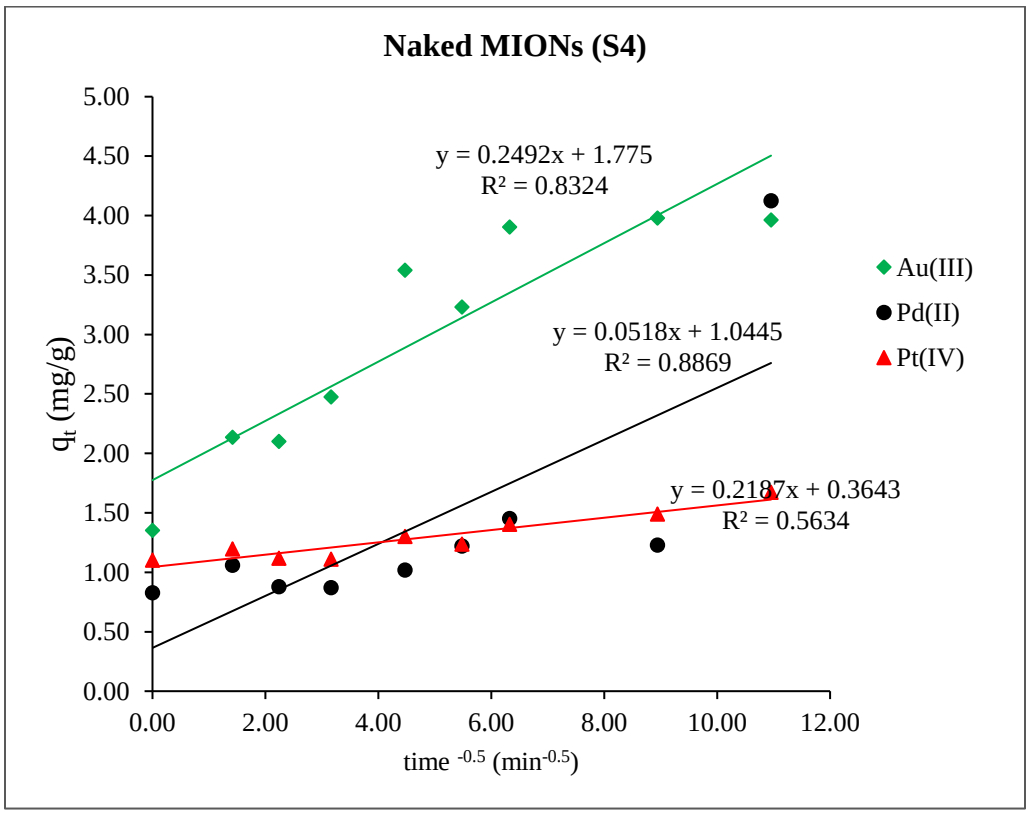

Figure 5.15: Intraparticle diffusion model plots adsorption of Au(III)-Cl, Pd(II)-Cl, and Pt(IV)-Cl using 30.15±0.005 mg of **S4** at room teperature (25±2 °C). Initial metal ion concentrations ((Au(III)-Cl: 12.01±0.50 ppm, Pd(II)-Cl: 12.50±0.59 ppm, Pt(IV)-Cl: 12.03±0.40 ppm) aqueous phase 10 mL, shaking speed 150 rpm.

Stellenbosch University https://scholar.sun.ac.za

As discussed above, adsorption of Au(III)-Cl, Pd(II)-Cl and Pt(IV)-Cl using the four adsorbents can best described using *pseudo*-second-order kinetics model suggesting that there was exchange of electrons between the adsorbent and adsorbate. These results match literature findings.[185]

5.2.3 Adsorption isotherms

Sorption is a physical and/or chemical process in which a substance is accumulated at an interface between phases. Several different equations can be used to predict theoretical adsorption capabilities for different adsorbents. For this study, the Freundlich isotherm and Langmuir isotherm equations have been used to predict adsorption capabilities of Au(III)-Cl, Pt(IV)-Cl and Pd(II)-Cl metal ions by naked MIONs from acidic solutions. These two models are the most frequently used equilibrium adsorption isotherm models in the literature. [13-15] The Langmuir model is based on monolayer adsorption on the active sites of the adsorbent. Furthermore, the Langmuir model assumes that there is no interaction between adsorbate species and that once a species occupies a site, no further adsorption can take place at that site. Theoretically, therefore, a saturation value is reached, beyond which no further adsorption can take place.

Figure 5.16 illustrates the adsorption isotherms of Au(III)-Cl, Pd(II)-Cl, and Pt(IV)-Cl complexes using **S12** by using Langmuir linear fitting. As depicted by this figure, Langmuir model represents a good fit of the experimental data hence was considered adequate for modeling the sorption isotherm. The corresponding Langmuir parameters along with corresponding coefficients (R^2) are listed in **Table 5.2**. The R^2 values for adsorption of these three metal ions using **S4**, **S12**, **S21**, and **S27** kinetic data fitted on Langmuir linear equation are in the following ranges: (0.9874 – 0.9999), (0.9939 – 0.9960), (0.0082 – 0.0580), and (0.5511 – 0.9926) respectively. This observation suggested that the adsorption of Au(III)-Cl, Pd(II)-Cl, and Pt(IV)-Cl using **S4**, **S12** followed Langmuir adsorption isotherm. The adsorption of Au(III)-Cl and Pd(II)-Cl using **S27** were also dominated by this model. The maximum adsorption capacity for adsorption of Au(III)-Cl on **S4** was 17.007 mg/g higher than adsorption capacity of Au(III)-Cl using **S12**, **S21**, and **S27**. Naked MIONs (**S4**) had a high adsorption capacity for Au(III)-Cl compared to the other three adsorbents.

The Freundlich model [15] explains the adsorption on a heterogeneous (multiple layers) surfaces with uniform energy. This model can be represented using the linearized equation in **Chapter 3**.

Stellenbosch University https://scholar.sun.ac.za

Figure 5.17 shows Freundlich linear plot for adsorption of Au(III)-Cl, Pd(II)-Cl, and Pt(IV)-Cl complexes using **S12**. The R^2 values are in the range of (0.5094 – 0.6707). The R^2 values and the other parameters are presented in **Table 5.2** and show that adsorption of these metal complex anions by **S4**, **S12** and **S21** cannot be described by this model.

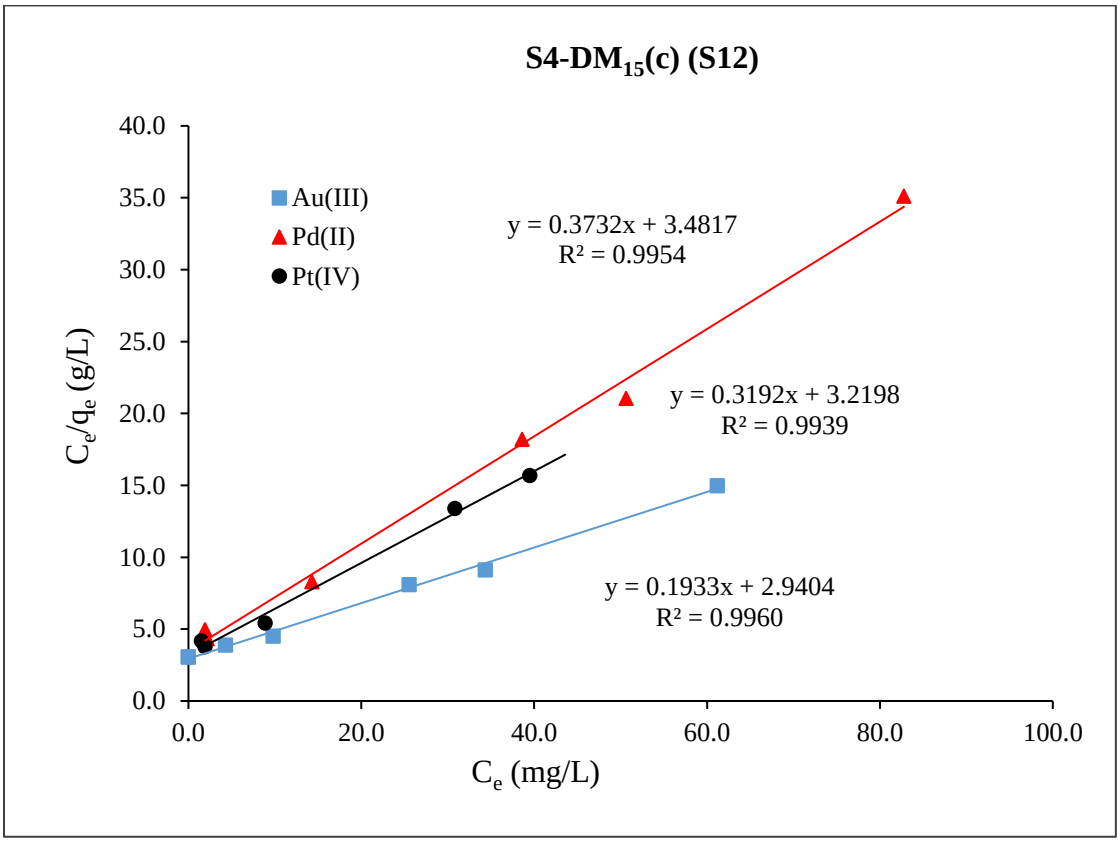

Figure 5.16: Langmuir isotherm linear plots of Au(III)-Cl, Pd(II)-Cl, and Pt(IV)-Cl adsorption using 30.15±0.005 mg of **S12** at room temperature (25±2 °). Other experimental conditions: [M-Cl]: 1.00 to 90 mg/L, total aqueous phase: 10 mL, shaker speed: 150 rpm.

Table 5.2 also shows the R^2 ((0.2432 – 0.7700), (0.0254 – 0.5921), and (0.00588 – 0.9474)) values exhibited by the Freundlich linear plot for adsorption of the three metal complex anions using **S4**, **S21** and **S27** respectively. All the R^2 values are generally very low except for the linear adsorption of Pt(IV)-Cl using **S27**, suggesting that adsorption of these three metal ions cannot be described using Freundlich adsorption isotherm. As shown in **Table 5.2**, equilibrium adsorption data for **S4**, **S12** and **S21** fitted the Langmuir isotherm model in case of Au(III)-Cl and Pd(II)-Cl while equilibrium adsorption of Pt(IV)-Cl using **S27** obeyed Freundlich isotherm model.

Stellenbosch University https://scholar.sun.ac.za

Table 5.2: Langmuir and Freundlich parameters for the adsorption of Au(III), Pd(II), and Pt(IV) from acidic aqueous solutions.

Adsorbents	Metal complex anions	Langmuir			Freundlich		
		q_{max} (mg/g)	b	R^2	K_F	*n*	R^2
(S4)	Au(III)	17.007	0.039	0.9999	N/A	N/A	0.7962
	Pd(II)	0.786	0.753	0.9943	N/A	N/A	0.7700
	Pt(IV)	2.893	0.074	0.9874	N/A	N/A	0.2432
(S12)	Au(III)	5.173	0.066	0.9960	N/A	N/A	0.601
	Pd(II)	2.680	0.107	0.9954	N/A	N/A	0.6707
	Pt(IV)	5.173	0.060	0.9939	N/A	N/A	0.5094
(S21)	Au(III)	N/A	N/A	0.0082	N/A	N/A	0.4231
	Pd(II)	N/A	N/A	0.0288	N/A	N/A	0.5921
	Pt(IV)	N/A	N/A	0.0580	N/A	N/A	0.0254
(S27)	Au(III)	7.022	1.000	0.9926	N/A	N/A	0.7608
	Pd(II)	1.019	0.247	0.9096	N/A	N/A	0.00588
	Pt(IV)	N/A	N/A	0.5511	0.275	1.106	0.9474

Stellenbosch University https://scholar.sun.ac.za

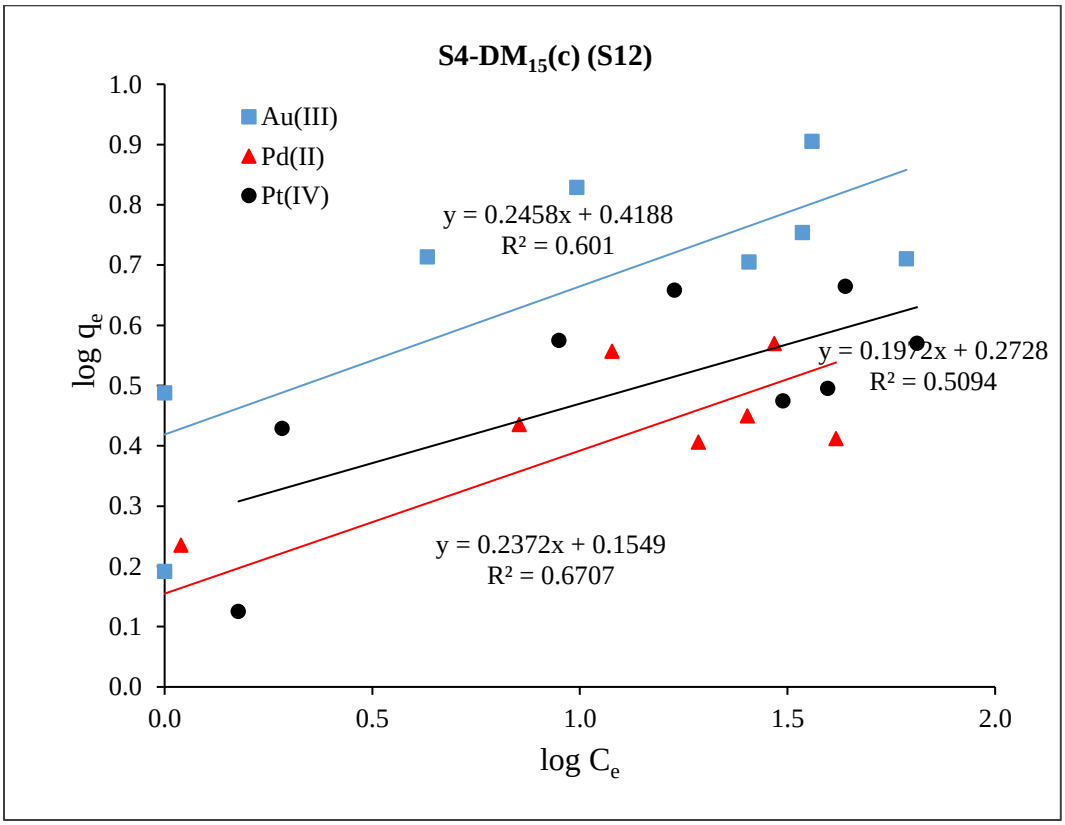

Figure 5.17: Freundlich isotherms linear plots of Au(III)-Cl, Pd(II)-Cl, and Pt(IV)-Cl adsorption using 30.15±0.005 mg of **S12** at room temperature (25±2 °C). Other experimental conditions: [M-Cl]: 1.00 to 90 mg/L, total aqueous phase: 10 mL, shaker speed: 150 rpm.

5.2.4 Desorption studies

The adsorbents recovered from the adsorption experiments were dried in the oven at 40 °C. A batch method was used to study the desorption of Au(III), Pd(II)-Cl, and Pt(IV)-Cl from **S4**, **S12**, **S21** and **S27**. This was carried out using the following stripping solutions: 1.0 M HNO_3, 0.5 M thiourea, and 1.0 M HNO_3 - 0.5 M thiourea solution. Several researchers used similar stripping solution to recover Au(III)-Cl, Pd(II)-Cl, and Pt(IV)-Cl.[42,151] A quantity of 10 ml of the stripping solution was added to the ±30 mg of recovered materials and the resultant mixture was shaken at 150 rpm for 2 h. The concentration of the metal anions was determined by ICP-OES. Desorption percentages were calculated using **Equation 5.5**.

Equation 5.5

$$\text{desorption } (\%) = \frac{C_e' V}{qm} \times 100\%$$

Stellenbosch University https://scholar.sun.ac.za

where $q\ (mg \cdot g^{-1})$ is the adsorption capacity of the adsorbent. $C_e'\ (mg \cdot L^{-1})$ is the concentration of Au(III)-Cl, Pd(II)-Cl, and Pt(IV)-Cl aqueous solutions after desorbed from the adsorbent. m (g) is the mass of the adsorbent, and $V\ (L)$ is the volume of the aqueous solution.

Figure 5.18 shows desorption percentages of the Au(III)-Cl, Pd(II)-Cl, and Pt(IV)-Cl from **S4**-metal ion loaded materials. The figure shows that the three stripping solutions released different amounts of metal ion from the adsorbent into the aqueous layer. For instance, 1 M HNO_3 was selective to Pd(II)-Cl and Pt(IV)-Cl. Au(III)-Cl was not released into the solution when 1 M HNO_3 was used as a stripping solution. This suggest that Au(III)-Cl was bound to naked MIONs. On the other hand, 0.5 M thiourea released 55 %, 65 % and 62 % of Au(III)-Cl, Pd(II)-Cl, and Pt(IV)-Cl respectively. The mixture of the two stripping solutions (1 M HNO_3/0.5 M thiourea) shows increased desorption percentages.

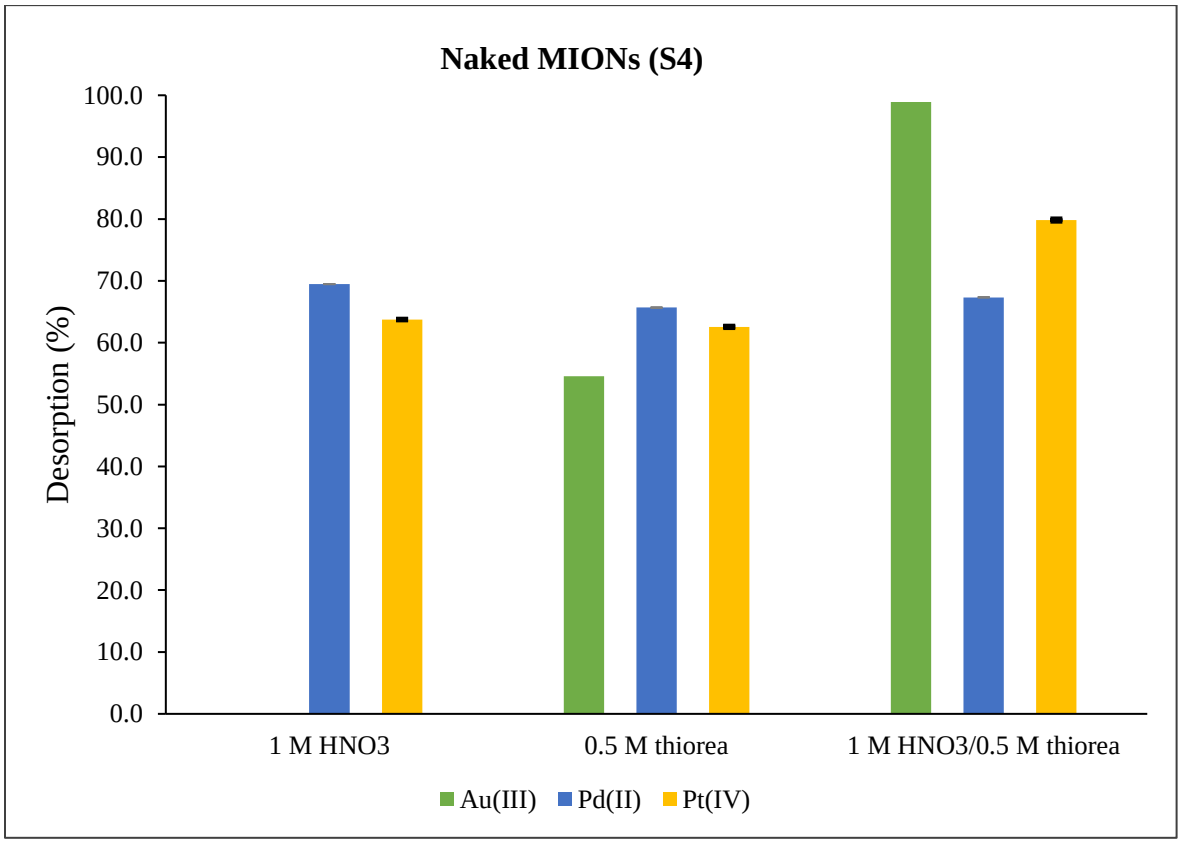

Figure 5.18: Desorption of Au(III), Pd(II), and Pt(IV) complexes from ±30 mg **S4** recovered after adsorption.

Stellenbosch University https://scholar.sun.ac.za

Desorption of these metal complex anions from **S12** (**Figure 5.19**) with 1 M HNO_3 only released Pt(IV)-Cl into solution. The other stripping solutions released all the three metal ions into the solution and the desorption percentages of 1 M HNO_3/0.5 M thiourea are higher than 0.5 thiourea. These results suggest that 1 M HNO_3/0.5 M is the best stripping solution. As for adsorbent **S21** and **S27** (**Figure 5.20** and **Figure 5.21**), only 1 M HNO_3/0.5 M thiourea released some of the metal ions into the solution. This solution was the best solvent for adsorbent **S21** which is selective to Au(III)-Cl.

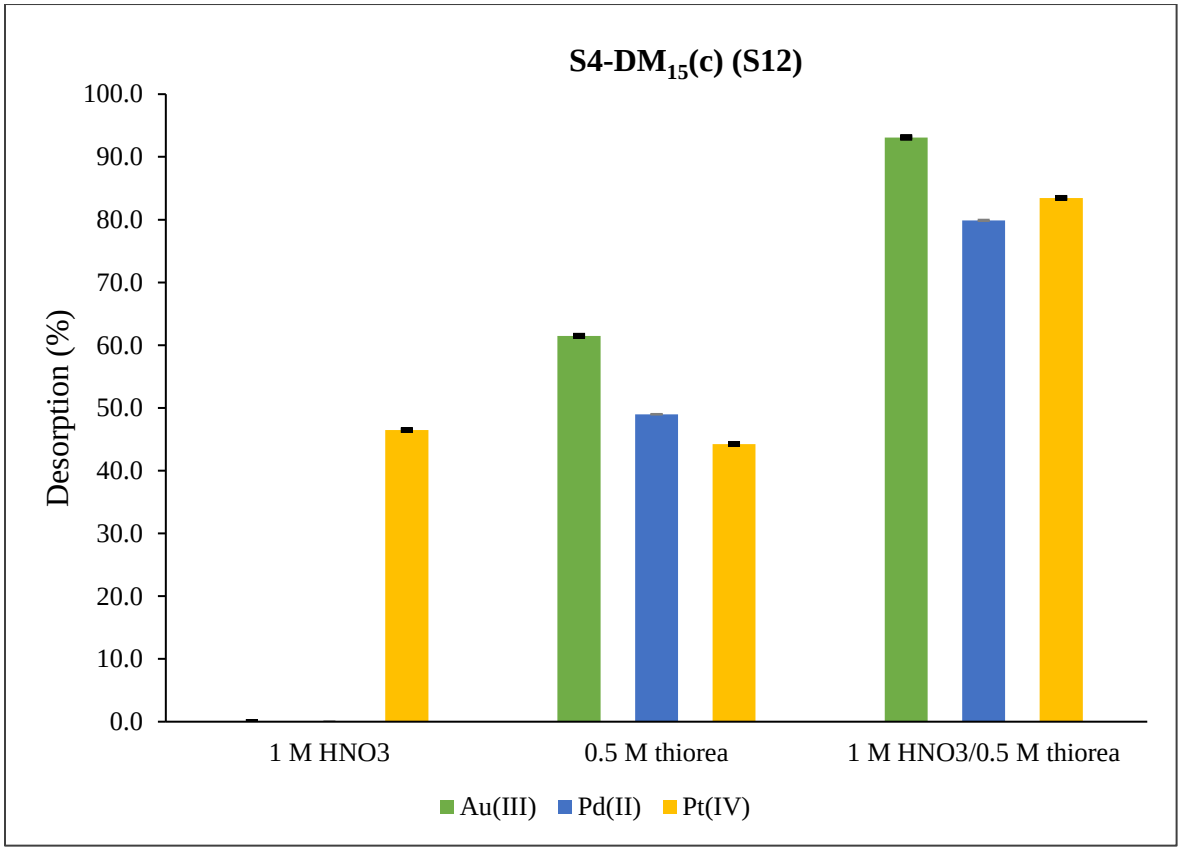

Figure 5.19: Desorption of Au(III), Pd(II), and Pt(IV) from ±30 mg **S12** recovered after adsorption.

Stellenbosch University https://scholar.sun.ac.za

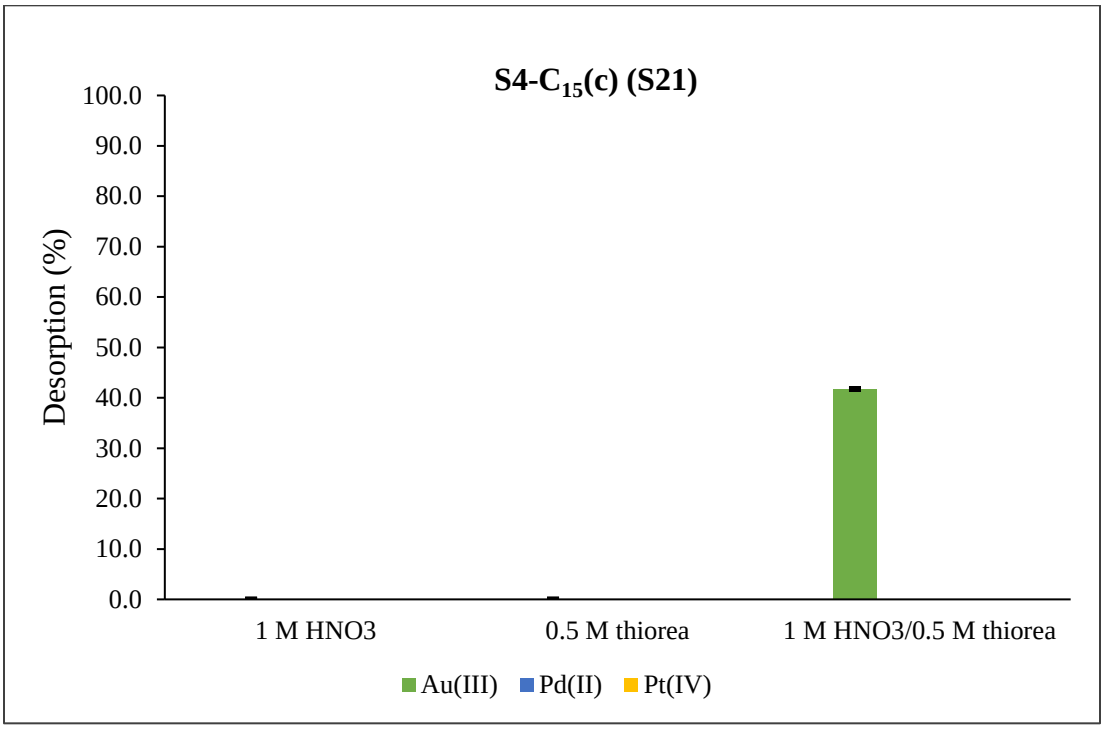

Figure 5.20: Desorption of Au(III), Pd(II), and Pt(IV) from ±30 mg of **S21** recovered after adsorption.

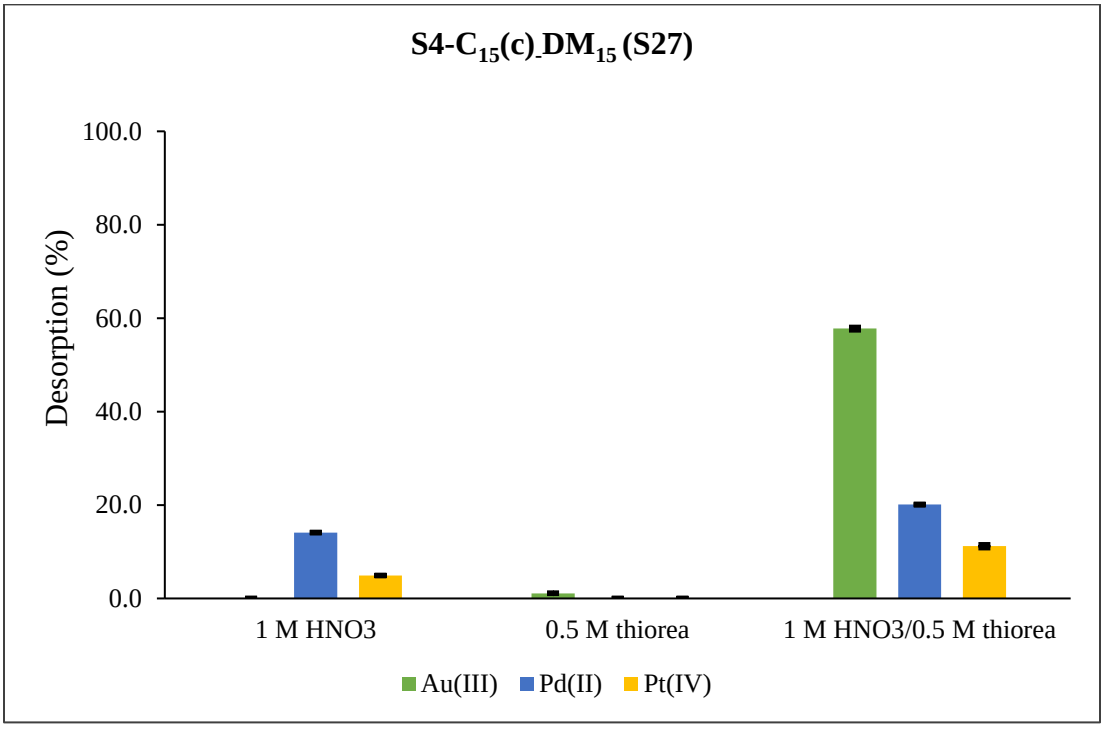

Figure 5.21: Desorption of Au(III), Pd(II), and Pt(IV) from ±30 mg of **S27** recovered after adsorption.

Stellenbosch University https://scholar.sun.ac.za

5.3 CONCLUSION

Competitive adsorption of Au(III)-Cl Pd(II)-Cl, and Pt(IV)-Cl using four magnetic adsorbents: naked MIONs (**S4**), **S4-DM$_{15}$(c)** (**S12**), **S4-C$_{15}$(c)** (**S21**) and **S4-C$_{15}$(c)-DM$_{15}$** (**S27**) from acidic aqueous solution was investigated. The efficacy of these adsorbents in adsorption of these precious metals was tested by varying the solution pH and the contact time. All these four adsorbents generally removed higher percentages of Au(III)-Cl over Pd(II)-Cl and Pt(IV)-Cl. Only naked MIONs (**S4**) were selective towards Au(III)-Cl at the pH of 1.0. However, modification of naked MIONs with the double layer surfactant of both palmitic acid and dendrimer micelles was vital as **S27** was stable at the pH of 1.0. Furthermore, comparing the removal percentages of Pd(II)-Cl and Pt(IV)-Cl using **S4** and **S12**, the C15 dendrimer micelles improved adsorption of these two metal chloro anions. The adsorbent **S21** performed poorly compared to the other three adsorbents.

The adsorption kinetics for Au(III)-Cl, Pd(II)-Cl, and Pt(IV)-Cl complexes using the three adsorbents were evaluated using three commonly used kinetics models which are *pseudo*-first-order, *pseudo*-second-order and intraparticle diffusion kinetics model. The adsorption kinetics for all the three metal ions best fitted the *pseudo*-second-order kinetics model. Moreover, experimental adsorption capacities (q_e) and the calculated q_e values were very close. The desorption studies showed that Au, Pd and Pt can be recovered from all the adsorbents.

5.4 EXPERIMENTAL

5.4.1 Materials

All the chemicals were purchased either from Merck or Sigma-Aldrich and were used without further purification. Distilled deionized water (Milli-Q, 18 MΩ cm) was deoxygenated by bubbling with pure N_2 gas for 30 min prior to use.

5.4.2 Adsorption and desorption procedures

The batch adsorption experiments were carried out by adding the pre-weighed adsorbent material to the solution containing the mixture of Au(III)-Cl, Pd(II)-Cl, and Pt(IV)-Cl complexes in 100 mL Schott bottles. The resultant mixture was mixed on the Labcon mechanical shaker for the

Stellenbosch University https://scholar.sun.ac.za

desired period. The adsorbents were recovered using the neodynamic magnets and dried in the oven at 40 °C. The supernatant was transferred to the conical centrifuge tubes. The samples were centrifuged, and matrix matched with the ICP-OES standards. The concentration of the metal ions before and after adsorption were determined with ICP-OES. For the batch desorption studies, the metal loaded adsorbent was dispersed in the appropriate desorbing solution for 2 h. The concentration of metal complexes was also analysed by ICP-OES. Adsorption experiments were carried out by the batch method. The pH value of the solutions was adjusted using 0.1 M HCl and 0.1 M NaOH. All the measurements were done in duplicates.

5.4.3 Characterisation techniques

5.4.3.1 pH meter

The pH measurements were carried out using Crison basic 20 plus pH meters that carries magnetic stirrer and stand for the sensor. The pH meter was used after calibration with Merck buffer solution at pH 4.01, 7.01 and 9.02. The pH of the solution was adjusted using (0.1 M and 0.01 M) NaOH and 0.1 M and 0.01 M) HCl.

5.4.3.2 Mechanical shaker

A horizontal mechanical shaker (Labcon, BR-30L) was used for constant agitation of the sample solutions for specified contact times. A strong ferrite magnet with a magnetic field strength of ~ 0.35 T was utilized as an external magnetic field for magnetic separation between the aqueous and solid phases.

5.4.3.3 Inductively coupled plasma atomic emission spectroscopy

The concentration of metal ions in the supernatant solutions was determined by Inductively Coupled Plasma Optical Emission Spectroscopy (ICP-OES) with a Liberty Series II spectrometer (Varian, Australia). Standards (traceable to NIST) were matrix matched to acid concentrations of the samples. After calibration and quality check analysis to verify the accuracy of standards, samples were analysed without dilution.

Stellenbosch University https://scholar.sun.ac.za

CHAPTER 6 SUMMARY AND CONCLUSIONS

6.1 SUMMARY AND CONCLUSIONS

The preliminary work done by Dr Eugene Lakay on his MSc project showed the potential use of naked magnetite nanoparticles (referred to as naked MIONs in this thesis) for adsorption of Au(III)-Cl, Pd(II)-Cl and Pt(IV)-Cl complexes from acidic aqueous solutions. Using Eugene's work as a baseline, a more detailed study using naked MIONs as sorbents for Au(III), Pd(II) and Pt(IV) complexes from acidic aqueous solutions was undertaken. MIONs are promising materials for adsorption studies of metal ions/complexes from wastewater due to their versatile magnetic properties, which allow a facile remote control, separation and analyte recovery from solution (**Chapter 1**).[36,62,69] These results were promising but naked MIONs were unstable at low pH's. Therefore, there was a need to extend this work by modifying the MIONs to improve their stability.

Therefore, **Chapter 2** covers the synthesis and characterisation of naked MIONs. The synthesis of naked MIONs was done using the chemical co-precipitation method. This method has been used by several researchers for the preparation of magnetite nanoparticles.[45,111] However, for the purpose of this study, this method was optimised to produce the purest magnetite nanoparticles (as opposed to mixtures of iron oxides). Optimisation was done by varying temperature and the total iron concentration. Naked MIONs prepared at 60 °C with the total iron (Fe^{2+} and Fe^{3+}) concentration of 0.125 M to 0.250 M (**S4** and **S5**) produced the purest magnetite.

The naked MIONs (**S4**) prepared using the optimised reaction conditions in **Chapter 3** were used as extractants for the single-component batch adsorption for Au(III), Pd(II), and Pt(IV) complexes from acidic aqueous solutions. Time dependent batch experiments were carried out to study the effect of the amount of naked MIONs, initial metal concentration and solution pH. All three parameters played a vital role in sorption of these precious metal complexes. For all the sorption experiment carried out, naked MIONs showed a higher adsorption affinity for Au(III)-Cl species than Pd(II)-Cl and Pt(IV)-Cl species. The optimum pH for adsorption of Au(III) and Pt(IV) species was in the pH range 2.2 to 5.0. However, Pd(II)-Cl complexes precipitated at pH 5.0. The dissolution studied confirmed that at very low pH's (pH 1.0), naked MIONs are unstable.

Stellenbosch University https://scholar.sun.ac.za

The kinetics data was tested using *pseudo*-first-order kinetics, *pseudo*-second-order kinetics, and the intraparticle diffusion model. The results showed that sorption of Au(III), Pd(II) and Pt(IV) complexes by naked MIONs can be described by the *pseudo*-second-order kinetics model. The sorption of Pd(II), and Pt(IV) complexes was more rapid that the sorption of Au(III) species and reached equilibrium within a very short time. The slow sorption kinetics of Au(III)-Cl species suggests that the adsorption mechanism does not only involve physical adsorption but chemisorption as well. The equilibrium sorption data for Au(III)-Cl by naked MIONs were fitted into Langmuir and Freundlich, and the model parameters were appropriately evaluated. The sorption of Au(III)-Cl by naked MIONs is best described by Langmuir sorption isotherm model suggesting a monolayer coverage of Au(III)-Cl complexes by the naked MIONs.

The UV-Vis spectroscopy corroborated with the ICP-OES results by confirming the removal of these metal complexes from the solution. Monitoring sorption of Au(III) and Pd(II) complexes with UV-Vis gave insight on the speciation of these complexes before and after their contact with naked MIONs. On the contrary, the UV-Vis of Pt(IV)-Cl was inconclusive because the UV-Vis spectrum of $PtCl_6^{2-}$ does not show well resolved peaks of the ligands to charge transfer bands (LMCT) bands.

The sorption of Au(III), Pd(II) and Pt(IV) complexes by naked MIONs from acidic aqueous solution was postulated to be due to electrostatic interaction, ligand exchange and reductive reactions. Therefore, the interaction between these metal complexes and the surface of naked MIONs is governed by both inner- and outer- sphere coordination mechanism.

In **Chapter 4**, an attempt to stabilise naked MIONs with dendrimer micelles (**DM_n** (where n = 5, 11 and 15), aliphatic carboxylic acids; **Cn-acids** (where n = 5, 11 and 15) and finally with both moieties, was discussed. The dendrimer micelles were prepared by modifying the commercially purchased dendrimers with the following alkyl chlorides: hexanoyl chloride, lauroyl chloride, and palmitoyl chloride. Successful amidation of the dendrimer end groups was characterised by FT-IR, ^{1}H NMR and ^{13}C NMR. Characterizations of the modified MIONs were carried out using the following analytical techniques: infrared spectroscopy (IR), powder X-ray diffraction (PXRD), thermogravimetric analysis (TGA), high-resolution transmission electron microscopy (HRTEM), field emission scanning electron microscopy (FESEM) and inductively coupled plasma optical

Stellenbosch University https://scholar.sun.ac.za

emission spectrometry (ICP-OES). Stability studies showed that the modified MIONs were more stable at naked MIONs at very low pH (pH 1.0 to pH 3.0). Therefore, modifying MIONs with organic ligands achieved their stability at low pH conditions.

In **Chapter 5**, both naked and modified MIONs were used as adsorbents for Au(III)-Cl, Pd(II)-Cl, and Pt(IV)-Cl complexes from acidic aqueous solutions. Besides stabilising MIONs, organic ligands were introduced to the surface of MIONs, they altered their selectivity towards these metal complexes. Competitive adsorption of Au(III), Pd(II), Pt(IV) complexes by the four adsorbents: (**S4**), (**S12**), (**S21**), and (**S27**) was investigated by varying the pH from 1.0 to 6.0 and the contact time (5 min to 160 min). Adsorption of Au(III)-Cl onto **S4**, **S12**, and **S17** showed significantly high adsorption or removal percentages at pH 1.0 to pH 6.0 compared to adsorption of Pd(II) and Pt(IV) species. The adsorption of the three metal complexes using adsorbent **S12**, which is dendrimer micelle functionalised naked MIONs, indicated that the presence of dendrimer micelles played a vital role in adsorption of Pd(II) and Pt(IV) complexes. However, adsorption by **S27** showed poor adsorption for Pd(II) and Pt(IV) complexes due to steric hindrance. Nonetheless, high density of the alkyl chain of the **DM_{15}** and C15-acid makes it practical to use adsorbent **S27** in very acidic conditions. The batch desorption studied showed that these metal complexes can be recovered from the adsorbent.

In this regard, MIONs are promising adsorbents for adsorbents of Au(III), Pd(II), and Pt(IV) chloro complexes from acidic solutions.

6.2 FUTURE WORK

The following can be considered for future work:

- Determination of the maximum loading capacity of naked MIONs for each metal complex.
- The competitive sorption of Au(III), Pd(II) and P(IV) complexes was carried out with naked MIONs, **C_{15}-acid** modified MIONs and **DM_{15}** modified MIONs. Therefore, competitive adsorption studies of these metal complexes with the other adsorbents could also be considered for future work.
- Furthermore, the loading capacity of these modified MIONs should be determined.

Stellenbosch University https://scholar.sun.ac.za

REFERENCES

1 B. P. Charlesworth, *Platin. Met. Rev.*, 1981, **25**, 106–112.

2 R. Barefoot, *Talanta*, 1999, **49**, 1–14.

3 H. Dong, J. Zhao, J. Chen, Y. Wu and B. Li, *Int. J. Miner. Process.*, 2015, **145**, 108–113.

4 F. L. Bernardis, R. A. Grant and D. C. Sherrington, *React. Funct. Polym.*, 2005, **65**, 205–217.

5 V. Yahorava and M. Kotze, *J. South. African Inst. Min. Metall.*, 2014, **114**, 173–181.

6 A. V. Pethkar and K. M. Paknikar, *J. Biotechnol.*, 1998, **63**, 121–136.

7 P. Taylor, A. N. Nikoloski and K. Ang, *Miner. Process. Extr. Met. Rev.*, 2014, **35**, 369–389.

8 K. Zargoosh, H. Abedini, A. Abdolmaleki and M. R. Molavian, *Am. Chem. Soc.*, 2013, **52**, 14944–14.

9 B. Sures, S. Zimmermann, J. Messerschmidt, A. Von Bohlen and F. Alt, *Environ. Pollut.*, 2001, **113**, 341–345.

10 K. H. Ek, G. M. Morrison and S. Rauch, *Sci. Total Environ.*, 2004, **335**, 21–38.

11 O. F. Odio, L. Lartundo-Rojas, P. Santiago-Jacinto, R. Martínez and E. Reguera, *J. Phys. Chem. C*, 2014, **118**, 2776–2791.

12 J. Siame and H. Kasaini, *Selective Precipitation of Pt and Base Metals in Liquid-Liquid Chloride Systems*, 2013.

13 J. Płotka-Wasylka, N. Szczepańska, M. de la Guardia and J. Namieśnik, *TrAC Trends Anal. Chem.*, 2015, **73**, 19–38.

14 M. L. Machesky, W. O. Andrade and A. W. Rose, *Geochim. Cosmochim. Acta*, 1991, **55**, 769–776.

15 A. Uheida, M. Iglesias, C. Fontàs, M. Hidalgo, V. Salvadó, Y. Zhang and M. Muhammed, *J. Colloid Interface Sci.*, 2006, **301**, 402–408.

16 A. H. Lu, E. L. Salabas and F. Schüth, *Angew. Chemie - Int. Ed.*, 2007, **46**, 1222–1244.

17 W. Wu, Q. He and C. Jiang, *Nanoscale Res. Lett.*, 2008, **3**, 397–415.

18 W. Wu, Z. Wu, T. Yu, C. Jiang and W.-S. Kim, *Sci. Technol. Adv. Mater.*, 2015, **16**, 1–43.

19 T. Phetla, E. Muzenda and M. Belaid, *World Acad. Sci. Eng.*, 2010, **4**, 248–254.

20 S. Syed, *Hydrometallurgy*, 2012, **115**–**116**, 30–51.

21 D. Parajuli, H. Kawakita, K. Inoue and M. Funaoka, *Ind. Eng. Chem. Res.*, 2006, **45**, 6405–

Stellenbosch University https://scholar.sun.ac.za

6412.

22 H. Baba, *Conserv. Recycl.*, 1987, **10**, 247–252.

23 X. Qu, P. J. J. Alvarez and Q. Li, *Water Res.*, 2013, **47**, 3931–3946.

24 M. Šafaříková and I. Šafařík, *J. Magn. Magn. Mater.*, 1999, **194**, 108–112.

25 P. Robinson, P. Dunnill and M. Lilly, *Biotechnol. Bioeng.*, 1973, **XV**, 603–606.

26 P. H. Towler, J. D. Smith and D. R. Dixon, *Anal. Chim. Acta*, 1996, **328**, 53–59.

27 A. Ríos, M. Zougagh and M. Bouri, *Anal. Methods*, 2013, **5**, 4558–4573.

28 H. Bae, T. Ahmad, I. Rhee, Y. Chang, S. Jin and S. Hong, *Nanoscale Res. Lett.*, 2012, **7**, 2–6.

29 P. Xu, G. Ming, D. Lian, C. Ling, S. Hu and M. Hua, *Sci. Total Environ.*, 2012, **424**, 1–10.

30 B. Socas-Rodríguez, J. Hernández-Borges, P. Salazar, M. Martín and M. Á. Rodríguez-Delgado, *J. Chromatogr. A*, 2015, **1397**, 1–10.

31 J. Ye, S. Liu, M. Tian, W. Li, B. Hu, W. Zhou and Q. Jia, *Talanta*, 2014, **118**, 231–237.

32 P. Tartaj, P. Morales, S. Veintemillas-verdaguer, T. Gonz, M. a D. P. Morales, S. Veintemillas-verdaguer, T. Gonz lez-Carre o and C. J. Serna, *J. Phys. D. Appl. Phys.*, 2003, **36**, R182–R197.

33 H. Wu, N. Gao, L. Zhang, Y. Li, Y. Shi and L. Du, *Food Anal. Methods*, 2015, **9**, 614–623.

34 M. Faraji, Y. Yamini and M. Rezaee, *J. Iran. Chem. Soc.*, 2010, **7**, 1–37.

35 A. G. Kolhatkar, A. C. Jamison, D. Litvinov, R. C. Willson and T. R. Lee, *Int. J. Mol. Sci.*, 2013, 14, 15977–16009.

36 S. Laurent, D. Forge, M. Port, A. Roch, C. Robic, L. Vander Elst and R. N. Muller, *Chem. Rev.*, 2008, **108**, 2064–2110.

37 A. Akbarzadeh, M. Samiei and S. Davaran, *Nanoscale Res. Lett.*, 2012, **7**, 1–13.

38 G. Salazar-alvarez, *Synthesis , Characterisation and Applications of Iron Oxide Nanoparticles*, 2004, vol. 1.

39 K. J. Landmark, *Dendrimer-coated iron oxide nanoparticles as targeted MRI contrast agents*, 2008.

40 S. Laurent and M. Mahmoudi, *Int. J. Mol. Epidemiol. Genet.*, 2011, **2**, 367–90.

41 M. Nemanashi-Maumela, I. Nongwe, R. C. Motene, B. L. Davids and R. Meijboom, *Mol. Catal.*, 2017, **438**, 184–196.

42 L. Liu, S. Liu, Q. Zhang, C. Li, C. Bao, X. Liu and P. Xiao, *J. Chem. Eng. Data*, 2013, **58**,

Stellenbosch University https://scholar.sun.ac.za

209–216.

43 C. Tamez, R. Hernandez and J. G. Parsons, *Microchem. J.*, 2016, **125**, 97–104.

44 X. Luo, B. Guo, J. Luo, F. Deng, S. Zhang, S. Luo and J. Crittenden, *ACS Sustain. Chem. Eng.*, 2015, **3**, 460–467.

45 J. Hu, G. Chen and I. M. C. Lo, *Water Res.*, 2005, **39**, 4528–4536.

46 G. Giakisikli and A. N. Anthemidis, *Anal. Chim. Acta*, 2013, **789**, 1–16.

47 M. Mahdavi, M. Bin Ahmad, M. J. Haron, F. Namvar, B. Nadi, M. Z. Ab Rahman and J. Amin, *Molecules*, 2013, **18**, 7533–7548.

48 J. K. Oh and J. M. Park, *Prog. Polym. Sci.*, 2011, **36**, 168–189.

49 W. Jiang, H. C. Yang, S. Y. Yang, H. E. Horng, J. C. Hung, Y. C. Chen and C. Y. Hong, *J. Magn. Magn. Mater.*, 2004, **283**, 210–214.

50 L. H. Reddy, J. L. Arias, J. Nicolas and P. Couvreur, *Chem. Rev.*, 2012, **112**, 5818–78.

51 M. Mahmoudi, S. Sant, B. Wang, S. Laurent and T. Sen, *Adv. Drug Deliv. Rev.*, 2011, **63**, 24–46.

52 T. Ahn, J. H. Kim, H. M. Yang, J. W. Lee and J. D. Kim, *J. Phys. Chem. C*, 2012, **116**, 6069–6076.

53 P. N. Dave and L. V. Chopda, *J. Nanotechnol.*, 2014, 2014, 1–14.

54 R. Massart, *IEEE Trans. Magn.*, 1981, **17**, 1247–1248.

55 M. Mahmoudi, A. Simchi, M. Imani, A. S. Milani and P. Stroeve, *J. Phys. Chem. B*, 2008, **112**, 14470–81.

56 Y. S. Kang, S. Risbud, J. F. Rabolt and S. Pieter, *Chem. Mater*, 2007, **34**, 192–193.

57 T. Hyeon, S. S. Lee, J. Park, Y. Chung and H. Bin Na, *J. Am. Chem. Soc.*, 2001, **123**, 12798–12801.

58 W. Baaziz, B. P. Pichon, S. Fleutot, Y. Liu, C. Lefevre, J. M. Greneche, M. Toumi, T. Mhiri and S. Begin-Colin, *J. Phys. Chem. C*, 2014, **118**, 3795–3810.

59 A. Demortiere, P. Panissod, B. P. Pichon, G. Pourroy, D. Guillon and B. Donnio, *Nanoscale*, 2011, **3**, 225–232.

60 S. Ge, X. Shi, K. Sun, C. Li, C. Uher, J. R. Baker, M. M. B. Holl and B. G. Orr, *J. Phys. Chem. C.*, 2009, **113**, 13593–13599.

61 J. Li, X. Shi and M. Shen, *Part. Part. Syst. Charact.*, 2014, **31**, 1223–1237.

62 C. L. Lin, C. F. Lee and W. Y. Chiu, *J. Colloid Interface Sci.*, 2005, **291**, 411–420.

Stellenbosch University https://scholar.sun.ac.za

63 J. Gass, P. Poddar, J. Almand, S. Srinath and H. Srikanth, *Adv. Funct. Mater.*, 2006, **16**, 71–75.

64 T. J. Daou, G. Pourroy, S. Bégin-Colin, J. M. Grenèche, C. Ulhaq-Bouillet, P. Legaré, P. Bernhardt, C. Leuvrey and G. Rogez, *Chem. Mater.*, 2006, **18**, 4399–4404.

65 J. Vidal-Vidal, J. Rivas and M. A. López-Quintela, *Colloids Surfaces A Physicochem. Eng. Asp.*, 2006, **288**, 44–51.

66 A. B. Chin and I. I. Yaacob, *J. Mater. Process. Technol.*, 2007, **191**, 235–237.

67 L.-H. Han, H. Liu and Y. Wei, *Powder Technol.*, 2011, **207**, 42–46.

68 M. Takafuji, S. Ide, H. Ihara and Z. Xu, *Chem. Mater.*, 2004, **16**, 1977–1983.

69 S. Sun and H. Zeng, *J. Am. Chem. Soc.*, 2002, **124**, 8204–8205.

70 P. I. Girginova, A. L. Daniel-da-Silva, C. B. Lopes, P. Figueira, M. Otero, V. S. Amaral, E. Pereira and T. Trindade, *J. Colloid Interface Sci.*, 2010, **345**, 234–40.

71 E. Murugan and J. N. Jebaranjitham, *Chem. Eng. J.*, 2015, **259**, 266–276.

72 A. K. Gupta and M. Gupta, *Biomaterials*, 2005, **26**, 3995–4021.

73 L. Quaroni and G. Chumanov, *J. Am. Chem. Soc.*, 1999, **121**, 10642–10643.

74 L. Bronstein, X. Huang, J. Retrum, A. Schmucker, M. Pink, B. D. Stein and B. Dragnea, *Chem. Mater.*, 2007, **19**, 3624–3632.

75 Y. Sahoo, H. Pizem, T. Fried, D. Golodnitsky, L. Burstein, C. N. Sukenik and G. Markovich, *Langmuir*, 2001, **17**, 7907–7911.

76 A. Hu, G. T. Yee and W. Lin, *J. Am. Chem. Soc.*, 2005, **127**, 12486–7.

77 V. Torrisi, A. Graillot, L. Vitorazi, Q. Crouzet, G. Marletta, C. Loubat and J.-F. Berret, *Biomacromolecules*, 2014, **15**, 3171–9.

78 L. Wang, Z. Yang, J. Gao, K. Xu, H. Gu, B. Zhang, X. Zhang and B. Xu, *J. Am. Chem. Soc.*, 2006, **128**, 13358–9.

79 C. Xu, K. Xu, H. Gu, R. Zheng, H. Liu, X. Zhang, Z. Guo and B. Xu, *J. Am. Chem. Soc.*, 2004, **126**, 9938–9.

80 A. Shavel and L. Liz-Marzán, *Phys. Chem. Chem. Phys.*, 2009, **11**, 3762–3766.

81 C. H. Yen, H. L. Lien, J. S. Chung and H. Der Yeh, *J. Hazard. Mater.*, 2017, **322**, 215–222.

82 A. Mendoza-Garcia and S. Sun, *Adv. Funct. Mater.*, 2016, **26**, 3809–3817.

83 Q. Zhang, N. Wang, L. Zhao, T. Xu and Y. Cheng, *ACS Appl. Mater. Interfaces*, 2013, **5**, 1907–1912.

Stellenbosch University https://scholar.sun.ac.za

84 J.-F. Lutz, S. Stiller, A. Hoth, L. Kaufner, U. Pison and R. Cartier, *Biomacromolecules*, 2006, **7**, 3132–8.

85 M. . Butterworth, L. Illum and S. . Davis, *Colloids Surfaces A Physicochem. Eng. Asp.*, 2001, **179**, 93–102.

86 S. Nigam and D. Bahadur, *Colloids Surfaces B Biointerfaces*, 2017, **155**, 182–192.

87 K. Uzun, E. Çevik, M. Şenel, H. Sözeri, A. Baykal, M. F. AbasIyanIk and M. S. Toprak, *J. Nanoparticle Res.*, 2010, **12**, 3057–3067.

88 W. Sun, S. Mignani, M. Shen and X. Shi, *Drug Discov. Today*, 2016, **21**, 1873–1885.

89 M. A. Barakat, M. H. Ramadan, M. A. Alghamdi, S. S. Algarny, H. L. Woodcock and J. N. Kuhn, *J. Environ. Manage.*, 2013, **117**, 50–57.

90 H.-B. Mekelburger, W. Jaworek and F. Vögtle, *Angew. Chem. Int. Ed. Engl.*, 1992, **6**, 391–405.

91 D. A. Tomalia, H. Baker, J. Dewald, M. Hall, G. Kallos, S. Martin, J. Roeck, J. Ryder and P. Smith, *Polym. J.*, 1985, **17**, 117–132.

92 G. R. Newkome, Z. Yao, G. R. Baker and V. K. Gupta, *J. Org. Chem.*, 1985, **50**, 2003–2004.

93 X. Wang, L. Guerrand, B. Wu, X. Li, L. Boldon, W. R. Chen and L. Liu, *Polymers (Basel).*, 2012, **4**, 600–616.

94 E. Abbasi, S. Aval, A. Akbarzadeh, M. Milani, H. Nasrabadi, S. Joo, Y. Hanifehpour, K. Nejati-Koshki and R. Pashaei-Asl, *Nanoscale Res. Lett.*, 2014, **9**, 1–10.

95 J. Hu, T. Xu and Y. Cheng, *Chem. Rev.*, 2012, **112**, 3856–3891.

96 Y. Niu and R. M. Crooks, *Comptes Rendus Chim.*, 2003, **6**, 1049–1059.

97 S. Zhang, H. Niu, Z. Hu, Y. Cai and Y. Shi, *J. Chromatogr. A*, 2010, **1217**, 4757–64.

98 M. T. Swihart, *Curr. Opin. Colloid Interface Sci.*, 2003, **8**, 127–133.

99 S. Chaitoglou, M. R. Sanaee and E. Bertran, *J. Nanomater.*, 2014, **2014**, 1–8.

100 C. J. Chen, H. Y. Lai, C. C. Lin, J. S. Wang and R. K. Chiang, *Nanoscale Res. Lett.*, 2009, **4**, 1343–1350.

101 S. Mornet, J. Portier and E. Duguet, *J. Magn. Magn. Mater.*, 2005, **293**, 127–134.

102 C. Boyer, M. R. Whittaker, V. Bulmus, J. Liu and T. P. Davis, *NPG Asia Mater.*, 2010, **2**, 23–30.

103 S. L. Easo and P. V Mohanan, *Carbohydr. Polym.*, 2013, **92**, 726–32.

Stellenbosch University https://scholar.sun.ac.za

104 Y. S. Ho and G. McKay, *Can. J. Chem. Eng.*, 1998, **76**, 822–827.

105 F. Keyhanian, S. Shariati, M. Faraji and M. Hesabi, *Arab. J. Chem.*, 2016, **9**, S348–S354.

106 T. Robinson, G. McMullan, R. Marchant and P. Nigam, *Bioresour. Technol.*, 2001, **77**, 247–255.

107 N. A. Travlou, G. Z. Kyzas, N. K. Lazaridis and E. A. Deliyanni, *Langmuir*, 2013, **29**, 1657–1668.

108 W. Konicki, A. Hełminiak, W. Arabczyk and E. Mijowska, *Chem. Eng. Res. Des.*, 2018, **129**, 259–270.

109 E. M. Lakay and K. R. Koch, *Superparamagnetic iron-oxide based nanoparticles for the separation and recovery of precious metals from solution*, 2009.

110 N. Ilankoon, *Int. J. Eng. Res. Appl.*, 2014, **4**, 55–63.

111 A. Uheida, M. Iglesias, C. Fontàs, M. Hidalgo and V. Salvadó, *J. Colloid Interface Sci.*, 2006, **301**, 402–408.

112 M. Wierucka and M. Biziuk, *TrAC - Trends Anal. Chem.*, 2014, **59**, 50–58.

113 L. Carlos, F. S. G. Einschlag, M. C. González and D. O. Mártire, in *Applications of Magnetite Nanoparticles for Heavy Metal Removal from Wastewater*, 2013, pp. 63–77.

114 S. Brunauer, P. H. Emmett and E. Teller, *J. Am. Chem. Soc.*, 1938, **60**, 309–319.

115 K. Petcharoen and A. Sirivat, *Mater. Sci. Eng. B*, 2012, **177**, 421–427.

116 J. S. Basuki, A. Jacquemin, L. Esser, Y. Li, C. Boyer and T. P. Davis, *Polym. Chem.*, 2014, **5**, 2611–2620.

117 Wahajuddin and S. Arora, *Int. J. Nanomedicine*, 2012, **7**, 3445–3471.

118 M. J. Nicol, C. A. Fleming and R. L. Paul, *The Chemistry of the Extraction of Gold*, 1992.

119 C. Ta, F. Reith, J. Brugger, A. Pring and C. E. Lenehan, *Environ. Sci. Technol.*, 2014, **48**, 5737–5744.

120 W. Robb, *Inorg. Chem.*, 1967, **6**, 382–386.

121 L. I. Elding and L. Gustafson, *Inorganica Chim. Acta*, 1976, **19**, 165–171.

122 F. Mahlamvana and R. J. Kriek, *"Applied Catal. B, Environ.*, 2014, **148**–**149**, 387–393.

123 L. I. Elding, *Inorganica Chim. Acta*, 1972, **6**, 647–651.

124 J. E. Samad, J. Keels and J. R. Regalbuto, *Catal. Letters*, 2016, **146**, 157–162.

125 C. D. Tait, D. R. Janecky and P. S. Z. Rogers, *Geochim. Cosmochim. Acta*, 1991, **55**, 1253–1264.

Stellenbosch University https://scholar.sun.ac.za

126 D. Nachtigall, S. Artelt and G. Wunsch, *J. Chromatogr.*, 1997, **775**, 197–210.

127 J. A. Peck, C. D. Tait, B. I. Swanson and E. B. J. Gordon, *Geochim. Cosmochim. Acta*, 1991, **55**, 671–676.

128 L. R. F. Grantham, T. S. Elleman and J. Martin D S, *J. Am. Chem. Soc.*, 1955, **77**, 2965–2971.

129 T. Ogata and Y. Nakano, *Water Res.*, 2005, **39**, 4281–4286.

130 I. V. Mironov and E. V. Makotchenko, *J. Solution Chem.*, 2009, 38, 725–737.

131 Z. He, L. He, J. Yang and Q. Lu, *Ind. Eng. Chem. Res.*, 2013, **52**, 4103–4108.

132 J. F. Boily and T. M. Seward, *Geochim. Cosmochim. Acta*, 2005, **69**, 3773–3789.

133 J. Kramer and K. R. Koch, *Inorg. Chem.*, 2006, **45**, 7843–7855.

134 J. J. Cruywagen and R. J. Kriek, *J. Coord. Chem.*, 2007, **60**, 439–447.

135 C. J. le Roux and R. J. Kriek, *Hydrometallurgy*, 2017, **169**, 447–455.

136 C. H. Gammons, *Geochim. Cosmochim. Acta*, 1996, **60**, 1683–1694.

137 R. Alorro, N. Hiroyoshi, M. Ito and M. Tsunekawa, *XXV Int. Miner. Process. Congr.*, 2010, 263–271.

138 O. N. Karasyova, L. I. Ivanova and Z. Leonid, *Aquat. Geochemistry*, 1998, **4**, 215–231.

139 R. D. Alorro, N. Hiroyoshi, H. Kijitani, M. Ito and M. Tsunekawa, *Miner. Process. Extr. Metall. Rev.*, 2015, **36**, 332–339.

140 S. Goldberg, L. J. Criscenti, D. R. Turner, J. A. Davis and K. J. Cantrell, *Vadose Zo. J.*, 2007, **6**, 407–435.

141 S. Pang and K. Yung, *Chem. Eng. Sci.*, 2014, **107**, 58–65.

142 a. Ramesh, H. Hasegawa, W. Sugimoto, T. Maki and K. Ueda, *Bioresour. Technol.*, 2008, **99**, 3801–3809.

143 C. B. Colvin, *Phys. Chem. Commons*, 1962, 1–98.

144 E. L. Ivar, *Acta Chem. Scand.*, 1970, **24**, 1331–1340.

145 K. Jainae, K. Sanuwong, J. Nuangjamnong, N. Sukpirom and F. Unob, *Chem. Eng. J.*, 2010, **160**, 586–593.

146 L. E. Cox, D. G. Peters and E. L. Wehry, *J. Inorg. Nucl. Chem.*, 1972, **34**, 297–305.

147 M. L. Machesky, W. Andrade and A. W. Rose, 1991, **55**, 769–776.

148 C. Souza, D. Majuste, M. S. S. Dantas and V. S. T. Ciminelli, *Hydrometallurgy*, 2014, **147**–**148**, 188–195.

Stellenbosch University https://scholar.sun.ac.za

149 A. L. White and M. L. Peterson, *Geochim. Cosmochim. Acta*, 1996, **60**, 3799–3814.

150 O. N. Karasyova, L. I. Ivanova, L. Z. Lakshtanov, L. Lövgren and S. Sjöberg, *Aquat. Geochemistry*, 1998, **4**, 215–231.

151 L. Liu, C. Li, C. Bao, Q. Jia, P. Xiao, X. Liu and Q. Zhang, *Talanta*, 2012, **93**, 350–357.

152 E. Guibal, A. Larkin, T. Vincent and J. M. Tobin, *Ind. Eng. Chem. Res.*, 1999, **38**, 4011–4022.

153 X. Li, C. Zhang, R. Zhao, X. Lu, X. Xu, X. Jia, C. Wang and L. Li, *Chem. Eng. J.*, 2013, **229**, 420–428.

154 W. Plazinski, W. Rudzinski and A. Plazinska, *Adv. Colloid Interface Sci.*, 2009, **152**, 2–13.

155 B. F. Pan, F. Gao and H. C. Gu, *J. Colloid Interface Sci.*, 2005, **284**, 1–6.

156 A. Boni, L. Albertazzi, C. Innocenti, M. Gemmi and A. Bifone, *Langmuir*, 2013, **29**, 10973–10979.

157 C.-M. Chou and H.-L. Lien, *J. Nanoparticle Res.*, 2011, **13**, 2099–2107.

158 E. Strable, J. W. M. Bulte, B. Moskowitz, K. Vivekanandan, M. Allen and T. Douglas, *Chem. Mater.*, 2001, **13**, 2201–2209.

159 N. E. Domracheva, V. I. Morozov, M. S. Gruzdev, R. A. Manapov, A. V Pyataev and G. Lattermann, *Macromol. Chem. Phys.*, 2010, **211**, 791–800.

160 B. Basly, P. Perriat, G. Pourroy and S. Be, *Contrast Media Mol. Imaging*, 2011, **6**, 132–138.

161 S. Stevelmans, J. C. M. van Hest, J. F. G. A. Jansen, D. A. F. J. van Boxtel, E. M. M. de Brabander-van den Berg and E. W. Meijer, *J. Am. Chem. Soc.*, 1996, **118**, 7398–7399.

162 D. Ribeiro, T. Fernanda, R. S. De Laurentiz, U. O. Bicalho, L. Martins, N. Luiz, D. Filho and L. L. Paim, *Am. Chem. Sci. J.*, 2013, **3**, 314–324.

163 S. Chandra, G. Noronha, S. Dietrich, H. Lang and D. Bahadur, *J. Magn. Magn. Mater.*, 2015, **380**, 7–12.

164 X. Liu, M. D. Kaminski, Y. Guan, H. Chen, H. Liu and A. J. Rosengart, *J. Magn. Magn. Mater.*, 2006, **306**, 248–253.

165 P. Guardia, A. Labarta and X. Batlle, *J. Phys. Chem. C*, 2011, **115**, 390–396.

166 A. Wooding, M. Kilner and D. B. Lambrick, *J. Colloid Interface Sci.*, 1991, **144**, 236–242.

167 S. E. Khalafalla and G. W. Reimers, *IEEE Trans. Magn.*, 1980, **16**, 178–183.

168 R. Lenin and P. A. Joy, *J. Phys. Chem. C*, 2016, **120**, 11640–11651.

Stellenbosch University https://scholar.sun.ac.za

169 A. C. Grigorie, C. Muntean and M. Stefanescu, *Thermochim. Acta*, 2015, **621**, 61–67.

170 L. Zhang, R. He and H. Gu, 2006, **253**, 2611–2617.

171 L. L. Vatta, J. Kramer and K. R. Koch, *Sep. Sci. Technol.*, 2007, **42**, 1985–2002.

172 G. R. Newkome and C. D. Shreiner, *Polymer (Guildf).*, 2008, **49**, 1–173.

173 L. Shen, P. E. Laibinis and T. A. Hatton, *Langmuir*, 1999, **15**, 447–453.

174 Y. Niu, R. Qu, H. Chen, L. Mu, X. Liu, T. Wang, Y. Zhang and C. Sun, *J. Hazard. Mater.*, 2014, **278**, 267–278.

175 Y. H. Niu and R. M. Crooks, *Chem. Mater.*, 2003, **15**, 3463–3467.

176 R. W. J. Scott, O. M. Wilson and R. M. Crooks, *J. Phys. Chem. B*, 2005, **109**, 692–704.

177 S. M. Diallo, S. Christie, P. Swaminathan, H. J. Johnson and A. G. I. William, *Environ. Sci. Technol.*, 2005, **39**, 1366–1377.

178 Y. X. Ma, D. Xing, W. J. Shao, X. Y. Du and P. Q. La, *J. Colloid Interface Sci.*, 2017, **505**, 352–363.

179 M. S. Diallo, L. Balogh, A. Shafagati, J. H. Johnson, W. A. Goddard and D. A. Tomalia, *Environ. Sci. Technol.*, 1999, **33**, 820–824.

180 B. Van der Bruggen, M. Mänttäri and M. Nyström, *Sep. Purif. Technol.*, 2008, **63**, 251–263.

181 R. W. J. Scott, H. Ye, R. R. Henriquez and R. M. Crooks, *Chem. Mater.*, 2003, **15**, 3873–3878.

182 Y. Kim, S. Oh and R. M. Crooks, *Chem. Mater*, 2004, **16**, 167–172.

183 K. Esumi, A. Suzuki, A. Yamahira and K. Torigoe, 2000, 2604–2608.

184 L. Wang, H. Peng, S. Liu, H. Yu, P. Li and R. Xing, *Int. J. Biol. Macromol.*, 2012, **51**, 701–704.

185 A. Kraus, K. Jainae, F. Unob and N. Sukpirom, *J. Colloid Interface Sci.*, 2009, **338**, 359–365.